



**UNIVERSITAT POLITÈCNICA
DE CATALUNYA
BARCELONATECH**

Programa de Doctorat en Enginyeria del Terreny

Programa de Doctorado en Ingeniería del Terreno

Doctoral Programme in Geotechnical Engineering

Advanced exploitation of Sentinel-1 data for supporting landslide risk analysis

Explotació avançada de dades Sentinel-1 per donar suport a l'anàlisi de riscos
d'esllavissades

Explotación avanzada de datos Sentinel-1 como ayuda en el análisis de riesgo de
deslizamientos

PhD candidate: Anna Barra

Supervisors: Oriol Monserrat and Gerardo Herrera

Tutor: Josep Gili

Table of Contents

Resumen.....	3
Abstract	4
<i>Prelude</i>	4
1 Introduction.....	5
1.1 Background.....	5
1.2 Objectives.....	7
1.3 Thesis context.....	8
1.3.1 Safety - Sentinel for Geohazards regional monitoring and forecasting	8
1.3.2 MOMIT – Multiscale Observation and Monitoring of railway Infrastructure Threats.....	9
1.3.3 U-Geohaz – Geohazard Impact assessment for urban areas	9
1.3.4 RISKCOAST- Development of tools to prevent and manage geological risks on the coast linked to climate change	9
1.4 Thesis Content.....	10
2 Satellite Interferometry.....	11
2.1 InSAR fundamental.....	11
2.2 Acquisition geometry	13
2.3 Basic concepts and terminology.....	16
2.4 Multi Temporal InSAR processing	19
2.4.1 Processing steps	20
2.5 Sentinel-1	23
3 Workflow and Methodology	26
3.1 First insights on the potential of Sentinel-1 for landslides detection	26
3.2 A methodology to detect and update active deformation areas based on Sentinel-1 SAR images	30
3.3 Fast detection of ground motions on vulnerable elements using Sentinel-1 InSAR data.....	32
3.4 ADAtools: Automatic detection and classification of active deformation areas from PSI displacement maps	33
3.5 Satellite interferometric data for landslide intensity evaluation in mountainous regions.....	34
3.6 From MTInSAR displacement gradients to the generation of potential damage maps	36
4 A methodology to detect and update active deformation areas based on Sentinel-1 SAR images ...	42
5 ADAtools: Automatic detection and classification of active deformation areas from PSI displacement maps.....	62
6 Satellite interferometric data for landslide intensity evaluation in mountainous regions.....	88

7 Conclusions..... 105

7.1 Ongoing research and future developments 106

Acknowledgments..... 108

References..... 109

Annex 1 First insights on the potential of Sentinel-1 for landslides detection 118

Annex 2 Fast detection of ground motions on vulnerable elements using Sentinel-1 InSAR data..... 129

Resumen

La interferometría satelital radar (InSAR) y la interferometría de dispersores persistentes (PSI) son herramientas consolidadas para la detección y el monitoreo de movimientos de la superficie de la Tierra. Sentinel-1 (S1) es el primer satélite que proporciona acceso gratuito a los datos y garantiza una adquisición regular en todo el mundo, cada 6 días, aumentando su potencial para aplicaciones de monitoreo a largo plazo. Varios Ground Motion Services regionales y nacionales ya están activos, proporcionando productos basados en datos S1. Pronto, en 2022, el primer servicio europeo (European Ground Motion Service - EGMS) estará disponible y facilitará libremente un mapa de movimientos de toda Europa, con actualizaciones anuales. Esto implica un aumento de la disponibilidad de mapas de movimientos basados en PSI y un fácil acceso para cualquier persona, con un interés creciente entre una amplia gama de usuarios, incluyendo instituciones públicas o gubernamentales, academias, industrias y ciudadanos. El análisis e interpretación de esta cantidad de datos es difícil y consume mucho tiempo, mayormente para usuarios no expertos en la técnica. El objetivo de este trabajo es desarrollar metodologías para simplificar el uso operativo de los mapas de desplazamiento PSI, generando productos derivados con un mensaje claro, fácil de interpretar, y rápido de leer. Se propone un método para detectar rápidamente las Áreas de Deformación Activas (ADAs) más significativas, a partir de mapas de desplazamiento PSI de escala regional. El mapa de las ADAs es un primer producto que permite un enfoque rápido en las áreas activas, útil para priorizar el análisis y las investigaciones adicionales. A partir de las ADAs, se propone una interpretación preliminar basada en datos auxiliares, que atribuye a cada área el fenómeno que está detrás del movimiento, generando el Geohazard Activity Map (GAM). Después, se propone una metodología para incluir la información de las ADAs en las actividades de protección civil, generando los Vulnerable Element Activity Maps (VEAM), a través de su aplicación en las Islas Canarias. Además, el mapa de las ADAs se utiliza en la región de Valle D'Aosta (norte de Italia) para generar mapas de vulnerabilidad y posibles pérdidas económicas. Finalmente, se propone una metodología para obtener mapas de daños potenciales de los edificios expuestos, basados en los gradientes espaciales de movimiento, y se aplica en un área costera de la provincia de Granada (España). A partir de los métodos propuestos para extraer y clasificar las ADAs, y de otros métodos de análisis existentes, se ha desarrollado un paquete de herramientas, los ADATools, de acceso abierto, fáciles de usar y rápidas, que optimizan la explotación operativa de los mapas de desplazamiento de escala regional. Todas las metodologías se han desarrollado en el marco de varios proyectos europeos (Safety, U-Geohaz, MOMIT y RISKCOAST), y están dirigidos a apoyar las actividades de gestión territorial y análisis de riesgos, con un enfoque específico a los deslizamientos de tierra.

Abstract

Satellite Synthetic Aperture Radar Interferometry (InSAR) and Persistent Scatterer Interferometry (PSI) are now consolidated tools for ground movement detection and monitoring. Sentinel-1 (S1) is the first satellite providing free data access and ensuring a regular acquisition worldwide, every 6 days, increasing its potential for long-term monitoring applications. Several regional and national ground motion services are already active, providing products based on S1 data. Soon in 2022 the first European Ground Motion Service (EGMS) will be available and freely provide a displacement map over the whole Europe, with annual updates. This implies a strong expansion of availability of PSI-based displacement maps and an easy access for anyone, with an increasing interest among a wider range of users, including public or governmental institutions, academia, industry, and citizens. The analysis and interpretation of this amount of data is difficult and time consuming, mostly for non-expert InSAR users. The objective of this work is developing methodologies to simplify the operational use of PSI displacement maps, generating derived products with a clear message, easy-to-interpret, and fast to read. We propose a method to be applied over regional scale PSI displacement maps, to fast detect the most significant Active Deformation Areas (ADAs). The ADA map is a first product that allows a fast focusing on the active areas, to prioritize further analysis and investigation. Starting from the ADAs, the potential phenomena are attributed to each area through a preliminary interpretation based on auxiliary data, to derive the Geohazard Activity Map. In this work, a methodology to include the ADA information in the Civil Protection Activities is proposed, with the main output called Vulnerable Elements Activity Maps (VEAM). An application of the VEAM is illustrated in the Canary Islands. Furthermore, the ADA map is used in the Valle d'Aosta Region (Northern of Italy) to generate vulnerability and potential loss maps. Finally, a methodology to derive potential damage maps of the exposed buildings, based on the spatial gradients of movement, is proposed, and applied in a coastal area of the Province of Granada (Spain). A pack of software tools has been developed based on the proposed methods to extract ADA and then classify them to generate a Geohazard Activity Map. The set of tools is called ADATools, it is open-access, easy to use and fast, improving the operational exploitation of PSI regional-scale displacement maps. All the methodologies have been developed in the frame of several European projects (Safety, U-Geohaz, MOMIT and RISKCOAST), and are aimed at supporting the multi-scale territorial management and risk analysis activities, with a specific focus on landslides.

Prelude

This work stems from my investigation activities as research assistant at CTTC. My stay there started with a 9-month scholarship from the University of Rome Sapienza, in March 2015. Then I have been working at CTTC as research assistant until March 2022. When I arrived, the first satellite Sentinel-1 was recently launched, and my new colleagues of the Geomatics Division were adapting their software chain to process those novel data. I was totally new in the world of satellite interferometry and suddenly submerged in this processing-adaptation process and 'influenced' by the enthusiasm for the latest satellite, Sentinel-1. My new colleagues made me feel part of the group since the beginning and dedicated me time to ease my introduction to this topic. I felt very lucky to meet them, and to arrive at CTTC exactly in that moment. We started exploring together the potentialities of Sentinel-1 for landslide detection and monitoring, and this was the real starting point of my PhD research. After one year, when I achieved the temporal position, in March 2016, I decided to officially start my PhD. At the same time, my first paper was accepted for publication, the second Sentinel-1 satellite was almost to be launched, and my first European Project (Safety) was starting.

1 Introduction

1.1 Background

A spatial and temporal characterization of ground movements and an updated hazard zoning or susceptibility map are fundamental tools for risk reduction activities and for a sustainable urban planning and development (Cascini et al., 2013; Mateos et al., 2020). From the research developed by Mateos et al. (2020) we learn that in the recent three years 2015-2017, 3846 damaging landslides occurred across Europe among them 143 caused 39 fatalities and 155 injured people. Moreover, it records a total of 150 fatalities and high economic losses (in the order of hundreds of millions up to 1-3 billion for each recorded country) due to 18 Multi Occurrence Regional Landslide Events (MORLEs, Crozier, 2005) in a 10-year period (2009-2019). The same work highlights the lack of legal measures to consider landslides risk in urban planning practices, and the absence of adequate landslide mapping in many European Countries, even where regulations requiring landslide maps are present. It is evident that a systematic and extensive screening of the territory would allow a prompt detection of exposed areas and an update of inventory maps and territorial plans, preventing new housing in landslide prone areas, or driving risk mitigation actions. In this perspective, remote sensing and Earth Observation (EO) techniques give us the capabilities of implementing a multi-scale and multi-frequency monitoring, from small-scale detection, with low updating frequency, to larger scale characterization and high updating frequency. The increasing need of awareness against natural hazards (“Hyogo Framework 2005- 2015”, “Sendai Framework 2015-2030”), has resulted in an increased use of EO data as an integrated operational tool for risk managers and policy makers, with the tendency of promoting open access data and software, data sharing and the integration of different observing systems. Since the end of nineties, relevant resources have been invested for national and transnational initiatives, programs and agreements to develop new EO constellations and exploitation services for different environmental applications, including rapid mapping of natural disasters. In October 1998 started the European Union's Earth Observation Programme GMES (Global Monitoring for Environment and Security), then called Copernicus from 2012. Copernicus is aimed at developing European information services, openly accessible to users, based on both satellite EO and non-space data (“Copernicus - The European Union’s Earth Observation Program”). Between them, it is worth mentioning the Copernicus Emergency Management Service (Copernicus EMS), which “provides all actors involved in the management of natural disasters, man-made emergency situations, and humanitarian crises with timely and accurate geo-spatial information derived from satellite remote sensing and completed by available in situ or open data sources”.

Among the EO techniques, satellite Synthetic Aperture Radar (Radio Detection And Ranging) Interferometry (InSAR) has been consolidated as a reliable and valuable tool for ground movements detection, measurement, and monitoring. SAR is an active system that overcomes the optical limitations due to cloud coverage or sunlight absence and provides complementary information to other EO techniques. Some examples of satellite interferometry applications are geological hazards detection and characterization (Calò et al., 2014; Massonnet et al., 1995, 1993; Massonnet and Feigl, 1998; Reyes-Carmona et al., 2021, 2020), risk assessment (Solari et al., 2020a, 2018), monitoring worksites (Botey i Bassols et al., 2021), engineering and mining (Krishnakumar et al., 2021; López-Vinielles et al., 2020; Solari et al., 2020b). In 1989 InSAR was applied for the first time to measure the expansion of water-absorbing clays, with the L-band Seasat sensor (Gabriel et al., 1989). Then, a continuous global SAR acquisition started at the beginning of nineties, when the European Space Agency (ESA) launched the medium resolution (C-band) satellites ERS-1 (1991-2000) and ERS-2 (1995-2011), followed by ENVISAT (2001-2012),

with free-of-charge access to online datasets. In parallel, other commercial satellites were launched, like RADARSAT 1/2 (CSA - Canadian Space Agency) and the high resolution (X-band) COSMO-SkyMed (ASI - Italian Space Agency) and TerraSAR-X (DLR - German Aerospace Center). The increased availability of satellite data and the funding of international projects, such as TerraFirma (2003-2014) (The TerraFirma Atlas, 2009; TerraFirma - EGD) and PanGeo (2011-2014), allowed the improvement and validation of different processing techniques (Novellino, 2017), generally called Multi Temporal InSAR, Advanced-InSAR (A-InSAR) or Persistent Scatterer Interferometry (PSI) (Crosetto et al., 2016). We are now able to derive high density of Measurement Points (MP) or Persistent Scatterers (PS) to measure centimetric to millimetric displacements of landslides, volcanos, subsidence, or even a single sector of a building. Moreover, the availability of historical dataset allows back-analysis and assessments. However, the monitoring exploitation of InSAR data faced a major operational limitation due to lack of a systematic source of radar images ("EGMS White Paper," 2017).

The new satellite generation is improving the monitoring capability, ensuring regular acquisitions with high temporal frequency and a free-for-all data access. Sentinel-1 (S1) A and B were launched respectively in 2014 and 2016 to supply the data needs of Europe's Copernicus programme, representing the first mission with those data requirements. S1 was designed to continue the data flow provided by the previous ESA missions, with a drastically improved temporal sampling and spatial coverage, and to provide a reliable operational service and consistent long term data archive (Salvi et al., 2012; Snoeij et al., 2008; Torres et al., 2012). It represents a turning point of satellite interferometry as a reliable tool for cost-effective systematic monitoring, at both regional and local scale. Starting from S1, more and more Ground Motion Services (GMS) have been emerging, providing PSI displacement maps that are freely accessible for anyone. Figure 1 shows the status of national GMS in June 2020. Some of them, like Germany (Kalia, 2017; Kalia et al., 2017), Norway (Dehls et al., 2019) and Italy are fully operational, others are in pre- or near-operational phase (Netherlands and Denmark), and in several countries are under development (Novellino et al., 2017; Papoutsis et al., 2020). In Italy, several operational continuous monitoring services are active at regional scale (Confuorto et al., 2021; Montalti et al., 2019; Raspini et al., 2018).

In the first semester of 2022, the first continental PSI displacement map of the new European Ground Motion services (EGMS) (Costantini et al., 2021; Crosetto et al., 2021, 2020a, 2020b) will provide ground displacement maps, actualized every year, freely accessible through a web Geographic Information System (GIS) portal. The direct consequence of S1 and the launch of GMSs is an increasing accessibility to satellite interferometry data and products, and thus an increasing interest among a wider range of users, including public institutions, industry, academia and even citizens. The EGMS represent an improvement in the exploitation of S1 data. However, the potential of both S1 and GMSs is still not fully and systematically exploited. The analysis and interpretation of this huge amount of data can be difficult, time consuming and not effective, especially for non-expert users. In this context, it is necessary to develop semi-automatic tools and methodologies to generate operational and interpreted products. In the last years, the research community and several European projects (e.g. Safety, U-geohaz, RISKCOAST, MOMIT, etc.) have been focused on post-processing methods to ease the interpretation and use of InSAR and PSI products and to make them more usable for non-expert users (Barra et al., 2018, 2017b; Boni et al., 2016; Bovenga et al., 2021; Mirmazloumi et al., 2022; Monserrat et al., 2018; Notti et al., 2014; Raspini et al., 2018).

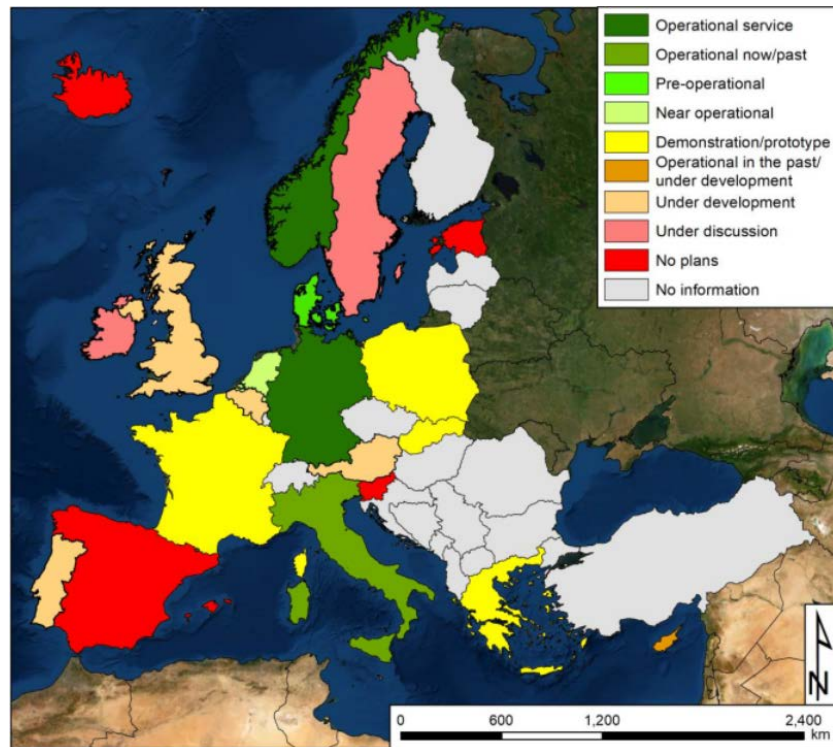


Figure 1 Status of Ground Motion Services in Europe (EEA Report, 2020).

1.2 Objectives

The main objective of this thesis is facilitating the full and operational exploitation of S1 data, for supporting geohazard management and risk analysis, with a specific focus on landslides. This objective can be achieved facing both processing and post-processing aspects. Processing regards the techniques to get the higher number of information (in terms of spatial coverage and temporal updating) with the minimum time and computational efforts. Post-processing regards all the methodologies and tools directed at the improved use of the processing results. This thesis focuses on the post-processing part.

The main aspects that limit the S1 data exploitation are the following:

- Satellite interferometry is not a straightforward technique. The accessibility of displacement maps is making them available to a wide range of users, most of them with few knowledge about InSAR. The InSAR derived displacement maps can be difficult to interpret, originating misunderstandings if accessed by not-expert users.
- The regional-scale application implies a huge amount of data that is time-consuming to be analysed and thus not suitable for an operational use.
- The regional-scale application implies a multi-target and multi-magnitude phenomena detection.

Overcoming those aspects is achieved by developing semi-automatic methodologies to fast derive reliable key information, and simplify the data communication, generating maps that can be operationally used by any user. The proposed methodologies are developed with the aim of being useful for the territorial and risk management at different scales, starting from a wide area displacement map.

Moreover, when this work started S1 was recently launched, and its potentialities were already clear. Nevertheless, there were many uncertainties related to the adaptation of the data processing software;

the data reliability, in terms of real availability and download facilities; and more in general to the satellite performances.

Based on those aspects, the Specific Objectives (SOs) of my thesis have been:

1. Testing the recently launched S1, exploring its capabilities and potentialities, and evaluating the usefulness of its short revisit time.
2. Assessing a preliminary methodology to exploit S1 in landslide and geohazards detection and monitoring.
3. Developing specific methodologies and tools for the operational use of regional scale displacement maps by non-expert users in geohazard management and risk analysis.
4. Simplifying the information communication to users, proposing effective maps with fast and easy readability.

The SOs have been achieved through several activities resumed in Section 3 (Workflow and Methodology) and explained in 5 published journal articles, plus one recently submitted to Remote Sensing of Environment.

1.3 Thesis context

The activities of my thesis have been possible thanks to a pre-doctoral collaboration between the Remote Sensing Department of CTTC and the Earth Sciences Department of Sapienza University of Rome (Italy). The aims of the collaboration were in line with the SOs 1 and 2 of this thesis. My first year at CTTC (March 2015 – March 2016) was supported by a 9-months scholarship from Sapienza University of Rome, representing the starting point of my PhD work. In this context the first article, included in this thesis as Annex 1, was published and disseminated (Barra et al., 2017a, 2016). From March 2016 to March 2022, I was part of the Remote Sensing Department of CTTC, where, among other activities, the investigations of my PhD have been developed. Its results and methodologies have been obtained in the frame of several European Projects related with the objectives of my PhD. Here I resume these projects.

1.3.1 Safety - Sentinel for Geohazards regional monitoring and forecasting

Safety (ref. ECHO/SUB/2015/718679/Prev02-SAFETY) was founded by the European Commission, Directorate-General Humanitarian Aid and Civil Protection (ECHO). The main objective of Safety (01/01/2016 – 31/12/2017) was developing and testing a procedure to provide Civil Protection Authorities (CPA) with the capability of periodically evaluating and assessing the potential impact of geohazards (volcanic activity, landslides, and subsidence) on urban areas and infrastructures, over regional areas, using S1 SAR data. Safety was in line with the SOs 3 and 4 of my thesis. The methodologies described in Barra et al. (2017b) and Solari et al. (2018), have been developed in the frame of this project and are part of this thesis as Section 4 and Annex 2, respectively. The direct participation in this project allowed me to take part of all the meetings, presenting the developed results, making a presentation in the Safety workshop, and one lecture in the Safety training. Moreover, among the dissemination activities, the results could be presented at several international conferences (Barra et al., 2018, 2017c; Monserrat et al., 2018, 2017).

Website: <https://safety.cttc.cat/>

1.3.2 MOMIT – Multiscale Observation and Monitoring of railway Infrastructure Threats

MOMIT (Ref. H2020 – 777630) was founded by Shift2Rail Joint Undertaking under the European Union's Horizon 2020 research and innovation programme. The objective of MOMIT (1/09/2017 – 30/10/2019) was developing a new use of remote sensing technologies for railway infrastructures monitoring with the aim of supporting the maintenance and prevention processes within the infrastructure management lifecycle. MOMIT wanted to demonstrate the benefits brought by Earth Observation and Remote Sensing to the monitoring of railways networks both in terms of the infrastructure and of the surrounding environment, where activities and phenomena impacting the infrastructure could be present. I participated in this project in the activities to implement the pack of software tools *ADATools* (Tomás et al., 2019). Specifically, the methodology algorithm explained in Barra et al. (2017b, Section 4) has been developed in the software ADAFinder (Navarro et al., 2018). Moreover, I also participate to the implementation of the algorithm of the tool ADAClassifier. The ADATools are explained in Navarro et al. (2020), which is part of this thesis as Section 5. The development of the ADATools is in line with the SOs 3 and 4 of my PhD. (Navarro et al., 2019a, 2019b).

Website: <https://www.momit-project.eu/>

1.3.3 U-Geohaz – Geohazard Impact assessment for urban areas

U-Geohaz (ref. UCPM-2017-PP-AG – 783169 U-Geohaz) was founded by the European Commission, Directorate-General Humanitarian Aid and Civil Protection (ECHO). U-Geohaz (01/01/2018 – 31/12/2019) aimed to advance with respect to SAFETY, evolving from periodically updated maps to a near-real time mapping and monitoring of geohazards activity, and filling the gaps detected in the Safety project. The main objective of U-Geohaz was providing maps, based on S1 6-day ground deformations monitoring, to continuously assess the potential impact of geohazard activity to urban areas and critical infrastructures, and to be used as key inputs to support early warning and impact assessment. U-Geohaz was in line with the SO 3, and 4 of my PhD. The methodology described in Solari et al. (2020a) has been developed in the frame of this project and is part of this thesis as Section 6. The results were presented at several international conferences (Barra et al., 2019; Bianchini et al., 2021; Monserrat et al., 2019). Again, the direct participation in this project allowed me to take part of all the meetings, presenting the developed results, making a presentation in the U-Geohaz workshop, and one lecture in the U-Geohaz training.

Website: <https://u-geohaz.cttc.cat/>

1.3.4 RISKCOAST- Development of tools to prevent and manage geological risks on the coast linked to climate change

RISKCOAST (Ref. SOE3/P4/E0868) has been founded by the European Regional Development Fund (ERDF) under the Interreg SUDOE Programme. The main objective of RISKCOAST (01/10-2019 - 30/09/2022) is developing innovative tools and methodologies focused on the prevention and management of geological risks on the coast in a more effective way. The products obtained are aimed to support the three phases of emergency management: prevention, response, and rehabilitation. In the frame of RISKCOAST the ADATools have been applied and the results presented in Navarro et al. (2020) (Section 5). Moreover, the methodology shortly explained in Section 3.6, and submitted to Remote Sensing of Environment, is part of the results of RISKCOAST, and in line with the SOs 3 and 4. My direct involvement in this project allowed me to participate to all the meetings and to present the developed results (Barra et al., 2021c, 2020).

Website: <https://riskcoast.eu/es>

1.4 Thesis Content

The thesis starts with a description of the main characteristics of Satellite Interferometry ([Section 2](#)), including the processing steps, and a specific part describing the specifics of Sentinel-1. Then, the PhD workflow is presented in [Section 3](#), where after an introduction of the general methodology, the main journal papers (included or annexed in this work) are presented and contextualized. Moreover, a work recently submitted to Remote Sensing of Environment is resumed in the same section. The next 3 sections correspond to the articles selected for this thesis, specifically, “A methodology to detect and update active deformation areas based on Sentinel-1 SAR images” (Barra et al., 2017b) in [Section 4](#), “ADAtools: Automatic detection and classification of active deformation areas from PSI displacement maps” (Navarro et al., 2020) in [Section 5](#), and, “Satellite interferometric data for landslide intensity evaluation in mountainous regions” (Solari et al., 2020a) in [Section 6](#). In section 7 the conclusions of the presented work and the future perspective concludes the thesis. Afterall, two journal papers are annexed, to complete the documentation of the main work done for the PhD project: “First insights on the potential of Sentinel-1 for landslides detection” (Barra et al., 2016), in [Annex 1](#), and “Fast detection of ground motions on vulnerable elements using sentinel-1 InSAR data” (Solari et al., 2018), in [Annex 2](#).

2 Satellite Interferometry

Satellite SAR Interferometry allows us measuring the displacements occurred between two or more images acquired over the same area in different times. The aim of this section is to explain the main characteristics of InSAR acquisition, processing, and results. Firstly, the fundamental of the technique (Section 2.1) and the main characteristics with the consequent limitations (Section 2.2) are explained. Section 3.3 introduces basic concepts and terminology, and Section 3.4 explains the main steps of a Multi Temporal InSAR processing.

2.1 InSAR fundamental

Synthetic Aperture Radar (SAR) is an active remote sensor, which sends microwave pulses and register the signal backscattered by the illuminated area. This allows to measure day and night and in any meteorological condition. Each pixel of a complex SAR image contains two values, which are the amplitude and the phase. The first one is related to the power of the electromagnetic signal, backscattered by the ground footprint of the pixel, and received by the sensor. The amplitude (i.e., intensity of the signal) depends on the ground surface characteristics like the shape, orientation, roughness, and electrical properties. Figure 2 schematically shows how the signal, sent by the spaceborne sensor, is backscattered by the surface elements. We have a strong backscattering (represented by long arrows in Figure 2) in correspondence of anthropic elements or rock outcrops, a medium intensity of the backscattered signal in vegetated areas, where part of the signal is dispersed in other directions (red arrows), and very low or null in water bodies, which actuate like a mirror, sending the signal in the opposite direction. Figure 3 is a comparison between a satellite optical image and the SAR amplitude of the same area (coast of Granada region, southern Spain), we see how the brighter pixels are located over urbanized areas.

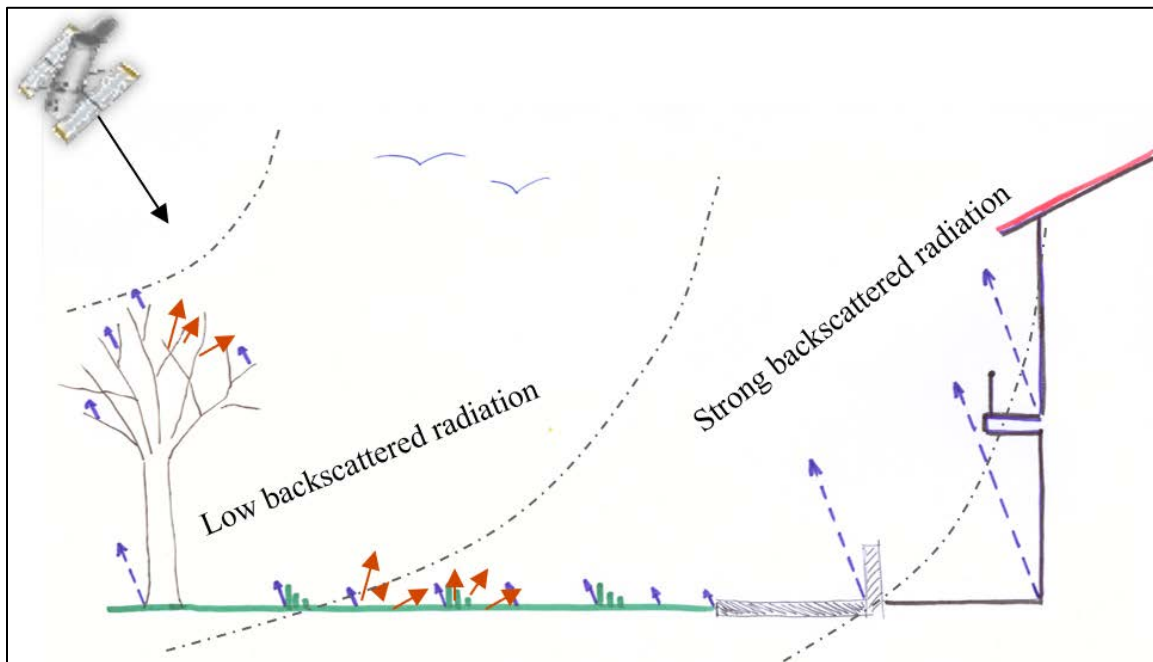


Figure 2 Schematic representation of the SAR signal backscattering power of different surface elements.

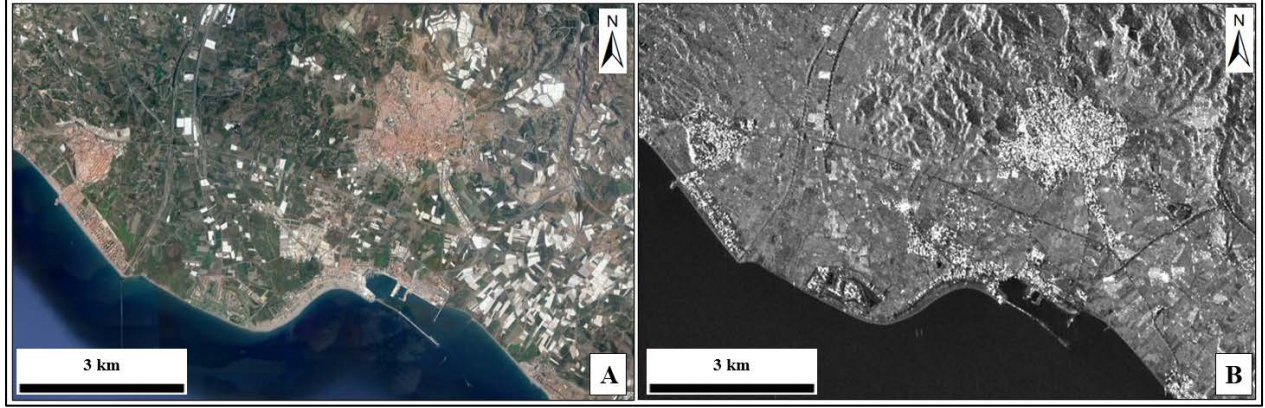


Figure 3 Comparison between an optical image (A) and a SAR amplitude image (B) of the same area (Motril, Granada, Spain).

The phase that the SAR sensor registers in the image mainly depends on the sensor to target distance, the atmosphere the signal has travelled across, and the characteristics of the backscattering elements within each pixel ground footprint. Let us focus on the main component, the geometric one (ϕ_{geom_M}), which is related to the two-way distance (MP, Figure 4) travelled by the signal from the sensor position M to the pixel footprint P, and vice-versa. Being λ the radar wavelength, the geometric phase received by the sensor is expressed by:

$$\phi_{geom_M} = \frac{2 \cdot \pi \cdot 2 \cdot MP}{\lambda} = \frac{4 \cdot \pi \cdot MP}{\lambda} \quad (1)$$

At a second pass to acquire over the same area, the satellite changes its position (S), within the same *orbital tube* (Prats-Iraola et al., 2015), resulting in a different SP distance and thus a different geometric component (ϕ_{geom_S}). If in the time between the two acquisitions the ground footprint suffers a movement from P to P' we have:

$$\phi_{geom_S} = \frac{4 \cdot \pi \cdot SP'}{\lambda} \quad (2)$$

To measure centimetric to millimetric displacements, the InSAR technique exploits the phase difference (i.e., interferometric phase) between two acquisitions, which is given by:

$$\Delta\phi_{geom_Int} = \phi_{geom_S} - \phi_{geom_M} = \frac{SP' - MP}{\frac{\lambda}{4 \cdot \pi}} \quad (3)$$

We can separate the component related to the topography (ϕ_{topo}) and the component related to the displacement (ϕ_{disp}):

$$\Delta\phi_{geom_Int} = \phi_{topo} + \phi_{disp} = \frac{SP - MP}{\frac{\lambda}{4 \cdot \pi}} + \frac{SP' - SP}{\frac{\lambda}{4 \cdot \pi}} \quad (4)$$

In the equation 4, we see that the topographic component depends on the relative position of the satellites M and S; specifically, the bigger is the difference SP-MP the stronger is ϕ_{topo} . On the contrary, the displacement component is

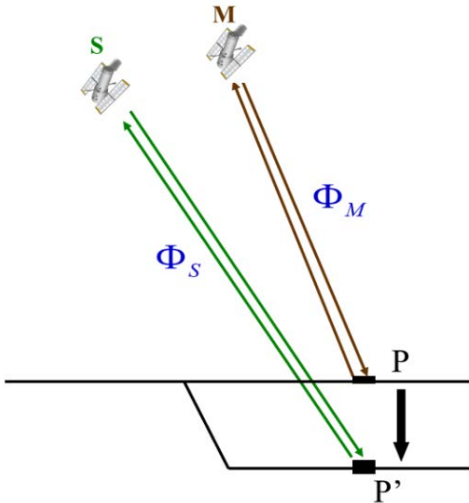


Figure 4 Schematic representation of a SAR acquisition system.

independent of such positions, allowing measuring the displacements with a centimetric to millimetric precision.

The interferometric phase registered by the sensor includes other components here resumed:

$$\Delta\phi_{Int} = \phi_{topo} + \phi_{disp} + \phi_{atm_S} - \phi_{atm_M} + \phi_{noise} + k \cdot 2 \cdot \pi \quad (5)$$

Where ϕ_{atm_S} and ϕ_{atm_M} are the atmospheric components of the two images S and M, due to the propagation of microwaves through ionosphere and troposphere at the two acquisition times; ϕ_{noise} is the noise related to changes in the ground footprint; and $k \cdot 2 \cdot \pi$ is related to the phase ambiguity k , in terms of the unknown numbers of 2π cycles (this aspect is explained later in Section 2.3). To extract the displacement, we need to estimate the other components. The topographic component can be simulated ($\phi_{topo_{sim}}$) by using a Digital Elevation Model (DEM) of the area covered by the SAR images. This can be subtracted from the interferometric phase, obtaining the so-called Differential SAR Interferometric (DInSAR) phase:

$$\Delta\phi_{D_Int} = \phi_{topo_{res}} + \phi_{disp} + \phi_{atm_S} - \phi_{atm_M} + \phi_{noise} + k \cdot 2 \cdot \pi \quad (6)$$

Where $\phi_{topo_{res}}$ is the residual topographic component, i.e., the difference between the DEM and the real position of the backscattering element (of z-position of the MP), which is due to an inaccuracy in the computation of $\phi_{topo_{sim}}$, or to a not precise DEM. Note that, in the following, InSAR and DInSAR will be used as synonyms, and that the DInSAR phase (Eq. 6) will be called *interferogram*. The *perpendicular baseline* of an interferogram is related to the distance between the two positions S and M measured in the direction perpendicular to the line-of-sight, whereas the time passed between the two acquisitions is called *temporal baseline*. The estimation of the atmospheric and residual topographic components is explained below in the processing steps. We need models (and assumptions) and appropriate estimation procedures to get the parameters of interest. All the components are measured in the radar Line-Of-Sight (LOS), which is the line that connects the sensor and the pixel footprint on the ground. This aspect is also part of the limitations and will be explained in Section 4.3.

2.2 Acquisition geometry

A radar system transmits the signal towards the ground surface in an oblique direction (with a *look angle*, also called *Off-Nadir angle*), illuminating a surface area with an extension (*swath*) that depends on the system and acquisition mode. Figure 5 shows the basic terminologies to refer to a radar acquisition system. The direction parallel to the flight path is called *azimuth*, whereas the perpendicular one is called *range*. We refer to azimuth and range as reference directions of a radar image. A same area is acquired by the satellite in two geometries of acquisition: the ascending one, is acquired when the satellite goes northward and has a side-look from west to east, and the descending one, when it goes southward and has a side-look from east to west. A SAR sensor can only measure along the LOS direction, also called *slant range*, consequently it can measure only a portion of the real movement (the LOS component), depending on the direction of the movement with respect to the LOS one. The smaller the angle between the direction of the movement and the LOS (from now, LOS-MOV angle), the greater the sensitivity of the technique to measure it. The worst case is when the movement is perpendicular to the LOS, when the measured portion of movement is null. Figure 6 shows an example of two sliding movements with the same magnitude and slope angle, but different directions with respect to the satellite, which is represented in the ascending geometry. If the movement is westwards (Figure 6A), the LOS-MOV angle is smaller than if the same movement is eastward (Figure 6B), consequently the measured LOS component is higher in the first case.

Note also that a movement towards the satellite is measured as positive (as in Figure 6A) and a movement going away from the satellite is measured as negative (Figure 6B). In a descending geometry of acquisition, the situation would be the opposite. Another case of low measurement sensitivity is when the movement is along the north-south direction (approximately) being the LOS-MOV directions at a right angle.

A consequence of the range measurements is the geometric distortion in the radar image. Depending on the relative geometry between the LOS and the local topography (*local incidence angle*), the ground range spatial sampling changes. In Figure 7, where the blue triangles represent the topography and θ are the look angles, all the geometric effects are shown. When the slope looks towards the satellite, we can have two situations called *layover* and *foreshortening* effects. The first one occurs if the signal is backscattered firstly by the point B and secondly by the point A, thus the ordering of A and B on the radar image is the reverse of their ordering on the ground. We have *foreshortening* when the ground units are compressed in a few pixels of the radar image like in the case of the A2-B2 slope. Those effects happens because the time delay between the radar echoes received from two different points determines their distance in the SAR image. On the opposite hillside (e.g., the slope B-C of Figure 7) the ground spatial sampling increases, but when the slope angle increases, we can have a *shadow zone*, where no data are acquired as in the case of the slope B2-C2.

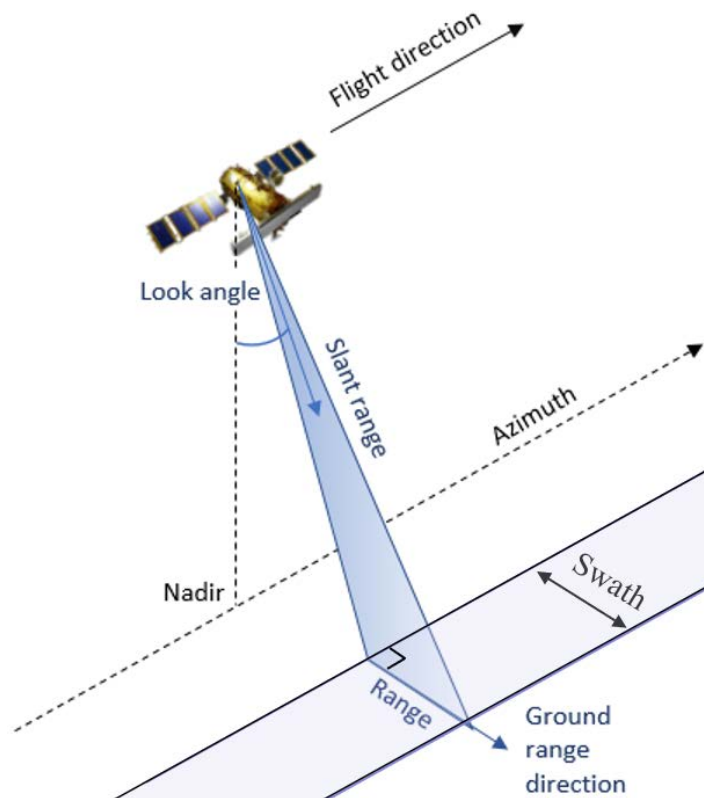


Figure 5 Representation of a SAR system directions. Modified from ("ENVI SARscape Tutorial").

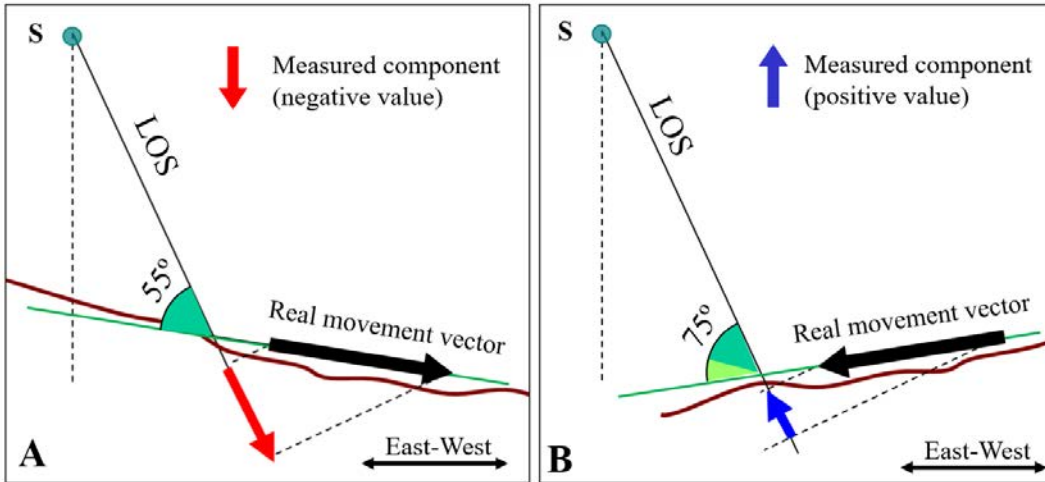


Figure 6 Example of an ascending LOS measurement (red and blue arrows) of two slope movements (black arrows), along the East-West direction, with the same magnitude and slope angle. In A the movement is westwards, going away from the satellite, in B the movement is eastwards, going towards the satellite. The LOS-MOV angles are showed.

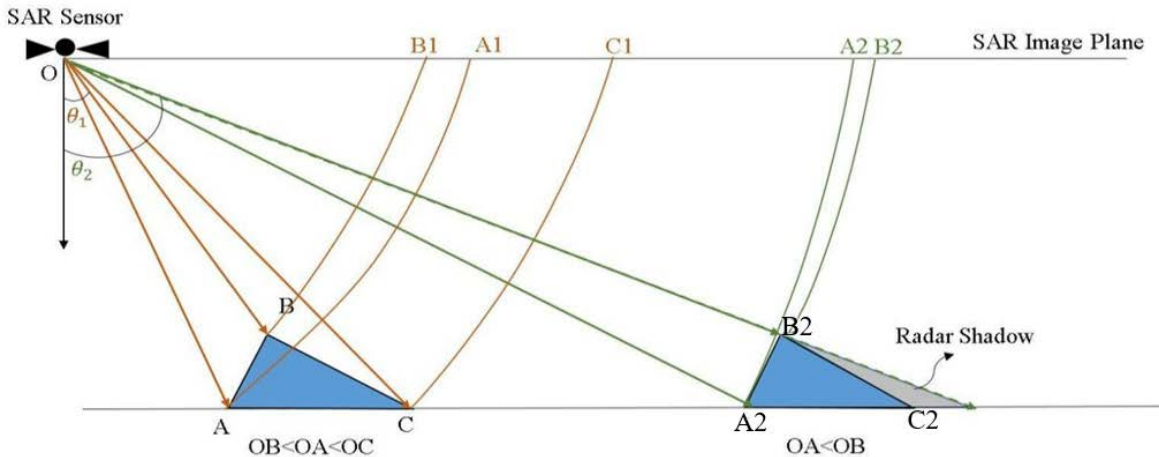


Figure 7 Schematic representation of the SAR geometric distortions. B1-A1 represents the layover effect, whereas A1-B2 represents the foreshortening effect. Modified from Sharma et al. (2018).

The explained geometric limitations must be especially considered in areas characterised by steep slopes and measuring movements with a strong horizontal component (e.g., landslide movements). To overcome these geometric limitations, a parallel processing of both ascending and descending data can be beneficial. The use of two geometries is also used to derive the horizontal and vertical (H-V) components of the movement, as represented in Figure 8 and explained in Notti et al. (2014). The H-V decomposition improves the cinematic interpretation of a phenomenon, as example, it could be crucial to understand if a landslide is mainly translational or rotational. The counterpart is that the H-V decomposition depends on the presence of both ascending and descending information for each surface unit, implying both a reduction of the spatial resolution and a loss of information where an area is not covered by both trajectories. Another approach, when a single geometry is available, is to project the LOS measurements on the maximum slope direction. This approach is used for landslide applications and helps the final users to have an easier visualization and interpretation of the results. Nevertheless, it is based on the strong assumption that the main movement is parallel to the slope, which is valid only for sliding phenomena. Moreover, the result is strictly dependent on the used DEM resolution and on the geocoding precision.

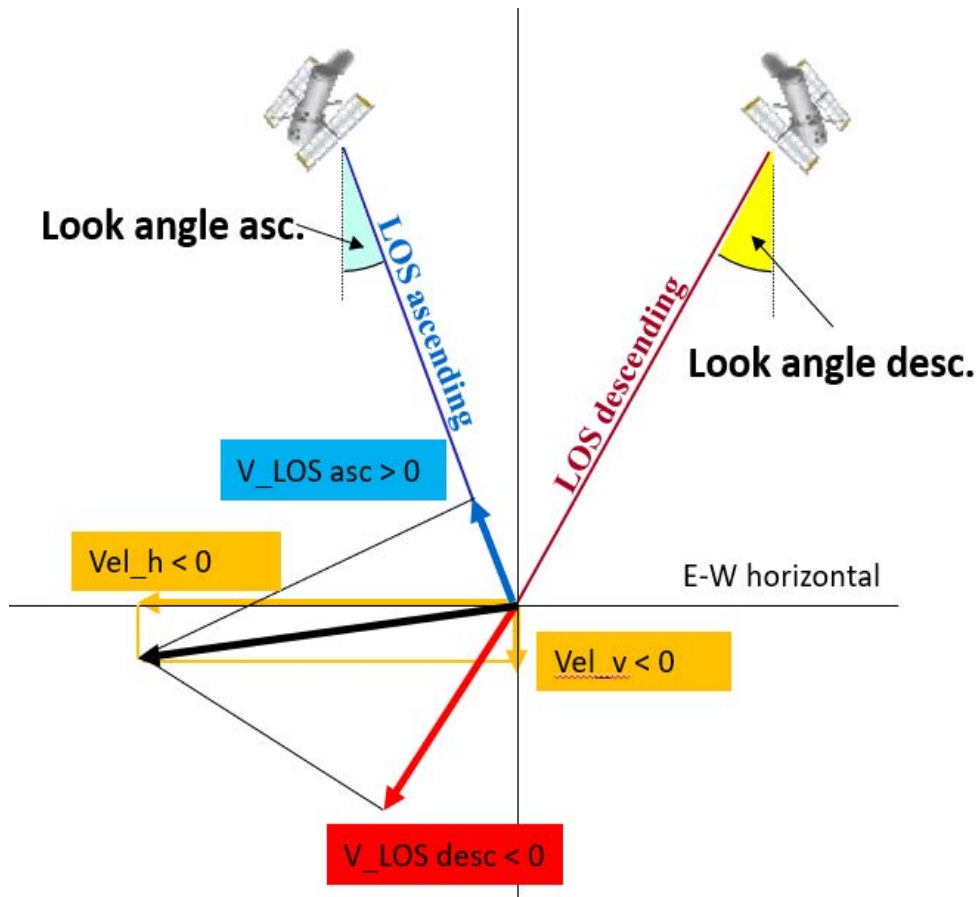


Figure 8 Schematic representation of an H-V decomposition from ascending (asc) and descending (desc) LOS measurements. Modified from Notti et al. (2014).

2.3 Basic concepts and terminology

Before explaining the main steps of a MTInSAR processing, we recall here some basic concepts and terminology to ease the text understanding.

Coherence

The coherence is a statistical parameter that evaluates the degree of similarity between two images. It represents the level of noise of the interferogram and varies between zero (low coherence, high noise) and one (high coherence, low noise). The coherence is an antonym of temporal decorrelation: it is low when the noise is high or when temporal decorrelation occurs. We expect high coherence in urban or rocky areas, and low coherence in vegetated areas or when the surface displacement is too high and spatially abrupt. In the processing, for each interferogram, its correspondent coherence image is generated. Figure 9 shows an example of coherence image (A) of an interferogram (B). The zooms show two examples of areas characterized by high (1) and low (2) coherence, the first one corresponds to an urban area. It is visible the difference in terms of the spatial correlation between the phase values of the pixels, high in 1 and lower in 2. The presence of water, as the sea in this case, causes a very low coherence, represented by a totally random distribution of the interferometric phase values.

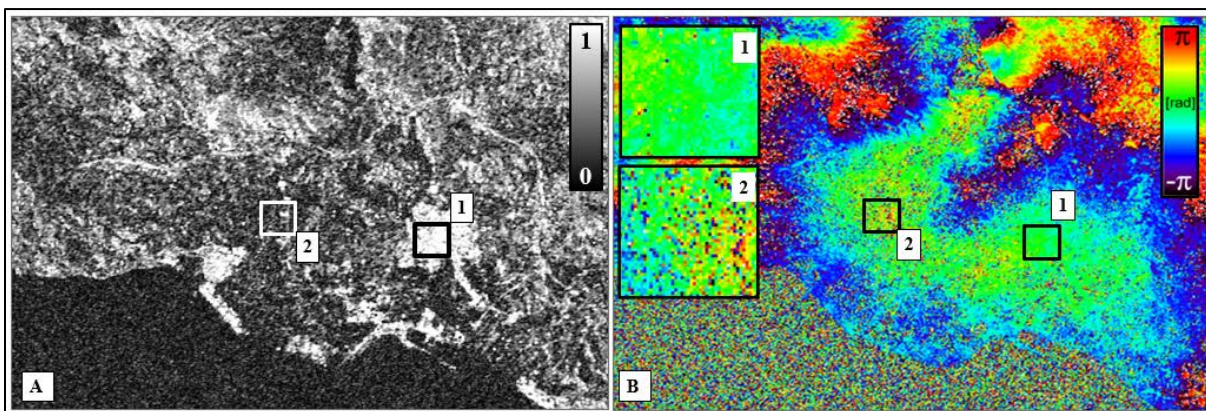


Figure 9 Example of coherence image (A) of the interferogram (B) over the coastal area of Motril, in the Province of Granada (Spain). A) The light greys represent high coherence, the darker greys low coherence. In the rectangle 1 and 2, a detail of two areas of low and higher coherence is shown. An optical and an amplitude image over the same area are showed in Figure 3.

Measurement Points

The output of a MTInSAR processing is the estimation of the mean annual velocity and of the displacement time series (TS) over a set of spatially distributed Measurement Points (MPs), also called Persistent Scatterer (PS). Not all the pixels of the image stack can be used to estimate the displacement. In fact, we can measure the displacement only over the pixels where the ϕ_{noise} component is low. This happens when the backscattering characteristics of the pixel footprint do not change much in time. The ϕ_{noise} depends on the surface characteristics, for example we can have high density of MPs over anthropic elements and rock outcrops, a lower number of MPs in agricultural areas and absence of MPs in forested areas. As we have seen before, another cause of temporal decorrelation is a “fast” movement, generating a ϕ_{disp} higher than π between neighbouring pixels. This implies the impossibility of measuring strong displacements occurred between two acquisitions. An important element that can affect both ϕ_{noise} and ϕ_{disp} is the temporal baseline. In fact, we generally expect less changes in the phase when the time passed between the two acquisitions is shorter. Moreover, if the selection of MPs is performed on the base of the temporal coherence, we can lose MPs if their movement in time is strongly nonlinear.

Temporal Coherence

The temporal coherence (γ_t) is a quality index of each MP; it describes how well the interferometric phase observations fit the model (which includes the linear displacement and the topo_res components). It varies between 0 and 1. If a linear model is used, $\gamma_t = 1$ implies that the deformation is perfectly linear over time, and the ϕ_{Noise} is zero in all N interferograms. Whereas, low coherence values can be due to “bad MP”, i.e. noisy phases, or to a strongly non-linear displacement.

Displacement model

To estimate the displacement, and solve the ambiguity in the phase unwrapping step, many processing approaches use a displacement model. The used model influences the final selection of MPs, the ones that have a behaviour that is far from the model are not selected. The most used is a linear model, which imply a strong limitation in detecting non-linear movement phenomena. Some approaches are model-free, implying a wider selection of MPs, independent of the temporal behaviour.

Phase ambiguity

We have explained before that InSAR exploits the phase difference between two SAR images acquired in two different times (t_1 and t_2), to extract the displacement. Since the phase has cyclic values ranging from $-\pi$ to π radians, the same registered phase value can result from an infinite number of distances. Consequently, the same interferometric phase can result from infinite number of displacements. Let us look at Figure 10, which graphically illustrates the phase ambiguity (k , Eq. 6). For each acquisition, the SAR system stores the position on the wave in which the echo of an object (pixel footprint) is received by the sensor. Specifically, the position is stored by registering the amplitude (A) and the phase (φ). When we calculate the phase difference between two images (interferogram), we are measuring the position changes along the received echo wave that is directly related to the displacement of the measured object. Looking at Figure 10, if two signals are received at the times t_1 and t_2 , the sensor registers the amplitude and phase A_1 and φ_1 (a) in the first image, and A_2 and φ_2 in the second one (b or c). Figure 10 shows that whether the point in t_2 is received in position (b) of the wave, which is within one wavelength (λ) with respect to t_1 , or in position (c), shifted by a wavelength ($b+\lambda$), the phase recorded in t_2 would be the same, and consequently also the phase difference. Thus, the same phase difference ($\Delta\varphi$) can represent the position (b) and all the positions $(b) \pm k\lambda$ (where k is an integer number ranging from 0 to infinity), as well as the phase difference could be $\Delta\varphi \pm k2\pi$. This aspect is generally described as "phase ambiguity". The distance of Figure 10 represents the roundtrip distance travelled by the signal, thus in terms of displacements the 2π ambiguity correspond to a $\lambda/2$ displacement. The phase ambiguity (k) estimation is performed in the phase unwrapping (see below). Errors in the k estimation are called aliasings, which are represented by phase jumps that are k multiples of 2π .

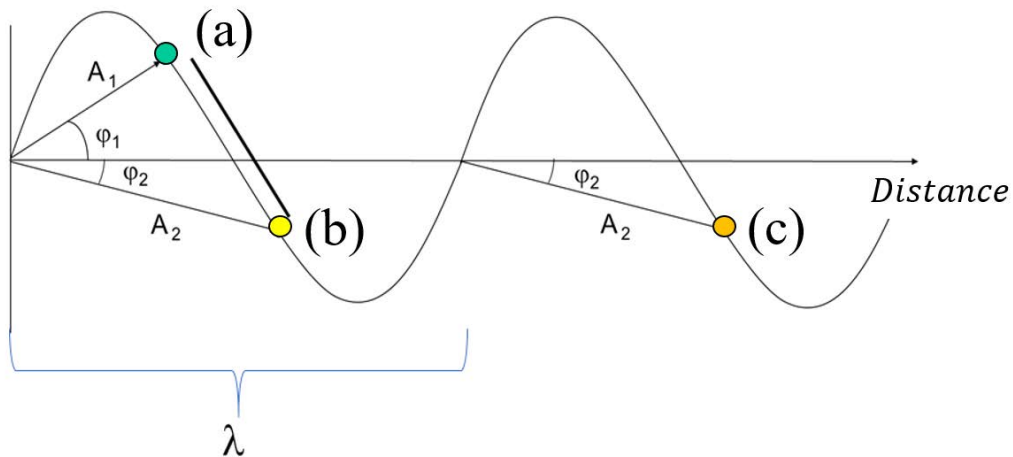


Figure 10 Schematic representation of phase ambiguity.

2.4 Multi Temporal InSAR processing

A single interferogram includes all the components of equation 6 and is most of the times showed with the wrapped phase values (i.e., between $-\pi$ and π). The information of single interferograms is used when the displacement component is stronger than the others, usually for punctual events, using single pairs of images acquired before and after the movements (Hanssen, 2001). The single-interferogram exploitation is generally called DInSAR. Some examples of application are co-seismic movements (Béjar-Pizarro et al., 2018; Vassilakis et al., 2022), subsidence related to mining activities (Przylucka et al., 2015), landslide acceleration or activations (Barra et al., 2016; Roberti et al., 2018), or glacier movements (Sánchez-Gómez and Navarro, 2017). To measure slower movements and to better estimate the phase components, it is necessary to use redundant observations. This is done by using a stack of images and generating a network of interferograms that are the observations. All the techniques based on a stack of images can be called Multi Temporal InSAR (MTInSAR). Figure 11 shows an example of a glacier delimited with a dashed line in an optical image (A), in two interferograms covering different times (B and C), and in a MTInSAR result (D). In B the spatial distribution of the movement is smoothed enough to generate a continuous interferometric phase variation between $-\pi$ and π , for a total of about 12 phase cycles (or colour fringes) corresponding to a relative displacement, between the first and the last fringes, of about 33 cm. The same glacier generates a loss of coherence in Figure 11C, due to an acceleration causing a spatially abrupt displacement between neighbouring pixels higher than $\lambda/4$. This strongly variable behaviour implies the absence of MPs in a MTInSAR result (Figure 11D). In this example, the single-interferogram information of B allows a complete spatial characterization of the movement occurred in the time covered by the image pair.

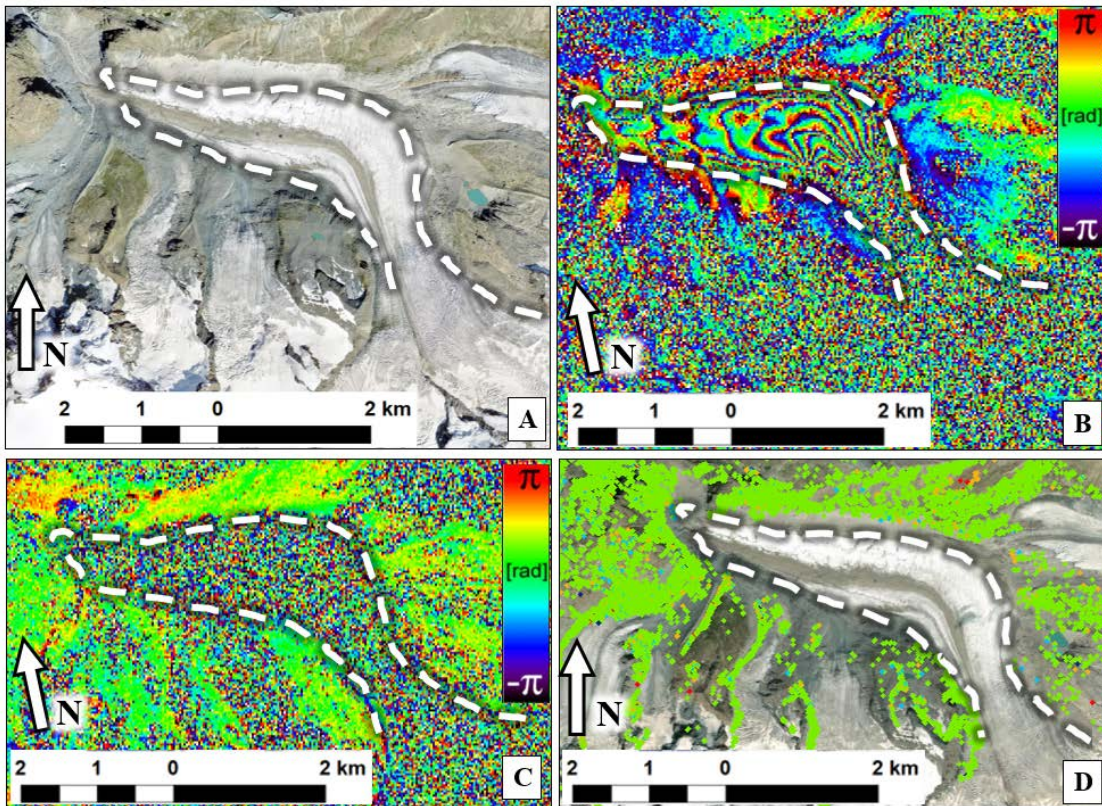


Figure 11 Example of glacial movement located in Valle d'Aosta region (Italy). The glacial shape is highlighted by the dashed line in an optical satellite image (A), in two interferograms covering two different times (B and C), the first one with good coherence and the second one with no coherence, and in a MTInSAR result (D), where no MPs are available over the glacier.

2.4.1 Processing steps

In the last decades, several MTInSAR processing approaches have been developed, which are also called Advanced InSAR (A-InSAR) or Persistent Scatterer Interferometry (PSI). Several aspects can be different between the proposed methods, like the pixel selection, the interferogram network generation, the linear-model or free-model displacement estimation, and so on. Some MTInSAR examples can be found in Ferretti et al. (2011, 2001, 2000); Berardino et al. (2002); Mora et al. (2003); Crosetto et al. (2015); Costantini et al. (2008); Hooper (2008); Hooper et al. (2004); Perissin and Wang (2012); and Devan  ry et al. (2014). Here the main processing steps for the interferogram generation and displacements estimation are explained with specific reference to the software chain developed by the Geomatic Division of CTTC (PSIG), which is the one used in this work. However, it is worth to note that some of the steps are common to all the MTInSAR processing approaches. The PSIG chain is explained in detail in Devan  ry et al. (2019, 2014). It is worth to underline that the PSIG software is adaptable depending on the specific case of study. The software is composed of several modules that can be used in different workflows, not necessarily the order explained here, adopting the one that is more appropriate for each application. Here we propose a general workflow, as showed in Figure 12.

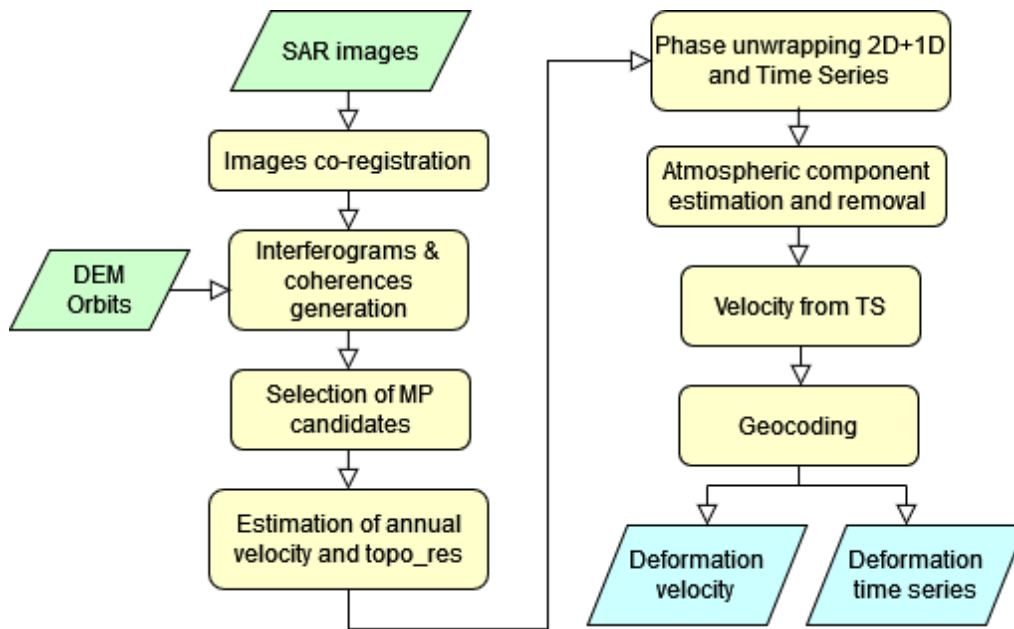


Figure 12 General workflow of the MTInSAR processing used at CTTC.

0. **Input data.** The MTInSAR procedure requires three types of input data: (i) a stack of complex SAR images covering the same area; (ii) the precise orbits corresponding to each SAR image; and (iii) a DEM of the covered area.
1. **Image co-registration.** All the SAR images needs to be co-registered, i.e. a pixel with image coordinates (i,j) of any image must correspond to the same footprint on the ground. This does not occur due to the slightly different acquisition geometries of the images. This step involves the choice of one image, to be used as geometric reference for the co-registration of all the other images. Co-registration requires the resampling of all images onto the grid of the reference one, to ensure pixel-to-pixel alignment along the entire image stack. All steps of the procedure are done in the geometry of the reference image.

2. **Interferograms and coherences generation.** The interferogram network is generated using several image-pairs combinations (Figure 13), in a way that each image is used to generate more than one interferogram (redundant network). The way the network is built depends on the processing approach and the case study. Usually, the network is based on limits imposed to the temporal or perpendicular baselines of the interferograms (Lanari et al., 2007), to reduce temporal decorrelation and topographic errors. Sometimes the coherence is used to eliminate the noisiest interferograms and the relative problematic images from the processing (Solari et al., 2020). For each pair of images, the phase difference is computed ($\phi_S - \phi_M$ in Eq. 4), and the topographic component is removed using an external DEM (Eq. 6), obtaining the differential interferometric phase. The coherence image is also computed for each interferogram (Figure 9). Then, using an external DEM and the orbits associated to the given image pair, the topographic term is simulated and subtracted from the interferometric phase.
3. **Selection of Measurement Points (MPs) candidates.** In this step are selected the so-called MP candidates. It is a first selection of the pixels that are potentially good (of low noise), however their actual quality is then evaluated during the processing. Properly identifying good MPs candidates is important for the following steps, especially the phase unwrapping and the estimation of the atmospheric component. This selection can be based on several approaches, here we use the Dispersion of Amplitude (DA) of the image stack (Ferretti et al., 2000; 2001). A pixel is considered a MP candidate if its DA is low, meaning that the backscattered energy is strong and stable in time.
4. **Estimation of annual velocity and topo_res.** The displacement velocity and the topographic residuals (topo_res) are estimated for each MP candidate, using the wrapped interferograms. The methodology is explained in Biescas et al. (2007). The topo_res is estimated and then removed from the wrapped interferograms. The topo_res is then used for a precise 3D location (geocoding), representing the elevation of the MP footprint with respect to the DEM information. For example, if a MP corresponds to the roof of a building, and the DEM is at ground level, then the topo_res represents the building height. The annual velocity represents the mean trend of the displacement in the period covered by the used images. To do that, the displacement is approximated by a linear model. Sometimes the linear displacement component is also removed from the wrapped interferograms, to be added again later to the displacement time series. This is done to ease the phase unwrapping and the atmosphere estimation. Together with the modelled velocity and topo_res, the temporal coherence γ_t is estimated and used to select low-noise MPs. Sometimes only the topo_res is estimated in this module, while the velocity is derived later by a linear regression on the generated Time Series.

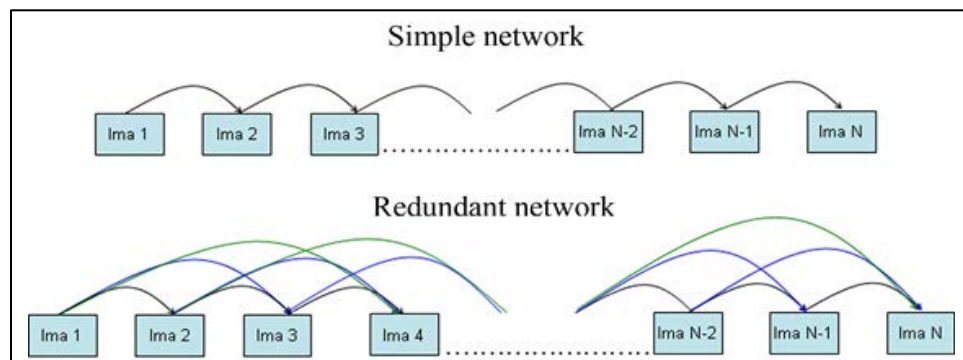


Figure 13 Example of how the images are paired to generate a simple or a redundant network. From Monserrat, 2012.

5. **Phase unwrapping.** This operation involves the estimation of the phase ambiguity k (Eq. 6) in both space and time. This is the most critical step of the entire procedure. Several approaches have been proposed to perform it, e.g. see Ghiglia and Pritt (1998), Costantini (1998), and Chen and Zebker, (2001). Firstly, a spatial 2D phase unwrapping is performed for each interferogram (Figure 14). Secondly, for each MP the 1D temporal phase unwrapping is performed using all the unwrapped interferograms to generate the displacement time series. For single interferograms, the condition to correctly unwrap the phases is that the difference between unwrapped phases over neighbouring MPs is less than π . If the sum of the components of Eq. 6 abruptly changes in space, generating a local difference of phase higher than π , the ambiguity cannot be solved, and spatial *aliasing* errors are generated. A 2D phase unwrapping can be compromised by a bad selection of MPs (introducing high ϕ_{noise}), a wrong removal of topo_res, a strong atmosphere spatial change, or a rapid movement. A continuous spatial coverage of MPs facilitates the phase unwrapping. Therefore, the actual capability to solve the ambiguity depends on the spatial pattern of the specific displacement phenomenon at hand (the smoother this pattern, the better is the phase unwrapping) and the available MP density over this phenomenon (the higher the density, the better is the phase unwrapping). For what concerns the 1D phase unwrapping, the condition is that the sum of the interferometric components for each interferogram is smaller than π . Assuming that all the terms of Eq. 6 but ϕ_{Defo} are zero, the differential displacement of a MP occurred between the two image acquisition dates needs to be less than $\lambda/4$. If this condition is not satisfied a temporal aliasing error can occur. As explained in Devanthéry et al. (2019, 2014), the redundant observation for each image allows to iteratively check and eventually correct the 2D phase unwrapping errors. The consequence of a not-resolved aliasing can be a jump in the TS (see Figure 15) or an underestimation of the displacement. The final output of the 1D phase unwrapping is the temporal evolution of the phase, one value per each acquisition date, starting from the first one that is set to be zero. All the phases are referred to a selected stable MP, which is set to be zero at all the image acquisition dates. It is worth underlining that the time series estimation procedure does not make any displacement model assumption.

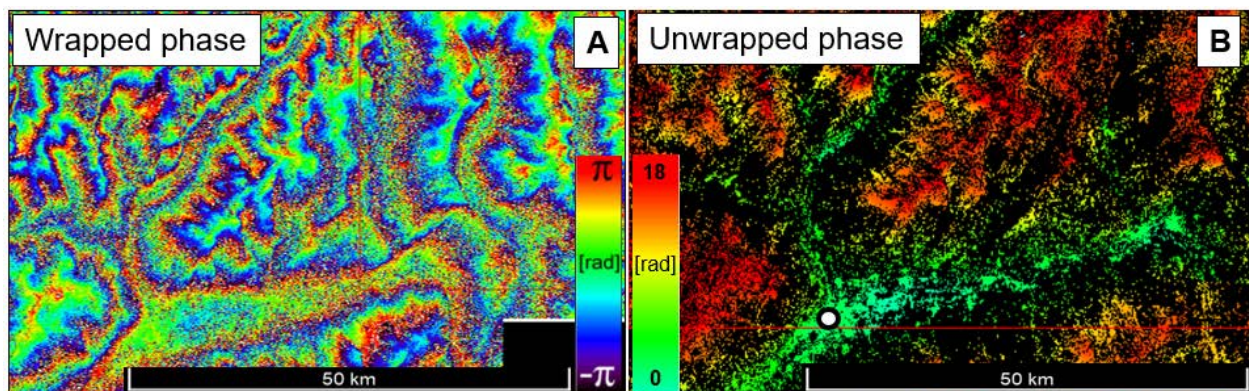


Figure 14 Example of a 2D phase unwrapping of an interferogram. On the left the wrapped and on the right the unwrapped interferogram. The circle shows the position of the reference-stable point set to zero

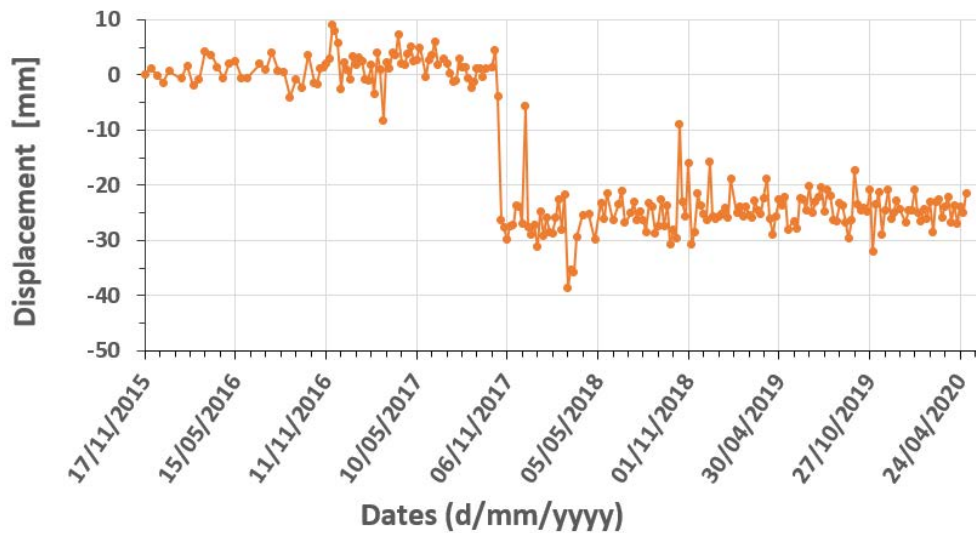


Figure 15 Example of aliasing due to an unsolved phase ambiguity in the 1D phase unwrapping.

6. **Atmospheric component estimation.** In this module, the atmospheric phase component ϕ_{Atm} is estimated and subsequently removed from the phases. The ϕ_{Atm} estimation is usually based on assumptions on the spatiotemporal characteristics of the data: ϕ_{Atm} is spatially correlated, but temporally uncorrelated, while the ϕ_{Defo} is typically correlated over time. The two components ϕ_{Defo} and ϕ_{Atm} are separated using low-pass and high-pass filters. However, if the assumptions are not fully satisfied, the estimation can be biased: some part of ϕ_{Atm} can be wrongly estimated as a spatially correlated ϕ_{Defo} , or conversely, a part of spatially correlated ϕ_{Defo} can be estimated as ϕ_{Atm} and then removed. The atmospheric component is estimated on the output of the 1D+2D phase unwrapping. Then it can be removed from the interferograms, to perform again the steps 3, 4 and 5, or directly from the Time Series.
7. **Geocoding.** The MPs coming from the previous module are in the radar geometry of the reference image by two coordinates: azimuth and range. The geocoding or geolocation procedure allows us to estimate the geographical or cartographic coordinates of the MPs. This operation makes use of the azimuth and range coordinates of the given MP, the orbits of the reference image, the topo_res of the MP, and the DEM. This is a key step to enable the interpretation and exploitation of the InSAR products.

2.5 Sentinel-1

The aim of this section is to resume the main characteristics of Sentinel-1 to understand its potentialities in geohazard detection and monitoring applications.

Wide area coverage

S1 supports the generation of products for 4 different acquisition mods, between them, the Interferometric Wide Swath (IW) is capable to provide acquisitions over wide areas (250x250 km²) through the imaging technique Terrain Observation with Progressive Scanning SAR (TOPSAR) (de Zan and Guarnieri, 2006). This characteristic is crucial for regional-to-national scale applications (Novellino et al., 2017). The TOPSAR technique has required an initial extra processing effort with respect to the previous missions, mainly in the co-registration step. The main consequence of the TOPSAR acquisition is the subdivision of

an image in several parts (3 sub-swaths, each one divided in 9 bursts, see Figure 16). Table 1 resumes the characteristics of the IW acquisition method, which is the most used in the geohazards applications.

Medium spatial resolution (C-band)

In the framework of Copernicus Programme, to give continuity to the ERS-1/2 and ENVISAT satellites, and to complement the national high-resolution sensors (TerraSAR-X by DLR/Astrium GmbH, Cosmo-SkyMed by ASI), S1 gives priority to the wide-area acquisition for medium resolution applications (~4 m in range by ~14 m in azimuth) (Snoeij et al., 2008; Torres et al., 2012). This characteristic improves its applicability at regional scale due to the reduced susceptibility to noise factors. Moreover, due to the longer wavelength, it allows monitoring faster movement with respect to the higher resolution data (Crosetto et al., 2010).

Reliable acquisitions

The S1 IW acquisition mode, with VV+VH polarization, is programmed to work in a conflict-free operational mode over lands allowing the exploitation of every data-take and the creation of a consistent long-term data archive for applications requiring long time series (Snoeij et al., 2008; Torres et al., 2012). Thus, contrary to what happened with the predecessors ERS-1/2 and ENVISAT, S1 is programmed to never fail acquisitions due to conflicting requests from users. This makes S1 data to be reliable for long-term monitoring.

High temporal sampling

The S1 constellation acquires data with a revisit frequency of 6 days or 12 days, depending on the zone (Table 1, Figure 17), improved with respect to its C-band predecessors. This characteristic has several key consequences in the InSAR applications and exploitations. The high temporal sampling improves the potential for a near-real-time monitoring. The short revisit time reduces the temporal decorrelation. Moreover, it allows measuring faster movements through the exploitation of the single interferogram information (Barra et al., 2016). Considering the revisiting time of Sentinel (6 days), the limit of $\lambda/4$ corresponds to a maximum measurable differential deformation rate of 85.2 cm/yr or 1.38 cm in 6 days. The high temporal sampling reduces the noise and increases the quality of the results in terms of displacement time series, spatial coverage, and density of the measurements.

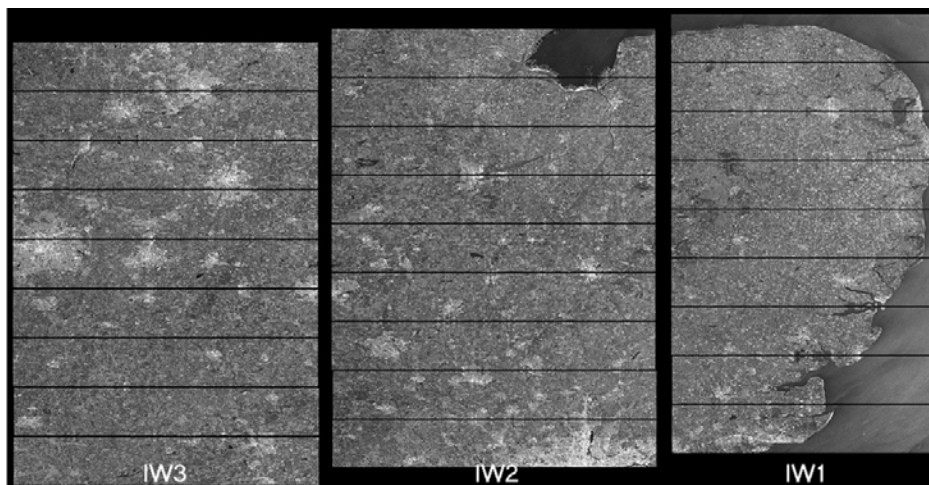


Figure 16 Example of a S1 image (amplitude) acquired in a descending geometry. The image is divided in three sub-swaths (IW) in range, and 9 bursts for each IW, in azimuth. From “ESA - User Guides”.

Free and easy download

Finally, it is important to underline that S1 data are completely free, without costs or use limitations. Easily downloadable from the portal Copernicus Open Access Hub (<https://scihub.copernicus.eu/>).

Table 1 Main characteristics of the S1 data acquired with the Interferometric Wide Swath acquisition mode.

Satellite	Sentinel-1
Acquisition mode	Interferometric Wide Swath (IW)
Revisit frequency (days)	6-12 (Fig. 1)
Image swath width (km)	250
N. of sub-swaths	3
Wavelength (λ) (cm)	5.55
Polarization options	Dual HH+HV, VV+VH Single HH, VV
Full resolution (azimuth/range) (m)	20/5
Orbital Earth fixed "tube" radius (m)	50
Incidence angle of the area of interest	29.1° - 46.0°

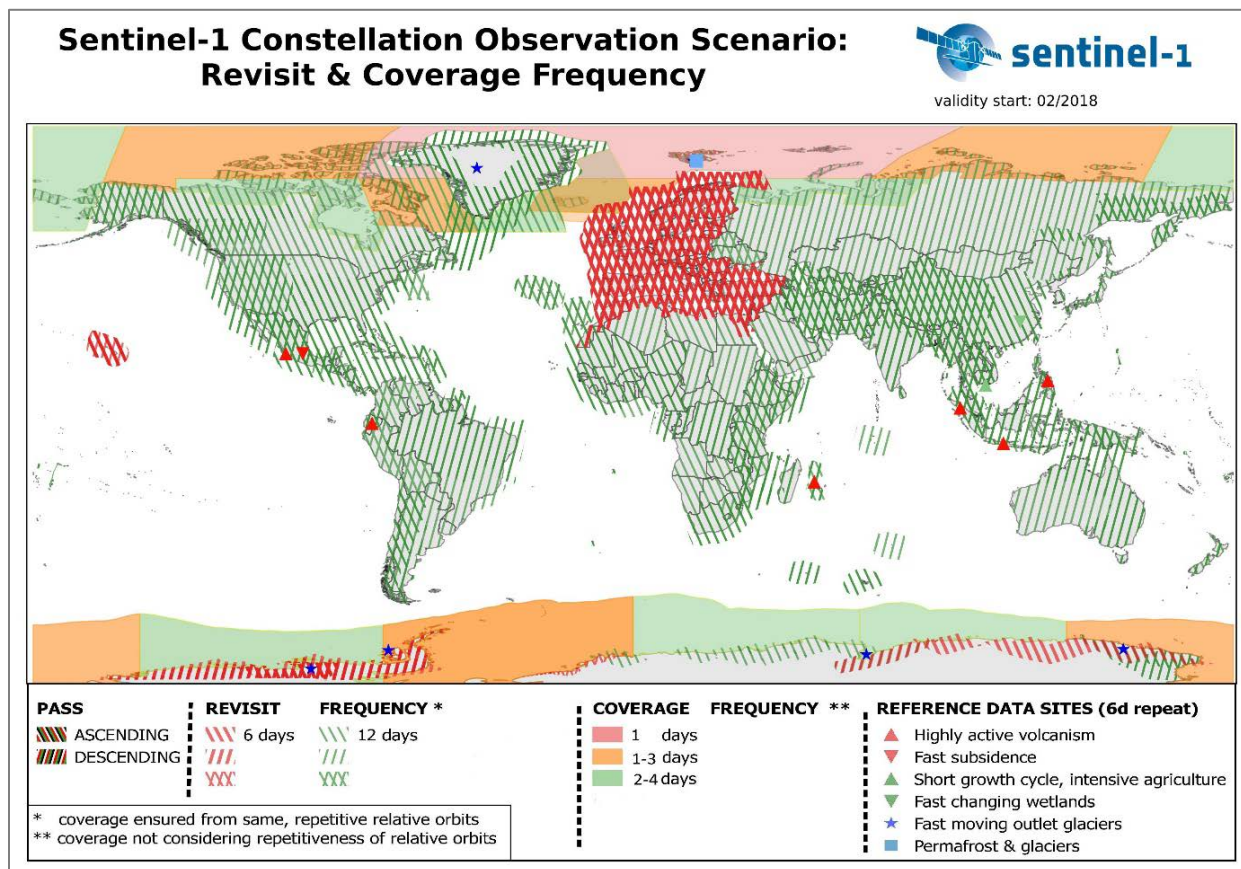


Figure 17 Sentinel-1 observation Scenario. From "ESA - Sentinel Online".

3 Workflow and Methodology

The proposed methodology has a multi-scale approach. Starting from a regional scale displacement map, we detect the most significant Active Deformation Areas (ADAs), to derive additional information useful for risk analysis and territorial management at both regional and local scales. The method can be divided in three blocks (Figure 18), all of them aimed at improving the exploitation of the wide area and 6-day temporal sampling of S1. The first one involves the processing to derive the displacement map, which is the main input of the methodology. This block must be faced for each processed test-site, with the aim of finding the best approach to improve the measurement capability. This block is not treated in detail in this thesis. We just refer to it to highlight the different inputs for the post-processing of blocks 2 and 3. The second block is the semi-automatic extraction of the ADAs. This block proposes a methodology to detect and regularly update the ADA map. Starting from the ADAs, the third block consists of semi-automatic methods to generate interpreted products, which are derived from the integration of the ADAs with auxiliary data. This section aims to describe the workflow through the proposed journal papers, the main methodologies and results are shortly described and some aspects which are not fully described in the original papers are included.

3.1 First insights on the potential of Sentinel-1 for landslides detection

In the context of the recently launched S1 satellite, the aim of Barra et al. (2016) (Annex 1) was to investigate the potentialities of S1 for landslide detection and activity characterization and to propose a methodology of analysis. The short revisit time (6-12 days), plus the C-band wavelength, and the regular acquisitions strategy, were premonitory characteristics of increased performances in terms of coherence and monitoring capabilities, compared to other SAR sensors such as ERS, ENVISAT or ALOS. Indeed, compared to previous satellites, S1 characteristics represent an improvement in terms of coherence and thus increasing capabilities for detection of landslides with displacement rates up to 1 m/yr., classified as slow by Cruden and Varnes (1996). At the same time there were many uncertainties related with the new data, like the real availability or the processing adaptation to the new TOPSAR mode of acquisition. The main objectives of this work were both to investigate the potentialities of S1 for landslide detection and activity characterization and to determine a methodology of analysis (SO 1 and 2). The methodology proposed in Barra et al. (2016, in Annex 1, and 2017a) is based on two main steps. The first one is a spatial and temporal analysis exploiting both single-interferogram (DInSAR) and MTInSAR information to extract the ADAs, which are moving areas without any interpretation on the causing phenomena. The second step consists in a GIS multilayer analysis based on supplementary data to both validate the ADAs and derive improved interpreted maps. The extraction of the ADAs is performed on two parallel data sources (block 2 of the workflow in Figure 18). The first one is derived from single interferograms, allowing the detection of faster movements or temporal accelerations (in terms of few centimetres per week) that can be detected in 6 or 12 days interferograms. The second one is derived by a MTInSAR result, allowing to detect slower movements (in terms of few millimetres or centimetres per year) and to analyse the temporal evolution in time of the movement (time series of displacement). The information of faster movements can be lost in a Multi Temporal processing due to loss of coherence over time, causing absence of MPs (see sections 2.3, 2.4 and Figure 11).

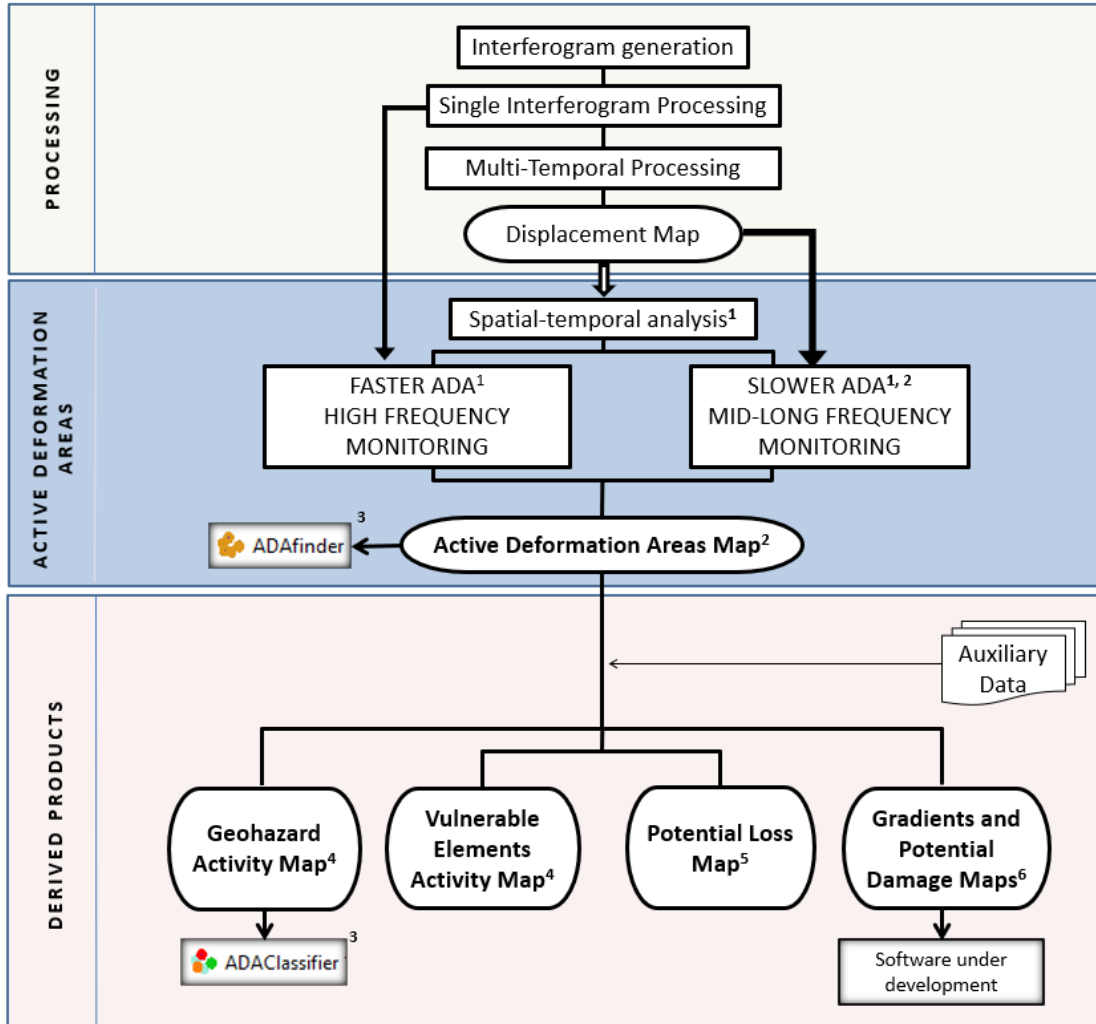


Figure 18 Flowchart of the thesis.

1. Barra, A., Monserrat, O., Mazzanti, P., Esposito, C., Crosetto, M., & Scarascia Mugnozza, G. (2016). First insights on the potential of Sentinel-1 for landslides detection. *Geomatics, Natural Hazards and Risk*, 7(6), 1874–1883. <https://doi.org/10.1080/19475705.2016.1171258> - Annex 1
2. Barra, A., Solari, L., Béjar-Pizarro, M., Monserrat, O., Bianchini, S., Herrera, G., Crosetto, M., Sarro, R., González-Alonso, E., Mateos, R.M., Ligüerzana, S., López, C., Moretti, S., 2017b. A methodology to detect and update active deformation areas based on Sentinel-1 SAR images. *Remote Sensing* 9, 1002. <https://doi.org/10.3390/rs9101002> - Section 4
3. Navarro, J. A., Tomás, R., Barra, A., Pagán, J. I., Reyes-Carmona, C., Solari, L., Vinielles, J. L., Falco, S., & Crosetto, M. (2020). ADAtools: Automatic detection and classification of active deformation areas from PSI displacement maps. *ISPRS International Journal of Geo-Information*, 9(10). <https://doi.org/10.3390/IJGI9100584> - Section 5
4. Solari, L., Barra, A., Herrera, G., Bianchini, S., Monserrat, O., Béjar-Pizarro, M., Crosetto, M., Sarro, R., & Moretti, S. (2018). Fast detection of ground motions on vulnerable elements using sentinel-1 InSAR data. *Geomatics, Natural Hazards and Risk*, 9(1), 152–174. <https://doi.org/10.1080/19475705.2017.1413013> - Annex 2
5. Solari, L., Bianchini, S., Franceschini, R., Barra, A., Monserrat, O., Thuegaz, P., Bertolo, D., Crosetto, M., & Catani, F. (2020). Satellite interferometric data for landslide intensity evaluation in mountainous regions. *International Journal of Applied Earth Observation and Geoinformation*, 87. <https://doi.org/10.1016/J.JAG.2019.102028> - Section 6
6. Barra, A., Reyes-Carmona, C., Herrera, G., Pedro Galve, J., Solari, L., María, R., Miguel Azañón, J., Béjar-Pizarro, M., López-Vinielles, J., Palamà, R., Sarro, R., Cuervas-Mons, J., Monserrat, O., n.d. From Satellite Interferometry displacements to potential damage maps: a tool for risk reduction and urban planning. Submitted to *Remote Sensing of Environment*.

The MTInSAR measurement is not spatially continuous, the density of MP depends on the stability in time of the back scattering characteristics that can be influenced by different aspects like the land cover or the velocity of the target among others (section 2). By contrast, the single-interferogram analysis brings a spatially continuous information, which however is sporadic in time (Figure 11). Both types of detection are complementary and allow a complete spatial and temporal characterization of the movements for a constantly updated inventory. This parallel analysis is explained in Barra et al. (2016, Annex 1), where both analyses are performed manually over an area of the region of Molise (Italy), strongly affected by landslides. The single interferogram analysis starts with a first detection of potential movements performed through a visual recognition of local patterns in the wrapped interferograms that are potentially associated with movements. Then the pairwise logic analysis (Massonnet and Feigl, 1998) allows to check each pattern and exclude the one that are due to atmospheric effects or topographic errors. The detected potential landslide areas are then compared and analysed in the MTInSAR displacement map. Finally, they are interpreted and validated in a GIS environment, using auxiliary data like optical images, topography, geology, and existing landslide inventory maps.

Figure 19 shows an example of parallel analysis of a single-interferogram (a) and the MTInSAR displacement map (b). The black rectangles are examples of detected ADAs in both analyses, while the white ones are represented in Figure 20. The interferogram corresponds to a period of high rainfall (between 24/01/2015 and 02/02/2015) that caused an acceleration of existing landslides. Figure 20 shows a detail of an ADA detected in the interferogram (A) and in the displacement map (B). It is visible how the colour pattern of the interferogram allows to have a spatial information that is clearer and more continuous than the MT displacement map. The TS information of the MT map (C) is an added information for a temporal characterization of the movement, the red circle in (C) shows the acceleration detected in the interferogram in (A). Figure 20-D displays the final delineation of the detected movement and its overlapping with inventoried landslides (from the IFFI Italian landslide inventory). The multi-layer analysis allowed to confirm the detected potential landslides and to update the spatial delimitation analysing optical images and the topography. Moreover, looking at the spatial distribution of the detected movements on the geological map (Figure 21), we see that the ADAs are all localized on shales shists and sedimentary unit or on clayey lithologies, which are strongly prone to slide and affected by the rainfall water content. The results achieved using only 14 images, covering a period of 7 months, were very promising. In a total of 62 landslide polygons, 13 were new detections, 31 allowed to update the IFFI inventory, while 18 confirmed the activity of already inventoried landslides.

The methodology proposed in Barra et al., 2016 was the precursor of the research advancements and the final methodology presented in this thesis. The main blocks of the thesis flowchart (Figure 18) remain the same, but most of them are now implemented with semi-automatic procedures and software tools. The automatization is a key aspect for an extensive application over wide areas.

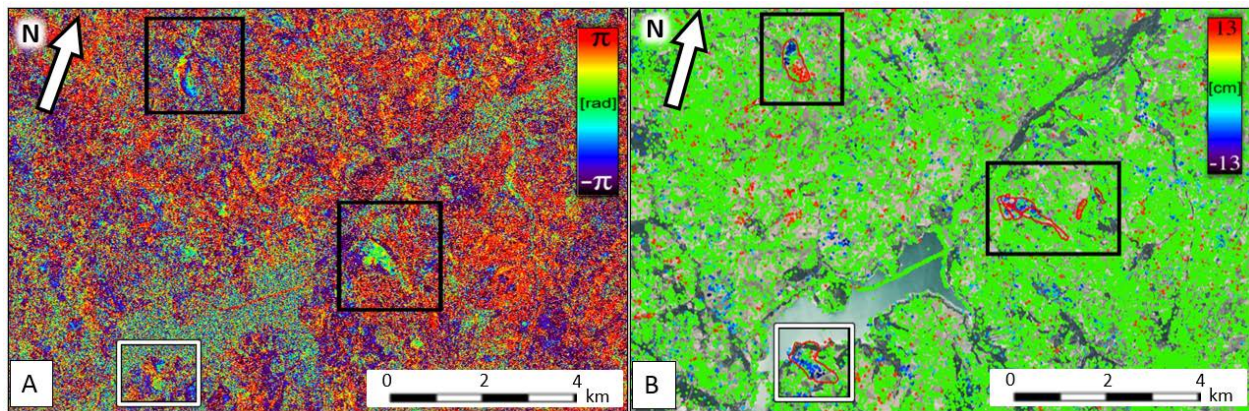


Figure 19 The black rectangles show few examples of ADAs detected from a single interferogram (A) and from the MTInSAR displacement map (B). Note that figure (a) is in radar geometry, while in figure (b) the displacement map is projected in geographic coordinates and showed on a satellite optical image. Modified from Barra et al. 2017a.

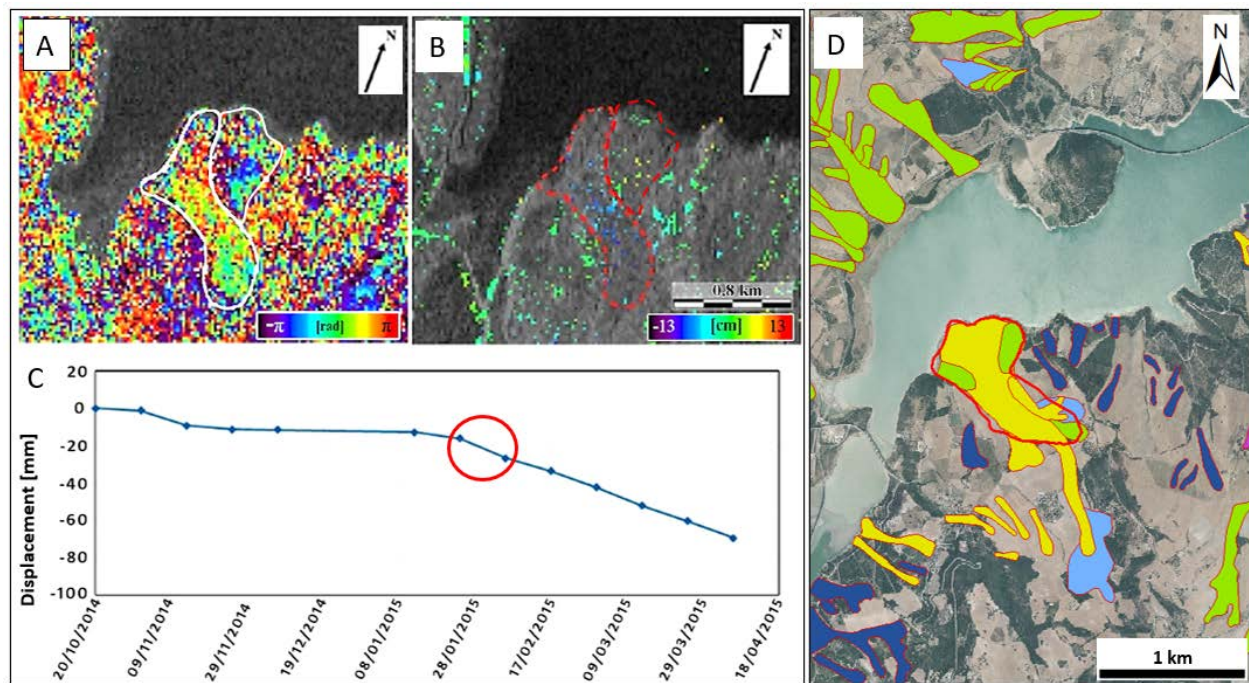


Figure 20 Potential pattern of ADA detected in a 12-day interferogram, delineated by a white line (a). The same pattern (red line) is showed with the MTInSAR displacement map (b) and in a GIS (d) together with the existing landslide inventory. The TS of the movement is showed in c. Modified from Barra et al. 2017a.

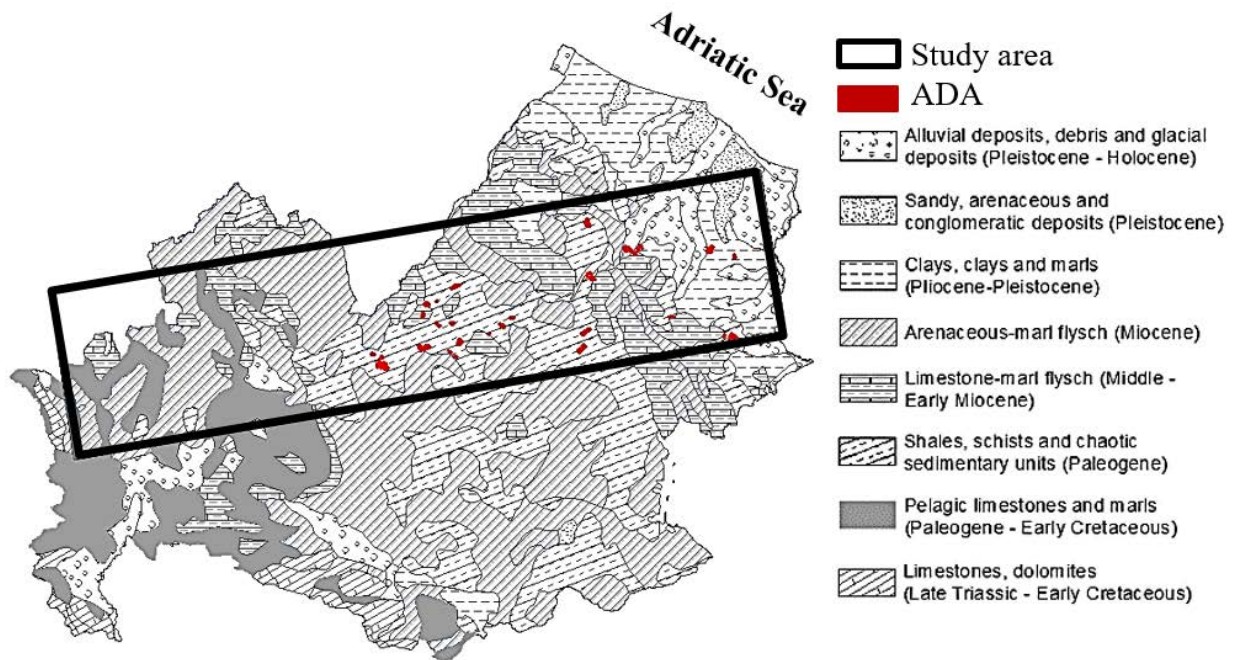


Figure 21 Detected ADAs overlapped with the geological map of Molise region. The black rectangle represents the processed part of the S1 image (burst).

3.2 A methodology to detect and update active deformation areas based on Sentinel-1 SAR images

An algorithm for the ADAs extraction from a MTInSAR displacement map is proposed in Barra et al. (2017b, section 4). Here, we propose a methodology to simplify the displacement map through a MP filtering, and then extract the ADAs in a semiautomatic way. The methodology is developed over the Islands of Gran Canaria, La Gomera and Tenerife (Canary Islands, Spain), in the framework of the Safety project. The displacement map simplification removes the spatial outlier and the isolated points, to derive a filtered Displacement Activity Map (DAM). This is a first product that reduces the spatial-temporal noise and improves the readability and reliability of the map, simplifying the use and interpretation by not expert users in line with the SO 3. An example of filtering is showed in Figure 22 over the Teide and Pico Viejo areas of Tenerife.

The second output of the methodology is the ADA map, which is the main input for the block 3 of the flowchart (Figure 18). The proposed procedure extracts the most significant active areas as a set of polygons, where each polygon contains the main information of the area (e.g. minimum, mean and maximum velocity, mean accumulated displacement, localization). Among this information, we underline the Quality Index (QI), based on statistical analysis, representing the temporal noise and spatial consistency of the TSs within each ADA. The QI is a key information to automatic assess the reliability of each extracted area, and thus reduces the analysis time for InSAR non-expert users. The ADAs are classified in four classes of reliability based on the QI, as explained in Figure 23. The ADA map simplifies the readability of PSI results, avoids misunderstanding in the interpretation, and allows a fast focusing over the most interesting active areas (SO 4). The automatic extraction of the ADA is key for an operational use of regional scale displacement maps (SO 3). In the application over Canary Islands, it allowed to pass from

around one million of points to around one hundred of ADAs. The number of areas is lower if we exclude the “not reliable” ADAs, and if we consider that more than one ADA polygon belongs to the same movement. The paper shows the potentialities of the methodology for a periodical updating of the ADA map. Figure 23 shows an example of the DAM and the ADA map, with the proposed classification of the ADA based on the QI. The outputs are complementary for both a regional scale overview given by the ADAs, and a local analysis given by the single PSS and TSS of the DAM.

This work represented the reference methodology for many successive applications. Based on the methodology proposed in Barra et al. (2017b), a software tool (the ADAFinder) was developed. The ADAFinder has been distributed to several institutions, and used in several European projects (Safety, U-Geohaz, Heimdall, MOMIT, MOMPA, RISKCOAST).

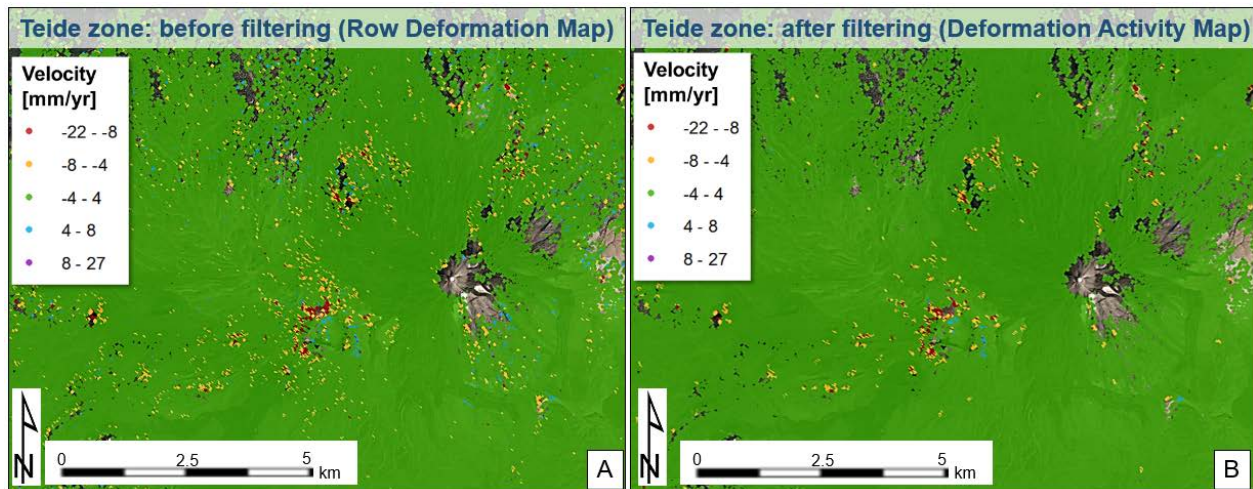


Figure 22 Example of noise filtering for a simplified MT displacement map read and interpretation.

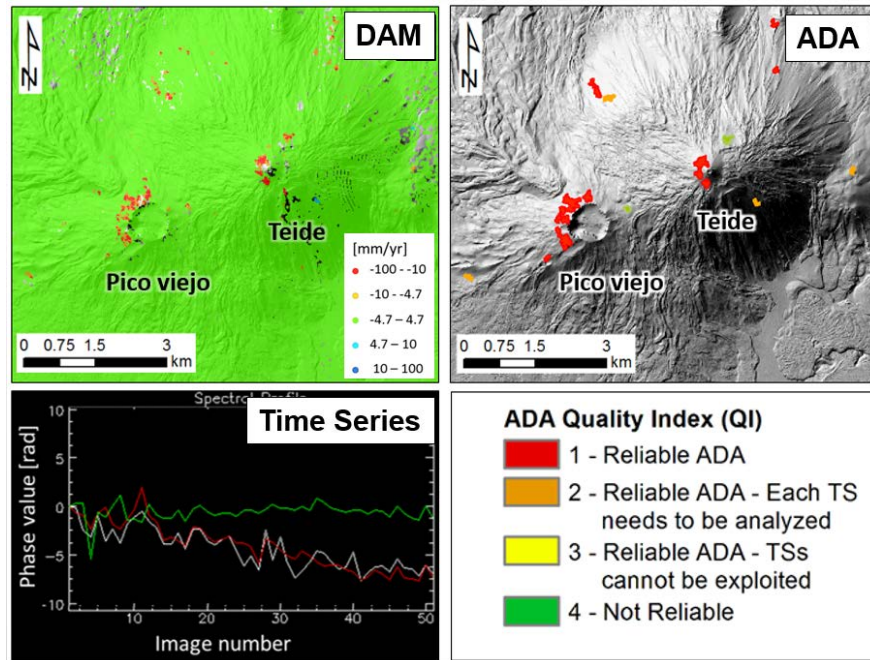


Figure 23 Example of the main outputs of the methodology proposed in Barra et al. (2017b). Modified from Monserrat et al. (2018)

3.3 Fast detection of ground motions on vulnerable elements using Sentinel-1 InSAR data

This work represents a first proposal on the use of the ADA map to generate secondary products (Block 3 of the workflow, Figure 18). It was developed in the frame of the Safety project, as the direct evolution of Barra et al. (2017b), with the objective of generating maps to be operationally useful for civil protection purposes. The whole methodology proposed in Safety, showed in Figure 24, was thought to be iteratively applied, with a frequency that depends on the monitoring target. In Solari et al. (2018, Annex 2) we develop and explain the methodology through its application in the Canary Islands of Tenerife, La Gomera and Gran Canaria (Spain). Firstly, the intersection of the ADA map with other existing data (e.g., geohazard inventories, terrain slope, susceptibility maps) allows validating the detected ADAs and attributing the possible geohazard that is threatening a certain area. The result of this cross-analysis is called Geohazard Activity Map (GAM), which consists in a preliminary interpreted ADA map (SO 3). The GAM consents to update the existing maps by adding new detected movements or changing the spatial and temporal activity state of already known phenomena. Secondly, we propose a qualitative Strategic Vulnerability Classification of the exposed elements, which is based on the role that each element plays in the three Civil Protection (CP) phases of prevention, emergency, and recovery. The intersection between the classified elements at risks with the ADAs allows to generate three Vulnerable Element Activity Maps (VEAM), one for each CP phase. The VEAM is aimed to be a clear map resuming, for each territorial unit, if a geohazard is affecting one or more strategic elements a risk (SO 4).

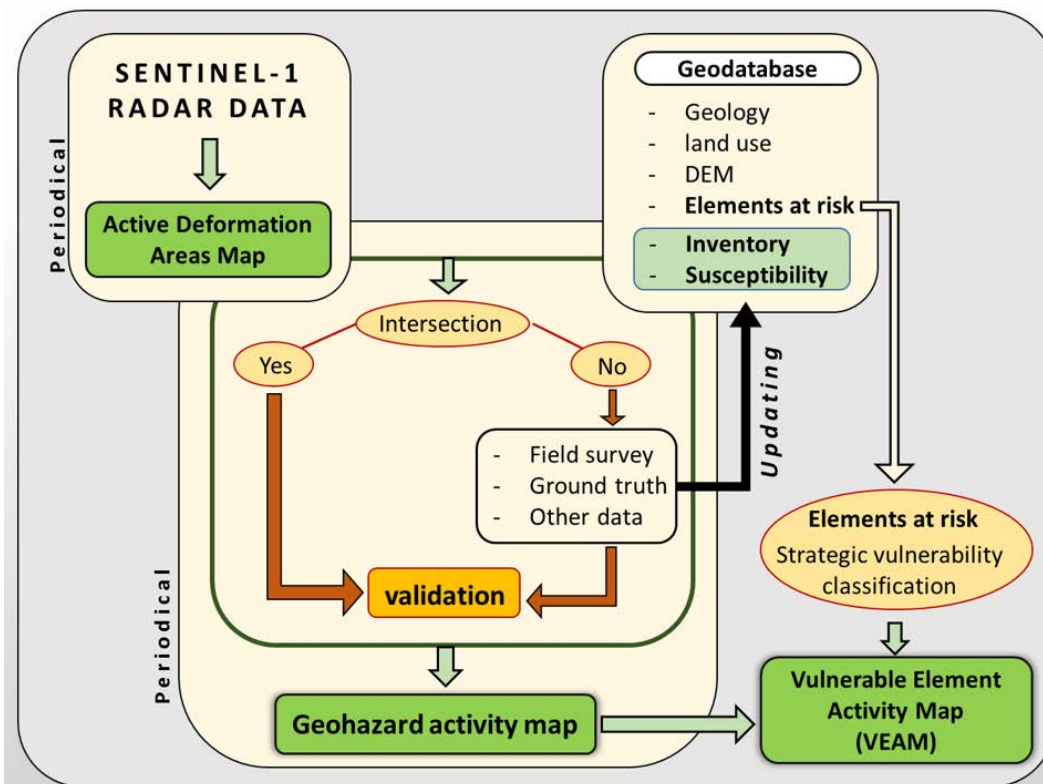


Figure 24 Flowchart of Safety project (see also Barra et al., 2018 and Monserrat et al., 2018).

3.4 ADAtools: Automatic detection and classification of active deformation areas from PSI displacement maps

In Navarro et al. (2020, Section 5) we see the automation of both the ADA extraction and preliminary classification through the development of the ADATools, a set of tools for the MTInSAR data analysis and interpretation. The ADATools have been implemented in C++ in the framework of MOMIT, with the collaboration of the University of Alicante (UA). They are based on methodologies that already existed and were executed manually, in a Geographic Information System (GIS) environment. The package is composed of 4 modules, namely, ADAfinder, ADAclassifier, THEXfinder, and los2hv. Specifically, the ADAfinder, which allows an automatic extraction of the ADAs from a MT displacement map, is based on the algorithm developed by Barra et al. (2017b). The ADAClassifier uses auxiliary data to make a preliminary semiautomatic classification of the geological or anthropogenic processes causing the movement. The ADAs are classified with a level of certainty of being a landslide, a sinkhole, a subsidence, or a constructive settlement (Figure 25). ADAClassifier derives from a methodology developed by the UA that is under constant research and is based on the same concept of the Geohazard Activity Map. THEXfinder, is the second classification tool to identify expansive soils and thermal expansion effects. Finally, los2hv is based on Notti et al. (2014) and computes the horizontal and vertical components if both the ascending and descending geometries are available (section 2.2, Figure 8). The output of los2hv is an optional input of the ADAClassifier. The ADAtools have been tested in two areas (in Italy and Spain) where the availability of ancillary data was strongly different, to show the flexibility and adaptability of ADAClassifier to a wide range of situations. The development of the ADAtools has allowed a wide distribution and application of the methodologies. The most consolidated tool is the ADAfinder, which has been intensively used and improved several times, thanks to the users' direct experience and feedbacks. ADATools are in line with the SO 3, improving the potentialities for an extensive application and use of the previously proposed methods.

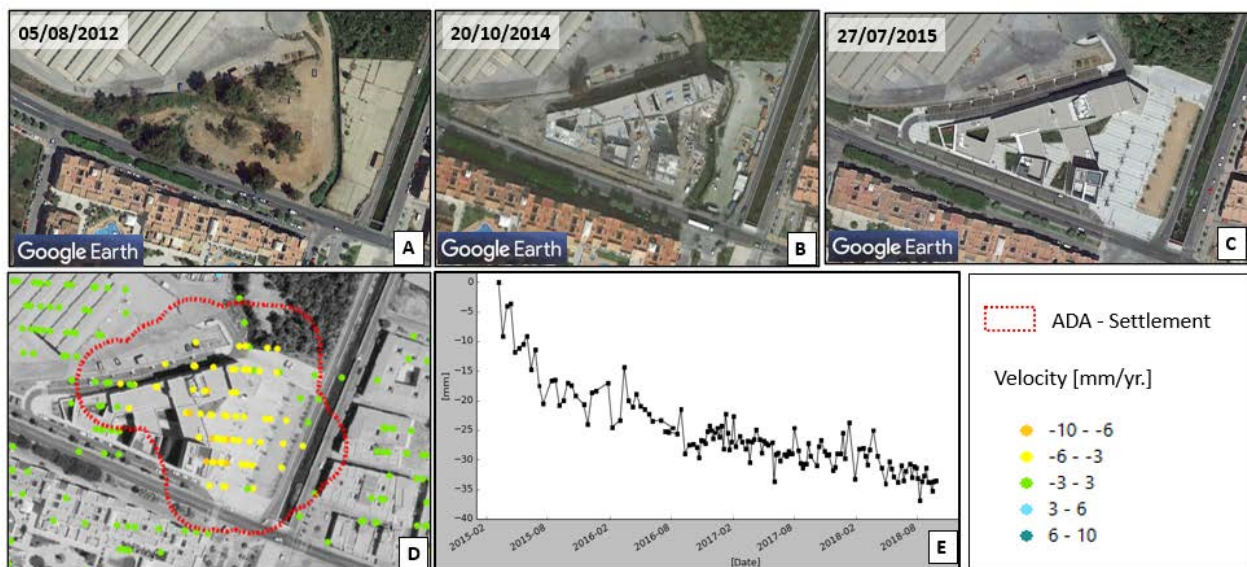


Figure 25 Example of ADA classified as settlement (D) showing an inverse exponential trend of the mean time series (E). The historical satellite images from Google Earth allowed to confirm the new construction of a building between 2014 and 2015.

3.5 Satellite interferometric data for landslide intensity evaluation in mountainous regions

In this work, developed in the frame of U-Geohaz project, we propose a methodology to be applied at a regional scale, to derive local scale maps that quantify the potential loss (from an economic point of view) suffered by a building or road exposed to a landslide (Solari et al., 2020a, Section 6). The main input is the ADA map, extracted from a MTInSAR displacement map, which is used to localise a potential destructive movement and to derive the landslide intensity. As a step forward from the previous application in Solari et al. (2018), here we use the ADA for both a direct and indirect intensity estimation. The direct intensity evaluation is done in case of slow movements directly affecting roads or buildings: in this case the mean ADA velocity is used as intensity value. The indirect approach is used when the ADA does not intersect any anthropic element, but it highlights the presence of an unstable debris, where a potential debris flow could be triggered. The ADA is thus used as indicator of the source zone for a model-based analysis to simulate the run-out. In line with the SO 3, this work faces two aspects for a preliminary risk analysis, proposing a physical vulnerability estimation and a quantitative exposure evaluation starting from the intensity evaluation. The methodology is applied over an area of Valle d'Aosta region, northern Italy (Figure 26A and B), strongly affected by landslides, mainly represented by slow deep-seated gravitational slope deformations and fast debris or mud flows. In this case the processing approach has been an important part of the work, due to the difficulties of the area from the InSAR point of view. The main aspect is a strong coherence change in space and time mainly due to the snow coverage in winter months. Other aspects are the strong topography (Figure 26A), the topography-related atmosphere component (Figure 26C), and the land cover which is mainly represented by vegetation. Figure 26 (C and D) shows the behaviour of the coherence depending on the image acquisition period. We can see how in summer (Figure 26C) the coherence is high over the whole area, whereas in winter (Figure 26D) the coherence is mostly maintained along the bottom of the valleys and totally lost with the altitude, where the snow was present. To face this problem, the coherence matrix was used for a coherence-based selection of the interferograms network to be processed, implying the elimination of some images from the processed dataset. Moreover, two different networks have been selected based on the temporal baseline of the interferograms, to firstly estimate the linear annual velocity (long temporal baselines), and secondly to generate the TS (short temporal baselines). The result is a strong improvement in terms of coverage, allowing to reach higher altitudes and density of measurements, as showed in Figure 10. The same approach was used in the project MOMPA (EFA295/19), to process an area of around 4,000 km² located in the Pyrenees. Starting from these necessities of an optimal selection of the images and interferograms, the tool *xarxa-setting* (i.e. network-setting) has been developed as a module of the PSIG chain. This tool makes an automatic selection of the images and the interferograms based on thresholds of the minimum coherence and image redundancy.

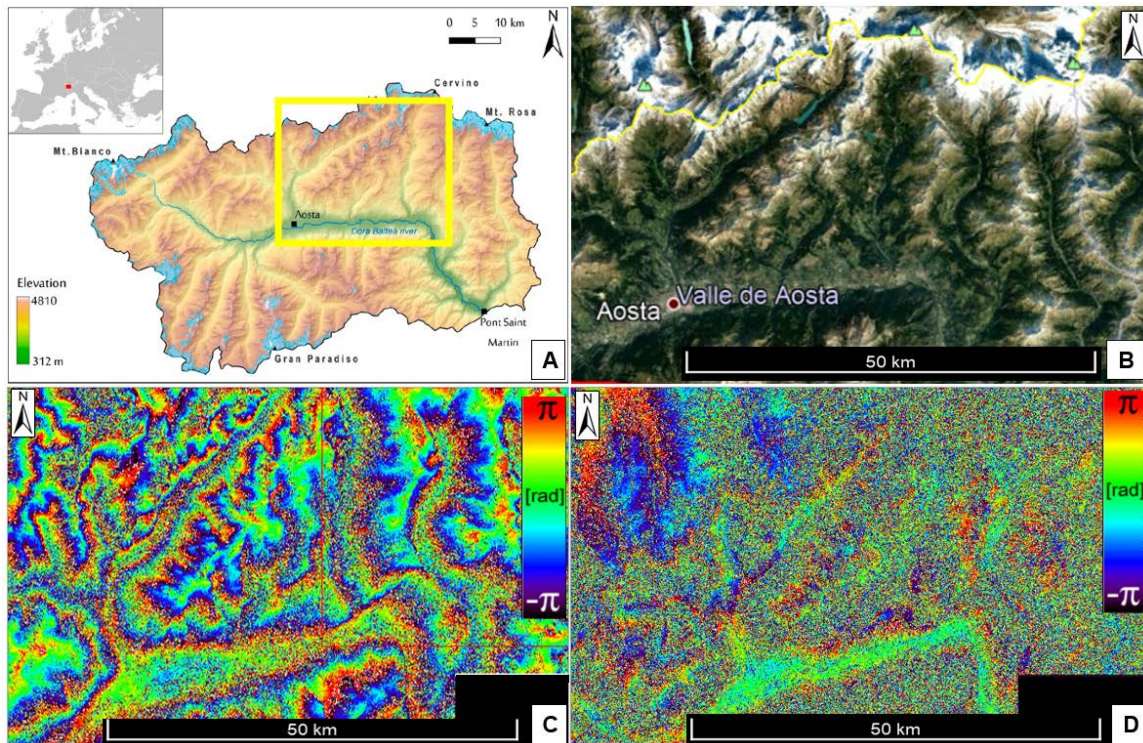


Figure 26 Localization and elevation map of the area of study (A), located in Valle d'Aosta region (northern of Italy). Optical image of the AOI. Example of a high coherence interferogram (C) covering the period 20/06/2017 – 26/06/2017, and a low coherence interferogram (D) covering the period 22/12/2016 – 28/12/2016. The phase fringes in C are mainly due to a topography-correlated atmosphere component.

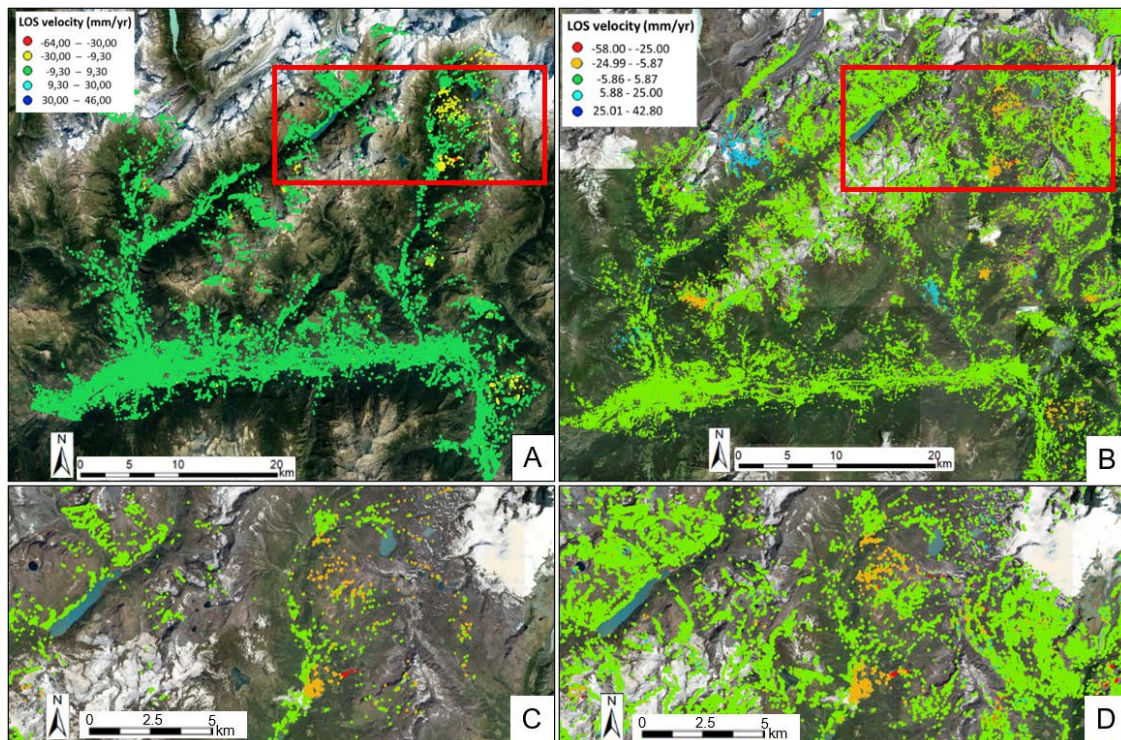


Figure 27 Comparison of the MT displacement map before (A) and after (B) applying the coherence matrix analysis. A detail of the area in the red rectangles in C and D.

3.6 From MTInSAR displacement gradients to the generation of potential damage maps

This work has been submitted to the journal *Remote Sensing of Environment* and is under revision. Here we propose a methodology (Figure 28) to start from a regional scale displacement map and derive local scale potential damage maps. We make an improvement with respect to the previous work (Solari et al., 2020a) in terms of slow-landslide intensity evaluation. One of the main destructive factors for a structure exposed to a slow movement are differential settlements or angular distortions. Here we use the spatial gradient of movement as landslide intensity value to localize areas where structures and infrastructures are susceptible to damage. The method has been applied over an area of around 700 km² located in the Province of Granada (Spain, Figure 29A), in the frame of RISKCOAST project. Starting from a regional scale MTInSAR-displacement map (Figure 29B), the ADAs are extracted with the ADAFinder tool, and selected on the base of the Quality Index (Figure 29C). The most significant detected ADAs are localized on coastal slopes, where several resorts (e.g. Cerro Gordo, Marina del Este, Punta de la Mona, Alfa Mar, etc.) are built. The ADA map represents the first-level information, which allows localizing exposed areas and assigning a first level of intensity, based on the velocity statistics. Figure 30 shows the results of the main steps of the methodology achieved over the resort of Monte de Los Almendros, localised in the white rectangles of Figure 29. The extracted ADA polygons (Figure 30A) are expanded through a buffer of 150 meters, thus the following steps are then performed within the ADA-buffer areas using common GIS tools. The ADA-buffer allows to include in the analysis the MPs that are in the ADA surrounding areas (Figure 30D), which can be stable, with a lower velocity or isolated with respect to the main moving cluster. Moreover, it is common that the stronger gradients of movements are expected to be located at the borders of the main moving areas. The velocity map is rasterized to have a regular grid information (Figure 30E) and to calculate the slope and aspect of the velocity map. The slope of the velocity represents the spatial gradient of movement, while the aspect the main gradient direction, allowing to derive the local *Gradient Vectors*. The rasterization and slope are also performed for the accumulated displacements at each acquisition date (i.e. derived from the displacement TS), allowing to have the evolution in time of the motion gradients (*Gradient Time Series*). The slope of the velocity map is then classified and used as *Gradient Intensity Map* (Figure 30F), one of the main outputs of the methodology.

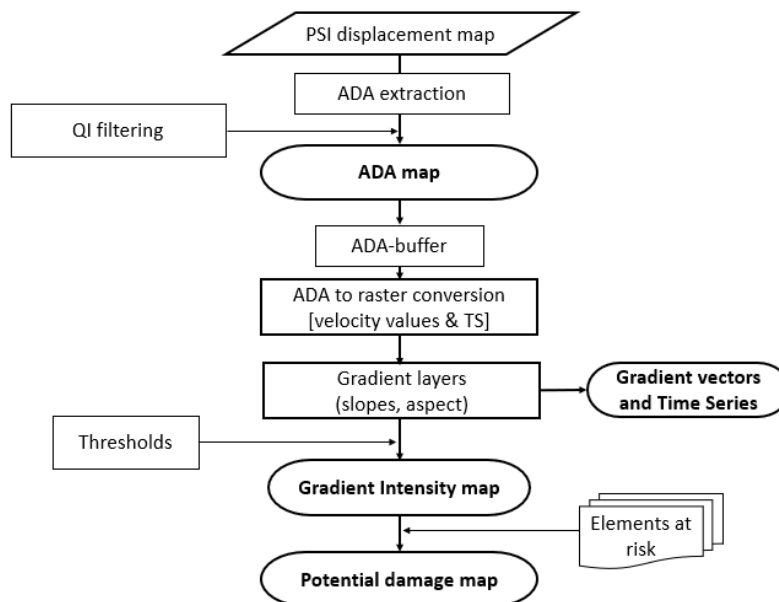


Figure 28 Flowchart of the methodology proposed in the last work submitted to *Remote Sensing of Environment*.

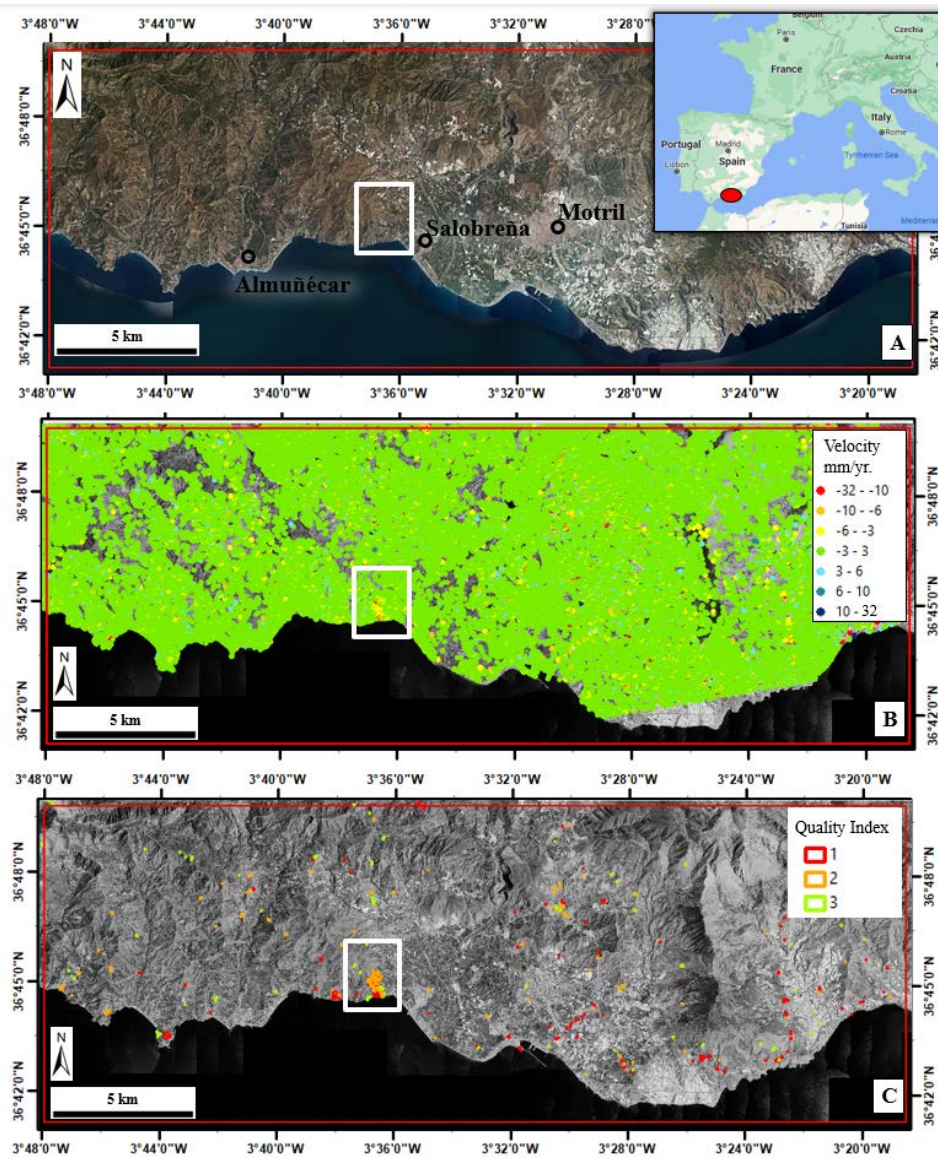


Figure 29 Area of study (above) and the extracted ADAs (below). The white rectangle shows the location of the Monte de Los Almendros resort (see Figure 31).

The proposed classification of the Gradient Intensity Map (Table 2) is based on Skempton and MacDonald (1956), to attribute to each class threshold a meaning in terms of potential damage expected over a period of 25 years (assuming constant gradient rates). Skempton and Macdonald (1956) establish general recommendations and limits for angular distortions (β). The first recommendation is avoiding angular distortions higher than 1/1000 or 1/500. They establish $\beta = 1/300$ as the limit that potentially produce cracking in walls and partitions and $\beta = 1/150$ as the one causing structural damage. The exposed buildings (freely available from the OpenStreetMap database) are then classified depending on their position over the Gradient Intensity Map, the maximum value of the gradient is attributed to each building to derive the *Potential Damage Map*, the second main output of the methodology. Figure 31 shows the Potential Damage Map (A) of the whole area of Monte de los Almendros and a detail over the local area within the black rectangle (Figure 31B, C, D and E). Figure 31B shows the input velocity map, Figure 31C the building polygons over the Gradient Intensity Map, and Figure 31D the derived Potential Damage Map. In Figure

31E the gradient vectors are showed (the colours represent the intensity class and the arrows the main direction) together with the velocity information derived from the rasterization (represented by the points). Finally, in Figure 31F is showed an example of gradient TS of the point highlighted by the white circle in Figure 31E. The Gradient Intensity Map and Potential Damage Map are useful to support field surveys and drive deeper analysis. The Potential Damage Map is a first step toward a vulnerability assessment, that would be possible with extra information on the structural characteristics of each building. The gradient vectors and TS are added information for single case analysis. Moreover, a constant monitoring of the gradient TS, through automatic trend change detection (Raspini et al., 2018), could allow a prompt detection of a change in the stress condition of a building. The ADA extraction allowed to pass from around 200,000 MP to 175 ADAs. Of the extracted area, the 15% is mapped as high or very high intensity gradient, which allowed to detect 192 over 633 buildings prone to moderate or higher damages (corresponding to cracks and structural damages).

Table 2 Classification of the Gradient Intensity Map and Potential Damage Map in terms of Angular Distortion expected in 25 years, assuming the annual intensity gradient doesn't change. The reference values are referred to Skempton and MacDonald (1956).

Class number	Intensity Class	Annual Gradient % (mm yr. ⁻¹ m ⁻¹)	Angular distortion (β) in 25 years	β reference values
0	Not measured	≤ 4	≤ 1/1000	≤ 1/1000
1	Low	8	1/500	1/500
2	Medium	12	1/333	1/300
3	High	20	1/200	1/150
4	Very high	> 20		>1/150

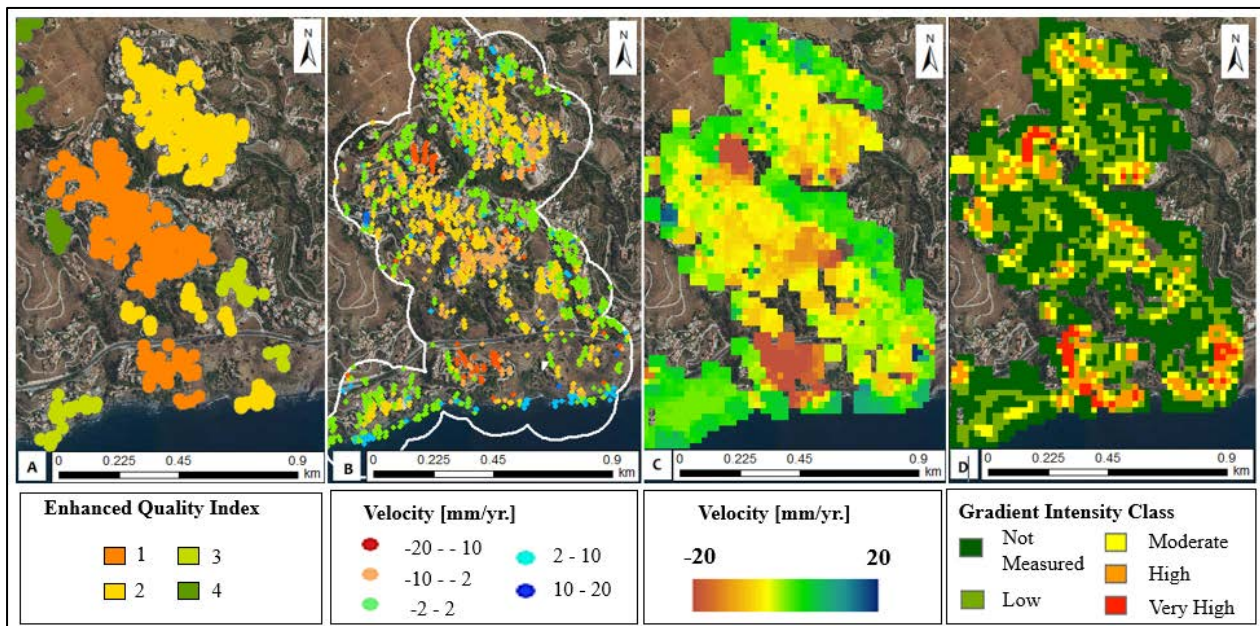


Figure 30 All the steps of the methodology obtained in the coastal resort of Monte de los Almendros.

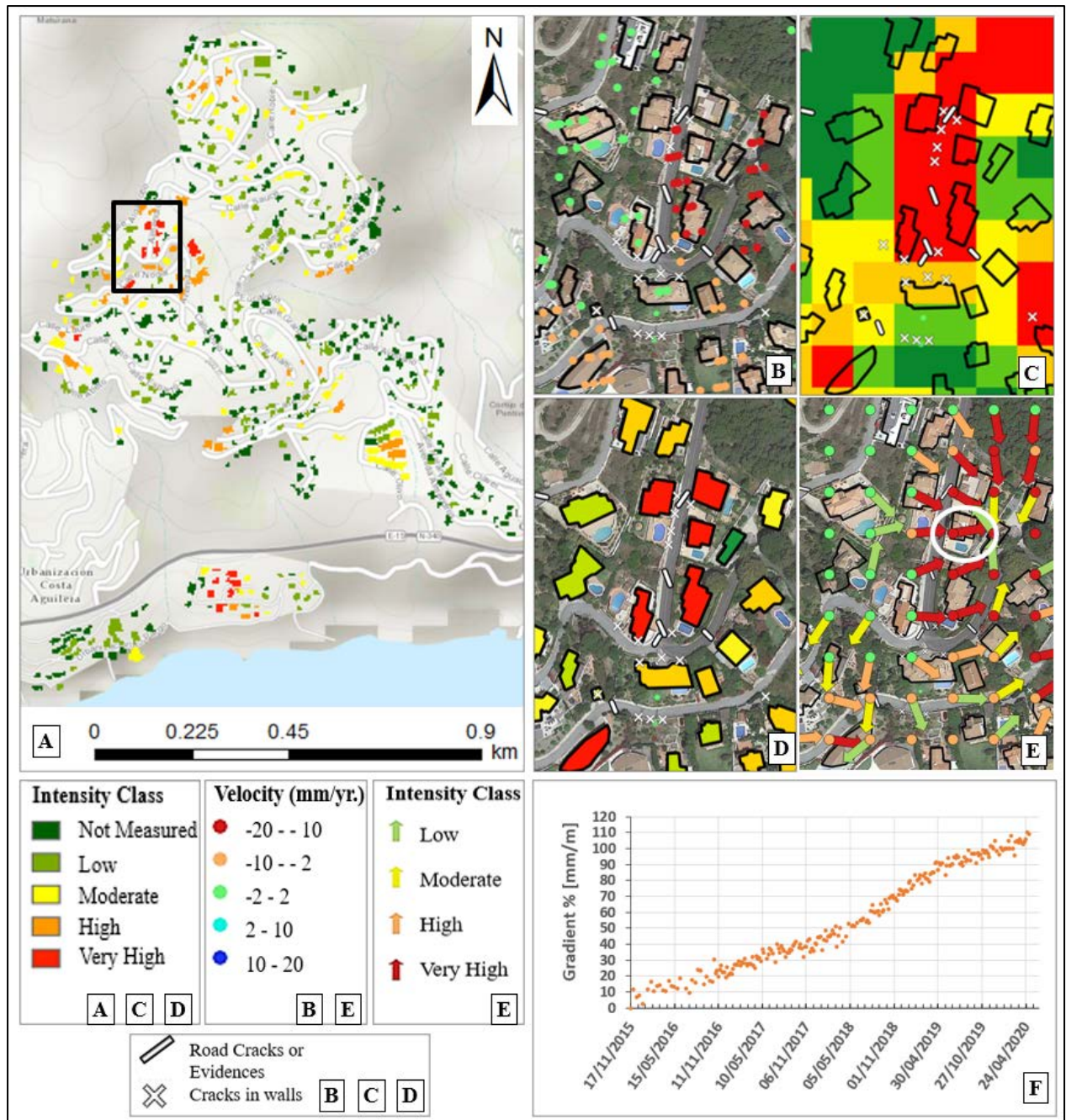


Figure 31 Potential Damage Map of Monte de los Almendros (A). Detail of the black rectangle area with the exposed buildings in black polygons (B, C, D and E). Input velocity map (B), Gradient Intensity Map (C), Potential Damage Map (D). Gradient vectors and displacement velocities (E). The gradient TS of the point within the white circle is showed in F.

An evaluation of the damage prediction capability of the methodology has been done using the Potential Damage Maps as test sample. To do that, a field survey was carried out in the coastal resorts of Los Almendros (both in May 2019 and July 2020), Alfa Mar (in May 2019), Cerro Gordo (July 2020) and Punta de la Mona (November 2021) to classify the buildings based on visible external damages. The classification proposed by Cooper (2008) was used, it is based on seven categories ranging from 1 and 2, which is barely perceptible only from the interiors, through 5, which is very severe with considerable damage, to 7, which

is total collapse. Table 3 shows the numbers of the buildings classified for each class of damage, used to compare the field evidence with the predicted damages. Figure 32 shows some examples of buildings affected by different types of damage (pictures taken in Cerro Gordo during the field survey).

The prediction test was done and evaluated through the generation of a series of ROC curves. Different thresholds of Intensity Gradients are used to set the difference between a positive (presence of damage) or negative (absence of damage) prediction. Thus, for each threshold the numbers of true-positive (TP, positive prediction in case of damaged building), false-positive (FP, positive prediction in case of no-damaged building), true-negative (TN, negative prediction in case of damaged building) and false-negative (FN, negative prediction in case of no-damaged building) are used to generate a ROC. A ROC curve describes the behaviour of the true-positive rate ($TPR=TP/(TP+FN)$) as a function of the false-positive rate ($FPR=FP/(TN+FP)$). The capacity of the model to discriminate where a building is more likely to be already damaged ($TPR-FPR$) is then proportional to the extension of the area under the ROC curve (Area Under Curve, AUC). As a rule, an AUC of 0.5 indicates no discriminating capability, whereas an AUC between 0.6 and 0.7 relates to a poorly discriminant model, an AUC between 0.7 and 0.8 is considered acceptable, an AUC between 0.8 and 0.9 is considered excellent, and an AUC higher than 0.9 is considered outstanding.

Figure 33A shows a graph with four ROC curves generated by considering as “damaged” four selections of the classes: starting from only the most severe (class 6), and then including for each curve the next class, i.e., the class corresponding to the next lower damage level. This is done to analyse how the prediction capability changes depending on the damage severity levels.

Table 3 Number of building inventoried over each urban area for each class of damage (Cooper, 2008).

Class \ Urb.	Alfa Mar	Cerro Gordo	Almendros	Totals
<3 (Not visible)	68	40	401	509 (~ 80%)
3 (Moderate)	17	5	49	71 (~ 11%)
4 (Serious)	5	6	9	20 (~ 3%)
5 (Very serious)	1	15	3	19 (~ 3%)
6 (Partial collapse)	2	9	3	14 (~ 2%)
TOT	93	75	465	633



Figure 32 Examples of landslide-field evidences and damages in Cerro Gordo. Image A belong to class 6 (partial collapses), Image B is an example of class 5, a very serious damage, with a distinct crack (separating two blocks) and tilts affecting the garages. Images C shows an example of wall cracks belonging to class 4 (serious damage).

The ROC curves seem to approach the diagonal, as we introduce classes of lower damage level. We can see that the prediction capabilities are acceptable and almost the same if we consider only the class 6 ($AUC_6=0.74$) or classes 5 and 6 together ($AUC_{5,6}=0.73$). The AUC slightly decrease ($AUC_{4,5,6}=0.68$) if we also introduce class 4, but in this case the test is poorly discriminant even though the AUC is about 0.7. Finally, the performance is strongly affected by the inclusion of class 3, with a ROC curve that is very close to the diagonal regardless the used threshold ($AUC_{3,4,5,6}=0.65$). This behaviour can be explained by the fact that the damage inventory was prepared by visual inspection from outside the buildings, the lower the damage level the more the observation is subjected to variables like visibility and recognisability. Moreover, the building external status can be altered, fixed, or occulted (e.g., fissures or small cracks can be easily filled and painted). Furthermore, it must be considered that lower damage levels are expected to be related to lower displacement intensity gradients, which are more difficult to be detected due to the sensitivity of MTInSAR techniques. Figure 33B shows a similar analysis performed by using as intensity value the absolute values of the velocities instead of gradients. We see that the prediction capability of the velocity abruptly decreases from acceptable ($AUC_6=0.77$) to poorly discriminant ($AUC_{5,6}=0.59$) as we move from considering only class 6 to considering the classes 5 and 6. This means a good discrimination only for the class 6 (partially collapsed), which is not satisfactory for preventing purposes. Therefore, it is evident that the use of gradients as intensity values to predict damages, provides a higher discriminant capacity than the use of velocities. The ROC analysis allowed to select the gradient threshold that maximize the discrimination capability (TPR-FPR). This threshold corresponds to a gradient of 8 % ($\text{mm} \cdot \text{yr}^{-1} \cdot \text{m}^{-1}$), which allowed to detect around the 70% (TPR) of the buildings belonging to classes 5 and 6, having the FNR and FPR of around 30% (Figure 33A). Whereas false positives could be interpreted as potential damage areas, the false negatives are mainly related to the intrinsic limitations of the MTInSAR technique (namely geometric limitations, absence of measurement points or non-precise geo-localization), and of the methodology (loss of precision due to the rasterization and interpolation process). Considering all the limitations related to the test-sample characterization, and that we did not consider the vulnerability variables related with the building characteristics (e.g., year of construction, securing interventions, geometry measurements, construction type and material, and foundation type), we believe this result represents a satisfactory outcome. The proposed methodology and the outputs, are in line with the SO 3 and 4, representing operational tools for landslide risk management and easy-to-read maps.

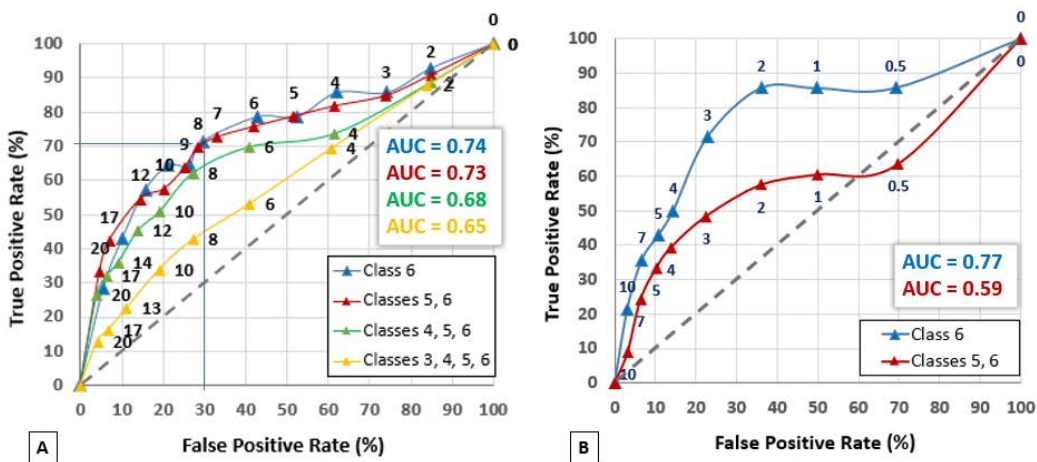




Figure 33 ROC curves generated with the same test-sample, considering the gradients (A) and the velocities (B) as intensity values. The different curves are generated considering as damaged only a sub-selection of classes. The numbers are the thresholds used to plot the curves

4 A methodology to detect and update active deformation areas based on Sentinel-1 SAR images

Article

A Methodology to Detect and Update Active Deformation Areas Based on Sentinel-1 SAR Images

Anna Barra ^{1,*} , Lorenzo Solari ² , Marta Béjar-Pizarro ³ , Oriol Monserrat ¹,
Silvia Bianchini ², Gerardo Herrera ³ , Michele Crosetto ¹, Roberto Sarro ³,
Elena González-Alonso ⁴, Rosa María Mateos ⁵, Sergio Ligüerzana ⁴, Carmen López ⁴ and
Sandro Moretti ²

¹ Centre Tecnològic de Telecomunicacions de Catalunya (CTTC/CERCA), Geomatics Division, 08860 Castelldefels, Spain; omonserrat@cttc.cat (O.M.); mcrosetto@cttc.cat (M.C.)

² Earth Sciences Department, University of Firenze, Via La Pira, 4, I-50121 Firenze, Italy; lorenzo.solari@unifi.it (L.S.); silvia.bianchini@unifi.it (S.B.); sandro.moretti@unifi.it (S.M.)

³ Geohazards InSAR Laboratory and Modeling Group (InSARlab), Geoscience Research Department, Geological Survey of Spain (IGME), Alenza 1, 28003 Madrid, Spain; m.bejar@igme.es (M.B.-P.); g.herrera@igme.es (G.H.); r.sarro@igme.es (R.S.)

⁴ Centro Nacional de Información Geográfica, Instituto Geográfico Nacional, C/General Ibáñez de Ibero, 3, 28003 Madrid, Spain; egalonso@fomento.es (E.G.-A.); cnig.slr@fomento.es (S.L.); clmoreno@fomento.es (C.L.)

⁵ Geological Survey of Spain (IGME), Urb. Alcázar del Genil, 4-Edif. Bajo, 18006 Granada, Spain; rm.mateos@igme.es

* Correspondence: anna.barra@cttc.cat or abarra@cttc.cat; Tel.: +34-93-645-2900

Received: 4 August 2017; Accepted: 21 September 2017; Published: 28 September 2017

Abstract: This work is focused on deformation activity mapping and monitoring using Sentinel-1 (S-1) data and the DInSAR (Differential Interferometric Synthetic Aperture Radar) technique. The main goal is to present a procedure to periodically update and assess the geohazard activity (volcanic activity, landslides and ground-subsidence) of a given area by exploiting the wide area coverage and the high coherence and temporal sampling (revisit time up to six days) provided by the S-1 satellites. The main products of the procedure are two updatable maps: the deformation activity map and the active deformation areas map. These maps present two different levels of information aimed at different levels of geohazard risk management, from a very simplified level of information to the classical deformation map based on SAR interferometry. The methodology has been successfully applied to La Gomera, Tenerife and Gran Canaria Islands (Canary Island archipelago). The main obtained results are discussed.

Keywords: SAR; DInSAR; deformation; measurement; landslide; subsidence; risk management

1. Introduction

This paper is focused on geohazard activity mapping and monitoring using Sentinel-1 (S-1) data and the DInSAR (Differential Interferometric Synthetic Aperture Radar) technique. In the last 25 years, the mapping and monitoring of geohazard phenomena have received an important contribution from the DInSAR technique. This approach was firstly proposed in 1989, using data from the L-band Seasat sensor [1]. Since then, the technique has experienced a continuous growth mainly related to two main components. The first one is the important research and development effort made in this period, which has generated a wide number of data processing and analysis tools and methods. They include the classical single-interferogram DInSAR methods (e.g., see [2–4]), the DInSAR stacking techniques [5] and several implementations of the so-called Persistent Scatterer Interferometry (PSI)

and Small Baseline Subsets (SBAS) methods [6–10]. A review of all these advanced methods, which are sometimes referred to as Advanced DInSAR (A-DInSAR) or Time Series Radar Interferometry (TSInSAR), is provided in [11]. In the last years, the number of DInSAR users has increased thanks to the availability of free platforms and software, such as Grid Processing on Demand (G-POD) and Sentinel Application Platform (SNAP), provided by ESA, which have widened the range of potential users [12,13].

The second component is satellite data availability, which has increased in terms of number of satellites with different spatial and temporal resolutions. Most of the DInSAR and PSI developments have been based on C-band data acquired by the sensors on-board the satellites ERS-1/2, Envisat and Radarsat. The available imagery collected by these satellites cover long periods of time (starting from 1992), a key aspect to guarantee a long-term deformation monitoring and to make historical studies [14]. DInSAR and PSI have experienced a major step forward since 2007, with the advent of very high-resolution X-band data [15] of TerraSAR-X and COSMO-SkyMed. This includes the capability to generate a dense sampling of Persistent Scatterers (PS), a high sensitivity to small displacements and a remarkable quality improvement of the time series with respect to the C-band [16,17]. Those improvements have had an important impact on the geohazard applications, improving the analysis at different scales and allowing the combination of the results from different satellites [18–24]. A review over the available satellite SAR sensors and their potentialities for landslide application can be found in [25,26]. A significant further improvement is given by the new C-band sensor on-board the S-1A and B satellites, launched on 2014 and 2016, respectively [27]. S-1 has improved the data acquisition throughout and, compared to previous sensors, has increased considerably the DInSAR and PSI deformation monitoring potential [4,28] allowing to make long-term geohazard monitoring planes over regional areas [29].

This work is aimed at exploiting the wide area coverage and the high coherence [4] and temporal sampling (revisit time up to six days) provided by the S-1 satellites to generate and periodically update regional-scale deformation activity maps for the geohazard management. The proposed methodology has been developed in the framework of the ongoing European ECHO (European Civil Protection and Humanitarian Aid Operations) project “Safety—Sentinel for geohazards regional monitoring and forecasting”, which aims at providing Civil Protection Authorities (CPA) with the capability of periodically evaluate and assess, at regional scale, the potential impact of geohazards (volcanic activity, landslides and subsidence) on urban areas.

The interpretation of the DInSAR derived maps (e.g., velocity maps) can be complex, mostly for users who are not familiar with radar data [30,31]. This is more evident working at regional scale, where the high number of PSs can difficult the analysis and in some cases misinterpret the real scenario. Several authors have shown different approaches to address this issue [25,32]. This work presents a procedure to generate clear products that can be easily exploited by the authorities involved in the geohazard and risk management chain. The main output is the so-called Active Deformation Areas (ADA) map. It is derived from the DInSAR Deformation Activity Map (DAM) by discriminating the more reliable deforming areas. A further step, which is the integration of the products of the methodology (DAM and ADA maps) in the Civil Protection risk management activities, is described in [33].

The procedure is illustrated through its application over the Canary Islands, a Spanish volcanic archipelago located in the Atlantic Ocean, northwest of Africa, which is one of the test sites of the Safety project. Canary Islands present different types of geohazards, including landslides, earthquakes and volcanic activity.

The paper starts with the description of the procedure (Section 2), then the results of the active deformation maps obtained over the Canary Islands test site are described (Section 3). This is followed by the discussion of the results by emphasizing the main advantages and main challenges of the proposed approach (Section 4). Finally, the conclusions of the work are drawn (Section 5).

2. Methodology

In this section, the procedure to derive the DAM and the ADA maps is described. The proposed procedure can be applied to the data acquired by any satellite SAR sensor. However, it provides the best performances with the S-1 characteristics.

The general scheme of the procedure, shown as a flowchart in Figure 1, is divided in two main blocks (Figure 1):

1. Raw Deformation Map (RDM) generation: This includes all the PSI processing steps to estimate the annual linear velocities and the time series of deformation (TS). The RDM is an intermediate product that is not delivered to the final users.
2. Deformation Activity Map (DAM) generation and Active Deformation Areas (ADA) extraction: In this block, the two final products of the procedure are generated. It includes a filtering of the RDM and all the steps to generate the ADA map. These two products are easily readable and thus exploitable by the risk management decision makers.

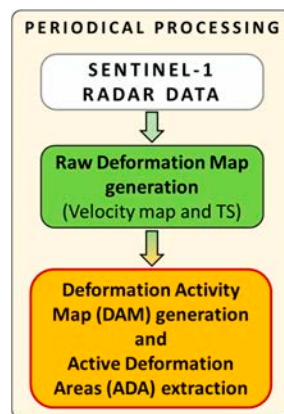


Figure 1. Flow chart of the proposed procedure.

All the deformation values included in the output maps are estimated along the satellite Line of Sight (LOS) direction. The procedure is designed to be periodically processed to have a continuous update of the products and thus a continuous input of regional-scale deformation maps for the authorities to detect potential hazards or to decide more focused analysis in critical areas.

2.1. Raw Deformation Map Generation

The main goal of this block is to derive the deformation scenario of an area of interest from the SAR data. The output is a deformation map that consists in a set of selected points with both the information of the estimated LOS velocity and the accumulated displacement at every satellite acquisition. The main input is a set of SAR images acquired at different times. Several Persistent Scatterer Interferometry (PSI) techniques have been developed in the last decade. The main common steps to generate a deformation map are: the interferogram network generation, the selection of points, the phase unwrapping, the Atmospheric Phase Screen (APS) estimation and removal and the estimation of the velocities and/or deformation time series (TS). The choice between the different techniques depends on many factors like the radar sensor characteristics, the target of the study or the characteristics of the test site (geology, land use, topography, etc.). In particular, for this research, the maps have been generated using an approach of the Persistent Scatterer Interferometry chain of the Geomatics (PSIG) Division of CTTC (PSIG) described in [32]. The main steps of the processing are briefly described in the following lines (Figure 2):

- Interferogram network generation: This step consists of the generation of the interferogram network. S-1 uses a sophisticated data acquisition procedure, the TOPS (Terrain Observation

by Progressive Scan) imaging mode [34], which is key to achieve the wide area coverage. The drawback is that, compared to other sensors, the S-1 data require extra processing. The key step is the image co-registration, which needs to be very accurate [35].

Since a fundamental aspect of the PSIG chain is the redundancy of the network of interferograms and images, all the possible interferogram pairs are generated. The selection of the interferogram network is done by statistically evaluating the coherence of the study area. This analysis provides key inputs for the network like the maximum temporal baseline to be used as well as the presence of periods characterized by low coherence (e.g., snow periods in mountain areas). As example, in the Canary Islands test site, the selected maximum temporal baseline was 156 days.

- **Point Selection:** Even if a single S-1 frame contains millions of pixels, only a small portion of them is exploitable for deformation purposes. There are different statistical criteria used to discriminate the noisier pixels from those with low level of noise [11]. However, the use of very restrictive thresholds can result in a critical loss of spatial coverage. The general purpose of this step is to find a good compromise between the quality of the selected points (little affected by noise) and a good spatial coverage. Hence, for each case, different criteria are evaluated in order to find the best trade-off. For example, in the Canary Islands test site, the selection of points was based on the Dispersion of Amplitude (DA) [6]. Only points with a DA value lower than 0.5 have been selected.
- **2+1D phase unwrapping:** This is a two-step spatial-temporal phase unwrapping [32]. The approach starts with a spatial phase unwrapping (2D) performed over the selected set of points and for each interferogram of the network. Then, in a second phase, a phase unwrapping consistency check (1D) is performed. This check is done point wise, exploiting the temporal component of the SAR images stack. It is based on an iterative least squares method (LS) and the analysis of the LS residuals at each iteration. For each pixel, the main outputs are: (i) the temporal evolution of the phases (TEP) with respect to a reference image; and (ii) some statistical parameters used to assess the quality of the LS inputs.
- **APS (Atmospheric Phase Screen) estimation and removal:** The APS is estimated using spatial-temporal filters [36]. The main input is the TEP estimated in the previous step. The estimated APS is removed from the TEP. The remaining phases are then transformed into deformations, obtaining the final deformation time series (TS).
- **Deformation velocity estimation:** This is the last step of the deformation map generation block. It consists of an estimation of the deformation velocity from the obtained time series. The used method is a robust regression line estimation.

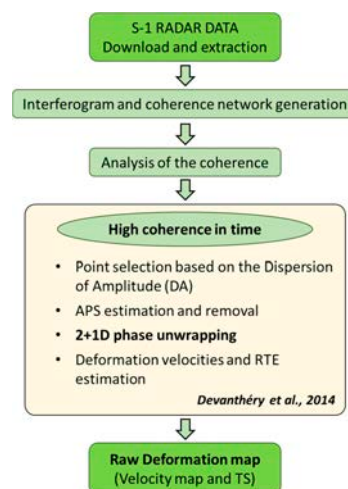


Figure 2. Flow chart of the Row Deformation Map (RDM) estimation.

The final output of this block is a raw deformation map (RDM) including, for each point, the deformation velocity and the accumulated deformation at each acquisition time (TS). The estimated deformations are in the satellite LOS direction.

It is worth noting that the described approach can slightly change depending on the site. A frequent variation is to perform the deformation velocity estimation before the 2+1D phase unwrapping. The deformation velocity is estimated over the wrapped phases and then removed from them before the phase unwrapping [5]. This is done to ease the 2D phase unwrapping step in areas strongly affected by deformation.

2.2. Deformation Activity Map and Active Deformation Areas Extraction

This block is aimed at obtaining both the final Deformation Activity Map (DAM), which is the filtered version of the raw deformation map (RDM), and the Active Deformation Areas (ADA) map, which is the main product of the procedure. The main goal is to identify and monitor, over wide areas, the most critical deformations to provide the Civil Protection authorities with the capacity to perform prevention and mitigation actions. Therefore, the three main aspects that have to characterize the final maps are: (i) the readability; (ii) the reliability; and (iii) the regional-to-local scale. The main constraining factors to achieve these goals are the spatio-temporal noise of the deformation map and the high number of PSs which in some cases can lead to wrong interpretations.

A key parameter of this block is the assessment of the general noise level (sensitivity) of the RDM. In this research, the sensitivity has been evaluated using the standard deviation (σ_{map}) of the RDM velocity values. A stability threshold of $2\sigma_{\text{map}}$ is set to distinguish the active points, those where we measure movements, from those we do not. A point is considered moving if $|v| > 2\sigma_{\text{map}}$, where $|v|$ is the absolute velocity value of the point. It is worth to underline that the points classified as “stable” can be truly stable as well as instable points, with a not detectable movement. To simplify the readability, we call “stable” all the points with the absolute LOS velocity below the stability threshold. As example, in the Canary Island test site, the stability threshold has been set as ± 4.7 mm/year.

This block can be summarized in three main steps (Figure 3): (i) filtering of the RDM; (ii) automatic extraction of the more reliable and relevant active areas (ADA); and (iii) Quality Index (QI) attribution to each ADA.

(i) Filtering of the raw deformation map

This action aims to filter the RDM obtained in block 1. The final point selection has been based on two different criteria: (i) the standard deviation of the 2+1D phase unwrapping residues (σ_{res}); and (ii) a spatial criterion based on the variability of a point with respect its neighbors. The first one is used to remove points susceptible to be affected by phase unwrapping errors. The used threshold for the σ_{res} is 2.4 rad (approximately 1 cm). We have selected this relatively high threshold in order to keep the maximum number of measurements. Regarding the spatial criterion, it is used to clean sparse measurements (isolated points) and points with strong discrepancy with respect its neighbors (outliers). The filtering is window based. The used window has a radius of 2 times the data resolution (e.g., around 80 m in Canary Island).

The filtering criteria are: (i) eliminate points without neighbors inside the window; and (ii) eliminate moving points without more than one moving neighbors inside the window. It is worth noting that the eliminated points can be real moving points related to a geohazard, like for example a landslide. However, an isolated point can be related to several factors including noise. In this context, we accept to lose information about few phenomena in order to highly reduce the general level of noise and simplify the readability of the map.

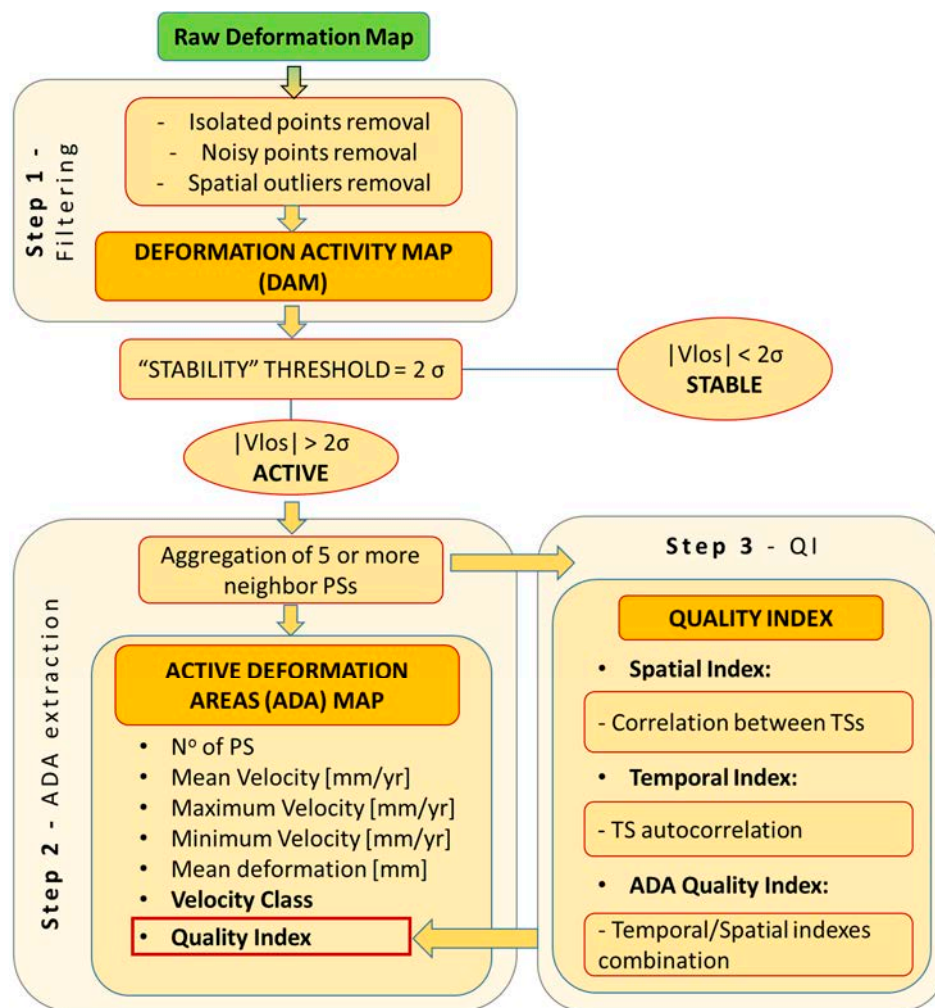


Figure 3. Flowchart of the Deformation Activity Map (DAM) and the Active Deformation Areas (ADA) maps generation.

(ii) Automatic extraction of the more reliable and relevant active areas (ADA)

The aim of the ADA map generation is to perform a rapid identification of the most reliable active deformation areas. The final map has to represent a clear input to be validated and integrated with other data (e.g., geohazard inventories, ground truth information, etc.) in order to determine the nature of the deformation and thus to generate the Geohazard Activity Map.

The ADA map has been by using an evolution of the approaches proposed by [37–40]. The main input is the filtered deformation velocity map obtained in Step (i). Only the moving points (with $|v| > 2\sigma_{\text{map}}$) are selected. Then, from this subset of points (PSm), groups of at least five neighbor PSs, sharing their influence area, are aggregated in polygons representing the Active Deformation Areas (ADA). To define the influence area of every PS we consider the approximated footprint of the PSs. For example, in Canary Island test site, the PS area is of 28 m by 40 m. Then we calculate the radius of the circle inscribing the PS area (40 m by 40 m in the Canary Island Site) and we multiply it by a factor of 1.3 to ensure that neighboring pixels are selected. If the grouped PSs are less than five, they are considered to represent a non-significant deformation for a regional scale map.

Finally, for each ADA, the following parameters are estimated:

- Number of aggregated active points (APs).
- Mean, maximum and minimum values of the APs velocities.

- Mean value of the APs accumulated deformations. To avoid strong influence of atmospheric or digital elevation model error effects, we estimate the final accumulated deformation as the average of the accumulated values of the last four acquisition times of all the APs of the ADA.
- Velocity class, which is a classification of the ADA as a function of its maximum velocity (v_m). The class is 1 if $|v_m| > 1$ cm/year or 0 if $2\sigma_{\text{map}} < |v_m| < 1$ cm/year.
- Quality Indexes, which are explained in the following lines.

(iii) Quality index attribution to each ADA

Although the ADA map is based on filtered data, the automation of the process needs a final quality assessment for each single ADA. The noise level of the TSs and thus the robustness of the deformation estimations vary significantly pointwise. This step describes an implemented Quality Index (QI) that provides an estimation of the noise level of the ADA. This QI is a key parameter to properly interpret the ADA map.

The QI is based on the evaluation of two parameters for each ADA: the noise of each AP time series is evaluated and the spatial homogeneity of the estimated deformations in time is considered (i.e., consistency between AP time series). Hence, each ADA is characterized by a temporal noise index (TNI) and a spatial noise index (SNI) that are used to derive the final QI.

- Temporal Noise Index (TNI)

To attribute the TNI, for each APs the first order autocorrelation ($\rho_{t,t-1}$) of its TS is evaluated. The first order autocorrelation allows evaluating the temporal noise degree for both linear and nonlinear deformation trends. The autocorrelation coefficient ranges from 0 to 1, where 0 means the prevalence of noise over the deformation trend. The temporal index (TNI) is a four-class classification of the ADA based on the median value ($Med(\rho)$) between the TS autocorrelation coefficients, it varies from 1 to 4, where 1 corresponds to a high $Med(\rho)$ and 4 to a very low $Med(\rho)$.

To find a relationship between the autocorrelation coefficient and the noise level, a simulation was performed on a set of 20 TSs characterized by a linear trend (b) and random noise (ϵ):

$$Y = bx + \epsilon$$

where b = velocity in (mm/day), $x = 0, 12, 24, 36, \dots, 468$ (days) is the 12 days spaced time series. The random noise was characterized by a normal distribution. For each velocity, we tested different levels of noise by setting the standard deviation of the simulated random noise. Since the autocorrelation also depends on the number of sampling (i.e., on the length of the TS and the revisit time), our simulation was calculated over 468-day time series (almost one year and half) with temporal steps of 12 days. This period corresponds to the temporal window used to generate the deformation maps in our test site (Canary Islands). Figure 4 shows the results of the two simulations performed with the velocities of 5 and 10 mm/year. The plotted values represent the median value of the set of TSs autocorrelation coefficients calculated for each tested noise level. By expressing the noise level in terms of percentage of the velocities, the relationship can be approximated by the linear regression of the whole data resulted by the simulation.

It is worth mentioning that this is a simplified model, helpful to evaluate the physical meaning of the thresholds. Note that, for equal noise level, the autocorrelation coefficient changes with temporal sampling. Therefore, the thresholds can change, depending on the study case, if both the Sentinel-1A and Sentinel-1B images are used (six-day revisit time).

The $\rho_{t,t-1}$ values of 0.53, 0.70 and 0.84, respectively, corresponding to the 35%, 25% and 15% of noise with respect to the velocities (Figure 4 and Table 1), were chosen as thresholds for the four classes of TNI.

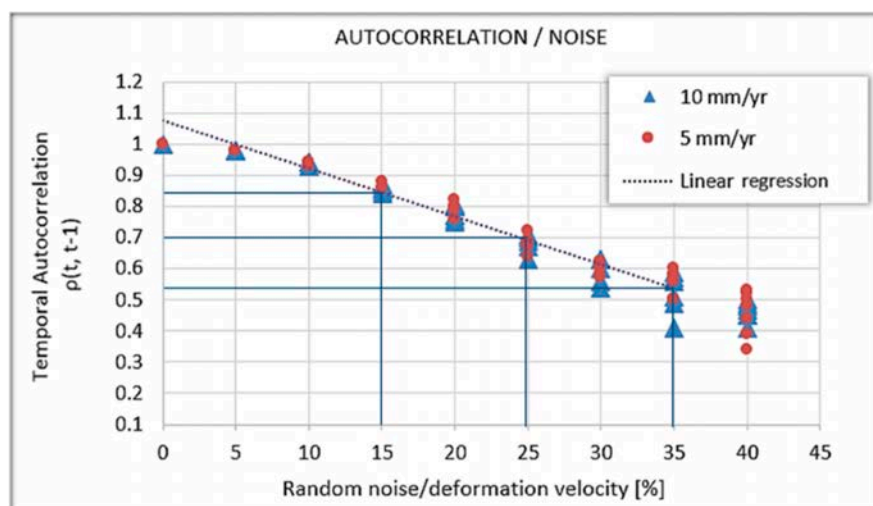


Figure 4. Plot of autocorrelation coefficient vs. level of noise (%). The level of noise is defined by the standard deviation of the simulated normal distributed random values. The blue lines indicate the selected thresholds for the Temporal Noise Index (TNI) classification.

Table 1. Final classification of TNI.

$Med(\rho)$	Noise-Velocity Ratio (%)	Class
<0.53	>35	4
0.53–0.70	35–25	3
0.70–0.84	25–15	2
>0.84	<15	1

- Spatial Noise Index (SNI)

The aim of the SNI estimation is to evaluate the spatial consistency of the detected ADA, i.e., to quantify how the PSs composing an ADA evolve with a similar trend. We assume that all the TSs of the same ADA belong to the same deformation phenomena. Thus, we expect different magnitude of the detected movements, but a spatial correlation between their temporal evolutions. With this aim, for each ADA the correlation coefficient between all the possible pairs of TSs are calculated ($CORR(X_i, Y_j)$), where i, j represents all the possible pair combinations of the APs and X_i and Y_j are their respective TSs. The spatial index (SNI) is a four-class classification of the ADA based on the median value ($Med(CORR)$) of all the ADA's TSs pairs correlation values. It varies from 1 to 4 where 1 corresponds to a high $Med(CORR)$ and 4 to a very low $Med(CORR)$. The classification thresholds (Table 2) have been set on the statistical distribution of the results, specifically the values corresponding to the quartiles that have been chosen.

Table 2. Final classification of the Spatial Noise Index (SNI).

$Med(\rho)$	Cumulative Frequency (%)	Class
<0.53	<2	4
0.53–0.7	2–25 (1st quantile)	3
0.7–0.84	25–75 (2nd and 3rd quantiles)	2
>0.84	>75 (4th quantile)	1

- ADA Quality Index (QI)

The global QI is derived from the combination of both the TNI and the SNI, and measures the degree of reliability of each detected ADA. The numerical classes (QI) assigned to each TNI-SNI

combination are represented by the matrix shown in Figure 5. The QI ranges from Class 4, which is the noisiest one, to Class 1, which represents the ADA characterized by very high quality time series (TS). More in detail: Class 4 represents a not reliable ADA; Class 3 means reliable ADA but TS that cannot be exploited; Class 2 means reliable ADA, but a further analysis of the TS is recommended; and Class 1 means reliable ADA and TS.

		Spatial Noise Class			
		1	2	3	4
Temporal Noise Class	1	1	1	2	4
	2	1	2	3	4
	3	2	3	3	4
	4	4	4	4	4

Figure 5. Quality Index (QI) matrix representing the derivation of the QI from the combination of the Spatial Noise Index (SNI) and the Temporal Noise Index (TNI) is generated.

3. Canary Island Results

In this section, the results of the above application of the procedure over the Canary Islands and some related technical aspects are discussed and presented.

The explained procedure has been applied to three islands: La Gomera, Tenerife and Gran Canaria (Spain). The test-site, covering a total land surface of around 4000 km², allows testing the regional scale potentialities of the procedure.

3.1. Dataset Description

The three islands are covered by a single Sentinel-1 frame. In particular, three swaths and 18 bursts have been processed. In Table 3, the main characteristics of the used dataset are described. The used image dataset consists of 64 Sentinel-1 Wide Swath images covering around a two years and a half period, with the first acquisition time in November 2014 and last acquisition time in March 2017. In this study only images from Sentinel-1A satellite have been used, thus the minimum temporal sampling is 12 days, while the maximum temporal sampling, which is defined by the images availability, is 48 days. Table 4 shows the list of all the acquisition times of the processed images.

As explained in the introduction, the aim of the procedure is to generate and periodically update deformation activity maps. With this aim, the dataset has been divided in two parts and processed separately to produce and compare two versions of the ADA map: version V1 and the temporally-updated version V2. The temporal windows covered by the two processing iterations and the number of the processed images are resumed in Table 4: for the first iteration, 51 images covering a period of around two years have been processed; and, for the second iteration, 42 images covering a period of one and a half years have been processed, the overlapping period between the two iterations is one-year long. Furthermore, considering the specific radiometric characteristics of the test-site, using temporal windows of one and a half years, to be processed each six months (i.e., with an overlapping period of six months) is the ideal way of generating and updating the maps.

The SRTM Digital Elevation Model provided by NASA has been used to process the interferometric products [41].

Table 3. Main characteristics of the processed data.

Satellite	Sentinel-1A
Acquisition mode	Wide Swath
Period	November 2014–March 2017
Minimum revisit period (days)	12
Wavelength (λ) (cm)	5.55
Polarization	VV
Full resolution (azimuth/range) (m)	14/4
Multi-look 1 \times 5 resolution (azimuth/range) (m)	14/20
Multi-look 2 \times 10 resolution (azimuth/range) (m)	28/40
Orbit	Descending
Incidence angle of the area of interest	36.47°–41.85°

Table 4. List of the acquisition dates of the dataset. The intersection between both periods is in bold.

Image	Date	Image	Date	Image	Date	Image	Date
1	5 November 2014	18	8 August 2015	35	28 February 2016	52	13 October 2016
2	17 November 2014	19	20 August 2015	36	11 March 2016	53	25 October 2016
3	29 November 2014	20	1 September 2015	37	23 March 2016	54	6 November 2016
4	11 December 2014	21	13 September 2015	38	4 April 2016	55	18 November 2016
5	23 December 2014	22	25 September 2015	39	16 April 2016	56	30 November 2016
6	4 January 2015	23	7 October 2015	40	28 April 2016	57	12 December 2016
7	16 January 2015	24	19 October 2015	41	10 May 2016	58	24 December 2016
8	28 January 2015	25	31 October 2015	42	22 May 2016	59	5 January 2017
9	9 February 2015	26	12 November 2015	43	3 June 2016	60	17 January 2017
10	21 February 2015	27	24 November 2015	44	15 June 2016	61	29 January 2017
11	5 March 2015	28	6 December 2015	45	9 July 2016	62	22 February 2017
12	17 March 2015	29	18 December 2015	46	21 July 2016	63	6 March 2017
13	29 March 2015	30	30 December 2015	47	2 August 2016	64	18 March 2017
14	9 June 2015	31	11 January 2016	48	14 August 2016		
15	3 July 2015	32	23 January 2016	49	7 September 2016		
16	15 July 2015	33	4 February 2016	50	19 September 2016		
17	27 July 2015	34	16 February 2016	51	1 October 2016		

3.2. Deformation Activity Maps

To derive the deformation maps, we have generated a network of 398 interferograms in the first iteration and 481 interferograms in the second iteration. The maximum temporal baseline used is 156 days. This threshold has been derived by statistical analysis of the coherence with respect to the temporal baseline. The reference points used for the processing are located in the historical centres of the three capitals of the islands (Figure 6a): San Sebastián de La Gomera; Santa Cruz de Tenerife; Las Palmas de Gran Canaria.

Due to the geologic and land cover settings, mainly of sparse vegetation and rocky surfaces, Canary Islands show a good radar response in terms of coherence. This characteristic results in a deformation map characterized by both a high coverage of points and a low spatio/temporal noise. Figure 6 shows the high density of points of the velocity map: only the few zones covered by forest show absence of points (northern humid flanks of the islands). The noise level of the map (i.e., the sensitivity) was estimated as two times the standard deviation of the velocity of all the measured points and is equal to 4.7 mm/year for both iterations. This value (see Section 2) also represents the stability threshold, i.e., the value that separates the moving points from the points with no-detected movement (stable points).

As explained in Section 2, three filters have been applied to the raw deformation map in order to reduce the spatio-temporal noise and thus to improve the readability and the reliability of the map measurements. Figure 6 shows the velocity map resulted from the first iteration before and after the spatial filtering. After the filtering, the number of measured points of the Deformation Activity Map (DAM) is 1,060,750 for the first iteration and 1,036,328 for the second iteration. The total number of points identified as non-stable is 2358 in the first iteration and 1859 in the second one, which represents less than 1% of the total number of measured points.

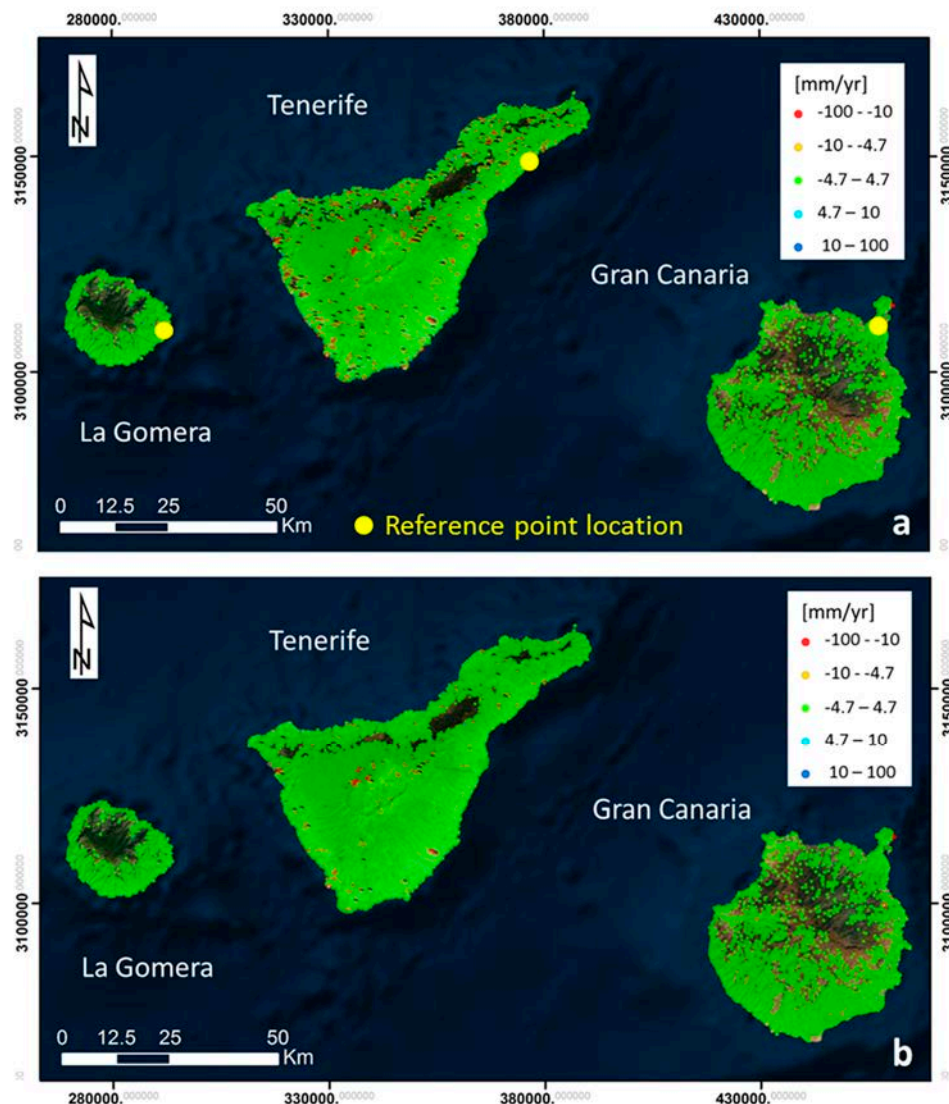


Figure 6. The velocity map of the first iteration (V1): before the raw deformation map (a); and after the filtering (b). The latter one is the final Deformation Activity Map (DAM).

3.3. Active Deformation Areas (ADA) Map

To extract the ADA from the DAM, the methodology shown in Figure 3 and explained in Section 2 has been applied. Figure 7 shows an example of ADA extraction over the Pico Viejo-Teide area, in the heart of Tenerife Island: only the active PSs are visualized, the red polygons are examples of extracted ADA (five or more active contiguous PSs), the green polygons highlight the spatial outliers PSs (one or two active isolated PSs), which are not included in the final DAM, while the orange polygons are active PSs that are not extracted as ADA (three or four contiguous PSs) but are included in the DAM for a local scale analysis. Figure 8 shows an example of two extracted ADA, located southeast of Tenerife (Figure 8a), which are both subsidence phenomena related to the activities of a waste dump. Figure 8b presents the DAM of the waste deposit area. There are four areas affected by movements, two with subsidence (red) and two with uplift (blue), both related to the waste dump activities.

Figure 8c shows the two ADA affected with subsidence in Figure 8b. Figure 8d shows the time series of three PSs located, as indicated in Figure 8c, in one of the two ADA. The area is classified with both the SNI and the TNI equal to 1, which means that the ADA is characterized by the highest spatial and temporal quality. It is interesting to note that the SNI method evaluates the spatial noise in terms

of spatial homogeneity of the ADA temporal evolution and is not affected by the spatial variation of the deformation magnitude. In this case, for example, the ADA presents very different velocities, following the subsidence spatial distribution, with the higher deformation rate in the centre of area (Figure 8c,d, PS-2) and the lower ones in the peripheral zones (PS-1 and PS-3). This subsidence area is active in both iterations, without a significant change in the mean velocity (less than the sensitivity of the map): -41.4 mm/year in the first iteration and -40.4 mm/year in the second iteration.

For each ADA, the information resumed in Table 5 is collected, forming the attribute table of the corresponding polygonal shapefile. This include the velocity class, which allows enhancing the visualization of the most critical ADA in terms of magnitude of deformation, and the QI class, which is a fundamental information for the interpretation of the map. An example of ADA map visualization of both the QI and the velocity class information is presented in Figure 9. In the first iteration, 72 ADA has been extracted: 69 are localized on Tenerife Island and the other three on Gran Canaria. In the second iteration, 120 ADA have been detected: 112 are on Tenerife, seven on Gran Canaria and one on Gomera. In total, 68% of the ADA detected in the first iteration (V1) fall in the QI classes 1 and 2, while, in the second iteration (V2), the percentage of 1 and 2 QI drops to 43% (see the Total columns of Table 6). This reflects the higher general noise level of the second version (V2) of the DAM and ADA maps.

To compare the two iterations, a simple intersection has been performed. Table 7 and Figure 10 summarize the comparison between the two iterations. Table 7 summarizes the global numbers of both iterations. The total number of detected ADA is 192: 68 of them have QI 1 from which 43 are present in both iterations (Intersect) and 25 only in one of them (No Intersect). Regarding the last ones, it is worth noting that, even if they are not in both iterations, they are considered reliable ADA. The reason an ADA is detected in some iterations, but not in others, can be due to different factors like the loss of coherence or a different behavior of the phenomenon in different periods.

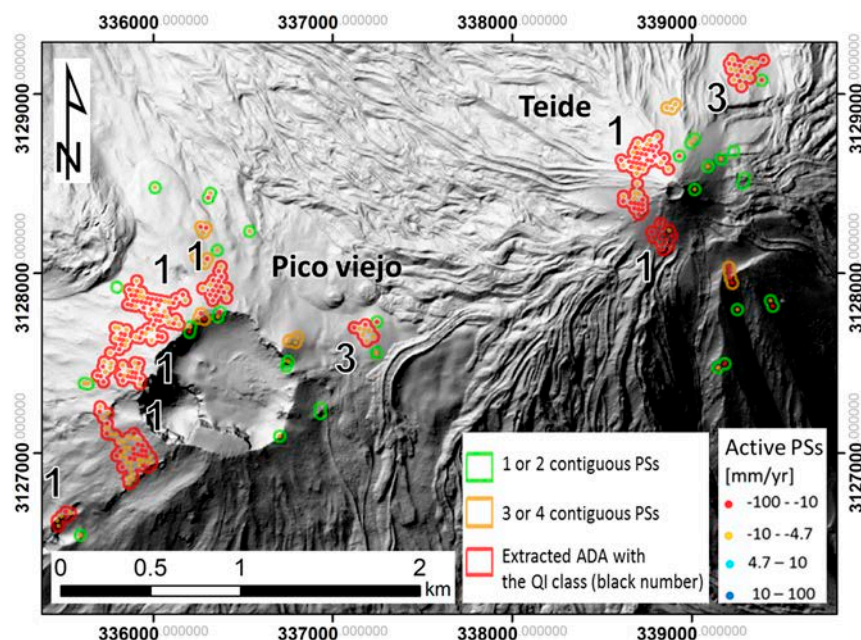


Figure 7. Example of ADA extraction from the active PSs of the first iteration velocity map (V1). The area includes the Pico Viejo and Teide craters, the highest elevations on Tenerife Island. Only the active PSs are visualized. The red polygons are the extracted ADA and the black numbers are the associated Quality Indexes.

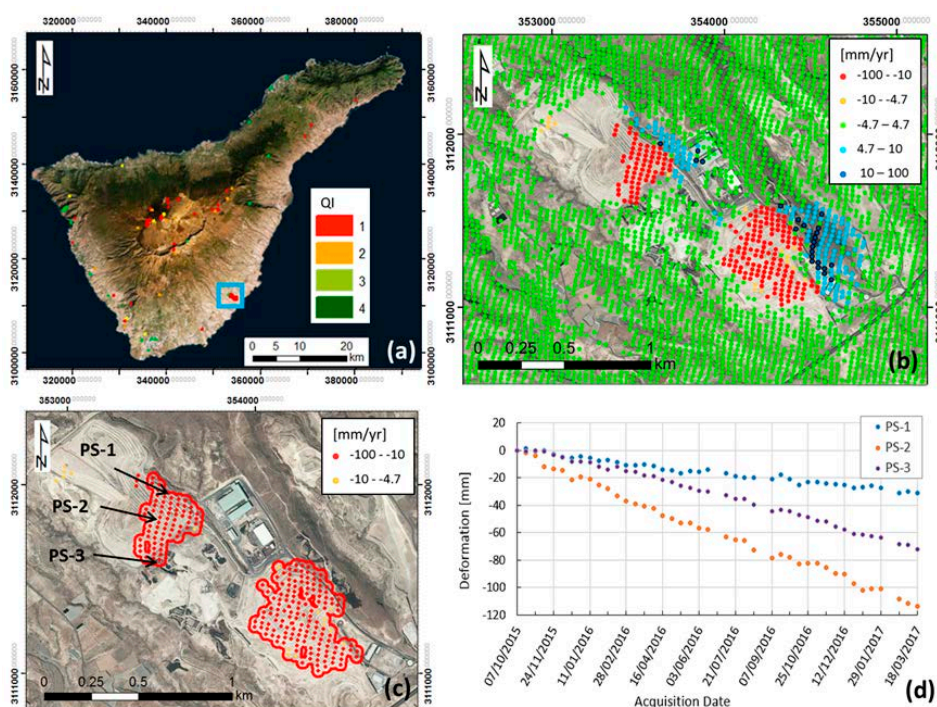


Figure 8. (a) The ADA V1 map of Tenerife, the blue square highlights the area that is showed in detail in (b,c); (b) the DAM (velocity map) in correspondence of the blue frame in (a), which is an industrial landfill area affected by subsidence (red points) and uplift (blue points); (c) two of the extracted ADA (red polygons) of the landfill subsidence (the uplift ADA are not represented here); and (d) deformation time series of points PS-1, 2 and 3.

Conversely, the total number of ADA with QI equal to 4 are 69, where the majority (62) have no intersection between the two iterations. Looking only at the intersecting ADA, 53 out of 66 (80%) falls in the first and second QI class. Summarizing, the ADA with worst QI (3 or 4) have a low probability to be detected in more than one iteration because they are highly affected by noise and thus they are less reliable. This fact is evidenced in Figure 10, where it can be observed that most of the non-intersecting ADA have a low QI. This fact can be considered as an indicator of the significance of the QI information. Among the intersecting ADA, some of them present a change of the QI: the QI values are mainly lower in the second iteration. This is due to the noise level of the DAM, which is slightly higher in the second iteration. All but one intersecting ADA are localized on Tenerife. The remaining one is localized on Gran Canaria.

Table 5. The attributes associated to each ADA.

Field	Description	Units
Join Count	Number of unstable points grouped in the hotspot	-
Fi	WGS84 Geographic Latitude (average of the grouped PSs)	°
Lambda	WGS84 Geographic Longitude (average of the grouped PSs)	°
E	WGS84 UTM zone 32N—East (average of the grouped PSs)	m
N	WGS84 UTM zone 32N—North (average of the grouped PSs)	m
H	SRTM Height (average of the grouped PSs)	m
Acc. Defo.	Accumulated deformation (average of the grouped PSs)	mm
Velocity mean	Mean velocity of the hotspot (average of the grouped PSs)	mm/year
Velo max	Maximum velocity of the PSs grouped in the hotspot	mm/year
Velo min	Minimum velocity of the PSs grouped in the hotspot	mm/year
QI	Quality index of the ADA	-
Class	Classification of the hotspots based on the Velo max.	-

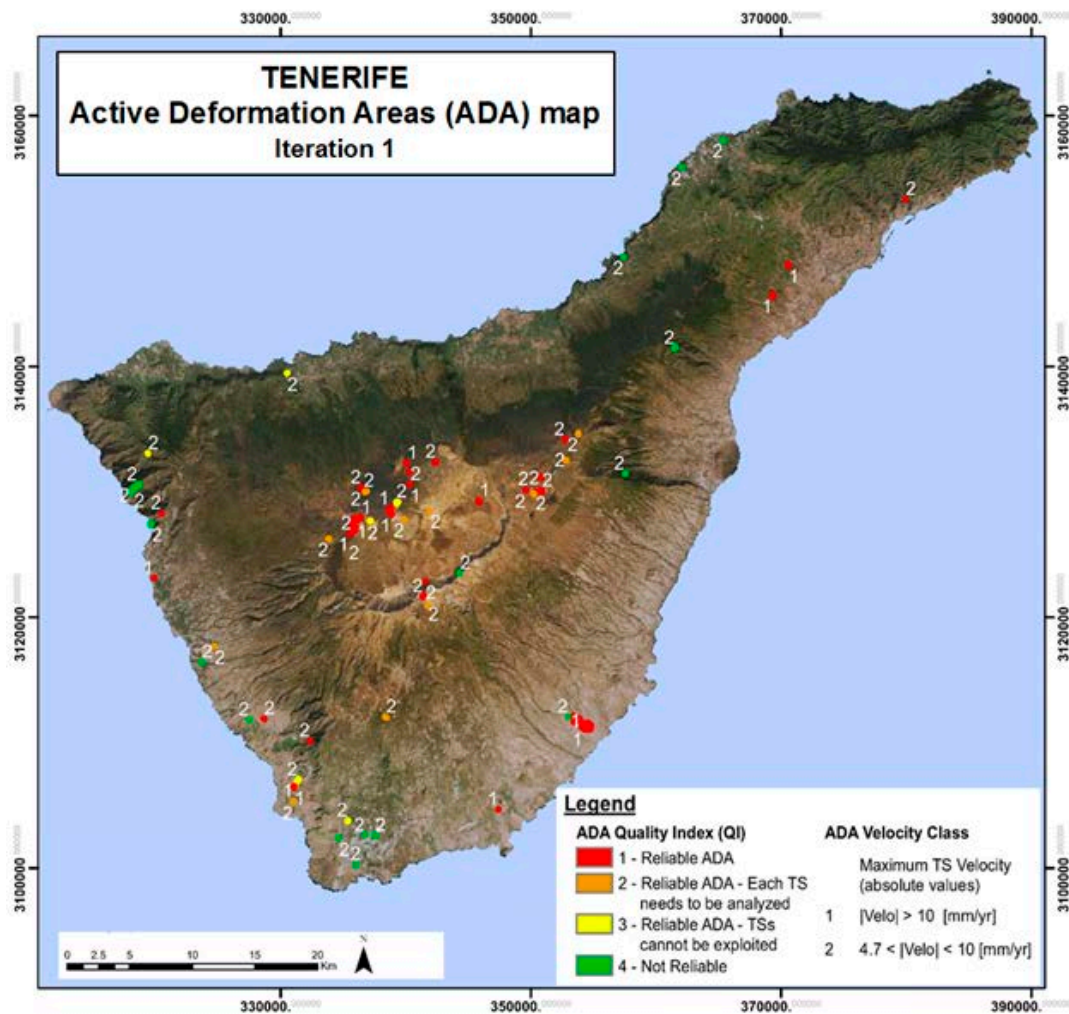


Figure 9. ADA map of Tenerife (Iteration 1). Both the QI (colors) and the velocity classes (white numbers) are represented. This visualization allows a rapid identification of the most critical and reliable deformations.

Table 6. Summary of the ADA extracted in the V1 (left) and V2 (right). In the Total column, the percentages for each QI class refer to the total number of the detected ADA. The Intersect column refers to the ADA that are detected in both iterations and the percentages are relative to each QI class. The No Intersect column refers to the ADA that are not detected in the other iteration and the percentages are relative to each QI class. In V1, 42% of the ADA are also detected in V2; of this, 80% are classified in the higher QI class (1). In V2, 31% of the ADA are also detected in V1; of this, 51% are classified in the higher QI class (1).

		V1						V2					
		Total		Intersect		No Intersect		Total		Intersect		No Intersect	
QI	n°	%	n°	%	n°	%	QI	n°	%	n°	%	n°	%
1	36	50%	24	33%	12	17%	1	32	27%	19	16%	13	11%
2	13	18%	3	4%	10	14%	2	19	16%	7	6%	12	10%
3	6	8%	1	1%	5	7%	3	17	14%	5	4%	12	10%
4	17	24%	2	3%	15	21%	4	52	43%	5	4%	47	39%
Total	72	100%	30	42%	42	58%	Total	120	100%	37	31%	84	70%

Table 7. Summary of the detected ADA in both iterations. The Intersection column refers to the ADA that are detected in both iterations. The No Intersection column refers to the ADA that are detected in only one iteration. See also Figure 10.

V1 and V2 ADA Summary			
QI Class	Tot	Intersection	No Intersection
1	68	43	25
2	32	10	22
3	23	6	17
4	69	7	62
Total	192	66	126

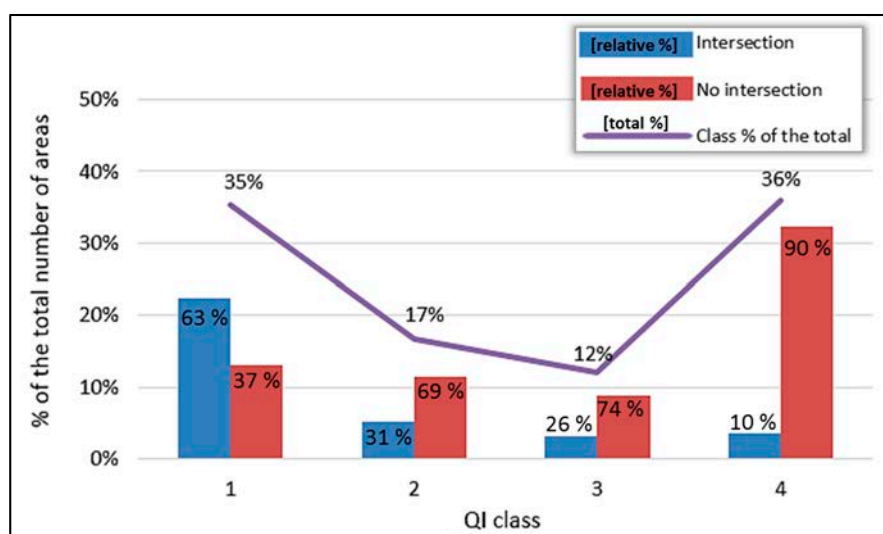


Figure 10. A representation of Table 7. The blue bars (Intersection) represent, for each QI class, the percentage of the ADA that have been detected in both the iteration. The red bars represent, for each QI class, the percentage of the ADA that have been detected in only one iteration. The purple line represents the QI percent of the total the detected ADA. The graphic shows that the majority (63%) of the ADA with a high Quality Index (1) are detected in both iterations, while the majority of the ADA with the lower Quality Index (4) are detected in only one iteration. This confirms the significance of the QI that permits to detect the noisier and not reliable ADA.

4. Discussion

In this section, some key aspects, as well as the strengths and limitations of the presented methodology are commented.

The presented methodology is aimed at generating and periodically updating geohazard activity maps over wide areas, using the satellite Sentinel-1 data. The main challenge is to generate rapidly and semi-automatically a product to be easily exploited in the geohazard management by the Civil Protections and the Geological Surveys. The regional scale potentialities of the methodology have been presented through its application over the three islands of Tenerife, La Gomera and Gran Canaria (in Spain, Figure 6). The main output of the methodology is the ADA map, which localizes only the most important detected active areas, summarizing and simplifying the significant information of the areas.

The methodology can be applied by using as input every type of satellite SAR images. Nevertheless, the best performances of the methodology are obtained using Sentinel-1 satellite data. On the one hand, S-1 acquires data with a 250 km swath at 4 m by 14 m spatial resolution (full resolution), allowing a wide area (regional scale) monitoring. On the other hand, the short revisit time of the S-1, varying 6–12 days depending on the area, reduces the temporal decorrelation of the

interferometric pairs and, together with the regular worldwide acquisition, it highly improves the monitoring potentialities. In other words, it allows making long-term monitoring planning throughout. Moreover, all the Sentinel-1 satellite data are free of charge, improving the long-term sustainability of the methodology from the point of view of the costs. For a qualitative estimation of the costs in terms of people and time needed by the methodology application, refer to [33].

The methodology results are influenced by intrinsic limitations of the SAR satellite data. Apart from the theoretical maximum and minimum measurable deformations, which depend both on the sensor characteristics and on the revisit time as described in [11], there are two other aspects that spatially influence the possibility of detecting movements: the acquisition geometry and the coherence. The last one, for equal acquisition characteristics (sensor and revisit time) and meteorological conditions, is mainly determined by the land cover. In forested areas, for example, it is very difficult to obtain reliable PSs, and thus ADA, with the PSI analysis. The geometrical limitation is determined by the geometry of SAR acquisition with respect to both: (a) the main deformation direction; and (b) the terrain topography. The InSAR techniques are capable of measuring only the LOS direction component of the real movement: it measures a percentage of the real movement that is zero if the deformation direction is perpendicular to the satellite LOS. The terrain topography, with respect to the radar wave-front angle, causes a slope-dependent ground spatial resolution variation with a consequent variation in the capability of detecting movement. Two extreme examples are the so-called shadow zones, where the slope is not seen by the radar beam (no radar visibility), and the foreshortening zones, where the slope is almost parallel to the wave-front. All those aspects, among others, belong to a fundamental knowledge background that is necessary for a correct interpretation of a PSI derived deformation map. As an example, an important aspect to underline is that the presence of “stable” (green) PSs, does not always mean ground stability. In this context, the ADA map, reporting only the active detected areas (no ADA only means no information), is a strong product that is more easily read and interpreted by not-expert final users. On the contrary, the interpretation of the Deformation Activity Map (DAM) is not straightforward and the real scenario can be misinterpreted by non-expert users. Moreover, the ADA map overcomes the problems of the noisy information and of the huge amount of measures (millions of points) to be managed, by localizing only the detected areas and summarizing the most important attributes of each area. Those aspects are fundamental for a regional scale overview. Nevertheless, the DAM is an important tool that can be used for a more detailed (local scale) spatio-temporal analysis of each ADA. To partially overcome the geometrical limitations, a parallel processing of both the ascending and descending datasets is highly recommended, if the images are available. The double geometry processing allows not only to improve the coverage, but also to have additional and independent information that is very important for the interpretation of the deformation phenomena.

An important aspect of the methodology is that it is a reproducible work flow, adaptable to each case study or final user’s needs. Depending on the site characteristics and on the main target of the monitoring, specifically the spatial and temporal magnitudes of the expected deformations, the methodology can be applied by changing for example the DInSAR processing technique, the minimum number of points to extract the ADA or the stability threshold. In addition, the temporal window between successive iterations for a regular updating of the ADA map is an aspect that has to be tuned on the base of the target deformation velocities (e.g., longer periods for slower deformations) and monitoring aims. For what concerns the temporal window to be processed, we have evaluated that a minimum of one year and a half is necessary in order to get acceptable results in terms of noise level.

It is worth underlining that the ADA map can be used to periodically update geohazard inventories and to drive or support the risk management activities. A step forward is the use of ADA map to rapidly evaluate the impact of the detected deformations on buildings and infrastructures, as explained in [33].

5. Conclusions

This paper aims at explaining the implemented methodology to generate and periodically update Geohazard Activity Maps, over wide areas, using the DInSAR technique and S-1 data. The methodology has been developed in the framework of the ongoing European ECHO (European Civil Protection and Humanitarian Aid Operations) project Safety, “Sentinel for geohazards regional monitoring and forecasting”. The aim was to find a way to simplify and summarize the SAR satellite derivable information in order to be exploited by any not radar-expert final user, specifically by the Civil Protection Authorities in the risk management activities. The outputs of the methodology are the Deformation Activity Map (DAM), in terms of velocity map and deformation time series, and the Active Deformation Areas (ADA) map. The last one is the main product that can be exploited to update the existing geohazard inventories. All the main steps of the methodology have been explained, starting from the PSI processing, the raw deformation map filtering to generate the DAM and the subsequent ADA extraction. Then, a methodology to evaluate the reliability of each ADA has been implemented and explained: a Quality Index is assigned to each ADA based on the temporal and spatial noise of its time series. The application and the results of the methodology over the islands of Gran Canaria, La Gomera and Tenerife (Spain) have been presented and discussed. Two temporally-displaced iterations have been processed to test the updating potentialities of the ADA map. A total of 72 ADA, in the first iteration, and 120 ADA, in the second iteration, have been detected over the three islands. The majority of the ADA that have been detected in both iterations, are classified as highly reliable according to the QI, demonstrating the significance of the QI information. The results exhibit the regional scale monitoring potentialities of the methodology.

Acknowledgments: This work has been funded by the European Commission, Directorate-General Humanitarian Aid and Civil Protection (ECHO), through the project Safety (Ref. ECHO/SUB/2015/718679/Prev02).

Author Contributions: Anna Barra (CTTC) wrote the paper and was involved in the data processing and analysis; Lorenzo Solari, Silvia Bianchini and Sandro Moretti, from UniFi, Marta Béjar-Pizarro, Gerardo Herrera, Roberto Sarro and Rosa María Mateos, from IGME, Elena González-Alonso, Sergio Ligüerzana and Carmen López, from IGN, provided inputs in the analysis of the detected ADA and in the Canary Island site characterization; Michele Crosetto and Oriol Monserrat (CTTC) contributed in the SAR data processing and analysis of the results.

Conflicts of Interest: The authors declare no conflict of interest.

References

1. Gabriel, A.K.; Goldstein, R.M.; Zebker, H.A. Mapping small elevation changes over large areas: Differential radar interferometry. *J. Geophys. Res.* **1989**, *94*, 9183–9191. [[CrossRef](#)]
2. Massonnet, D.; Feigl, K.L. Radar interferometry and its application to changes in the Earth’s surface. *Rev. Geophys.* **1998**, *36*, 441–500. [[CrossRef](#)]
3. Rosen, P.A.; Hensley, S.; Joughin, I.R.; Li, F.K.; Madsen, S.N.; Rodriguez, E.; Goldstein, R.M. Synthetic aperture radar interferometry. *Proc. IEEE* **2000**, *88*, 333–382. [[CrossRef](#)]
4. Barra, A.; Monserrat, O.; Mazzanti, P.; Esposito, C.; Crosetto, M.; Scarascia Mugnozza, G. First insights on the potential of Sentinel-1 for landslides detection. *Geomat. Nat. Hazards Risk* **2016**, *7*, 1874–1883. [[CrossRef](#)]
5. Biescas, E.; Crosetto, M.; Agudo, M.; Monserrat, O.; Crippa, B. Two radar interferometric approaches to monitor slow and fast land deformation. *J. Surv. Eng.* **2007**, *133*, 66–71. [[CrossRef](#)]
6. Ferretti, A.; Prati, C.; Rocca, F. Permanent scatterers in SAR interferometry. *IEEE TGRS* **2001**, *39*, 8–20. [[CrossRef](#)]
7. Berardino, P.; Fornaro, G.; Lanari, R.; Sansosti, E. A new algorithm for surface deformation monitoring based on small baseline differential SAR interferograms. *IEEE TGRS* **2002**, *40*, 2375–2383. [[CrossRef](#)]
8. Mora, O.; Mallorqui, J.J.; Broquetas, A. Linear and nonlinear terrain deformation maps from a reduced set of interferometric SAR images. *IEEE TGRS* **2003**, *41*, 2243–2253. [[CrossRef](#)]
9. López-Quiroz, P.; Doin, M.P.; Tupin, F.; Briole, P.; Nicolas, J.M. Time series analysis of Mexico City subsidence constrained by radar interferometry. *J. Appl. Geophys.* **2009**, *69*, 1–15. [[CrossRef](#)]

10. Hooper, A. A multi-temporal InSAR method incorporating both persistent scatterer and small baseline approaches. *Geophys. Res. Lett.* **2008**, *35*. [[CrossRef](#)]
11. Crosetto, M.; Monserrat, O.; Cuevas-González, M.; Devanthery, N.; Crippa, B. Persistent scatterer interferometry: A review. *ISPRS J. Photogramm. Remote Sens.* **2016**, *115*, 78–89. [[CrossRef](#)]
12. De Luca, C.; Cuccu, R.; Elefante, S.; Zinno, I.; Manunta, M.; Casola, V.; Casu, F. An on-demand web tool for the unsupervised retrieval of earth's surface deformation from SAR data: The P-SBAS service within the ESA G-POD environment. *Remote Sens.* **2015**, *7*, 15630–15650. [[CrossRef](#)]
13. Cignetti, M.; Manconi, A.; Manunta, M.; Giordan, D.; De Luca, C.; Allasia, P.; Ardizzone, F. Taking advantage of the esa G-pod service to study ground deformation processes in high mountain areas: A valle d'aosta case study, Northern Italy. *Remote Sens.* **2016**, *8*, 852. [[CrossRef](#)]
14. Pepe, A.; Sansosti, E.; Berardino, P.; Lanari, R. On the generation of ERS/ENVISAT DInSAR time-series via the SBAS technique. *IEEE Geosci. Remote Sens. Lett.* **2005**, *2*, 265–269. [[CrossRef](#)]
15. Crosetto, M.; Monserrat, O.; Iglesias, R.; Crippa, B. Persistent Scatterer Interferometry: Potential, limits and initial C- and X-band comparison. *Photogramm. Eng. Remote Sens.* **2010**, *76*, 1061–1069. [[CrossRef](#)]
16. Monserrat, O.; Crosetto, M.; Cuevas, M.; Crippa, B. The thermal expansion component of Persistent Scatterer Interferometry observations. *IEEE Geosci. Remote Sens. Lett.* **2011**, *8*, 864–868. [[CrossRef](#)]
17. Fornaro, G.; Reale, D.; Verde, S. Bridge thermal dilation monitoring with millimeter sensitivity via multidimensional SAR imaging. *IEEE Geosci. Remote Sens. Lett.* **2013**, *10*, 677–681. [[CrossRef](#)]
18. Bovenga, F.; Wasowski, J.; Nitti, D.O.; Nutricato, R.; Chiaradia, M.T. Using COSMO/SkyMed X-band and ENVISAT C-band SAR interferometry for landslides analysis. *Remote Sens. Environ.* **2012**, *119*, 272–285. [[CrossRef](#)]
19. Bovenga, F.; Nitti, D.O.; Fornaro, G.; Radicioni, F.; Stoppini, A.; Brigante, R. Using C/X-band SAR interferometry and GNSS measurements for the Assisi landslide analysis. *Int. J. Remote Sens.* **2013**, *34*, 4083–4104. [[CrossRef](#)]
20. Motagh, M.; Wetzell, H.U.; Roessner, S.; Kaufmann, H. A TerraSAR-X InSAR study of landslides in southern Kyrgyzstan, Central Asia. *Remote Sens. Lett.* **2013**, *4*, 657–666. [[CrossRef](#)]
21. Kiseleva, E.; Mikhailov, V.; Smolyaninova, E.; Dmitriev, P.; Golubev, V.; Timoshkina, E.; Hanssen, R. PS-InSAR monitoring of landslide activity in the Black Sea coast of the Caucasus. *Procedia Technol.* **2014**, *16*, 404–413. [[CrossRef](#)]
22. Calò, F.; Ardizzone, F.; Castaldo, R.; Lollino, P.; Tizzani, P.; Guzzetti, F.; Manunta, M. Enhanced landslide investigations through advanced DInSAR techniques: The Ivancich case study, Assisi, Italy. *Remote Sens. Environ.* **2014**, *142*, 69–82. [[CrossRef](#)]
23. Del Ventisette, C.; Righini, G.; Moretti, S.; Casagli, N. Multitemporal landslides inventory map updating using spaceborne SAR analysis. *Int. J. Appl. Earth Obs. Geoinf.* **2014**, *30*, 238–246. [[CrossRef](#)]
24. Costantini, M.; Ferretti, A.; Minati, F.; Falco, S.; Trillo, F.; Colombo, D.; Rucci, A. Analysis of surface deformations over the whole Italian territory by interferometric processing of ERS, Envisat and COSMO-SkyMed radar data. *Remote Sens. Environ.* **2017**, in press. [[CrossRef](#)]
25. Wasowski, J.; Bovenga, F. Investigating landslides and unstable slopes with satellite Multi Temporal Interferometry: Current issues and future perspectives. *Eng. Geol.* **2014**, *174*, 103–138. [[CrossRef](#)]
26. Wasowski, J.; Bovenga, F. Remote sensing of landslide motion with emphasis on satellite multitemporal interferometry applications: An overview. In *Landslide Hazards, Risks and Disasters*; Academic Press: Boston, MA, USA, 2015; pp. 345–403.
27. Rucci, A.; Ferretti, A.; Monti Guarnieri, A.; Rocca, F. Sentinel 1 SAR interferometry applications: The outlook for sub millimeter measurements. *Remote Sens. Environ.* **2012**, *120*, 156–163. [[CrossRef](#)]
28. Huang, Q.; Crosetto, M.; Monserrat, O.; Crippa, B. Displacement monitoring and modelling of a high-speed railway bridge using C-band Sentinel-1 data. *ISPRS J. Photogramm. Remote Sens.* **2017**, *128*, 204–211. [[CrossRef](#)]
29. Tang, P.; Chen, F.; Guo, H.; Tian, B.; Wang, X.; Ishwaran, N. Large-area landslides monitoring using advanced multi-temporal InSAR technique over the giant panda habitat, Sichuan, China. *Remote Sens.* **2015**, *7*, 8925–8949. [[CrossRef](#)]
30. Bouali, E.H.; Oommen, T.; Escobar-Wolf, R. Interferometric stacking toward geohazard identification and geotechnical asset monitoring. *J. Infrastruct. Syst.* **2016**, *22*, 05016001. [[CrossRef](#)]

31. Barboux, C.; Delaloye, R.; Lambiel, C. Inventorying slope movements in an Alpine environment using DInSAR. *Earth Surf. Process. Landf.* **2014**, *39*, 2087–2099. [[CrossRef](#)]
32. Devanthéry, N.; Crosetto, M.; Monserrat, O.; Cuevas-González, M.; Crippa, B. An approach to Persistent Scatterer Interferometry. *Remote Sens.* **2014**, *6*, 6662–6679. [[CrossRef](#)]
33. Solari, L.; Barra, A.; Herrera, G.; Bianchini, S.; Monserrat, O.; Bejar, M.; Crosetto, M.; Sarro, R.; Salviati, P.; Moretti, S. Vulnerable Elements Activity Maps based on Sentinel-1 InSAR. *Nat. Hazard Earth Sci.* **2017–2018**. submit.
34. Yague-Martinez, N.; Prats-Iraola, P.; Rodriguez Gonzalez, F.; Brcic, R.; Shau, R.; Geudtner, D.; Eineder, M.; Bamler, R. Interferometric Processing of Sentinel-1 TOPS Data. *IEEE Trans. Geosci. Remote Sens.* **2016**, *54*, 2220–2234. [[CrossRef](#)]
35. Prats-Iraola, P.; Scheiber, R.; Marotti, L.; Wollstadt, S.; Reigber, A. TOPS interferometry with TerraSAR-X. *IEEE Trans. Geosci. Remote Sens.* **2012**, *50*, 3179–3188. [[CrossRef](#)]
36. Hanssen, R. *Radar Interferometry*; Kluwer Academic Publishers: Dordrecht, The Netherlands, 2001.
37. Meisina, C.; Zucca, F.; Notti, D.; Colombo, A.; Cucchi, A.; Savio, G.; Giannico, C.; Bianchi, M. Geological Interpretation of PSInSAR Data at Regional Scale. *Sensors* **2008**, *8*, 7469–7492. [[CrossRef](#)] [[PubMed](#)]
38. Bianchini, S.; Cigna, F.; Righini, G.; Proietti, C.; Casagli, N. Landslide HotSpot Mapping by means of Persistent Scatterer Interferometry. *Environ. Earth Sci.* **2012**, *67*, 1155–1172. [[CrossRef](#)]
39. Herrera, G.; Gutiérrez, F.; García-Davalillo, J.C.; Guerrero, J.; Notti, D.; Galve, J.P.; Fernández-Merodo, J.A.; Cooksley, G. Multi-sensor advanced DInSAR monitoring of very slow landslides: The Tena Valley case study (Central Spanish Pyrenees). *Remote Sens. Environ.* **2013**, *128*, 31–43. [[CrossRef](#)]
40. Notti, D.; Herrera, G.; Bianchini, S.; Meisina, C.; García-Davalillo, J.C.; Zucca, F. A methodology for improving landslide PSI data analysis. *Int. J. Remote Sens.* **2014**, *35*, 2186–2214.
41. Farr, T.G.; Rosen, P.A.; Caro, E.; Crippen, R.; Duren, R.; Hensley, S.; Seal, D. The shuttle radar topography mission. *Rev. Geophys.* **2007**, *45*, 1–33. [[CrossRef](#)]



© 2017 by the authors. Licensee MDPI, Basel, Switzerland. This article is an open access article distributed under the terms and conditions of the Creative Commons Attribution (CC BY) license (<http://creativecommons.org/licenses/by/4.0/>).

5 ADAtools: Automatic detection and classification of active deformation areas from PSI displacement maps

Article

ADAtools: Automatic Detection and Classification of Active Deformation Areas from PSI Displacement Maps

J. A. Navarro ^{1,*}, R. Tomás ², A. Barra ¹, J. I. Pagán ², C. Reyes-Carmona ³, L. Solari ¹,
J. L. Vinielles ^{3,4}, S. Falco ⁵ and M. Crosetto ¹

¹ Centre Tecnològic de Telecomunicacions de Catalunya (CTTC/CERCA), Av. Carl Friedrich Gauss 7, 08860 Castelldefels, Spain; anna.barra@cttc.cat (A.B.); lorenzo.solari@cttc.cat (L.S.); michele.crosetto@cttc.cat (M.C.)

² Dpto. de Ingeniería Civil, Escuela Politécnica Superior de Alicante, Universidad de Alicante, P.O. Box 99, E-03080 Alicante, Spain; roberto.tomas@ua.es (R.T.); jipagan@ua.es (J.I.P.)

³ Geohazards InSAR Laboratory and Modeling Group (InSARlab), Geoscience Research Department, Geological Survey of Spain (IGME), Alenza 1, 28003 Madrid, Spain; c.reyes@igme.es (C.R.-C.); jlvinielles@hemav.com (J.L.V.)

⁴ HEMAV SL, Carrer d'Esteve Terrades 1, 08860 Castelldefels, Spain

⁵ e-GEOS—An ASI/Telespazio Company, 00156 Rome, Italy; salvatore.falco@e-geos.it

* Correspondence: jose.navarro@cttc.es

Received: 1 September 2020; Accepted: 4 October 2020; Published: 6 October 2020



Abstract: This work describes the set of tools developed, tested, and put into production in the context of the H2020 project Multi-scale Observation and Monitoring of Railway Infrastructure Threats (MOMIT). This project, which ended in 2019, aimed to show how the use of various remote sensing techniques could help to improve the monitoring of railway infrastructures, such as tracks or bridges, and thus, consequently, improve the detection of ground instabilities and facilitate their management. Several lines of work were opened by MOMIT, but the authors of this work concentrated their efforts in the design of tools to help the detection and identification of ground movements using synthetic aperture radar interferometry (InSAR) data. The main output of this activity was a set of tools able to detect the areas labelled active deformation areas (ADA), with the highest deformation rates and to connect them to a geological or anthropogenic process. ADAtools is the name given to the aforementioned set of tools. The description of these tools includes the definition of their targets, inputs, and outputs, as well as details on how the correctness of the applications was checked and on the benchmarks showing their performance. The ADAtools include the following applications: ADAfinder, los2hv, ADAclassifier, and THEXfinder. The toolset is targeted at the analysis and interpretation of InSAR results. Ancillary information supports the semi-automatic interpretation and classification process. Two real use-cases illustrating this statement are included at the end of this paper to show the kind of results that may be obtained with the ADAtools.

Keywords: software tools; process automation; ground deformation analysis; ground deformation classification; InSAR

1. Introduction

The Multi-scale Observation and Monitoring of Railway Infrastructure Threats (MOMIT) project (see [1] for details) aims to develop and demonstrate a new use of remote sensing techniques for railway infrastructure monitoring. MOMIT solutions are targeted at supporting the maintenance and prevention processes within the infrastructure management lifecycle. The overall concept underpinning

MOMIT is the demonstration of the benefits brought by Earth Observation and Remote Sensing data to the monitoring of railways networks both in terms of the infrastructure and the surrounding environment, where activities and phenomena impacting the infrastructure could be present. MOMIT leverages state-of-the-art techniques in the fields of space-based remote sensing and remotely-piloted aircraft systems (RPASs) to perform different kinds of analysis thanks to the wide variety of sensors they may be equipped with.

To achieve its goals, six demonstrators showing how these data and techniques may contribute to such objectives have been built, namely:

- Ground movements nearby the infrastructure.
- Hydraulic activities nearby the tracks.
- Global supervision for natural hazards.
- Electrical system monitoring.
- Civil engineering structures monitoring.
- Safety monitoring.

The Division of Geomatics of the Centre Tecnològic de Telecomunicacions de Catalunya (CTTC) took care of building some of the components integrating the first demonstrator, whose objectives are detailed in [1]. The University of Alicante (UA) mainly defined the methodology used in the first demonstrator, supported CTTC in the tuning of the software, and applied the tools developed in several case studies. The goal most relevant to the work presented here is to introduce the ADAtools, a set of software components targeted at the detection and interpretation of active deformation areas (ADA) using displacement maps created by means of persistent scatterer interferometry (PSI) method.

Several PSI approaches have been developed in the last twenty years; a review of them is provided in [2]. The basic concept behind the PSI techniques is to collect a stack of several synthetic aperture radar (SAR) images for the same area, with very similar acquisition angles; these images are later processed to detect the so-called persistent scatterers (PS), which are artificial and natural structures that show interferometric coherence over the time; through advanced data processing, it is possible to determine the displacement time series (TS) of the detected PS. PSI results have been applied for several applications at different working scales, ranging from wide-area processing at national level [3,4] to single infrastructures monitoring [5–7]. PSI is widely accepted as a reliable tool for the precise measure of a variety of geohazards, including landslides [8–10], natural and anthropogenic subsidence [11–13], sinkholes [14–16], earthquakes [17–19], and volcanoes [20–22]. Nowadays, the increasing number of PSI applications and the tendency to process wide areas with millions of measurement points require the definition of reliable semi-automatic and automatic tools to ease the analysis and interpretation of the PSI results [23,24].

This paper describes in depth a set of tools for PSI data analysis and interpretation developed at CTTC, the so called ADAtools. The package is composed of 4 modules, namely, ADAfinder, ADAclassifier, THEXfinder, and los2hv [25]. The main goal of such applications is a semi-automatic extraction and preliminary interpretation of the areas affected by deformation detected by the PSI technique. The goal is to update and assess the activity of phenomena related to geohazards (volcanic activity, landslides, or ground subsidence, among other phenomena) or human activities of a given area. The first one, ADAfinder, is a tool dedicated to the detection of the ADA, extracted from a PSI-derived displacement map. ADAclassifier and THEXfinder go a step beyond ADAfinder, trying to classify the kind of deformation process undergone by the ADA, and trying to answer the question: is the detected deformation process a landslide, a sinkhole, or something else? Finally, los2hv computes the East-West horizontal and vertical components of the movement measured along the satellite's line of sight (LOS). The East-West horizontal component of motion is also one of the inputs for the ADAclassifier.

Finally, but no less important, it is worth noting that although the development of these tools was motivated by the needs of the MOMIT project, the applications described in the next sections are not

limited to this purpose. On the contrary, these may be used to track deformation processes occurring anywhere, as is shown by the real use-cases proposed in Section 7.

2. ADAtools

The four tools presented in this paper rely in preexisting methodologies, i.e., these applications have automated a set of procedures that already existed and were executed manually, step by step, using Geographic Information System (GIS) tools.

In the case of ADAfinder, the methodology to perform the identification and assessment of ADA was presented in [26,27] back in 2017 and 2019, respectively. In these works, the authors explain in detail the procedure to identify the active deformation areas and to assess their quality. The input is a set of persistent scatterers (PS; or “the points”) covering the area to analyze. Each ADA is then defined on the basis of the location and density of PS, depending on some thresholds as the minimum number of points making an ADA or the area of influence of each PS. A quality index describing the noise level and the consistency of the displacement time series of the PS forming each ADA is calculated as well. The concept of ADA has been exploited to estimate geohazard-related risk (mainly landslides) in different European environments (see [28–30]). It is worth underlying that the ADA extraction does not overcome the intrinsic limitations of the PSI technique: ADAfinder extracts what PSI technique can detect. As an example, the absence of ADA does not necessarily mean no-deformation; it could be absence of deformation as well as a not-detectable movement due to an unfavorable geometry [31] or absence of information for low coherence (noisy area).

ADAclassifier and THEXfinder rely on a methodology developed by the UA that is under constant research; although it is mature enough to be automated, which eases the experimentation process and helps to improve the methodology itself. The task of ADAclassifier and THEXfinder is to identify the kind of geological or anthropogenic process motivating the presence of ADA. Up to six different phenomena (see Section 2.2) are probed to obtain an estimation of the causes motivating the ground deformation; these are landslides, sinkholes, subsidence, constructive settlements, expansive soils, and thermal phenomena. ADAclassifier takes care of the first four, while THEXfinder is responsible for the last two. For more details about the methodology on which these two tools rely, see [32].

Finally, los2hv computes the East-West horizontal and vertical components of the ground displacement measured with PSI along the satellite’s LOS (the horizontal component is one of the inputs needed by ADAclassifier). los2hv performs a tessellation of the area of interest to obtain an averaged result for each of the resulting tiles. Such an approach means that overcoming the strict requirement stating that data from ascending and descending orbits are necessary to perform such decomposition of the movement; treating the PS in the same tile as a single coarser point makes possible to obtain an averaged but still useful value for the purposes of ADAclassifier. See Section 2.3 and [32] for a detailed description of this tool. As stated above, the aforesaid procedures usually rely on the heavy use of GIS tools and the expertise of the operator; the number of steps these procedures consist of makes them time-consuming, error-prone processes, which entails the need for qualified personnel.

The goals of the ADAtools package are: (1) to automate the respective procedures and to limit unnecessary human errors; (2) to reduce the time needed to identify and pre-classify the ADA, thus opening the door to more frequent updates and analyses; and (3) to reduce the expertise required to obtain such results, making possible to integrate the process in a semi-automated production workflow, if necessary.

2.1. ADAfinder

This application, based on the methodology explained in [26], is used to identify the main areas where a displacement has been measured by the PSI processing, squeezing the information contained in the input deformation map and assessing the quality of the time series information (i.e., spatial-temporal noise) of each ADA. Additionally, ADAfinder includes the option to filter the input displacement map from the isolated or potential outlier PS. We refer to [26] for more details on

the quality assessment and the outlier filtering methods. This tool allows the amount of data to be managed in terms of both hardware space and computational time to be reduced.

As inputs, ADAfinder requires:

- An ESRI shapefile containing the PS that will be used by the detection algorithm. Besides their coordinates, ADAfinder needs some attributes defining the PS; their average velocity expressed in mm/yr, and the deformation time series measuring the movements undergone by these.
- Optionally, the user can upload a polygon to resize the area of interest. All PS in the input shapefile are considered when such a polygon is not provided.
- A set of parameters defined by the methodology described in [26] (Figure 1).

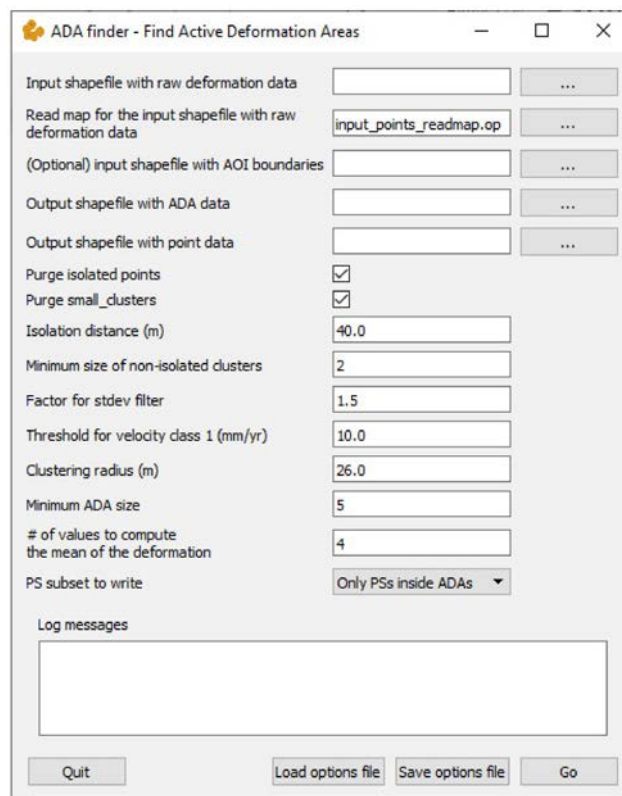


Figure 1. The graphical user interface (GUI) version of the ADAfinder tool.

The outputs are two ESRI shapefiles, the first containing the polygons defining the boundaries of the ADA; the second including the set of filtered PS. For what concerns the PS output, ADAfinder allows choosing between two different options, depending on the user necessities. The output can include all the filtered PS of the area of interest or only the ones included in the extracted ADA.

Figure 1 depicts the graphical user interface (GUI) version of the ADAfinder tool. Note that some of the values to be provided by the user are already set; the reason is that the tool loads a default options file (see Section 3.3 for details on options files) that serves two purposes: providing some hints to the user about the values of some parameters and saving time spent in typing many of them when working in the same project. The default options file may be changed by the user, to adjust the defaults to their preferences at any time. Finally, the user may also save a set of options differing from those included in the default in a separate options file that later may be loaded as many times as needed.

It is worth remarking that the output ADA shapefile includes among its attributes the results of the quality assessment of the PS displacement TS in terms of both spatial and temporal noise, based on simple statistical analysis of the TS within each ADA [3]. Such assessment is represented by a four-level classification of TS reliability of the extracted ADA, where 1 means “very reliable”, 2 means

“reliable” but an analysis of the TS is suggested, 3 means “not so reliable”, i.e., a deeper analysis of the TS is necessary, and 4 means “not reliable”. Figure 2 shows some ADA; their colors map the four levels just mentioned.

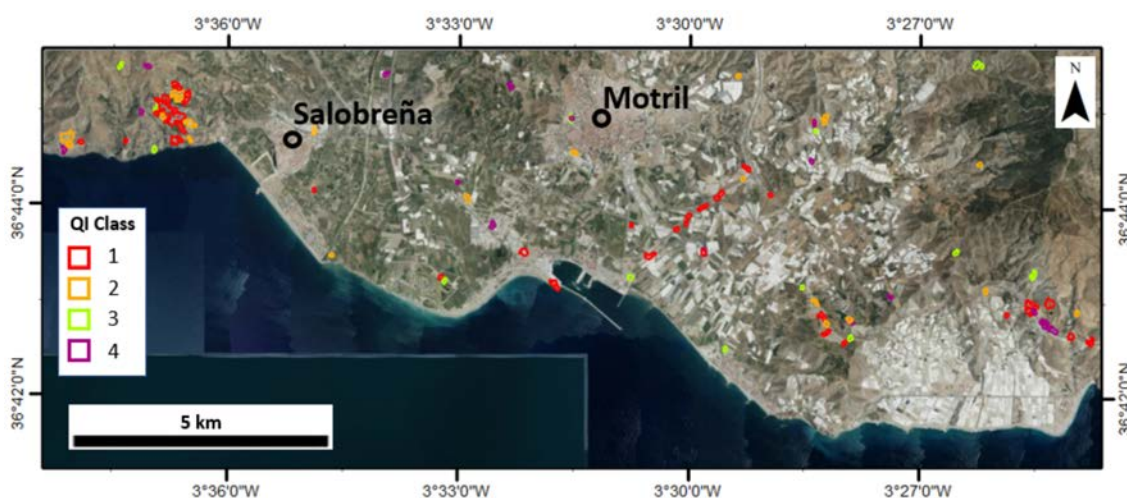


Figure 2. An example of the output of ADAfinder in the coastal area of Granada (S Spain). Colors are used to show the quality of the time series (TS) information according to the quality index attribute in the output shapefile. Red: “very reliable”, orange: “reliable”, lime-green: “not so reliable” and purple: “not reliable”.

For a detailed description of the ADAfinder tool, please refer to its user guide [33].

2.2. ADAclassifier and THEXfinder

These tools try to determine the kind(s) of deformation process(es) undergone by the terrain.

Up to six different kinds of deformation phenomena are detected. The ones analyzed by ADAclassifier are landslides, sinkholes, land subsidence, and constructive or consolidation settlements. THEXfinder takes care of the identification of deformation processes due to expansive soils and temperature effects. A different algorithm (or sub-methodology) has been devised for each of these. Figure 3 depicts the workflow of the algorithms implemented by ADAclassifier to detect the four aforementioned phenomena.

ADAclassifier and THEXfinder need a substantial number of inputs. For ADAclassifier these are:

- The ADA and PS files created by ADAfinder (see Section 2.1). Strictly speaking, these files do not need to be created by ADAfinder; any other tool or manual process identifying ADA may be used instead. However, the set of attributes included in the attribute table of the shapefiles must match those required by ADAclassifier –attributes that ADAfinder does include in its output.
- A digital terrain model (DTM), to compute slopes.
- A series of polygon vector maps (inventories from now on,) in the form of ESRI shapefiles, to check whether an ADA has already been catalogued as belonging to any of the four aforesaid deformation processes. The required inventories are those for landslides, sinkholes, land subsidence, and infrastructures. A geologic map (another polygon vector map) is also needed. In this last case, a read-map file defining how the inventory is structured is also needed to point to the attributes stating the kind of soil covered by each polygon in the inventory. See Section 3.4 for a detailed description about the so-called read-map files.
- An ESRI (polygon) shapefile storing the horizontal component of the movement for the study area. This is the output of los2hv (see Section 2.3 for details).
- The set of parameters—typically thresholds—needed by the different algorithms in charge of the classification processes must be supplied. Examples of such parameters are slopes, determination

coefficients to state whether some statistical check is positive, or the minimum percentage of overlap of an ADA and the polygons in some inventory to consider that they do intersect. These thresholds appear as Th1 to Th11 in Figure 3.

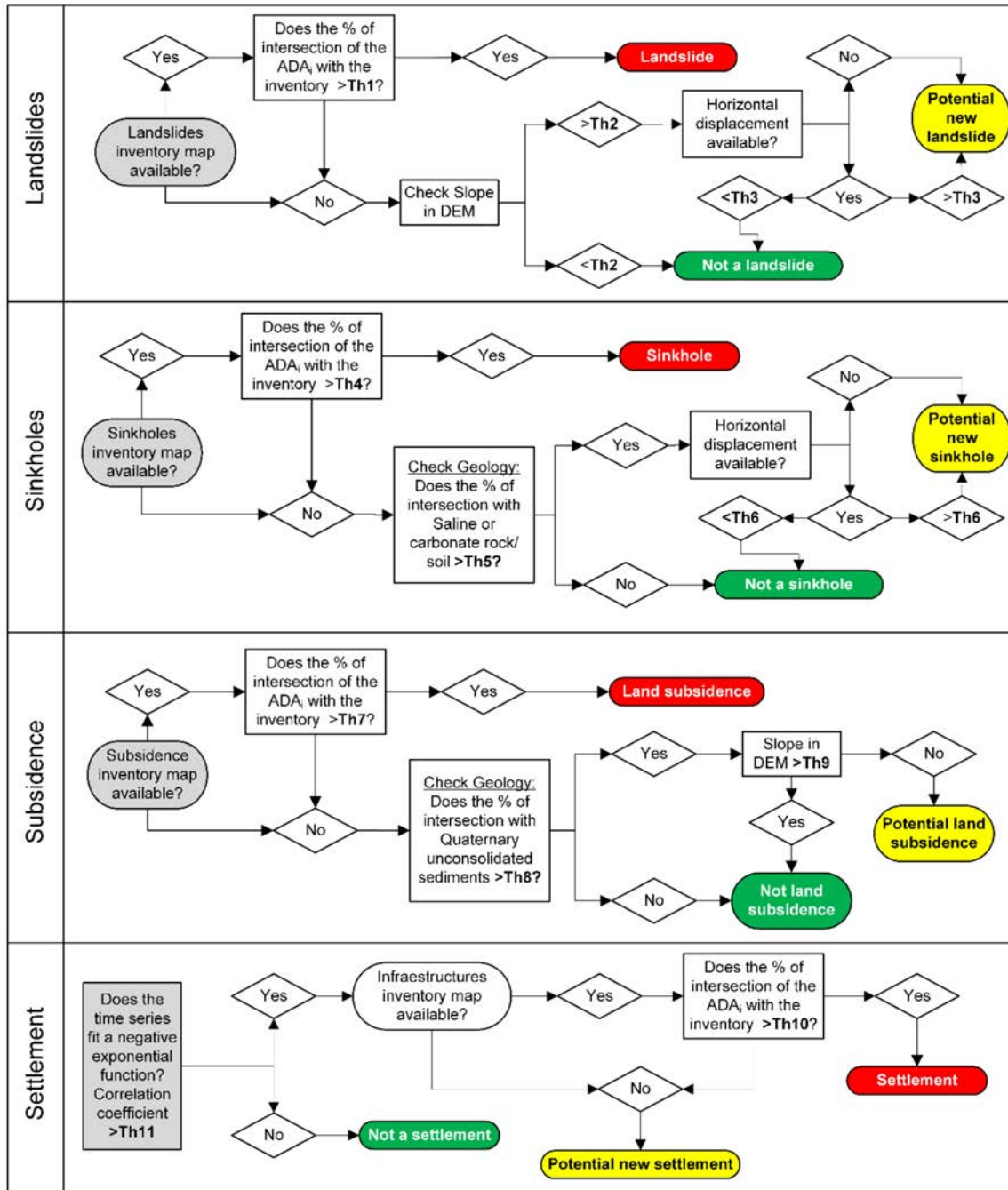


Figure 3. Sketch of the algorithms of ADAclassifier, modified from [4]. Note that the Th1–Th11 labels in the diagram correspond to some thresholds described in detail in the ADAclassifier user guide [34].

The output of ADAclassifier is another file with ADA, where the attribute table has been extended to include four additional fields. Each of them states the probability that the ADA belongs to the corresponding deformation process. This is so because all of the detection algorithms are applied to each ADA. Consequently, and although it could be considered incongruous, some ADA might be classified as positives in more than one deformation process. This is due to the fact that the ADAclassifier is making a most probable cause analysis.

Four levels of certainty are defined by the methodology: “it is an X”, “it could be an X”, “it is not an X” and “unable to check whether it is an X”, where “X” stands for any of the four deformation detection processes executed by ADAclassifier; for instance, when talking about landslides, “it is a landslide” would be one of the values of the corresponding attribute.

Note that one of the four values is “unable to check whether it is an X”. This is because ADAclassifier may decide not to apply one or more of the four detection processes because of the lack of data. As stated above, a noticeable number of inputs is required. Just the inventory files already amount to five. Taking also into account the DTM and the horizontal components of the movement, it is easy to realize that in many cases the full set of files will not be available.

To limit this common problem, ADAclassifier makes almost every input file optional (this includes the DTM, the inventories, and the horizontal components). Each time the application is run, it analyzes the dependencies of each sub-algorithm and decides which of these may be executed as a function of the inputs provided by the user. Consequently, it is necessary to add the “unable to check whether it is an X” value as one of the possible outputs of each classification process.

Note that this behavior makes the tool much more flexible: while concentrating the detection of four deformation processes in a single application, it may be used to check just only one of these, just providing the available set of data for the target deformation process.

Figures 4 and 5 depict the GUI of the ADAclassifier tool; the first one shows the options tab where the set of thresholds controlling the application are set; in the second one the list of (mostly optional) files may be appreciated.

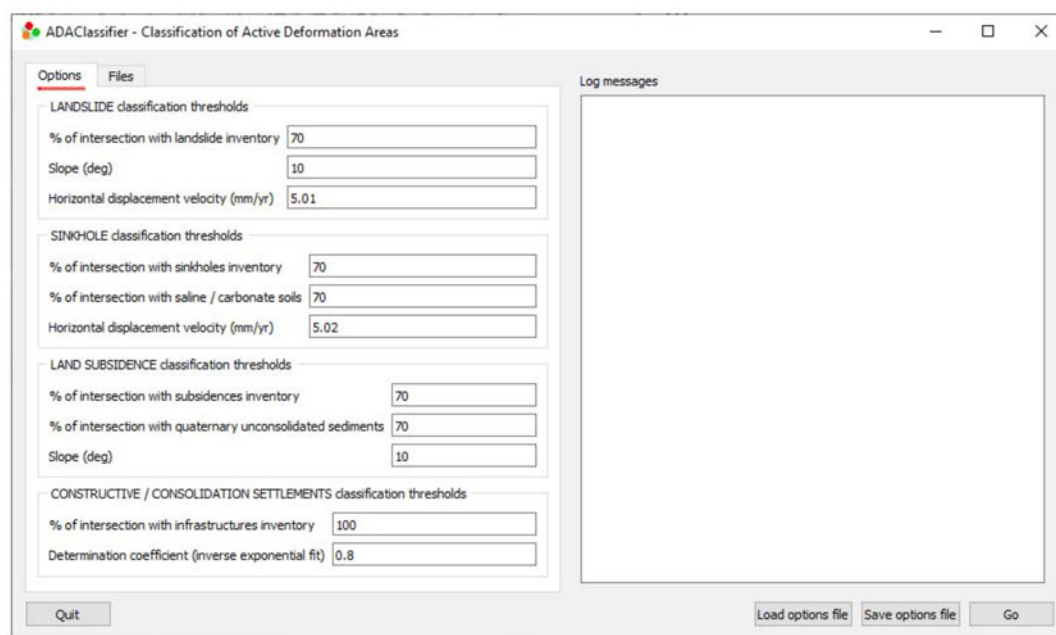


Figure 4. The ADAclassifier GUI (options tab).

As it happens with ADAfinder (and with los2hv too), a default options file may be set by the user to load a predefined set of threshold values. It is also possible to save/load option files created by the user. The ADAclassifier tool is fully described in its user guide [34].

THEXfinder, the second classification tool, does not work in the same way that ADAclassifier does. ADAclassifier takes the output of ADAfinder as input, i.e., it deals with ADA that have already been identified; starting here, it checks whether these ADA correspond to one or more deformation processes.

On the contrary, THEXfinder performs both tasks, that is: (a) identifying the ADA themselves (thus ignoring ADAfinder); and later (b) running the checks targeted at classifying such ADA either as expansive soils or thermal effects.

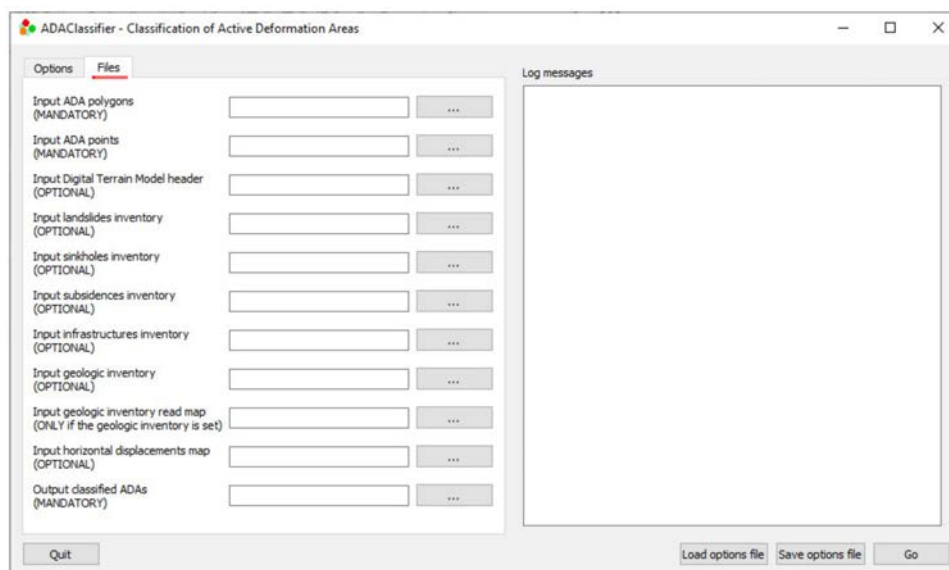


Figure 5. The ADAclassifier GUI (files tab).

In fact, the first version of the toolset did not include THEXfinder as a separate tool. Instead, ADAclassifier was responsible for detecting not the current four, but the whole set of six deformation phenomena, including the two for which THEXfinder is now responsible. The availability of the first version of ADAclassifier made possible to attempt to classify ADA much faster, thus obtaining results more easily. Because of this extra abundance of output data, it was discovered that the mechanism to identify ADA used by ADAfinder was not appropriate when the phenomena to track were expansive soils or thermal effects. Therefore, the detection of these phenomena was removed from ADAclassifier and THEXfinder was created, implementing an appropriate detection mechanism for this kind of ADA together with the classification algorithms themselves. This means that THEXfinder identifies and classifies ADA in a single process.

The inputs for THEXfinder are the following:

- The original set of PS files as well as the read-map file defining the structure of the PSI file (see Section 3.4). Note that, in this case, the tool starts from the original PSI data set, not from the ADA. See the discussion above.
- An optional polygon defining the area of interest (shapefile).
- Optional ESRI shapefiles representing the infrastructures (buildings, bridges, etc.) and geologic inventories. In the case of the geologic map, an extra read-map file is also required.
- The parameters (thresholds) controlling the behavior of the application.

There are up to four output files, two for the expansive soils' analysis and two more for the thermal expansion case. Each set contains one file with the ADA and another one with the points inside these ADA.

From the structural standpoint, the output files with ADA are almost identical to those created by ADAclassifier; practically, the whole set of attributes is identical. The only difference is that ADAclassifier includes a set of four fields to state the probability of an ADA matching each of the deformation processes tested, while the files created by THEXfinder contains only one of these fields per file. This is so because the ADA files created by THEXfinder correspond to just a single deformation process.

In the same line that ADAclassifier, THEXfinder will only try to check whether an ADA corresponds to some deformation process when all the input files required to do it exist. This is the reason why most of the input (and output) files are optional, making the tool more flexible.

Figures 6 and 7 show the interface of the THEXfinder application.

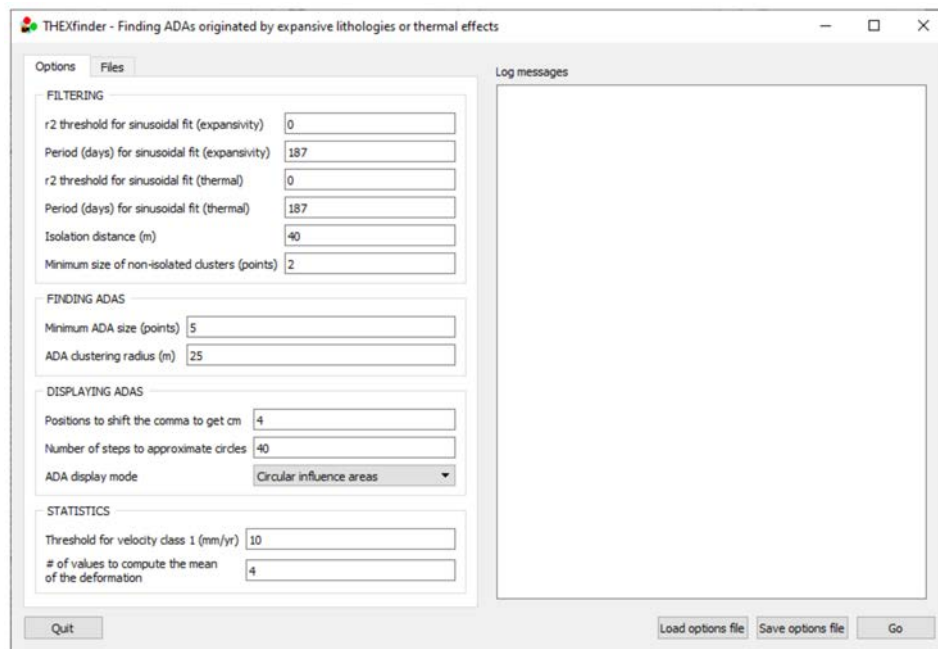


Figure 6. The THEXfinder GUI (options tab).

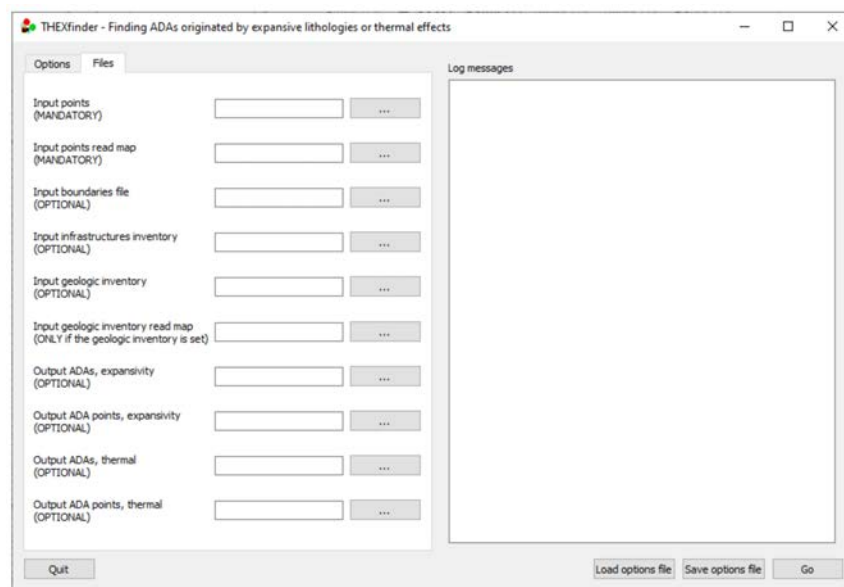


Figure 7. The THEXfinder GUI (files tab).

2.3. Los2hv

The los2hv tool is targeted at the computation of the separate East-West horizontal and vertical components of the ground displacement measured with PSI along the satellite's LOS. These components are inputs required by ADAclassifier to execute some of the classification algorithms it implements. Both ascending and descending datasets are required.

The tool accepts (input) and produces (output) ESRI shapefiles for compatibility reasons. On output, los2hv creates two files, to store, respectively, the East-West horizontal and vertical components of the movement as observed along the LOS. It should be clarified that North–South displacements are not calculated since, due to the nearly North–South orbit direction of SAR satellites, InSAR is insensitive to this displacement component [35]. It is noteworthy that this limitation is associated with the InSAR information itself instead of the los2hv tool.

Figure 8 shows the GUI of los2hv. As usual, the values shown are obtained from a default options file; also, the user may save/load their own options very easily.

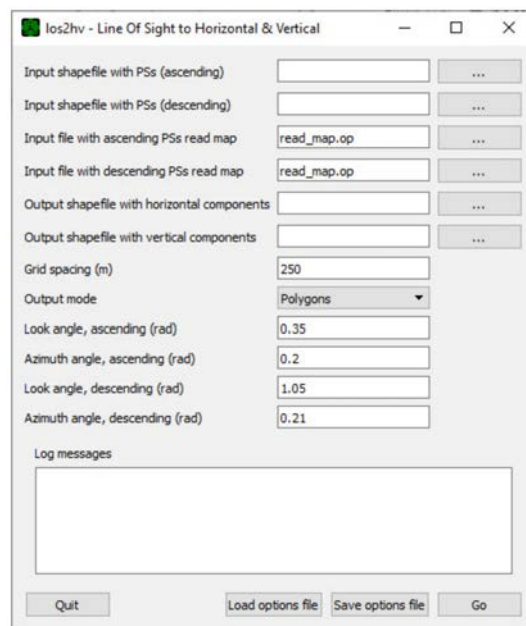


Figure 8. los2hv GUI.

los2hv performs a tessellation of the whole area covered by the PS included in the two input files. The size of the tesserae (grid spacing) is decided by the user. Consequently, each PS belongs just to one of the resulting tesserae.

There may be tesserae where: (1) there are no PS; (2) there are only PS from the ascending input file; (3) there are only PS from the descending input file; and finally (4) there are PS from both input files (see Figure 9). For those tesserae of type (4), the ground movement is averaged using the values of all the PS included in the tile. The resulting amount, measured along the LOS, is then converted to East-West horizontal and vertical components according to the formulae described in [36]. The value of the East-West horizontal and vertical components of the ground movement corresponds now to the whole area covered by the tile where the points involved in the computation were located.

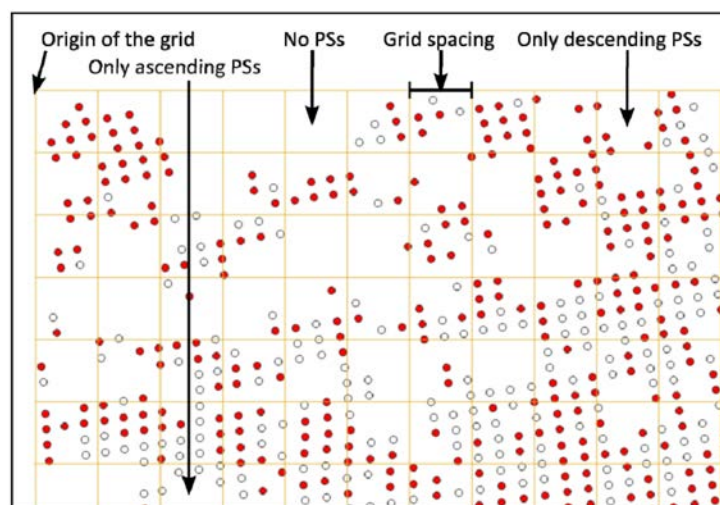


Figure 9. los2v: tesserae and ascending and descending persistent scatterers (PS). The white points represent the PS in ascending orbit; the red points the PS in descending orbit. Source: [25].

These values are saved to the corresponding output files. Note that the user may select to store points (centroids of the tesserae with data) or polygons (more precisely, squares, the boundaries of the tesserae). The second kind of output (squares) is the one used by ADAclassifier. The centroid output is provided for whatever other purposes.

Please refer to the complete user guide of the los2hv tool [37] for more information.

3. Implementation and Integration

3.1. The Language of Choice

The toolset has been implemented in C++ to boost performance. The ADAfinder tool, for instance, may need a sensible amount of resources when working with large datasets (see Section 5 for details on performance of the whole toolset). Therefore, the use of a compiled (not interpreted) language was of capital importance. Other popular languages, as Python, have been avoided precisely for this reason, despite their popularity.

Although developed using the C++ compiler included in Microsoft's Visual Studio, special precautions have been taken to make the source code portable, particularly for the most popular C++ compiler used in the Linux operating system, gcc. The use of Qt (see below) is also a factor contributing to the portability of the code.

Several open source libraries were used to implement the toolset. These are:

- Qt (see [38]). Although it has been used with several purposes in mind, the main target was to guarantee portability. Since the applications have a GUI, it was very important that such GUI was built using a portable library to avoid the need to write different code for each of the platforms which these tools are targeted at (at least Windows and Linux). Qt is a framework that guarantees such portability; in fact, developing cross-platform applications is its motto.
- Shapelib. This library is a very convenient tool to read and write ESRI shapefiles. See [39] for further details.
- Clipper. A library available for the Delphi, C, C++ and Python, used for clipping and offsetting lines and polygons. For a complete description of this library, please refer to [40].
- Dlib [41] and Eigen [42] to implement some mathematical algorithms required by the detection processed included ADAclassifier and THEXfinder, such as curve or plane fitting.

3.2. The Three Incarnations

The tools described in this paper may be used in several quite different work environments. For instance, a user could use the ADAfinder application repeatedly to play with the parameters controlling the algorithm and then decide what would be the best strategy to identify the ADA in some area. This would imply the use of an ergonomic tool, where changing such parameters should be extremely easy and proof safe. On the contrary, once such parameters have been found, ADAfinder could be used routinely, with no human intervention, to detect ADA as one more step in an automated batch process. In this case, the parameters would be mostly the same for the whole dataset, and there would need to change only a few of them. There are other situations where the detection of ADA could be seen as a part of a much bigger process, being thus interesting to be able to embed the logic implemented in ADAfinder (or in any of the other tools) in another application.

These are the reasons why each of the applications described in Section 2 are available in three different flavors or incarnations:

- As a C++ class (one for each application) in a library. Third party (C++) software willing to embed the logic of ADAfinder, ADAclassifier, THEXfinder, or los2hv as a black box only needs to instantiate the corresponding class. Thus, embedding the necessary logic to be able to identify or classify ADA or to compute the horizontal components of the movement is just one procedure

call away. Only software components developed in C++ will be able to integrate the logic in the library, since no bindings for other languages have been developed.

- As a command-line utility. This makes possible to integrate these tools in batch workflows, since no human intervention is required to run them. See Section 3.3 for details on options files, the mechanism used to obtain the information controlling the behavior of the applications.
- As an application featuring a GUI. This flavor is the best one for experimenting because of its ease of use. GUI-based applications, however, cannot be integrated in batch workflows.

There also exist pluggable versions of the three applications for the Quantum GIS (QGIS) version 2 tool. These plugins just call the GUI versions of the toolset thus avoiding the need to quit the GIS environment when running any of its applications. The tools are connected by means of some glue code written in this case in Python; since this is the unique choice when working with QGIS. Note that the plugins have not been yet migrated to QGIS 3 due to the changes affecting how this kind of software must be built for the latest version of this tool.

It is worth remarking that the command-line and GUI versions of the applications are just interfaces calling the classes in the library that actually implement the logic of the tools. This approach allows for a simplified maintenance process; the logic is concentrated in just one place, no matter how this logic is used (library, console or GUI application). Changing the classes implies an immediate update in the three flavors of each application.

3.3. Option Files

Both the command-line and GUI incarnations of the applications in the toolset rely on option files to retrieve the information defining how to behave; this includes input or output files and thresholds controlling some condition, among other data. Note that this is so for the GUI-based tools too; in fact, the GUI is just a mechanism to fill the gaps in an option file template, the so-called *defaults* files. This simplifies the design of the classes implementing the logic, since only one interface (the option file) needs to be taken care of. The command-line incarnations of the three tools have a single parameter: the name of the options file with the program's parameters. The option files used by the toolset are uncomplicated, plain text files including couples of labels and values. Comments to clarify the purpose of each of these couples may be included just by adding a leading “#” character preceding the descriptive text. Figure 10 depicts a real, quite self-descriptive options file used to control the *los2hv* application.

3.4. Real-Life Shapefiles: Read-Map Files

ESRI shapefiles, although standardized, may include variable sets of attributes. Even when a shapefile includes the full set of attributes needed by a tool (for instance, the *x* and *y* coordinates as well as the velocity and the deformation time series in the case of *ADAFinder*), they may appear in different columns of the attribute (.dbf) file. This usually depends on the provider of the files.

This variability might become a serious problem, since the input module should be adapted for each kind of shapefile to process.

The solution to avoid this problem are the “read-map files” defining how the relevant attributes in a shapefile are organized. Of course, the attributes needed by the tools to work properly must always be present in the files, but thanks to these read-map files it is possible to deal with changes in the positions where these appear.

Thus, a read-map file is just an extra options file (see Section 3.3) where, by means of couples of labels and values, the positions of the attributes on which each tool rely are specified. Figure 11 is an example of an *ADAFinder* read-map file for the input PS.

```

# -----
# THIS IS A LOS2HV OPTIONS FILE
# ----- OPTIONS -----
#
# Spacing of the grid used to group the points.
# Use the same units than the projected coordinates of the points.
#
GRID_SPACING          = 500
#
# The output will consist of points centered on the squares defined by the
# grid (1) or the polygons defining the squares themselves (2).
#
OUTPUT_MODE           = 1
# The ascending look (incidence) & azimuth angles (in radians).
LOOK_ANGLE_ASCENDING  = 0.5
AZIMUTH_ANGLE_ASCENDING = 0.0
# The descending look (incidence) & azimuth angles (in radians).
LOOK_ANGLE_DESCENDING = 0.5
AZIMUTH_ANGLE_DESCENDING = 0.0
# ----- FILES -----
# Input files
#
# Shapefiles with points. ASCENDING & DESCENDING
FILE_POINTS_ASCENDING      = points_ascending.shp
FILE_POINTS_DESCENDING     = points_descending.shp
#
# Read maps describing the structure of both input shapefiles with points.
#
FILE_POINTS_READ_MAP_ASCENDING = points_read_map_ascending.op
FILE_POINTS_READ_MAP_DESCENDING = points_read_map_descending.op
#
# Output files
#
# Output shapefile. HORIZONTAL & VERTICAL components of the movement.
FILE_COMPONENTS_HORIZONTAL  = horizontal_components.shp
FILE_COMPONENTS_VERTICAL    = vertical_components.shp

```

Figure 10. A real example of a los2hv options file.

```

POSITION_X           = 5
POSITION_Y           = 6
POSITION_VELOCITY    = 9
POSITION_TIME_SERIES = 11
N_VALUES_TIME_SERIES = 50

```

Figure 11. Example of an input shapefile read-map plain text file.

The meaning of the pairs or labels and values in Figure 11 is the following:

- the x-coordinate of the PS must be read from column 5 in the .dbf file,
- the column to read to obtain the y-coordinate is the sixth one,
- the velocity may be found in column number 9 and, finally,
- the set of values making the time series start at column number 11 and there is a total of 50 of these values.

Obviously, if a shapefile with input PS is organized in a different manner, the values in the example above must be changed to match the actual positions where the fields of interest lie.

Note how such a simple mechanism makes the toolset much more flexible and able to deal with real-life datasets.

4. Quality Assurance

Prior to the delivery of the tools to the MOMIT consortium, these went through a rigorous testing process to guarantee that they worked correctly. Note that both a test plan and a test report concerning the whole toolset are described, respectively, in [43,44]. There, the full details on how testing was devised and took place are provided. However, and for the sake of completeness, the next sections briefly present the most relevant steps taken to guarantee the quality of the code.

Note, however, that the tests described in this section do not include THEXfinder as the independent application that it is now. This is so because the testing process took place before ADAclassifier was split in two (see Section 2.2). Consequently, only ADAclassifier, and not THEXfinder, was tested.

This apparently poses a question about the validity of the tests related to ADAclassifier, since it took care of classifying two extra phenomena (expansivity, thermal effects) that should not be implemented by this tool. The problem is caused by the mechanism used by ADAfinder to identify the ADA. It has been said (see Section 2.2) that such an algorithm is not appropriate to find ADA that are the result of expansivity or thermal phenomena. Therefore, if ADA affected by these phenomena cannot be properly identified by ADAfinder, it will be impossible for ADAclassifier to catalogue these properly.

Although this is essentially true, the tests applied to ADAclassifier were synthetic ones (see the description of the tests for ADAclassifier later in this section). Data were prepared in such a way that it was possible to predict the results of testing the six kinds of phenomena, assuming that ADA had been properly identified before. Consequently, the problem related to the appropriate identification of ADA did not invalidate the tests for ADAclassifier. This makes the tests for the specific algorithms for the identification of expansivity and thermal effects valid, since these were executed using correct (although synthetic) input data. This means that the results that were considered correct at that moment are still valid, including the two specific cases for which now THEXfinder is responsible.

THEXfinder has not been fully checked yet, however. From the discussion above it should be clear that the specific algorithms to diagnose expansivity or thermal effects are correct, since these were checked as components of ADAclassifier; nevertheless, the procedure used by THEXfinder to detect (not classify) ADA has not been rigorously tested yet. This is also the reason why performance results for this tool are not given in Section 5.

Going back to the tests themselves, in the case of ADAfinder, a manual methodology had been used for some time in GIS environments when this tool was developed, so datasets including both inputs and outputs were available. Therefore, the tests consisted essentially of comparing the results of the manual procedure with those created by the tool.

A mechanism to quickly compare the results produced by the manual and automated solutions was devised. From the numerical standpoint, it basically consisted of exporting the values of the attributes to check for both outputs (manual and automated), sorting these to easily match the attributes in each file and then computing the differences of their values, which, in all cases, were under the

threshold set by the precision of the typical 8-byte IEEE 754 double (around the 15th decimal position). This means that the results (for instance, the coordinates of the output points) were equivalent.

To check the correctness of the algorithm, two kinds of tests were performed. Firstly, the values of the attributes standing the level of certainty were checked for absolute equality, since these were represented by integer (non-floating point) magnitudes. Then, the number of ADA and their contents were also checked. This means that both the manual and automated algorithm had to identify the same number of ADA and that the set of points included in each of them had to be the same. Both numerical and correctness tests were passed satisfactorily.

The situation for ADAclassifier and los2hv was different; no previous results existed, so no reliable dataset to compare their outputs was at hand. The approach, therefore, was to create synthetic datasets for both applications. The rationale behind the way these datasets were created was to organize the information in easily identifiable geometric patterns, so, when combined, the area(s) where positive results were obtained was (were) also predictable.

For instance, and to check the landslides algorithm in the ADAclassifier application, all ADA were created as identical square-shaped polygons containing a regular grid of 5×5 PS. These ADA were distributed in a 24×24 checkerboard pattern (see Figure 12a); the horizontal components of the movement were distributed in 4 adjacent vertical stripes covering 6×24 ADA each. A known value for each of them was set (respectively, from left to right, 0, 10, 20, and 30 mm/year). This is shown in Figure 12b. Other easily identifiable patterns were used for the rest of input files; such as the values of the slopes in the DTM.

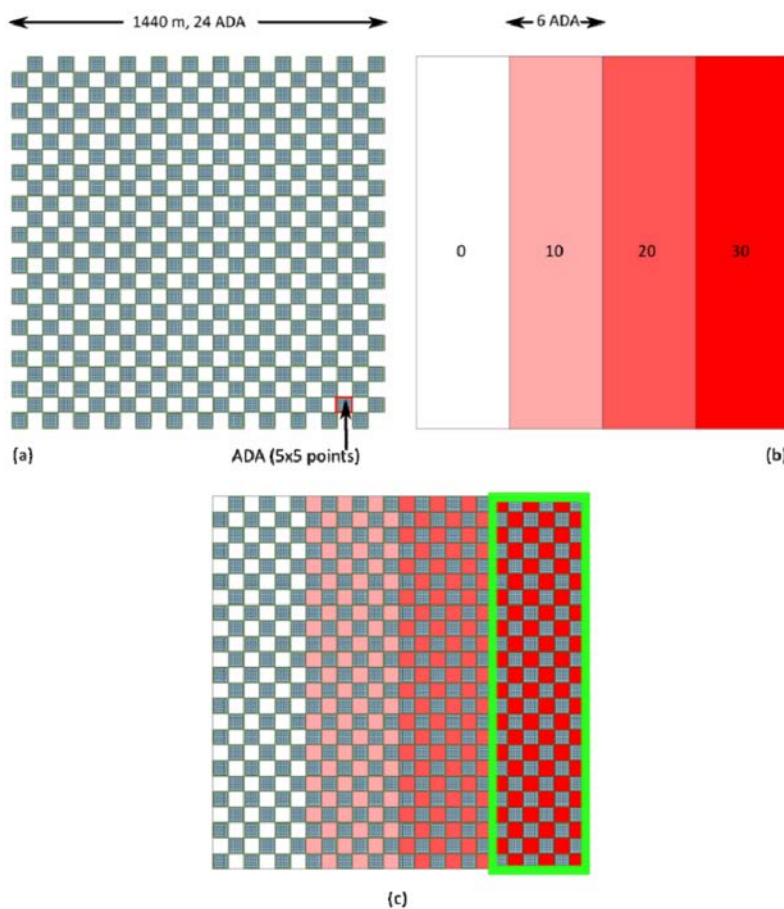


Figure 12. ADAclassifier: synthetic dataset samples. (a) represents the checkerboard pattern for ADA, while (b) shows the stripes with values for the horizontal components of the movement. The green rectangle in (c) depicts the area where positive results for the landslides algorithm should be expected since there the conditions set by the algorithms are satisfied. Source: [25].

Then, for example, if the landslide algorithm imposes that the value of the horizontal component of the movement must be higher than 25 mm/year, then only the rightmost column made of 6×24 ADA will meet the requirement. This may be seen in Figure 12c where the ADA and the horizontal components of the movement (Figure 12a,b) have been overlapped.

A similar setup was used to check the los2hv application. In this case, the area to test was tessellated using a 7×7 grid. There, two groups of PS belonging to the ascending and descending datasets were arranged in alternate rows and columns so only in a well-known subset or the tiles defined by the checkerboard of PS coming from both datasets would coincide. See Figure 13 for a graphical depiction of this setup. There, the tiles surrounded by a green square are the only ones containing both ascending and descending PS and therefore the unique places where the horizontal and vertical components of the movement may be computed by los2hv.

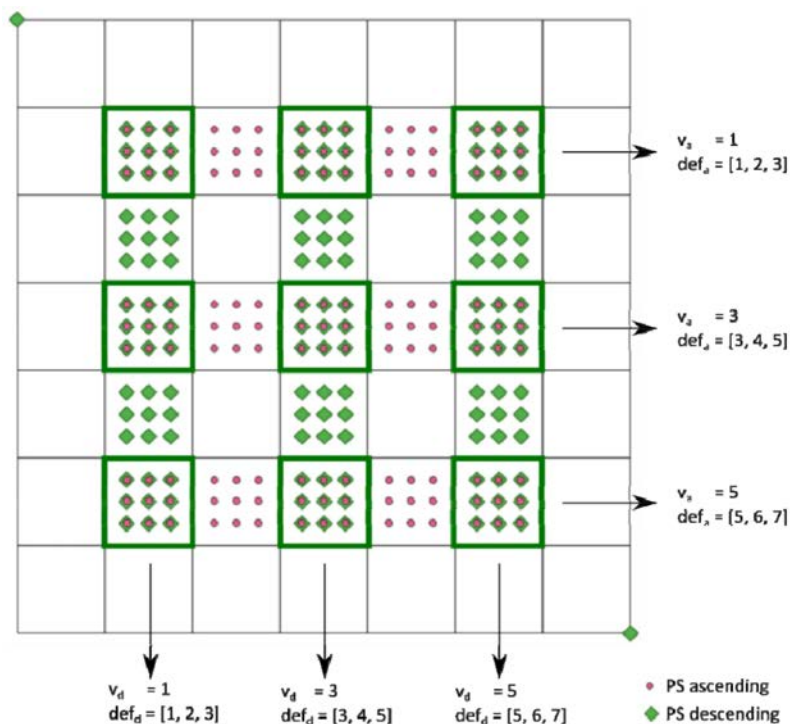


Figure 13. Synthetic dataset for los2hv. The green tiles are the only ones where both ascending and descending PS exist, and therefore, the unique areas where the horizontal component of the movement may be computed.

Known values were set for the velocity (v_a and v_d for ascending and descending datasets respectively, see again Figure 13) and the (ascending/descending) deformation time series (def_a and def_d) for each PS were assigned. This made possible to compute manually (and easily) the results that should be expected from los2hv and thus validate its correctness.

5. Performance Evaluation

Only one of the applications developed and tested, ADAfinder, relies on a procedure for which previous results already existed. Therefore, it was the only one for which a performance reference was available for comparisons. Since such a procedure was executed manually (a series of steps performed by an operator using the tools offered by a GIS), a noticeable improvement of performance was expected due to automation.

There were no performance references for los2hv and ADAclassifier (Section 4 explains that when the tests took place, ADAclassifier took care of the detection of expansivity and thermal effects. Now, these two algorithms have been moved to THEXfinder. This implies that the performance results

given for ADAclassifier in [44] are, actually, pessimistic, since these include the time needed to check two extra phenomena that now are not the responsibility of this tool.), so no specific expectations about performance improvements existed. All tests took place using a computer with the following characteristics: Windows 10 64-bit, Intel Core i5-5300U @ 2.3 GHz, 2 cores, 4 threads, 8 Gb RAM, 500 Gb magnetic (non-SSD) hard disk. Table 1 shows the performance of three of these tools.

Table 1. Performance of the toolset.

Tool.	Dataset	Time (s)
ADAFinder	20,351 PS	2
ADAFinder	926,916 PS	179
los2hv	2 (ascending, descending) × 135 PS. Grid: 7 × 7 tesserae 144 ADA, 3600 PS	55
ADAclassifier	Between 4 - 8 polygons per inventory DTM with 14411441 z values	125

Note that there are no performance results for THEXfinder yet; this tool has not been fully tested at the moment this work was published. Note as well that in the case of ADAclassifier, the process includes the identification of the whole set of deformation phenomena (that is, the test covers all the possible classification processes available). Testing for fewer options will reduce the time needed to process data.

6. Availability

Although the authors are not yet ready to offer the set of tools described herein as an open source project, it is possible to obtain, strictly on demand, a free, executable version (Windows) of ADAfinder, ADAclassifier, THEXfinder, and los2hv directly from the authors, for both commercial and non-commercial purposes. Please, contact the first author of this work for more details.

7. Real Test Cases

In this section two case studies are shown to illustrate the tools presented above. Unfortunately, THEXfinder has not been applied to these areas, since this tool has not been fully tested yet (see Section 5). In the near future, a new paper will deal with THEXfinder applied to some area of interest.

The first case, which has been processed and studied in the framework of the RISKCOAST project (SOE3/P4/E0868), is an area of around 100 km² located in the coastal area of the province of Granada, in southern Spain (Andalusia), including Salobreña and Motril towns. For this test site a limited number of auxiliary data were available for the classification analysis. The second area, for which most of the optional information for ADAclassifier was available, is located in southeastern Italy, between Tropea and Zaccanopoli, in the Calabrian coast of the province of Vibo Valentia, and extends for 12 km².

Figure 14 depicts the location of these two test areas.

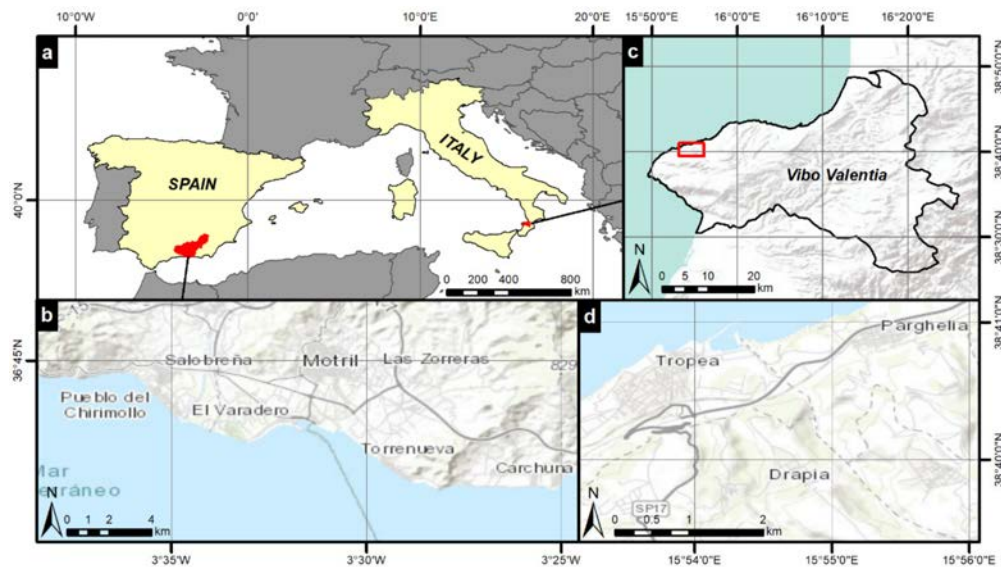


Figure 14. (a) Location of the real test cases in the province of Granada (Spain) and Vibo Valentia (Calabria, Italy); (b) Detail of the test area located in the Granada coast. (c) Test site of Vibo Valentia; and (d) Detail of the test area of Vibo Valentia.

7.1. Southern Spain

7.1.1. Input Data

The InSAR-derived displacement map, which is the main input of the ADAfinder, has been generated applying the PSIG approach using the processing tools developed from the Geomatic Division of CTTC. The processing allowed the annual velocity and the displacement time series to be estimated; refer to [45] for more details on the PSI processing. A set of 138 images acquired by C-band Sentinel-1 satellites (developed by ESA for the Copernicus Programme), in ascending geometry and Wide Swath acquisition mode, has been processed at full resolution covering the period from March 2015 to September 2018. The resolution of Sentinel-1 data is approximately $4 \times 14 \text{ m}^2$ and the temporal sampling is 6 days. The auxiliary data used for the ADAclassifier are: (1) the digital terrain model of the project PNOA-LIDAR (from the National Center of Geographic Information; CNIG) with a resolution cell of 5 m, (2) the geologic map from the Instituto de Estadística y Cartografía de Andalucía, at 1:400.000 scale; (3) the cadastral data from the Spanish General Directorate for Cadaster to select the urbanized and construction areas; and (4) the Corine Land Cover 2018 to complete the cadastral inventory information about structure and infrastructure areas.

7.1.2. Results

The input shapefile (PSI displacement map) for the ADAfinder includes 61,802 measured points. From this map a total number of 82 ADA have been extracted, where 32 have $QI = 1$, 20 have $QI = 2$, 13 have $QI = 3$ and 17 $QI = 4$ (Figure 2). The QI class allows the user to easily understand the noise level (i.e., the reliability) of the displacement time series (TS) within each extracted ADA. Based on the QI classification we have decided to be more restrictive by selecting only the ADA with higher reliability of TS information (QI equal to 1 or 2, for a total of 53 ADA) for the ADAclassifier, where the decision of whether or not the ADA is a potential settlement is based on the mean TS trend. For the output classification (Figure 15 below and Table 2 on page 22), we want to underline that very few auxiliary data have been selected as input. For example, no landslide or subsidence inventories have been used, nor the horizontal-vertical decomposition was available (we have worked with only the ascending geometry of acquisition). For this reason, for both landslide and subsidence phenomena, only results tagged as “potential” will be possible at most. The minimum slope angle to be a potential landslide has been set to 5 degrees, while the maximum slope angle to be a potential subsidence has been set to

10 degrees. We remind that the considered slope is the mean slope value within the ADA. The different slope thresholds allow a double classification of the ADA that are at the limit between the 2 potential phenomena. Moreover, an ADA is classified as potential subsidence only if it lays on a quaternary lithology. For what concerns the consolidation settlement due to new constructions, 6 ADA have been classified as settlement due to the clear inverse exponential trend of the mean TS and the intersection with polygons related to infrastructures and urban areas. One ADA has been classified as potential settlement because it presents an inverse exponential trend, but it does not intersect with any polygon of the cadastral inventory. Among the settlement ADA, 5 lay on the recently built A-7 railway and one on a building close to the port of Motril; both structures were built between 2014 and 2015. For the ADA classified as potential landslides, some of them are already known slope instabilities affecting the coast of Granada [46–48], in this test area movements affecting the urbanizations of Los Almendros and Alfamar are included.

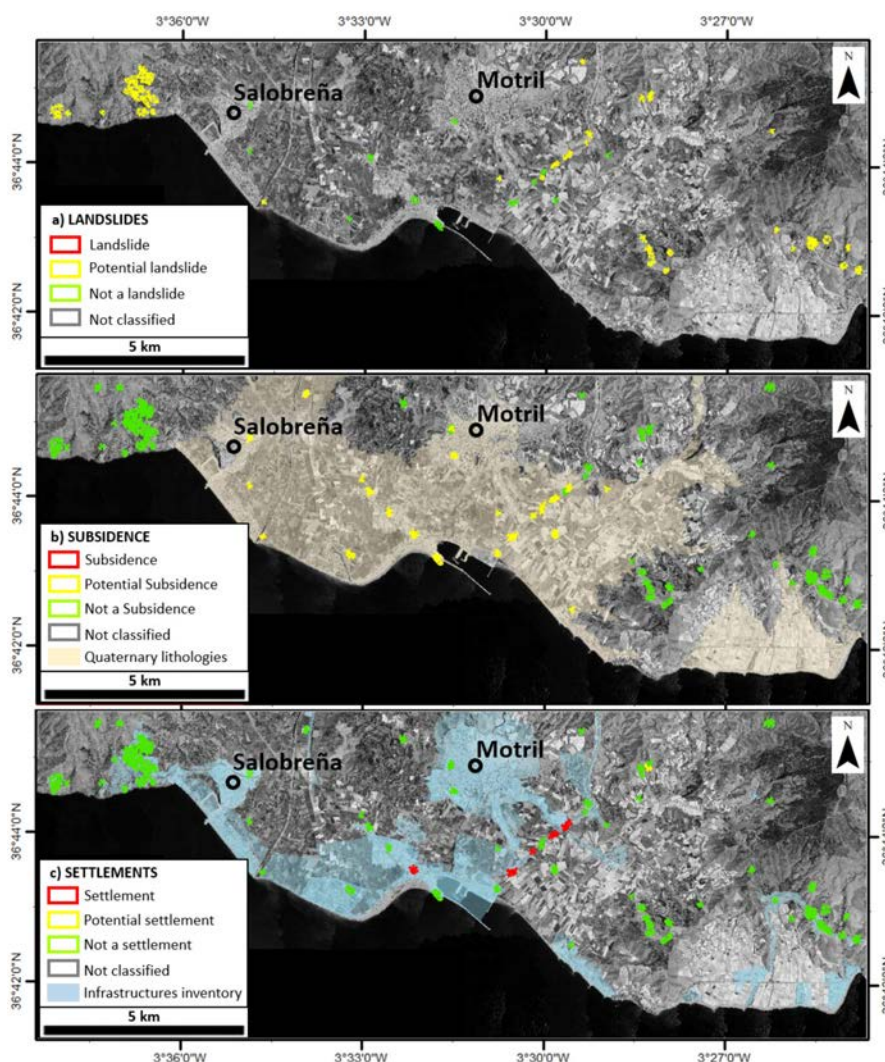


Figure 15. Classification of ADA in the study area located in the South of Spain (province of Granada, Andalucía).

We consider that a multiple classification of the same ADA lets the final user know that the detected movement is a complex case. For example, the ADA classified as both potential settlement and landslide needs to be further analyzed, as it could be a landslide movement that has been stabilized (causing the inverse exponential trend), or a settlement due to a construction not yet inventoried.

Table 2. Summary of ADA extracted with $QI < 3$ and classified in the test areas.

Dataset	# ADA	# Active PS			Area ADA (m ²)			Landslide			Subsidence			Settlement			Sinkhole		
		Avg	Min	Max	Avg	Min	Max	C	P	N	C	P	N	C	P	N	C	P	N
Southern Spain																			
ASC	53	19	5	255	13,216	3620	134,852	0	41	12	0	17	36	6	1	46	0	0	35
Southeast Italy																			
ASC	38	8	5	23	92.2	52.0	312.3	7	6	25	0	14	24	2	0	36	0	0	38
DESC	133	11	5	97	124.8	51.4	704.8	66	20	47	0	28	105	13	0	120	0	0	133
TOTAL								73	26	72	0	42	129	15	0	156	0	0	171

7.2. Southeastern Italy

7.2.1. Input data

In this case, the InSAR-derived deformation maps were obtained using the Persistent Scatter Pairs approach (PSP, [49]). The processing involved three COSMO-SkyMed Stripmap frames, one ascending and two descending; X-band COSMO-SkyMed Stripmap images have a ground resolution of 3×3 m. The ascending frame is composed of 71 images, acquired between March 2013 and October 2018 with an average incidence angle of 29° . The first descending frame is composed of 29 images acquired between March 2017 and March 2019 with an average incidence angle of 26° ; the second descending frame is composed of 94 images acquired between October 2011 and October 2018 with an average incidence angle of 29° .

Complementarily, a Digital Elevation Model (DTM), a landslide inventory map, a geological map and a land use map have been integrated into the classification process performed by ADAclassifier. The DTM consists in a 5 m cell resolution of the Calabria Region. A geological map—scale 1:25.000—and the Italian Landslide Inventory map—IFFI project—of the study area have been used also used. Finally, the Corine Land Cover, Level IV has been used to map urban areas.

7.2.2. Results

A total of 38 and 133 active deformation areas (ADA), all them exhibiting a $QI = 1$, were detected, respectively, for ascending and descending InSAR datasets. The sizes of the ADA vary from 51.4 to 704.8 m² and they are mainly located in the urban areas and the reliefs located at the southeastern part of the analyzed area.

The classification of the ADA identified using ascending and descending datasets by means of ADAclassifier shows that the ADA are classified as: (1) landslides (42.7%) and potential landslides (15.2%); (2) potential land subsidence (24.6%); and (3) consolidation settlement (8.8%). No potential sinkholes were identified by ADAclassifier. Table 2 summarizes the obtained results, depicted in Figure 16.

The landslides are mainly located in the areas with a certain slope in which the inventory map indicates the presence of gravitational processes. Most of the landslides (66 and 7, for descending and ascending frames, respectively) have been confirmed since they are known phenomena included in the IFFI database. Complementarily, 26 ADA (20 and 6, for descending and ascending frames, respectively) are potential landslides since they fall within areas with slopes higher than 10° and/or exhibit not-negligible horizontal displacements. A literature review confirms that this area is particularly prone to weathering processes, lateral spreading, and landslides [50].

In the urban areas of Tropea and Zaccanopoli, 42 potential subsidence areas (28 and 14, for descending and ascending frames, respectively) have been identified. These ADA are located over very flat areas geologically composed of Quaternary sediments. Some of these ADA classified as subsidence areas can be related to the overexploitation of underground water resources, typical for the coastal plains of the Calabria Region [51,52]. The ADA classified as consolidation settlements are mainly placed in the harbor and in some specific locations of the urban area. These areas fit an inverse exponential function with a determination coefficient (r^2) higher than 0.8 and thus are probably

associated with post-constructive consolidation settlements of the dikes of the harbor and of some recent buildings.

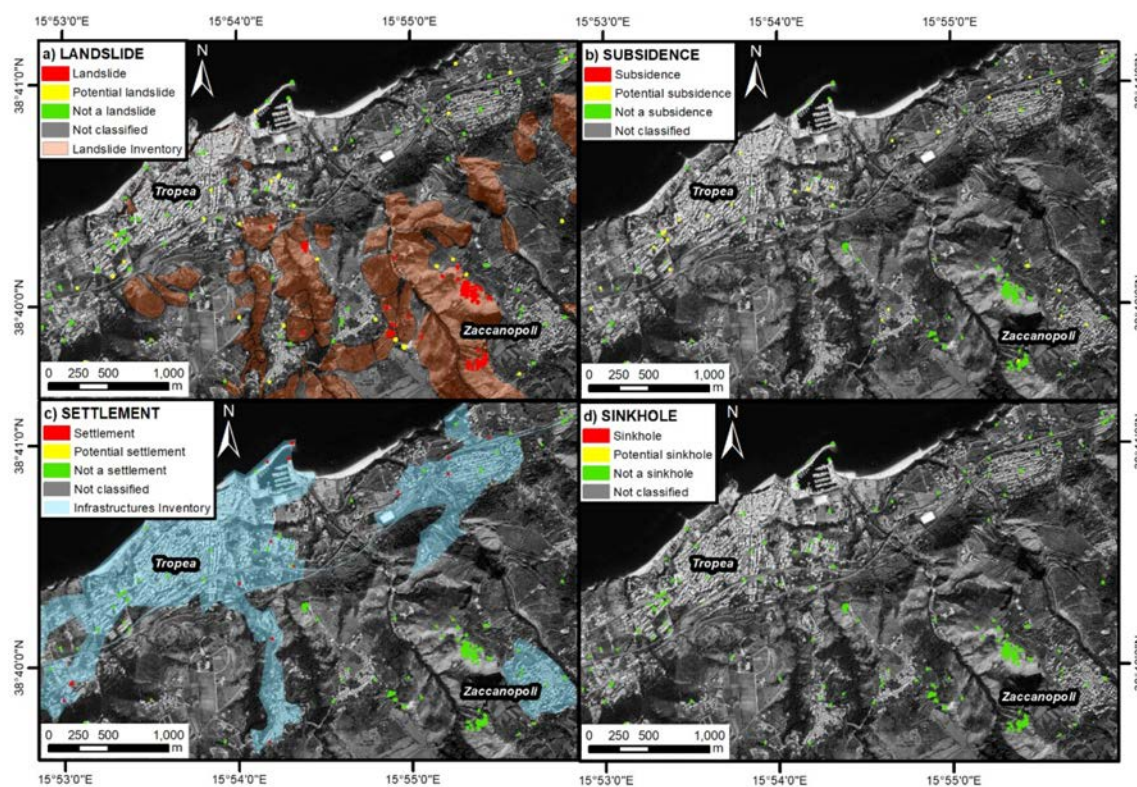


Figure 16. Classification of active deformation areas (ADA) in the study area of Tropea-Zaccanopoli as: (a) landslides; (b) subsidence; (c) consolidation settlements; and (d) sinkholes.

8. Discussion & Conclusions

This work presents the set of tools integrated by ADAfinder, losh2v, ADAclassifier and, to a lesser degree, THEXfinder, since this tool could not be fully tested at the time this work was published. These applications are targeted at automating the identification and classification of ADA. All of them rely on methodologies that had been thoroughly used in real (production) use cases prior to their materialization as software modules. Their implementation is based on well-proven techniques. Although the tools—not the underlying methodologies—were originally conceived to track ground deformation phenomena close to railway infrastructures, they may be used in any other context, as presented by other authors [28–30].

The applications have been sufficiently described in enough detail, considering aspects such as the algorithms implemented, inputs, outputs, or the way these may be used (GUI or console incarnations, or classes in an embeddable library). The procedures to guarantee correctness, as well as the performances of ADAfinder, los2hv, and ADAclassifier, have also been discussed.

Note that, especially in the case of the so-called classification tools (ADAclassifier and THEXfinder), the ability of these applications to work with a big number of optional inputs (i.e., inventories of several kinds) leads to a high degree of flexibility, making the tools useful in a wide variety of situations that are usual in real-life production environments. In other words, ADAclassifier can deliver results for just one deformation phenomenon or go up to four of these, depending on how many optional inputs are provided. The flexibility of the ADAclassifier is displayed in the two use cases (see Sections 7.1 and 7.2), where the availability of input data for the classification process was completely different. The situation in the Spanish use case (Section 7.1), where only a few ancillary data are available, is unfortunately more usual than that of the Italian case (Section 7.2), for which a noticeable number of

data sources were available. The fact to note here is that ADAclassifier (and THEXfinder) is (are) able to deal with these two extreme situations.

It is worth noting that the results provided by these tools are affected by the drawbacks inherent to the InSAR technique used as input, such as the loss of coherence and the low sensitivity to measure North–South directions displacements.

No less important is the fact that automating preexisting methodologies by means of reliable tools (Section 4), provides good response times (Section 5) which may be completely controlled by the user via a whole set of editable parameters, paving the way to better analysis of the areas of interest. Every area is different, and adjusting the parameters controlling the behavior of the process to obtain reliable results is therefore a task that depends on where such areas are located. Avoiding error-prone manual processes thanks to these automated tools, and having results in a few seconds or minutes, make it possible to assess whether or not the starting set of parameters is or is not the most appropriate, it thus being possible—and fast—to repeat test after test at almost no cost, thus increasing the quality of the results. This is a technique that is also applied when using manual procedures, for instance, relying on GIS environments; therefore, being able to do this at a much lower cost and risk allows to obtain better results in less time.

Concerning the real use cases, the results obtained illustrate the applicability of the tools developed to automatically and successfully identify and classify the geological and geotechnical processes affecting wide areas of the territory. Landslides, potential landslides, consolidation settlements, and potential land subsidence have been identified in both test sites using inputs with different characteristics (i.e., InSAR and DTM resolutions, inventory maps, and land use maps). Thus, the possibility of using different input data reveal a high versatility of the proposed tools. Furthermore, this methodology has the advantage that results can be periodically updated by incorporating new InSAR datasets and updated ancillary information.

The outputs provided by ADAtools consist of a set of maps that can be of high interest for geological hazard management to be incorporated into land management and planning.

Moreover, ADAtools can be considered a first step towards satisfying the need for post-processing tools due to the increasing use of PSI data at a regional, national, and European level [3]. The ADAtools will allow different stakeholders to have a fast selection and preliminary interpretation of deformation maps composed of millions/billions of points. This will reduce the amount of data to be managed in terms of hardware, space, and time of analysis, thus increasing the operational use of PSI displacement maps over wide areas. To finish, it is worth noting that the ADAtools may be obtained on demand, completely free of charge, for both commercial and non-commercial purposes (refer to Section 6 for details).

Author Contributions: Conceptualization: R. Tomás, A. Barra; data curation: C. Reyes-Carmona, J. L. Vinielles, S. Falco; formal analysis: R. Tomás, J. I. Pagán; funding acquisition: R. Tomás, M. Crosetto; investigation: R. Tomás, A. Barra, J. I. Pagán; methodology: R. Tomás, A. Barra, L. Solari; project administration: R. Tomás, M. Crosetto; software: J. A. Navarro; supervision: M. Crosetto; validation: J. A. Navarro, R. Tomás, J. I. Pagán; visualization: J. I. Pagán; writing—original draft preparation: J. A. Navarro, R. Tomás, A. Barra; writing—review and editing: all authors. All authors have read and agreed to the published version of the manuscript.

Funding: This work has received funding from the Shift2Rail Joint Undertaking under the European Union’s Horizon 2020 research and innovation programme, with grant agreement No 777630, project MOMIT, “Multi-scale Observation and Monitoring of railway Infrastructure Threats”. It has been also partially funded by Interreg-Sudoe program of the EU, through the project RISKCOAST (Ref: SOE3/P4/E0868).

Acknowledgments: The authors want to acknowledge the work done by M. Costantini in the context of the MOMIT project; the processing of the InSAR data used for the Italian test case took place under his supervision.

Conflicts of Interest: The authors declare no conflict of interest.

References

1. MOMIT Consortium. Home | MOMIT Project Consortium. *Multi-Scale Observation and Monitoring of Railway Infrastructure Threats*. Available online: <http://www.momit-project.eu/> (accessed on 3 July 2020).

2. Crosetto, M.; Monserrat, O.; Cuevas-González, M.; Devanathéry, N.; Crippa, B. Persistent scatterer interferometry: A review. *ISPRS J. Photogramm. Remote. Sens.* **2016**, *115*, 78–89. [[CrossRef](#)]
3. Crosetto, M.; Solari, L.; Mróz, M.; Balasis-Levinsen, J.; Casagli, N.; Frei, M.; Oyen, A.; Moldestadk, D.A.; Bateson, L.; Guerrieri, L.; et al. The Evolution of Wide-Area DInSAR: From Regional and National Services to the European Ground Motion Service. *Remote Sens.* **2020**, *12*, 2043. [[CrossRef](#)]
4. Costantini, M.; Ferretti, A.; Minati, F.; Falco, S.; Trillo, F.; Colombo, D.; Novali, F.; Malvarosa, F.; Mammone, C.; Vecchioli, F.; et al. Analysis of surface deformations over the whole Italian territory by interferometric processing of ERS, Envisat and COSMO-SkyMed radar data. *Remote Sens. Environ.* **2017**, *202*, 250–275. [[CrossRef](#)]
5. Milillo, P.; Perissin, D.; Salzer, J.T.; Lundgren, P.; Lacava, G.; Milillo, G.; Serio, C. Monitoring dam structural health from space: Insights from novel InSAR techniques and multi-parametric modeling applied to the Pertusillo dam Basilicata, Italy. *Int. J. Appl. Earth Obs. Geoinf.* **2016**, *52*, 221–229. [[CrossRef](#)]
6. Selvakumaran, S.; Plank, S.; Geiß, C.; Rossi, C.; Middleton, C. Remote monitoring to predict bridge scour failure using Interferometric Synthetic Aperture Radar (InSAR) stacking techniques. *Int. J. Appl. Earth Obs. Geoinf.* **2018**, *73*, 463–470. [[CrossRef](#)]
7. Reyes-Carmona, C.; Barra, A.; Galve, J.P.; Monserrat, O.; Pérez-Peña, J.V.; Mateos, R.M.; Notti, D.; Ruano, P.; Millares, A.; López-Vinielles, J.; et al. Sentinel-1 DInSAR for Monitoring Active Landslides in Critical Infrastructures: The Case of the Rules Reservoir (Southern Spain). *Remote Sens.* **2020**, *12*, 809. [[CrossRef](#)]
8. Solari, L.; Del Soldato, M.; Raspini, F.; Barra, A.; Bianchini, S.; Confuorto, P.; Casagli, N.; Crosetto, M. Review of Satellite Interferometry for Landslide Detection in Italy. *Remote Sens.* **2020**, *12*, 1351. [[CrossRef](#)]
9. Frattini, P.; Crosta, G.B.; Rossini, M.; Allievi, J. Activity and kinematic behaviour of deep-seated landslides from PS-InSAR displacement rate measurements. *Landslides* **2018**, *15*, 1053–1070. [[CrossRef](#)]
10. Zhang, Y.; Meng, X.; Jordan, C.; Novellino, A.; Dijkstra, T.; Chen, G. Investigating slow-moving landslides in the Zhouqu region of China using InSAR time series. *Landslides* **2018**, *15*, 1299–1315. [[CrossRef](#)]
11. Ciampalini, A.; Solari, L.; Giannecchini, R.; Galanti, Y.; Moretti, S. Evaluation of subsidence induced by long-lasting buildings load using InSAR technique and geotechnical data: The case study of a Freight Terminal (Tuscany, Italy). *Int. J. Appl. Earth Obs. Geoinf.* **2019**, *82*, 101925. [[CrossRef](#)]
12. Zhou, C.; Gong, H.; Zhang, Y.; Warner, T.A.; Wang, C. Spatiotemporal evolution of land subsidence in the Beijing plain 2003–2015 using persistent scatterer interferometry (PSI) with multi-source SAR data. *Remote Sens.* **2018**, *10*, 552. [[CrossRef](#)]
13. Tosi, L.; Lio, C.D.; Teatini, P.; Strozzi, T. Land subsidence in coastal environments: Knowledge advance in the Venice Coastland by TerraSAR-X. PSI. *Remote Sens.* **2018**, *10*, 1191. [[CrossRef](#)]
14. Malinowska, A.A.; Witkowski, W.T.; Hejmanowski, R.; Chang, L.; van Leijen, F.J.; Hanssen, R.F. Sinkhole occurrence monitoring over shallow abandoned coal mines with satellite-based persistent scatterer interferometry. *Eng. Geol.* **2019**, *262*, 105336. [[CrossRef](#)]
15. Theron, A.; Engelbrecht, J. The role of earth observation, with a focus on SAR Interferometry, for sinkhole hazard assessment. *Remote Sens.* **2018**, *10*, 1506. [[CrossRef](#)]
16. Baer, G.; Magen, Y.; Nof, R.N.; Raz, E.; Lyakhovskiy, V.; Shalev, E. InSAR measurements and viscoelastic modeling of sinkhole precursory subsidence: Implications for sinkhole formation, early warning, and sediment properties. *J. Geophys. Res. Earth Surf.* **2018**, *123*, 678–693. [[CrossRef](#)]
17. Cheloni, D.; De Novellis, V.; Albano, M.; Antonioli, A.; Anzidei, M.; Atzori, S.; Avallone, A.; Bignami, D.; Bonano, M.; Calcaterra, S.; et al. Geodetic model of the 2016 Central Italy earthquake sequence inferred from InSAR and GPS data. *Geophys. Res. Lett.* **2017**, *44*, 6778–6787. [[CrossRef](#)]
18. Moro, M.; Saroli, M.; Stramondo, S.; Bignami, C.; Albano, M.; Falcucci, E.; Gori, S.; Doglioni, C.; Polcari, M.; Tallini, M.; et al. New insights into earthquake precursors from InSAR. *Sci. Rep.* **2017**, *7*, 1–11. [[CrossRef](#)]
19. Fang, J.; Xu, C.; Wen, Y.; Wang, S.; Xu, G.; Zhao, Y.; Yi, L. The 2018 Mw 7.5 Palu earthquake: A supershear rupture event constrained by InSAR and broadband regional seismograms. *Remote Sens.* **2019**, *11*, 1330. [[CrossRef](#)]
20. Di Traglia, F.; Nolesini, T.; Solari, L.; Ciampalini, A.; Frodella, W.; Steri, D.; Benedetto, A.; Rindi, A.; Marini, L.; Monni, N.; et al. Lava delta deformation as a proxy for submarine slope instability. *Earth Planet. Sci. Lett.* **2018**, *488*, 46–58. [[CrossRef](#)]

21. Schaefer, L.N.; Di Traglia, F.; Chaussard, E.; Lu, Z.; Nolesini, T.; Casagli, N. Monitoring volcano slope instability with Synthetic Aperture Radar: A review and new data from Pacaya (Guatemala) and Stromboli (Italy) volcanoes. *Earth Sci. Rev.* **2019**, *192*, 236–257. [[CrossRef](#)]
22. Anantrasirichai, N.; Biggs, J.; Albino, F.; Hill, P.; Bull, D. Application of machine learning to classification of volcanic deformation in routinely generated InSAR data. *J. Geophys. Res. Earth* **2018**, *123*, 6592–6606. [[CrossRef](#)]
23. Bakon, M.; Czikhhardt, R.; Papco, J.; Barlak, J.; Rovnak, M.; Adamisin, P.; Perissin, D. remotIO: A Sentinel-1 Multi-Temporal InSAR Infrastructure Monitoring Service with Automatic Updates and Data Mining Capabilities. *Remote Sens.* **2020**, *12*, 1892. [[CrossRef](#)]
24. Raspini, F.; Bianchini, S.; Ciampalini, A.; Del Soldato, M.; Solari, L.; Novali, F.; del Conte, S.; Rucci, A.; Ferretti, A.; Casagli, N. Continuous, semi-automatic monitoring of ground deformation using Sentinel-1 satellites. *Sci. Rep.* **2018**, *8*, 1–11. [[CrossRef](#)] [[PubMed](#)]
25. Navarro, J.A.; Cuevas-González, M.; Tomás, R.; Barra, A.; Crosetto, M. A toolset to detect and classify Active Deformation Areas using interferometric SAR data. In Proceedings of the 5th International Conference on Geographic Information Systems, Theory, Applications and Management (GISTAM 2019), Crete, Greece, 3–6 May 2019.
26. Barra, A.; Solari, L.; Béjar-Pizarro, M.; Montserrat, O.; Bianchini, S.; Herrera, G.; Crosetto, M.; Sarro, R.; González-Alonso, E.; Mateos, R.M.; et al. A methodology to detect and update Active Deformation Areas based on Sentinel-1 SAR images. *Remote Sens.* **2017**, *9*, 1002. [[CrossRef](#)]
27. Tomás, R.; Pagán, J.I.; Navarro, J.A.; Cano, M.; Pastor, J.L.; Riquelme, A.; Cuevas-González, M.; Crosetto, M.; Barra, A.; Monserrat, O.; et al. Semi-Automatic Identification and Pre-Screening of Geological–Geotechnical Deformational Processes Using Persistent Scatterer Interferometry Datasets. *Remote Sens.* **2019**, *11*, 1675. [[CrossRef](#)]
28. Solari, L.; Barra, A.; Herrera, G.; Bianchini, S.; Monserrat, O.; Béjar-Pizarro, M.; Crosetto, M.; Sarro, R.; Moretti, S. Fast detection of ground motions on vulnerable elements using Sentinel-1 InSAR data. *Geomat. Nat. Hazards Risk* **2018**, *9*, 152–174. [[CrossRef](#)]
29. Solari, L.; Bianchini, S.; Franceschini, R.; Barra, A.; Monserrat, O.; Thuegaz, P.; Bertolo, D.; Crosetto, M.; Catani, F. Satellite interferometric data for landslide intensity evaluation in mountainous regions. *Int. J. Appl. Earth Obs. Geoinf.* **2020**, *87*, 102028. [[CrossRef](#)]
30. Aslan, G.; Fomelis, M.; Raucoules, D.; De Michele, M.; Bernardie, S.; Cakir, Z. Landslide Mapping and Monitoring Using Persistent Scatterer Interferometry (PSI) Technique in the French Alps. *Remote Sens.* **2020**, *12*, 1305. [[CrossRef](#)]
31. Ferretti, A.; Monti-Guarnieri, A.; Prati, C.; Rocca, F.; Massonet, D. *InSAR Principles-Guidelines for SAR Interferometry Processing and Interpretation, TM-19*; ESA Publications: Auckland, New Zealand, 2007.
32. Tomás, R.; Cano, M.; Pastor, J.L.; Riquelme, A. Automatic Classification of Active Deformation Areas. MOMIT Project Technical Note 2018. Available online: https://www.momit-project.eu/sites/default/files/2018-12/MOMIT_technical_note_%20Automatic%20classification%20of%20Active%20Deformation%20Areas.pdf (accessed on 3 July 2020).
33. Navarro, J.A.; Cuevas, M. ADAfinder-A Tool to Automate the Detection of Active Deformation Areas. MOMIT Project Technical Note. Available online: https://www.momit-project.eu/sites/default/files/2018-12/MOMIT_technical_note_ADAlfinder%20documentation.pdf (accessed on 3 July 2020).
34. Navarro, J.A.; Cuevas, M.; Crosetto, M. ADAclassifier-Classify ADAs Automatically. MOMIT Project Technical Note. Available online: https://www.momit-project.eu/sites/default/files/2018-12/MOMIT_technical_note_ADAClassifier%20documentation.pdf (accessed on 3 July 2020).
35. He, L.; Wu, L.; Liu, S.; Wang, Z.; Su, C.; Liu, S.-N. Mapping Two-Dimensional Deformation Field Time-Series of Large Slope by Coupling DInSAR-SBAS with MAI-SBAS. *Remote Sens.* **2015**, *7*, 12440–12458. [[CrossRef](#)]
36. Notti, D.; Herrera, G.; Bianchini, S.; Meisina, S.; García-Davalillo, J.C.; Zucca, F. A methodology for improving landslide PSI data analysis. *Int. J. Remote Sens.* **2014**, *35*, 2186–2214. [[CrossRef](#)]
37. Navarro, J.A.; Cuevas, M. los2hv-Compute Horizontal and Vertical Components of the Movement. MOMIT Project Technical Note. Available online: https://www.momit-project.eu/sites/default/files/2018-12/MOMIT_technical_note_los2hv%20documentation.pdf (accessed on 3 July 2020).
38. The Qt Company. Qt | Cross-platform software development for embedded & desktop. Available online: <https://www.qt.io/> (accessed on 3 July 2020).

39. Warmerdam, F. Shapelib C Library. Available online: <http://shapelib.maptools.org/> (accessed on 3 July 2020).
40. Johnson, A. Clipper—An Open Source Freeware Polygon Clipping Library. Available online: <http://www.angusj.com/delphi/clipper.php> (accessed on 3 July 2020).
41. King, D.E. Dlib-ml: A Machine Learning Toolkit. *J. Mach. Learn. Res.* **2010**, *10*, 1755–1758.
42. Guennebaud, G.; Benoît, J. Eigen v3. Available online: <http://eigen.tuxfamily.org> (accessed on 3 July 2020).
43. Navarro, J.A.; Cuevas, M.; Crosetto, M. SW Data Processing Components Test Plan. MOMIT Project Deliverable. Available online: <https://www.momit-project.eu/sites/default/files/2018-12/MOMIT%20-%20D3.3%20-%20SW%20data%20processing%20components%20test%20plan.pdf> (accessed on 3 July 2020).
44. Navarro, J.A.; Tomás, R.; Cuevas, M.; Crosetto, M. SW Data Processing Components Test Report. MOMIT Project Deliverable. Available online: https://www.momit-project.eu/sites/default/files/2018-12/MOMIT%20-%20D3.4%20-%20SW%20data%20processing%20components%20test%20report_v1.0.1.pdf (accessed on 3 July 2020).
45. Devanathéry, N.; Crosetto, M.; Monserrat, O.; Cuevas-González, M.; Crippa, B. An approach to Persistent Scatterer Interferometry. *Remote Sens.* **2014**, *6*, 6662–6679. [[CrossRef](#)]
46. Notti, D.; Galve, J.P.; Mateos, R.M.; Monserrat, O.; Lamas-Fernández, F.; Fernández-Chacón, F.; Roldán-García, F.J.; Pérez-Peña, J.V.; Crosetto, M.; Azañón, J.M. Human-induced coastal landslide reactivation. Monitoring by PSInSAR techniques and urban damage survey (SE Spain). *Landslides* **2015**, *12*, 1007–1014. [[CrossRef](#)]
47. Galve, J.P.; Pérez-Peña, J.V.; Azañón, J.M.; Closson, D.; Caló, F.; Reyes-Carmona, C.; Jabaloy, A.; Ruano, P.; Mateos, R.M.; Notti, D.; et al. Evaluation of the SBAS InSAR service of the European space Agency's Geohazard Exploitation Platform (GEP). *Remote Sens.* **2017**, *9*, 1291. [[CrossRef](#)]
48. Chacón, J.; Alameda-Hernández, P.; Chacón, E.; Delgado, J.; El Hamdouni, R.; Fernández, P.; Fernández, T.; Gómez-López, J.M.; Irigaray, C.; Jiménez-Perálvarez, J.; et al. The Calaiza landslide on the coast of Granada (Andalusia, Spain). *Bull. Eng. Geol. Environ.* **2019**, *78*, 2107–2124. [[CrossRef](#)]
49. Costantini, M.; Falco, S.; Malvarosa, F.; Minati, F.; Trillo, F.; Vecchioli, F. Persistent Scatterer Pair Interferometry: Approach and Application to COSMO-SkyMed SAR Data. *IEEE J. Sel. Top. Appl. Earth Obs. Remote Sens.* **2014**, *7*, 2869–2879. [[CrossRef](#)]
50. Ietto, F.; Perri, F.; Fortunato, G. Lateral spreading phenomena and weathering processes from the Tropea area (Calabria, southern Italy). *Environ. Earth Sci.* **2015**, *73*, 4595–4608. [[CrossRef](#)]
51. Bianchini, S.; Moretti, S. Analysis of recent ground subsidence in the Sibari plain (Italy) by means of satellite SAR interferometry-based methods. *Int. J. Remote Sens.* **2015**, *36*, 4550–4569. [[CrossRef](#)]
52. Raspini, F.; Cigna, F.; Moretti, S. Multi-temporal mapping of land subsidence at basin scale exploiting Persistent Scatterer Interferometry: Case study of Gioia Tauro plain (Italy). *J. Maps* **2012**, *8*, 514–524. [[CrossRef](#)]



© 2020 by the authors. Licensee MDPI, Basel, Switzerland. This article is an open access article distributed under the terms and conditions of the Creative Commons Attribution (CC BY) license (<http://creativecommons.org/licenses/by/4.0/>).

6 Satellite interferometric data for landslide intensity evaluation in mountainous regions



Contents lists available at ScienceDirect

Int J Appl Earth Obs Geoinformation

journal homepage: www.elsevier.com/locate/jag

Satellite interferometric data for landslide intensity evaluation in mountainous regions



Lorenzo Solari^{a,*}, Silvia Bianchini^b, Rachele Franceschini^b, Anna Barra^a, Oriol Monserrat^a, Patrick Thuegaz^c, Davide Bertolo^c, Michele Crosetto^a, Filippo Catani^b

^a Centre Tecnològic de Telecomunicacions de Catalunya (CTTC/CERCA), Geomatics Division, 08860, Castelldefels, Spain

^b University of Firenze, Department of Earth Sciences. Via Giorgio La Pira 4, 50121, Firenze, Italy

^c Regione Autonoma Valle d'Aosta, Assessorato Opere pubbliche, Difesa del suolo e edilizia residenziale pubblica. Loc. Amérique, 11020, Quart, Italy

ARTICLE INFO

Keywords:

Satellite interferometry
Landslide intensity
Potential loss
Mountainous region

ABSTRACT

Multi-Temporal Interferometric Synthetic Aperture Radar (MTInSAR) data offer a valuable support to landslide mapping and to landslide activity estimation in mountain environments, where in situ measures are sometimes difficult to gather. Nowadays, the interferometric approach is more and more used for wide-areas analysis, providing useful information for risk management actors but at the same time requiring a lot of efforts to correctly interpret what satellite data are telling us. In this context, hot-spot-like analyses that select and highlight the fastest moving areas in a region of interest, are a good operative solution for reducing the time needed to inspect a whole interferometric dataset composed by thousands or millions of points. In this work, we go beyond the concept of MTInSAR data as simple mapping tools by proposing an approach whose final goal is the quantification of the potential loss experienced by an element at risk hit by a potential landslide. To do so, it is mandatory to evaluate landslide intensity. Here, we estimate intensity using Active Deformation Areas (ADA) extracted from Sentinel-1 MTInSAR data. Depending on the localization of each ADA with respect to the urban areas, intensity is derived in two different ways. Once exposure and vulnerability of the elements at risk are estimated, the potential loss due to a landslide of a given intensity is calculated. We tested our methodology in the Eastern Valle d'Aosta (north-western Italy), along four lateral valleys of the Dora Baltea Valley. This territory is characterized by steep slopes and by numerous active and dormant landslides. The goal of this work is to develop a regional scale methodology based on satellite radar interferometry to assess the potential impact of landslides on the urban fabric.

1. Introduction

Considering the increasing socio-economic impacts of landslides worldwide, mainly due to the growth of urban settlements in landslide-prone areas (Petley et al., 2005), several methods and guidelines have been proposed for qualitative and/or quantitative landslide risk estimation. Risk has been investigated as a general framework or as for single components, such as intensity, vulnerability or exposure (i.e. Dai et al., 2002; Ko et al., 2004; Glade et al., 2006; Corominas et al., 2014). These parameters can be evaluated in different ways, depending on the input data quality and on the working scale; a unique way to derive them cannot be found in literature (Fell et al., 2008).

Landslide risk is particularly difficult to assess over wide areas

because detailed information about landslide occurrence, spatial and temporal probability, runout modelling, vulnerability and exposure assessment is usually quite challenging to derive (Van Westen et al., 2006; Strozzi et al., 2013). At regional to medium scale (1:250,000 – 1:25,000) landslide risk products are used for urban planning activities and to define long-term strategies for risk reduction (Corominas et al., 2014).

Vulnerability is generally defined as the degree of loss of a given element at risk to the occurrence of a landslide of given magnitude. It is related to the amount of damage the exposed elements at risk could suffer due to a certain hazard (Winter et al., 2014). It is a difficult parameter to estimate if detailed damage data are not available and because landslide magnitude cannot be easily foreseen (Van Westen

* Corresponding author at: Centre Tecnològic de Telecomunicacions de Catalunya (CTTC/CERCA), Geomatics Division, 08860, Castelldefels, Spain.

E-mail addresses: lorenzo.solari@cttc.cat (L. Solari), silvia.bianchini@unifi.it (S. Bianchini), rachele.franceschini@stud.unifi.it (R. Franceschini), anna.barra@cttc.cat (A. Barra), oriol.monserrat@cttc.cat (O. Monserrat), p.thuegaz@regione.vda.it (P. Thuegaz), d.bertolo@regione.vda.it (D. Bertolo), michele.crosetto@cttc.cat (M. Crosetto), filippo.catani@unifi.it (F. Catani).

<https://doi.org/10.1016/j.jag.2019.102028>

Received 10 July 2019; Received in revised form 31 October 2019; Accepted 2 December 2019

Available online 13 December 2019

0303-2434/ © 2019 The Authors. Published by Elsevier B.V. This is an open access article under the CC BY-NC-ND license

(<http://creativecommons.org/licenses/by-nc-nd/4.0/>).

et al., 2006). Vulnerability is a concept that can be applied to people or buildings/infrastructures (in this case is known as “physical vulnerability”). Considering the large and intrinsic uncertainties, the degree of loss of human life is rarely assessed. Some authors proposed solutions based on population census data or consequence analysis (Bell and Glade, 2004). Physical vulnerability has been more widely used in landslide studies, still requiring some information about building/infrastructure typology or potential damage degree. Usually, physical vulnerability is expressed by a relative scale ranging from 0 (no damage) to 1 (complete damage) and can be estimated using heuristic methods (e.g. Winter et al., 2014), data driven methods (the most frequently used, e.g. Kaynia et al., 2008) or analytical methods (less frequently implemented because of their complexity, e.g. Mavrouli and Corominas, 2010).

Exposure is assumed to be a characteristic of the element at risk (person or structure) and it is referred to its location and economic value (Glade et al., 2006). Population exposure requires specific studies aimed to evaluate the day/night fluctuation of exposed people. It depends on building use as well (e.g. Schwendtner et al., 2013). Building exposure essentially depends on the type of element at risk considering the interaction between the structure and a given event under a constant level of risk (Glade et al., 2006).

Landslide intensity is a crucial parameter to be defined for a correct evaluation of vulnerability and of the expected degree of loss. As defined by Hungr (1997), intensity is an evaluation of landslide destructiveness. It is related to the type of landslide, its propagation mechanism and volume. Intensity is a highly site-dependent, non-straightforward task for which no standardized methodology exists (Uzielli et al., 2008). Cardinali et al. (2002) proposed a landslide intensity classification based on two parameters: volume and velocity of the phenomenon. Lateltin et al. (2005) presented an overview about risk management in Switzerland, reporting that landslide intensity is related to different parameters, depending on the type of event (such as thickness and velocity of the mass for debris flows). Jakob (2005) demonstrated how debris flows intensity is closely related to their size, in terms of volume, peak discharge and inundated area. Therefore, the estimation of intensity classically relies on landslide models or empirical formulas aimed at calculating landslides volume.

Nowadays, it is possible to assess intensity by means of earth observation products such as Multi-temporal Interferometric Synthetic Aperture Radar (MTInSAR) data. These earth observation products can help defining the magnitude of potential slow-moving landslides, parameter useful for landslide intensity (Guzzetti et al., 2006). MTInSAR data have been used by some authors for this kind of evaluation. For example, Cigna et al. (2013) exploited MTInSAR products for landslide state of activity and intensity appraisal by means of an “activity matrix” whose inputs were interferometric-derived ground velocity information. This approach has been followed by Oliveira et al. (2015) to assess the potential of MTInSAR data for new landslide definition in the Grande da Pipa River basin (Portugal). Bianchini et al. (2017b) presented a GIS-based (Geographical Information System) procedure aimed to evaluate specific risk in a hilly municipality of Tuscany Region (central Italy). Interferometric products were used as landslide intensity zonation tools.

In a more general framework, MTInSAR data have a high potential to provide useful information about “new” landslides, highlighting unknown phenomena that have not been previously mapped. The effectiveness of MTInSAR data have been especially proven in mountain environments, where in situ information are difficult to obtain, especially by hotspot approaches (Hölbling et al., 2012; Liu et al., 2013; Del Ventisette et al., 2014; Raspini et al., 2016; Bianchini et al., 2012, 2017a; Imaizumi et al., 2018; Lu et al., 2019; Solari et al., 2019).

In this work, we go beyond the concept of MTInSAR data as mapping tools by proposing a simple and reproducible work flow which has as starting point a deformation map derived from satellite radar data. The deformation map is analyzed to automatically extract the fastest

moving areas (Active Deformation Areas – ADA) with common Persistent Scatterers (PS) behavior. The ADA extraction methodology was newly conceived and developed in Barra et al. (2017) and already used in some recent literature (Pastonchi et al., 2018; Solari et al., 2018; Tomás et al., 2019). The ADA are the first product of the chain, whose final goal is to quantify the potential loss (by an economic point of view) suffered by a building or road if the motion persists or accelerates. The methodology aims to derive landslide intensity using the ADA in a dual form: as direct estimation of landslide magnitude (and intensity) and as an indicator for the presence of unstable debris covers that could be the source areas of future debris flows, whose runoff is foreseen by means of a basin scale model. The methodology has been tested in Eastern Valle d’Aosta (north-western Italy) along four lateral valleys of the Dora Baltea Valley in a territory characterized by steep slopes and widespread active and dormant landslides. Palomba et al. (2015) reported that from 1984 the number of landslide events above 2000 m a.s.l. may have slightly increased, highlighting the need for remotely sensed motion data in partially or totally inaccessible areas.

The methodology has been conceived in the framework of the “U-Geohaz - Geohazard impact assessment for urban areas” project, co-funded by the European Commission, Directorate-General Humanitarian Aid and Civil Protection (ECHO). The main goal of the project is to develop a methodology based on Sentinel-1 radar images to continuously assess the potential impact of geohazards on urban areas and critical infrastructures.

2. Study area

The test area of our methodology is eastern Valle d’Aosta (VdA), an alpine region in north-western Italy. The area of interest is mainly mountainous with peaks reaching 4000 m a.s.l. and it is characterized by a main East-West valley, where the Dora Baltea flows, and by five tributary valleys (from west to east: Valpelline, Saint Bartelemy, Valtourneche, Ayas and Gressoney valleys - Fig. 1).

The current landscape has been highly influenced and controlled by the glacial action and by the tectonic/geodynamic evolution of VdA (Martinotti et al., 2011). The latter reflects the complex collision between the European and Adria plates that created an imbricated pile of metamorphic continental and oceanic domains (Polino et al., 1990). These tectono-metamorphic units were later affected by neotectonic faulting, i.e. along the Aosta-Ranzola fault that crosses the eastern part of the Dora Baltea valley (Bistacchi et al., 2001). This post collisional activity influences the relief evolution and the current slope dynamics due to the inherited geo-structural and tectonic settings (Carraro and Giardino, 2004). After the last glaciation maximum, the action of ice concurred in modelling the landscape of VdA, configuring the current valleys orography, leaving erosional or depositional landforms and directly influencing mass wasting processes due to debuitressing (Carraro and Giardino, 2004).

Land cover is dominated by forests and grasslands below 2000 m a.s.l., gradually replaced above this altitude by debris, sparse vegetation and bare rock. At the highest altitudes few perennial glaciers are still present. Urban areas can be found only along valley bottoms and overall below 1500 m a.s.l.; large valley sectors are considered inhabited.

Climate is highly influenced by altitude and it is characterized by precipitation regimes of 1000–1110 mm/year in the tributary valleys and of 600 mm/year in the Dora Baltea Valley (Ratto et al., 2003). During winters, snowfalls are frequent. Extreme rainfall events are common between late spring (end of April – May) and early autumn (September – beginning of October), registering cumulated rainfalls higher than 250 mm in few days (Salvatici et al., 2018).

The area of interest is characterized by 972 mapped landslides, included in the IFFI (Inventario dei Fenomeni Franosi in Italia – Italian landslide inventory, Trigila et al., 2010) catalogue of the region (Fig. 2). Different types of landslide are well represented in eastern VdA, ranging

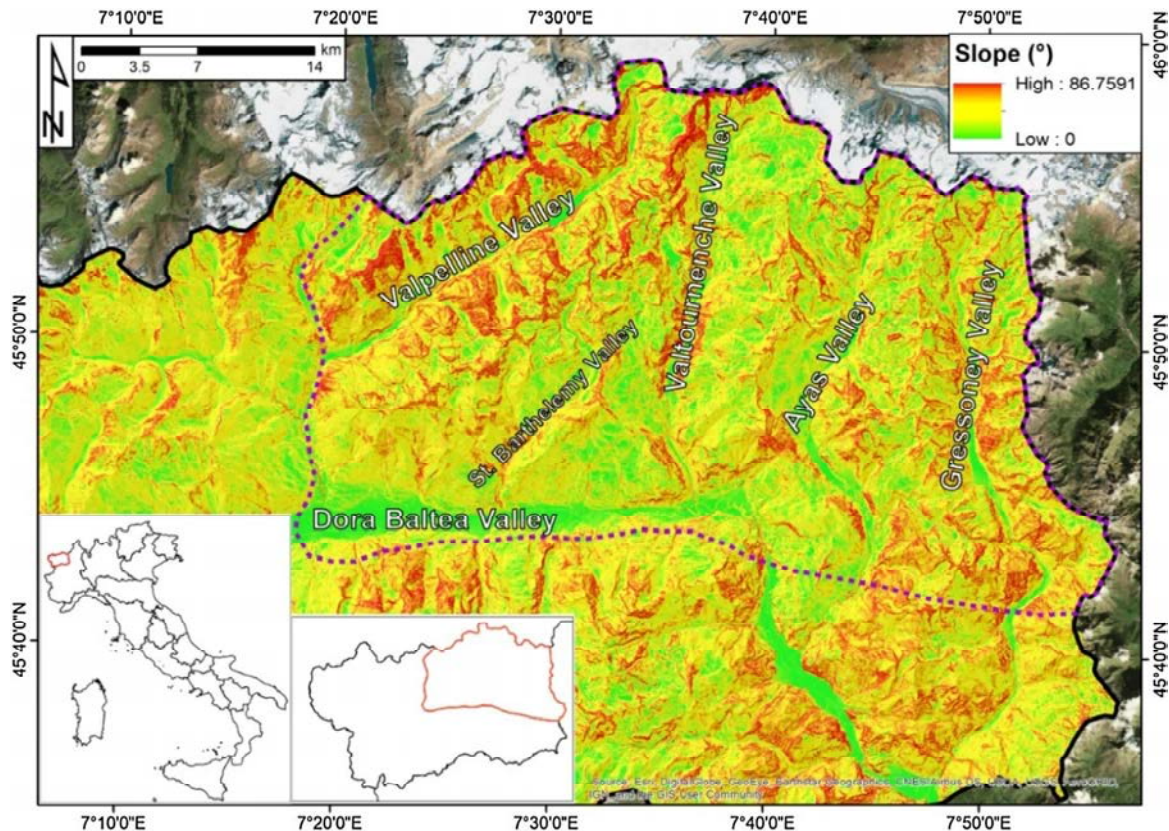


Fig. 1. Slope map of the area of interest derived from a 10 m Digital Elevation Model (DEM). The background image is an ESRI World Imagery orthophoto.

between very slow and slow-moving phenomena (DSGSD - Deep-Seated Gravitational Slope Deformation, rotational and complex landslides) to fast-moving landslides, such as debris and mud flows. Considering the areal extent of landslides, the most representative type is DSGSD which alone covers 152 km², with single mapped phenomena covering more than 10 km². The landslide index of this area (ratio between the area covered by landslides and the whole territory) is equal to 20 %, consistent with the regional value (18 %, Solari et al., 2019). In the area of interest, landslides are a major threat, causing high economic losses (both direct and indirect) and in some cases casualties, such as in October 2000 when a series of debris flows severely hit this sector of VdA, killing 17 people (Ratto et al., 2003).

3. Methodology

The methodology aims to derive vulnerability and potential loss maps starting from a regional scale deformation map obtained through MTInSAR analysis, which is the main input (Fig. 3). Because of the morphological context, landslides are our target; the methodology can be anyway adapted to other geohazards.

The first product to be derived is the ADA database which contains all the moving areas detected in the area of interest, following the approach proposed by Barra et al. (2017). Depending on the localization of each ADA, landslide intensity is defined in a twofold manner:

- 1) “ADA-related intensity”. Landslide intensity depends on the average velocity of the ADA. This approach is applied only when a moving area directly overlaps one or more buildings/roads or an urban area (“Urban area – YES” condition in the workflow of Fig. 3);
- 2) “Model-related intensity”. Landslide intensity depends on the run out of a potential landslide that could be originated from a debris-covered area showing high deformation rates and highlighted as

ADA. We define as “debris” every type of slope or colluvial deposits containing blocks and more fine-grained materials and originated by slope dynamics (e.g. rockfalls deposits). The landslide run-out could hit one or more buildings/roads. This approach is applicable when a moving area is found outside of an urban area (“Urban area – NO” condition in Fig. 3) and in correspondence of a potential source of debris flows (“Geo-indicators – YES” condition in Fig. 3).

The geo-indicators are defined using a qualitative approach based on a preliminary analysis of all the ancillary data available. Topographic maps and DEMs (and DEM-derived products – slope and aspect) are used for the delineation of the geomorphological characteristics of a slope (e.g. curvature, presence of trenches or channels, water shed). Orthophoto, geological maps and ground data (when available) are used to estimate the presence of debris deposits (as previously defined).

If an ADA does not fall into one of the two limiting conditions of the workflow, the approach cannot be applied.

Once the landslide intensity is calculated, exposure of the elements at risk and vulnerability are defined. Exposure evaluation is performed on a cadastral polygonal database of buildings and roads which is re-classified on the basis of the presumed asset value. Vulnerability is expressed as the degree of potential loss (ranging from 0 to 1) with respect to a given intensity (Fell et al., 2008). The potential loss is calculated as product between vulnerability and exposure considering a certain level of intensity and it is estimated as a monetary value. These concepts are developed later in this document.

The final products are two. A database of elements at risk indicating, in addition to the type of structure and its exposure, the value of vulnerability and potential loss for an event of given intensity (as defined in Fig. 3). Color coded maps of vulnerability and potential loss for each case study in which the methodology has been applied.

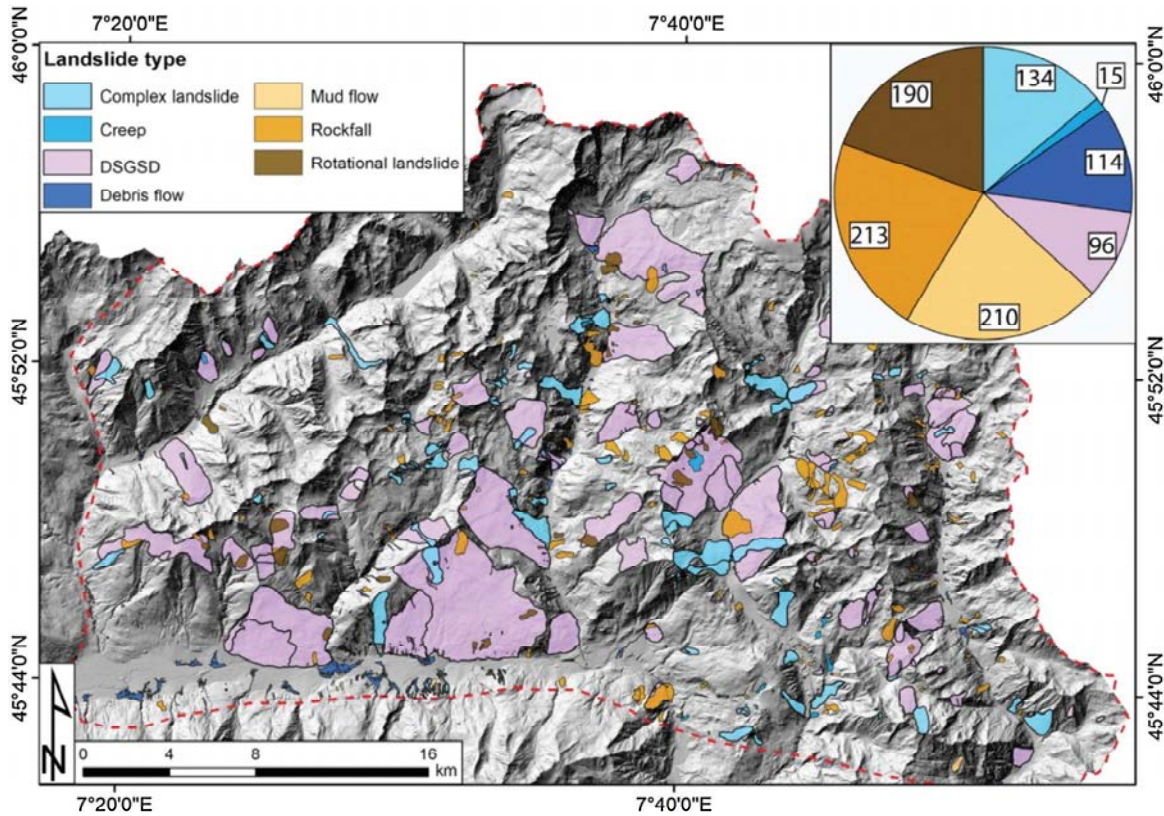


Fig. 2. Landslides distribution extracted from the IFFI catalogue of the Valle d'Aosta Region. The colors of the pie chart are referred to the map legend. The background image is a hillshade derived from a 10 × 10 m DEM.

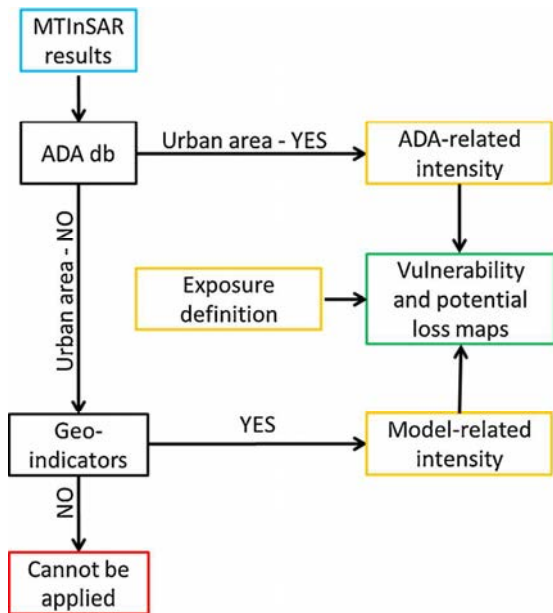


Fig. 3. Workflow of the methodology. MTInSAR, Multi-Temporal Interferometry; ADA, Active Deformation Areas; db, database.

In the following sections each phase of the workflow will be described, starting from the generation of the deformation map.

3.1. Deformation map generation

In this work, a total of 153 Sentinel-1 images were analyzed by means of a specifically developed MTInSAR approach. Sentinel-1 images are acquired in C-band (wavelength 5.55 cm) with a revisiting time of 6 days considering both satellites (1A and 1B) and a ground resolution of 14 by 4 m. The radar images cover the period January 2015 – August 2018 and have been acquired in descending orbit with VV polarization; the area of interest is covered by 2 bursts and 2 swaths. The incidence angle of the electromagnetic wave is on average equal to 38.7°. The low temporal baseline granted by Sentinel-1 allows reducing temporal decorrelation effects in the interferometric pairs and increasing the number of coherent pixels (Hanssen, 2001).

The MTInSAR strategy used here is subdivided into 3 phases aimed to generate the final deformation map: 1) generation of interferograms and coherence maps, 2) estimation of the annual linear velocity along the LOS (Line Of Sight) and 3) generation of deformation time series. We will now introduce the key steps of this interferometric chain and we refer to Devanthey et al. (2014) and Barra et al. (2017) for further technical details.

Interferograms are generated with a maximum temporal baseline of 600 days at full (20 × 4 m) resolution. The related coherence maps were derived using a 2 × 10 multi-looked resolution (40 × 40 m). The whole interferometric stack is composed of 4012 interferograms that will be selected for further analyses depending on their temporal baseline and coherence. This latter parameter is of great importance in a mountain region such as VdA where coherence is particularly affected by seasonal variations because of snow cover (Kumar and

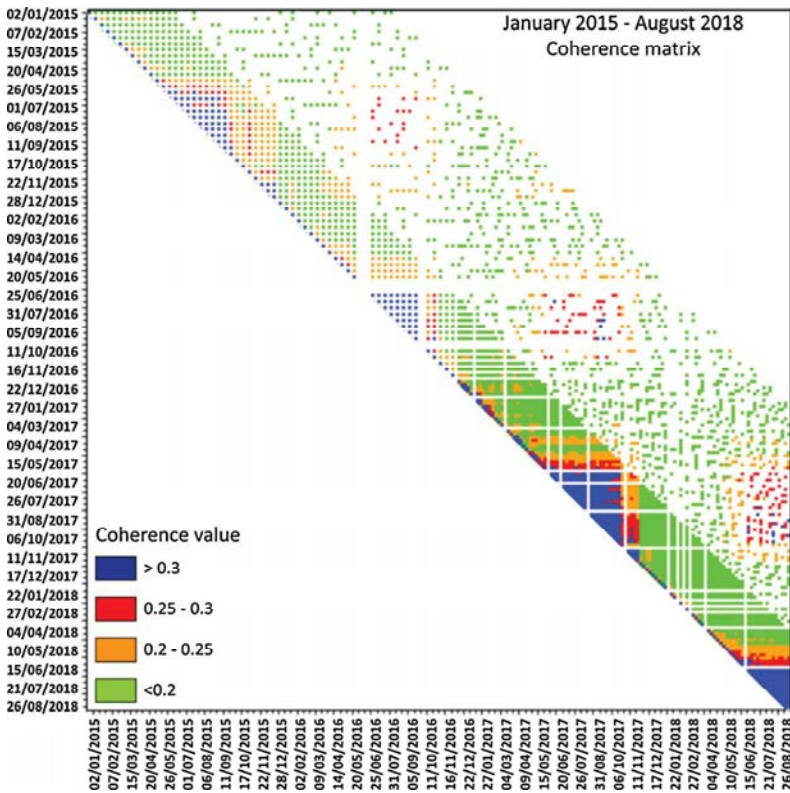


Fig. 4. Coherence matrix generated for the interferometric stack. The absence of an interferogram is due to the unavailability of one of the two required images or because the maximum temporal baseline (600 days) has been reached. The higher density of interferograms in the right lower corner is due to the increase of the revisiting time of Sentinel-1 constellation from 6 to 12 days.

Venkataraman, 2011). For this reason, a Coherence Matrix (CM) is adopted to study the temporal variation of coherence of the whole interferometric stack (Fig. 4). The CM is an asymmetric diagram showing the calculated mean coherence value over a selected area for each master-slave pair. The diagonal of the matrix represents the theoretical interferograms with temporal baseline equal to zero. By moving away from the diagonal, the temporal baseline increases with 6 days steps.

To remove the topographic contribution from the interferograms, we have used the 90 m resolution Shuttle Radar Topographic Mission (SRTM) Digital Elevation Model provided by NASA (National Aeronautics and Space Administration), and the precise orbits provided by the European Space Agency (ESA). The resolution of the DEM is enough to properly remove the topographical component from the interferogram network and calculate the residual topographic error.

The CM is useful to highlight that coherence is on average low (only few interferograms with values higher than 0.35) and characterized by a clear seasonal oscillation. From May to November interferograms are generally more coherent than interferograms generated with images acquired between December and April, when coherence is always below 0.25. This means that not only coherence of 6-days interferogram is higher in summer but also that in some cases a winter 6-days interferogram has lower coherence than a one-year interferogram between two summer seasons.

Thanks to the CM is possible to select the best combination of interferograms for extracting ground deformation data. For the velocity estimation, the network is composed of 432 interferograms with minimum temporal baseline of 150 days and minimum average coherence of 0.2. For the time series generation, the network is composed of 1325 interferograms with low temporal baselines (up to 6 days) and minimum average coherence of 0.2.

Several statistical criteria have been presented to discriminate between noisy and coherent pixels (for a literature review we refer to Crosetto et al., 2016). In this work, the first selection of pixels is based on the Dispersion of Amplitude (DA, Hanssen, 2001); the DA threshold

here used is equal to 0.4. The best-fitting linear model of velocity is estimated for these points. A second selection of pixels relies on the gamma threshold, which quantifies the residuals between the model and the observations, i.e. the level of fitting between the linear model and the observations (Biescas et al., 2007; Devan  thy et al., 2014). Since the deformation model is linear, a restrictive gamma threshold can cause the non-selection of the points with a non-linear movement. Here the gamma threshold is fixed to 0.37, which resulted to be the best trade-off between low noise level and spatial density of pixels for the whole study area.

Annual velocities are calculated following the approach proposed by Biescas et al. (2007) and Crosetto et al. (2011). Time series estimation is based on a two-step phase unwrapping process. In the first step each interferogram is spatially unwrapped using the Minimum Cost Flow method (Costantini et al., 1999). In the second step the consistency of the spatial unwrapping is evaluated in time and on a pixel-wise basis (Devan  thy et al., 2014). The non-linear component of deformation is estimated and included in the time series. To decrease the aliasing errors, it is important to have a spatial continuous sampling of PS and a low temporal baseline of interferograms. The redundancy of the observations is also crucial to detect and correct possible aliasing errors (a minimum of 5 interferogram for each image is required).

3.2. ADA database generation

The concept of ‘‘Active Deformation Area - ADA’’ has been developed by Barra et al. (2017) and adapted by Solari et al. (2018) for Civil Protection purposes. An ADA is composed by spatially aggregated moving points above a selected velocity threshold. The cluster is defined depending on parameters such as the minimum number of PS that an ADA must contain, or the clustering radius built around every moving PS. Each PS is characterized by a quality index which estimates the spatial and temporal correlation between all the time series of each PS composing an ADA. A high quality index means that time series are

well correlated, and thus a more reliable information about the phenomenon is detected. We refer to Barra et al. (2017) for an in-depth explanation of the ADA approach.

The procedure developed by Barra et al. (2017) has been automatized into a software, “ADA-finder” (Navarro et al., 2018; Tomás et al., 2019), which analyzes a large stack of PS points in just few seconds/minutes. The software is implemented in C++ and uses as input a ESRI shapefile of PS points with some mandatory fields such as geographic coordinates, velocity and displacement values. The user has to fix just a few input parameters before running the software:

- input/output files path;
- isolation distance, i.e. the minimum distance at which a point can be considered isolated from the others. Isolated points are not considered by the software and removed. This selection is implemented before the definition of the “moving points” to a priori exclude isolated PS. As demonstrated by the experience, these PS are probably not representative of a landslide but are more probably related to noise or single objects motion (Solari et al., 2018). We used a value of 100 m as isolation distance. The value is a good compromise between spatial resolution of the satellite and PS density;
- standard deviation factor (σ), i.e. the standard deviation value of the LOS deformation velocity of the PS population. The σ value represents a measure of the dispersion of the dataset and can be used to set the stability range of PS velocity. This value is used to define whether a PS is “moving” or not. Here we fixed a value equal to 2;
- clustering radius, i.e. the maximum distance at which a PS can be considered as part or not of a cluster. The clustering approach implemented in the software relies on a Depth First Search method (Horowitz and Sahni, 1976) to identify the connected components between PS points. The clustering radius is here equal to 28 m, i.e. two times the ground resolution of Sentinel-1. If the distance between two points is higher than the clustering radius, they will not be considered as part of the same cluster;
- minimum ADA size, i.e. the minimum number of PS points which an ADA must contain for being representative for a small landslide. Considering C-band satellites, the ideal number of PS points to detect a small landslide is five (Herrera et al., 2013).

The software’s output is an ADA database containing two shapefiles: one polygonal for the clusters and one punctual for the PS included in every cluster. The ADA generated in this way are the main input for all the subsequent evaluations regarding landslide vulnerability and potential loss.

3.3. Landslide intensity evaluation

Each ADA can be used for landslide intensity assessment in two different ways: one as direct estimation of landslide magnitude (and thus intensity) and as an indicator for the presence of unstable debris deposits that could be the source areas of future debris flows, whose runoff is foreseen by means of a basin scale model. The first approach is named as “ADA-related intensity”, the second one as “Model-related intensity” (Fig. 3). Intensity is needed to derive vulnerability of the elements at risk and the potential loss as it will be explained in section 3.4 and 3.5. The first intensity approach is aimed to investigate in a direct way those landslides showing the highest deformation rates in VdA (complex or rotational). The second intensity approach is implemented to indirectly (using the ADA as source areas) derive information about potential debris flows.

3.3.1. ADA-related intensity

This approach has been inspired by the landslide activity matrix proposed by Cigna et al. (2013), in which intensity is a direct expression of landslide velocity (derived from LOS deformation rates of the interferometric products). Here, we do not use a “representative velocity”

(Cigna et al., 2013) for each landslide but we rely on the ADA as indexes of slope movements. This approach has been already followed by Solari et al. (2018) for geohazards mapping in Canary Islands (Spain). Landslide intensity is defined by the average LOS velocity of the ADA, following the classification:

- intensity 1, average velocity lower than 16 mm/yr;
- intensity 2, average velocity ranging between 16 and 32 mm/yr;
- intensity 3, average velocity higher than 32 mm/yr.

The first threshold (16 mm/yr) is representative for the passage between extremely slow and very slow landslides, as assumed by Cruden and Varnes (1996). We derived the second one (32 mm/yr) by doubling up the first value.

The ADA-related method does not consider volume for determining landslide intensity. Although volume is an important component of intensity, its estimation over wide areas requires the definition of magnitude–frequency distributions based on long-term inventories and spatially distributed power law exponents (Catani et al., 2016). Considering these requirements, we think that velocity is enough to describe landslide intensity at the regional scale using a reproducible method and few ancillary inputs.

3.3.2. Model-related intensity

In the area of interest, the use of the ADA-related approach is limited. In fact, the urban density is quite low and just a part of the ADA respect the input condition (“Urban area – YES”, Fig. 3). For this reason, a second approach (Model-related intensity) has been defined to maximize the information extracted from the satellite data.

If one ADA does not directly intersect elements at risk, further evaluations are made. In this case the presence or not of debris (following the concept previously introduced) discriminates between the possibility or not to apply this approach (“Geo-indicators – YES” condition in Fig. 3). It is based on the use of ADA as indicators of active mass wasting processes, especially involving unstable debris deposits of different origin that could be source areas for catastrophic debris flows. These types of events, usually triggered by extreme rainfalls, are the most damaging, in terms of economic and life loss, for the Valle d’Aosta Region (Ratto et al., 2003). If an ADA coincides with a debris-covered area, defined on the basis of geological and orthophoto information, a run-out model will be used to evaluate the possible landslide evolution, in terms of landslide path and spatial distribution of the accumulation zone. In this work, the Gravitational Process Path model (GPP, Wichmann et al., 2017) has been chosen to define the potential run-out of moving debris along slopes.

The GPP model is specifically designed to simulate the path and run-out area of gravitational processes, such as debris flows, avalanches and rockfalls, or snow avalanches. The model is suited for regional or basin scale analysis requiring only few and simple terrain parameters for the source area and a DEM of the slope. In brief, the GPP model simulates the motion of a mass point from a source to the deposition area through the use of different release, process path, run-out and deposition models. The modelling approaches are not entirely physically based but follow empirical principles simulating the main features of a mass moving along a slope (Wichmann et al., 2017). The simplest model configuration requires only a DEM and a contour of the potential source area to run; thus, it is the best operational solution for basin/regional scale investigations, where detailed geotechnical and hydrogeological parameters, inputs for physically based numerical simulations, cannot be gathered. The GPP model is implemented into the open source GIS SAGA (System for Automated Geoscientific Analyses, Conrad et al., 2015).

In this work, we used a 2 m DEM as input for the model. The source areas have been defined within each ADA and selected considering the distribution of moving points and the local morphology. If the material height (thickness) for each starting cell of the source area is given as

input data, the GPP model allows modelling both sink filling along path and deposition. In order to obtain the soil/debris thickness, we used the results derived within the area of interest by Salvatici et al. (2018) using the Geomorphologically Indexed Soil Thickness model (Catani et al., 2010).

The random walk model defines the process path of a single particle from the initiation area to the deposition area following multiple flow directions (Wichmann, 2017). Three model parameters must be set: 1) a terrain slope threshold defining when the flow diverges (equal to 40° in our case); 2) an exponent for divergent flow which controls how much the flows diverges (a high value determine a higher lateral spread, we set this parameter to 1.5) and 3) a persistence factor that expresses how much a flow direction is preserved accounting for the inertia of the flow (Takahashi et al., 1992). We set this parameter to 1.5. We used the two-parameter friction model developed by Perla et al. (1980) to simulate the run-out length of the starting particles. This model, originally developed for snow avalanches, has been later adapted for debris flows (Wichmann et al., 2009). It is a center-of-mass model in which two parameters which govern the motion of the particle must be defined: the sliding friction coefficient (μ) and the mass-to-drag ratio. The sliding friction coefficient decreases as the catchment area increases and it is calculated from the following empirical law (Gamma, 2000): $\mu = 0.19 * a^{-0.24}$, where a is the catchment area. The mass-to-drag ratio depends on the size distribution of the material. For debris flows made by granular materials and blocks is on average equal to 70, value adopted in this work (Zimmermann et al., 1997). Finally, for modelling the material deposition we exploited a slope and on stop approach (the mass starts to be deposited when a slope threshold is reached – Wichmann et al., 2017) in which the deposition of material starts when the slope falls below 15°. Considering the material availability (depending on the soil thickness layer), the model distributes the height of material for each iteration; if a sink is encountered, it is progressively filled at every new iteration. All values reported are referred to the two case studies that will be presented in the section 4.3.

In summary, once the ADA that fulfill the “Geo-indicators” condition are selected, they are firstly grouped for geomorphological macro-areas (at flank scale). Then, the GPP model is run to reconstruct the spatial development of a known debris flow in each macro-area to obtain the input parameters to be used for the new models (based on the ADA distribution). If this is not possible, one of the ADA in each macro-area has to be selected as test site for the GPP model. The derived input parameters are then transferred to other ADA-sources.

The outputs of the model are four: 1) process area, defining the transition frequencies at every cell; 2) deposition, equal to the height of the material deposited at each cell; 3) maximum velocity reached by the flow at every cell and 4) stopping position, i.e. all the cells where the run-out length is reached. In this work, we used the deposited height of material at every cell as a proxy for landslide intensity. The three intensity classes are:

- intensity 1, height of the material lower than 1.25 m;
- intensity 2, height of the material between 1.26 and 2 m;
- intensity 3, height of the material higher than 2.01 m.

The values chosen are defined following the vulnerability functions derived by Papathoma-Köhle et al. (2012) using real debris flow events in South Tyrol (Austria) and represent a degree of loss of 30 %, 60 % and higher than 60 %, respectively.

3.4. Vulnerability and exposure definition

A value of vulnerability and exposure is assigned to every building or road, depending on their typology and using a simple classification approach illustrated in Table 1. The building/road database derives from the 1:2000 cadastral map of the VdA region, from which the polygons/lines have been extracted.

Table 1

Vulnerability and exposure values for the area of interest. V, vulnerability; I, intensity; E, exposure. Range values of E refers to the average between minimum and maximum values among the 33 municipalities. Single value are valid for all the 35 municipalities.

Type of building/road	V (I = 1)	V (I = 2)	V (I = 3)	E (€/sqm)
Barn	0.2	0.4	0.6	80
Camping	0.4	0.6	0.8	2600
Greenhouse	0.2	0.4	0.6	50
Hotel	0.15	0.3	0.5	1550 – 4600
Industrial laboratory	0.1	0.2	0.5	740 – 1000
Local road	0.6	0.8	1	50
Motorway	0.4	0.6	0.8	350
Municipal road	0.6	0.8	1	150
Office/service sector	0.1	0.3	0.6	1175 – 2600
Private house	0.2	0.35	0.6	1075 – 4350
Provincial road	0.6	0.8	1	180
School complex	0.3	0.5	0.7	4000
Shed	0.2	0.4	0.6	540-890
Commercial building (shop, restaurant, etc...)	0.2	0.35	0.6	865 – 2100
Shopping mall	0.2	0.35	0.6	1400 – 2200
Sport facilities	0.3	0.5	0.7	15-120
Stable	0.15	0.4	0.6	120
Regional/State road	0.4	0.6	0.8	250
Warehouse	0.2	0.4	0.6	680 - 1000

One of the first frameworks for landslide hazard and risk mapping over wide areas was developed by Catani et al. (2005) for the Arno River basin. Considering our working scale on large area, we followed a similar method in which vulnerability varies between 0 (no damage) and 1 (complete loss) as a function of landslide intensity. Three vulnerability classes are used, corresponding to three damage levels: aesthetic, functional and structural. This subdivision has been firstly proposed by Cardinali et al. (2002) and it is classically used for qualitative vulnerability evaluation (Sterlacchini et al., 2014). Each value of vulnerability is defined by the typology of element at risk following a data driven approach and considering the possible interactions between elements and landslide. Linear elements have the highest vulnerability values for each intensity class. If intensity is equal to zero, then vulnerability is null.

Exposure is referred to the economic value of an object and is estimated separately in different ways for each building class. We decided to implement different sources of information (market and income value, construction cost, renovation cost) to provide a plausible value for every structure. This is the maximum level of detail we could reach when working at basin scale; further information regarding people occupancy and day/night activity cannot be collected at this scale in a reasonable time. Our approach well fits in the one proposed by Pellicani et al. (2014) for wide areas with small data availability. These authors derived for each municipality of an Apennine portion of Apulia region (southern Italy), the maximum, minimum and average economic values of 25 types of assets, including industries and agricultural terrains. For each municipality the maximum value is given by the market value (OMI database) and the minimum by the construction cost in euros/sqm or the agricultural unit in euros/hectare. More detailed approaches can be proposed when damage data connected to a single event are available. For example, Vranken et al. (2013) estimated both direct and indirect damage due to landslides in the Flanders (Belgium) using the repair and prevention costs for infrastructures and private houses. On one side, this approach allows having a more realistic value of exposure for each object. On the other side, it requires single events information which are not simple to collect over wide areas but are more connected to the activities of single municipalities.

VdA is a region mainly devoted to tourism and just few large industries are present. Considering this, an effort was made to properly define the value of private houses, potentially being rented by tourists, and, in general, of building related to the tertiary sector. In this work,

we did not consider the exposure of cultural heritages, due to the difficulties in defining a common range of values for all the different structures.

Exposure for private houses is determined by the market value, as defined in the OMI (Osservatorio del Mercato Immobiliare – Real estate market observatory) database. Every Italian municipality is subdivided by the Agency of Revenue into subzones with different market values depending on the location (city center, industrial area and so on) and on the building state. The database is open and available online (OMI database, 2018). This is a certified source of information coming directly from the Italian central government and it is based on real estate market information collected every year. This database has been already used by other researchers and it can be considered a reliable dataset for scientific usage. Peduto et al. (2018) exploited the OMI database as “most likely market value” for a quantitative analysis of masonry buildings response to landslide in a small town of Calabria (Southern Italy). This solution refers to the work of Lari et al. (2012) who calculated the minimum and maximum market value for each census parcel of the city of Brescia (northern Italy) to derive exposure to floods, earthquakes and industrial accidents. Considering these examples and our working scale, we believe that the use of OMI-derived market value is the right choice for those building categories contained into the OMI catalogue (private houses, commercial buildings, offices, sheds). It is in fact the most detailed information we can gather at regional scale without the need of on field information sometimes impossible to obtain in short times and with low human efforts. This is in accordance with Sterlacchini et al. (2014) who reported that OMI-derived market value is suited for medium scale estimations (1:25000-1:50,000), with the main advantage of well distinguishing between areas of higher economic importance and economically marginal areas.

The area of interest of our work is composed of 33 municipalities; for each one on them the average market price for private houses is taken as reference (depending on the OMI zonation) and used to estimate exposure. The OMI database contains also information regarding the quotation of buildings used as offices (or as service sector in general), of commercial buildings (including shopping malls) and of industrial laboratories (including warehouses and sheds). For each of these categories the average market value is used again as reference. All the real estate market values extracted from the OMI database are reported in Table 1.

The exposure value of all the other buildings and roads categories is calculated on the basis of the construction/renovation cost for square meter. These values are tabulated by engineers or architects' associations in Valle d'Aosta or in other similar environments. Hotels are an example of this (Table 1). Their exposure range express the different construction costs of structures of different categories, with the highest values for luxury hotels. The construction cost is a good trade-off solution to be used when the market value cannot be used. This approach has been used by Peduto et al. (2018) by multiplying the construction cost for the footprint area, the number of the floors, and the height of each store of the building. Since our reference scale is different, we assumed exposure equal to the construction cost multiplied by 10 without adopting single buildings characteristic. It is recalled that the values of vulnerability of Table 1 are common for both the ADA-related and Model-related approaches; only landslide intensity is derived in two different ways.

Following the definition of Puissant et al. (2014), our methodology is aimed to derive a “macro-scale analysis” in which the final goal is “strategic regional planning” based on expert knowledge. For Puissant et al. (2014) the goals of such analysis are: 1) make an inventory of elements at risk, 2) rank their value for categories of structures and 3) select those elements at risk that could be impacted by a landslide. Only the potentially impacted elements are going to be considered at the macro-scale. We believe that our approach perfectly fits in the concept proposed Puissant et al. (2014) since, 1) we have a cadastral inventory, 2) we assign a market value or a construction cost to every building and

3) we use ADA as proxy for landslide impact.

3.5. Potential loss estimation

Once exposure and vulnerability (depending on the intensity level) are evaluated, the potential loss is calculated as product between vulnerability and exposure (Catani et al., 2005). The potential loss is referred to the direct impact of a landslide on a building or road and it is expressed in quantitative terms (Euros for square meters). If one or both vulnerability and exposure are null, the potential loss is obviously zero.

4. Results

The results of the previously illustrated methodology are presented here, through the selection of some case studies that highlight how vulnerability and potential loss are derived, using the two intensity approaches.

4.1. Deformation map

Despite the challenging environment, the MTInSAR processing of Sentinel-1 images gave good results in terms of spatial coverage of PS points and quality of measurements. A total of 364,451 PS points was obtained, with an average point density of 332 PS for square kilometer (Fig. 5).

The point distribution is strongly affected by land cover (i.e. presence of vegetation and perennial snow) and local morphology. The maximum density is registered along the Dora Baltea Valley (see Fig. 1 for the localization) where Aosta, the major city of VdA, is located and where the urbanization is higher. Along the tributary valleys the density will be again higher in correspondence of small cities and hamlets and where the mountain flanks orientation, slope and land cover allow a proper PS identification. On the other hand, PS density will be minimum, tending to zero, where the local morphological conditions create strong foreshortening, layover (i.e. along east-facing slopes, given the descending acquisition geometry) shadowing effects (i.e. along steep west-facing slopes) and where woods and perennial ice covers are present.

Within the PS velocity, the stability threshold criteria were based on the statistical analysis of the PS data population characterized by an approximately normal (Gaussian) distribution. The stability threshold was fixed at ± 5 mm/year, which is equal to the standard deviation value of the dataset, representing the dispersion of data around zero (Bianchini et al., 2013). Considering the stability threshold of 5 mm/yr, the 93 % of the PS points is considered “stable”, meaning that the point is motionless or that the motion cannot be distinguished from the noise. Some moving areas, made by tens of PS points, are already visible at this scale; these areas are connected to the slow motion (usually below 10 mm/yr) of large deep-seated landslides that affect some portion of the area of interest (Solari et al., 2019).

4.2. ADA database

The ADA database was generated in an automated way, following the previously presented methodology. We obtained a total of 54 ADA composed by a minimum of 5 PS points with LOS velocities higher than 10 mm/yr (i.e. two times the standard deviation of the interferometric dataset). The largest part of the ADA registers average velocities between 10 and 20 mm/yr (76 % of the total); only few ADA exceed 30 mm/yr (Fig. 6). The ADA are well distributed in the area of interest, preferably along west-facing slopes at different altitudes. The distribution is affected by the satellite LOS in descending orbit with respect to slope aspect and angle; some east-facing flanks are simply impossible to measure because of geometrical effects. No moving areas are found along valley bottoms, meaning the absence of subsidence motions with high deformation rates.

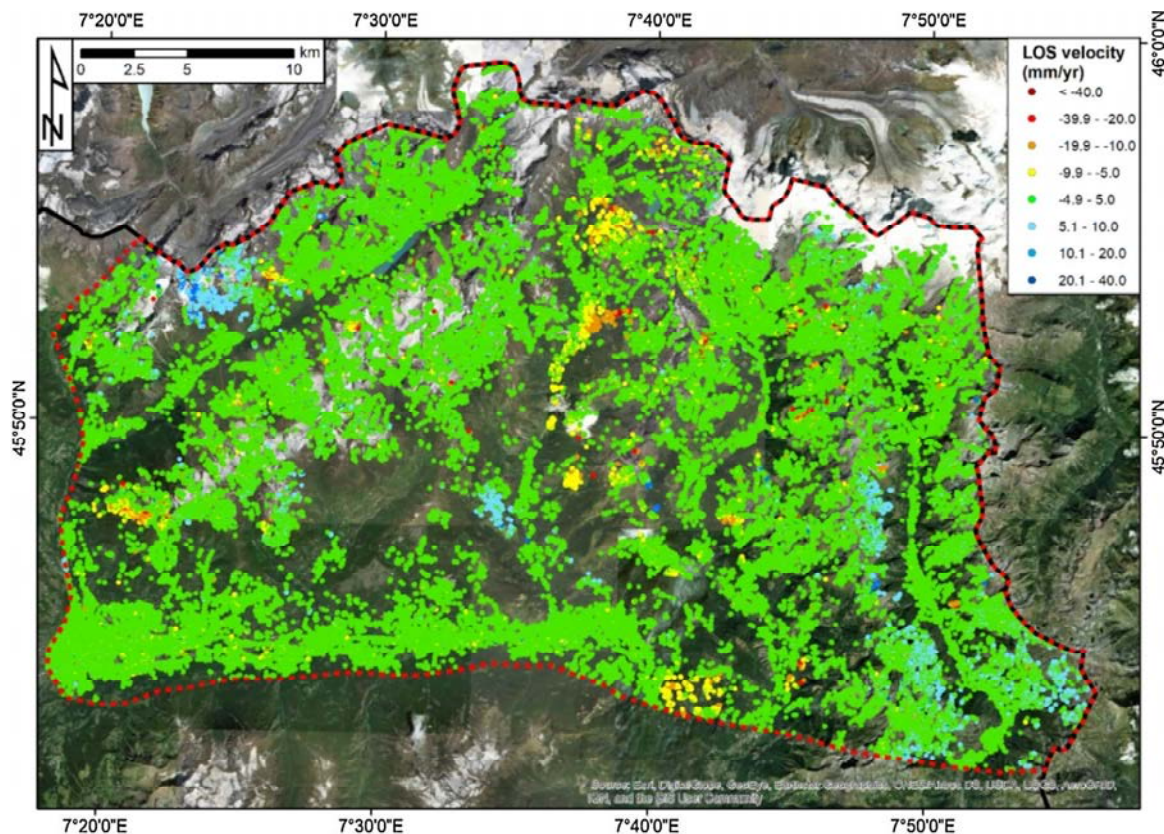


Fig. 5. Deformation map for the area of interest (red contour) obtained from Sentinel-1 radar images acquired in descending orbit. The background image is an ESRI World Imagery map (For interpretation of the references to colour in this figure legend, the reader is referred to the web version of this article.).

Considering the input conditions presented in Section 3.3, 15 ADA have been used to determine intensity using the ADA-related approach. Most of the ADA have been used as source areas for debris flow modelling, evaluating intensity on the basis of the Model-related approach. Nine ADA were not used for any intensity evaluation, as they do not fulfil the input conditions of our approach, and they were not exploited for vulnerability and potential loss evaluation.

4.3. Some examples of vulnerability and potential loss estimation

The first three examples came from the Valtournenche and Ayas Valleys, located in the eastern portion of the area of interest. Considering the direct overlapping between ADA and elements at risk, landslide intensity has been estimated using the ADA-related approach. The derived potential loss maps are shown in Fig. 7.

Inset 1 of Fig. 7 refers to the Cielo Alto hamlet in the southern portion of Breuil-Cervinia one of the main and most famous ski resorts in VdA. Three ADA are found in this area, affecting some elements at risk and fulfilling the input condition of the ADA-related approach. From a geomorphological point of view, the ADA are found along a west-facing slope between 2050 and 2150 m a.s.l. The area is characterized by the presence of a large DSGSD (“Cime Bianche” DSGSD) that affects the whole valley flank from an altitude of 2900 m a.s.l. to the valley bottom. The DSGSD occupies an area of 8 km². Its evolution is mainly related to deglaciation processes and subordinated fluvial activity; the presence of weak levels of pseudocarnioles and evaporites (Mont Fort Unit – Sartori, 1987), acting as basal shear plane, is the main controlling factor of the landslide (Martinotti et al., 2011). The motion of the Cime Bianche DSGSD is known, especially in its lower and marginal portion, as testified by the presence of tilted walls and damaged buildings (Martinotti et al., 2011). The ADA are found within

the toe area of the Cime Bianche DSGSD, where Giordan et al. (2017) already reported the highest displacement rates by analyzing RADARSAT-1 interferometric data. See Fig. S1 for the localization of the ADA with respect to the DSGSD contour.

The ADA intensity is equal to 1, since all ADA average velocities are lower than 16 mm/yr. The velocity sign is negative and coherent with a motion along slope, away from the satellite LOS. The elements at risk in this area are mainly residential buildings, composed by 3–5 floors residences. A shopping mall and a restaurant are present as well. For landslide intensity equal to 1, vulnerability ranges between 0.15 and 0.3 for buildings and equal to 0.6 for roads (Fig. S4—inset 1). Considering a value of exposure for private houses equal to 2450 €/m², the potential loss is equal to 490 €/m² (Fig. 8—inset 1). The highest potential loss (532 €/m²) is registered by a four-stars hotel; the lowest (21 €/m²) by a tennis court.

Inset 2 of Fig. 8 presents the results obtained in Chaloz, one of the main villages of the Valtournenche municipality, 9 km south than Cielo Alto. The moving areas are detected along a west-facing slope in which several landslides are mapped (Fig. S2). In particular, a large DSGSD (“Valtournenche” DSGSD) involves the entire flank on which the Chaloz hamlet is located, from a height of 2900 m a.s.l. to 1500 m a.s.l. The activity of the Valtournenche DSGSD has been already testified by Giordan et al. (2017). These authors showed that the landslide can be subdivided into different sectors with different velocities, as testified by the ADA distribution obtained from Sentinel-1 data (Fig. S2). In addition to the DSGSD, 7 rotational landslides are mapped in the toe area of the deep-seated phenomenon (Fig. S2).

Four ADA are found within the Chaloz hamlet with average LOS velocities between 11 and 16 mm/year; intensity is then equal to 1 for all the ADA. Several buildings of the Chaloz hamlet are exposed to landslide risk; in particular, 390 structures are found within the contour

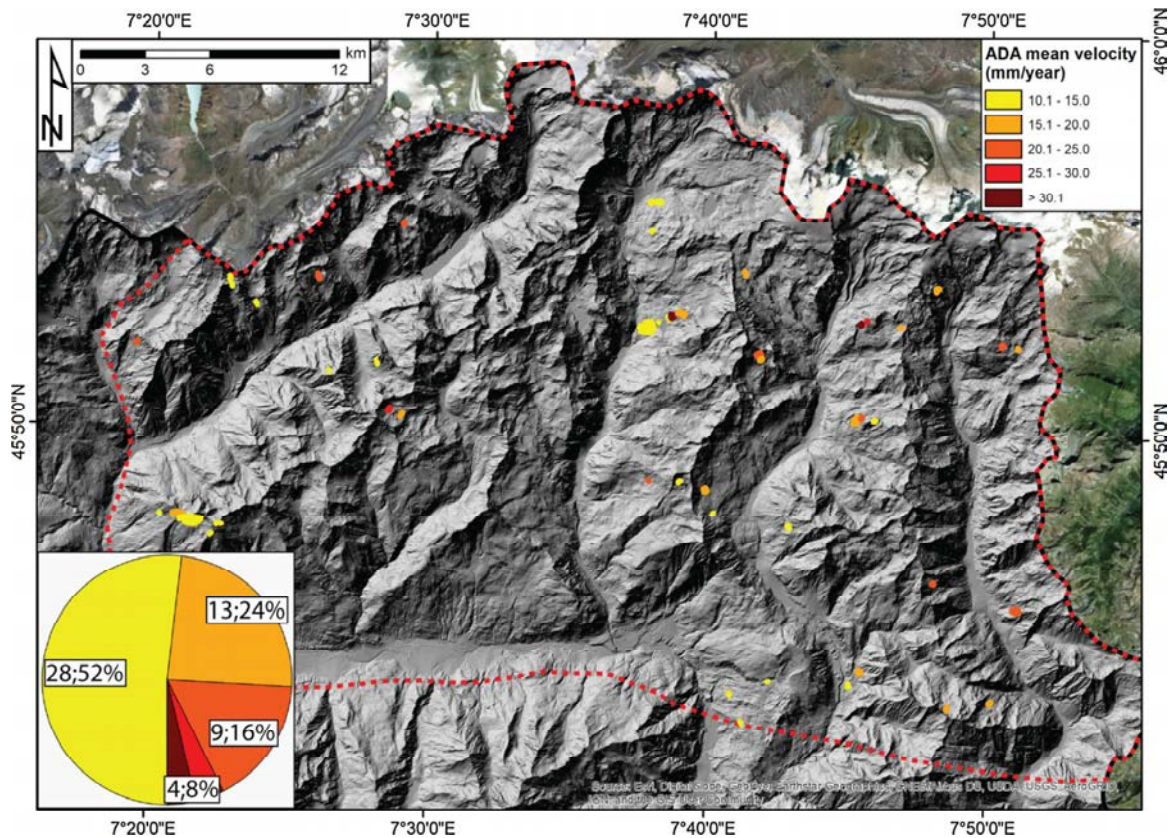


Fig. 6. ADA map for the area of interest. Each ADA is classified on the mean velocity value, obtained by averaging the velocities of all the PS points that form the moving area. The ADA map is overlaid on a 10 m DEM-derived hillshade. The background image is an ESRI World Imagery map.

of the ADA. Of these, 90 % are private houses; some shops, warehouses, four hotels, barns and a tennis court are present as well. Some local roads and a provincial road cut through the area of interest. Considering the type of edifice/road and the intensity level, vulnerability varies between 0.1 and 0.2 for buildings and between 0.4 and 0.6 for roads (local roads are more vulnerable than provincial roads, Fig. S4—inset 2). The potential loss ranges between 21 and 490 €/m²; the highest value is reached by private houses (Fig. 7 — inset 2).

Inset 3 of Fig. 7 illustrates another example of ADA used for landslide intensity. The ADA is found in the Alèsaz hamlet, part of the Challand Saint Anselme municipality in the southern portion of the Ayas Valley (Fig. 1). In this area, an ADA with intensity equal to 1 is found, affecting 100 elements at risk, mainly composed by private houses, but also including some barns and a school. A local road crosses the moving area. The village of Alèsaz rises on the lowermost portion of a complex landslide (1.8 km long and 600 m large) whose crown area is located 600 m above the village, at an altitude of 1770 m a.s.l. (Fig. S3). The activity of this landslide is demonstrated by the presence of two ADA, one affecting the village of Alèsaz and one the uppermost portion of the landslide, where elements at risk are not found (Fig. S3). Considering the landslide intensity (equal to 1) and the type of elements at risk, vulnerability ranges between 0.2 and 0.3 (Fig. S4—inset 3) whereas the potential loss varies between 16 and 1200 €/m². In the Valtournenche municipality the market value of private houses is lower than in the Challand Saint Anselme municipality; considering the same value of intensity and vulnerability, the potential loss will be lower in this second case, despite the same building typology. The highest value of potential loss is reached by the school located in the southern portion of the ADA affecting the village of Alèsaz (Fig. 8 —inset 3).

Figs. 8 and 9 present two examples of potential loss maps derived using the Model-related intensity approach. Both case studies are taken

from the Montjovet municipality in the Lower VdA, on the left flank of the Dora Baltea Valley. The ADA of interest are located along the same slope, 1.5 km apart from each other. The input parameters of the model can be found in Section 3.3 and have been used for both case studies, assuming the same geological context in a similar morphological environment.

The first example shows an ADA located few hundred meters above the village of Ciseran. The whole valley flank is affected by a large DSGSD (“Emarese” DSGSD) whose crown is located at 1800 m.a.s.l., 1000 m above the moving area (Fig. S5). The slow motion of this landslide has been already measured using ERS 1/2 interferometric data (Broccolato and Paganone, 2012). No other landslides are found in this area (Fig. S5). The moving area does not directly intersect any element at risk, but, considering the presence of debris material, the GPP model is applicable to determine landslide intensity. Two source areas (S1 and S2 in Fig. 8) are extracted from the ADA and selected to run the model. The ADA is found on the upper portion of the watershed; therefore, the flows directions are divergent. From S1 the debris follows the slope morphology along the WNW direction, depositing the maximum height of material (2.5 m) at an altitude of 650 m a.s.l. The second debris flow, originated in S2, follows a WSW direction, filling a small depression located at an altitude of 770 m a.s.l. and depositing the remaining available material between 625 and 660 m a.s.l. (Fig. 8). The material deposited by the flow originated from S1 does not interact with any element at risk, whereas the flow having S2 as source area hits a house located 150 m below. The height of the material in correspondence of the building is below 1.25 m (intensity 1). The vulnerability value is 0.2 and, estimating an exposure of 1300 €/m², the potential damage is equal to 260 €/m².

The second example of Model-related intensity is presented in Fig. 9. Tron hamlet is located within the contours of one DSSGD and

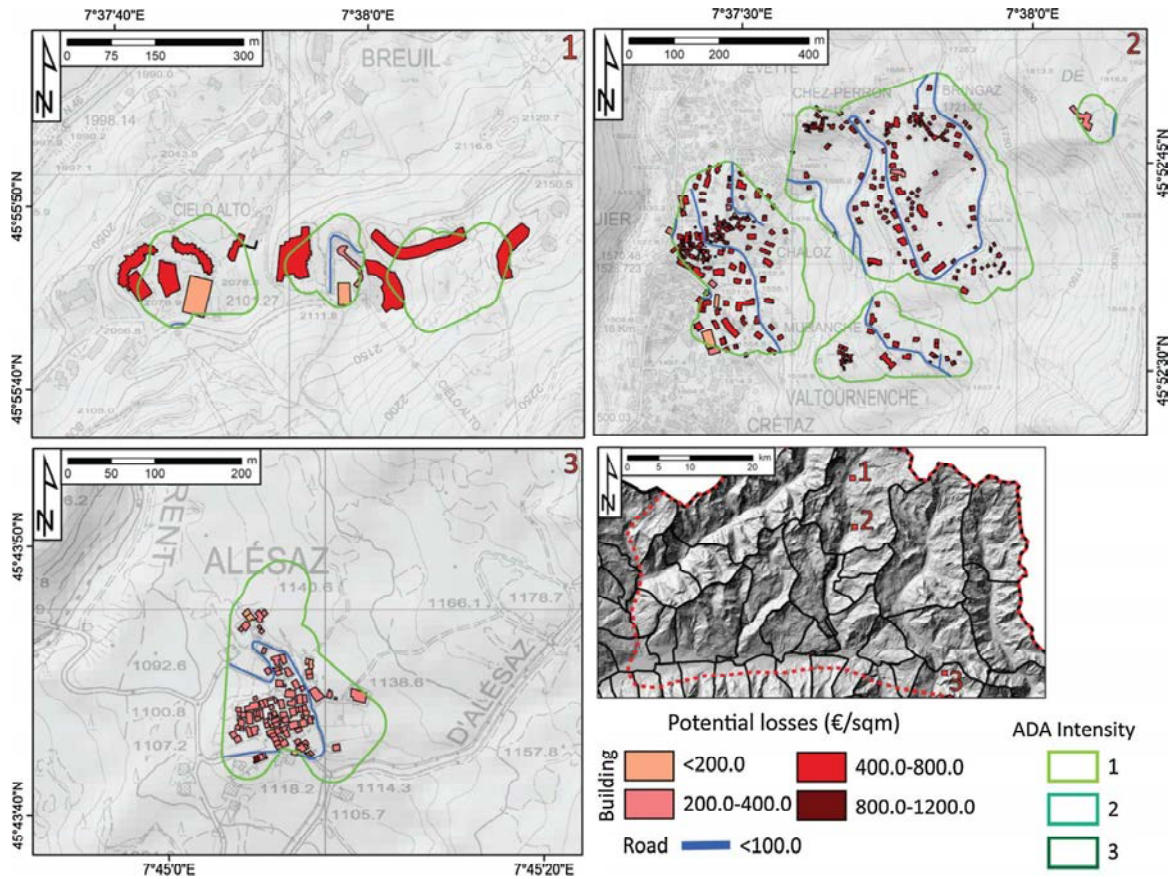


Fig. 7. Potential loss maps derived using the ADA-related intensity approach. The examples 1 and 2 are taken from the Valtournenche Valley, municipality of Valtournenche; the example 3 is taken from the municipality of Challand-Saint Anselme, at the Ayas Valley mouth. The maps are overlaid on a 1:10,000 cadastral map of the VdA region.

two complex landslides connected to the geometry and evolution of the Emarese DSGSD (Fig. S6). The ADA is located in the upper portion of these landslides, where debris deposits are found. The motion of this sector has been also reported by Broccolato and Paganone (2012) for ERS 1/2 data. The GPP model is exploited to simulate the run-out of debris flows from two different source areas (S1 and S2 in Fig. 9). The thickness of the material for S1 is between 2 and 2.4 m, whereas for S2 the input material thickness is lower, varying between 0.6 and 1 m. The flows originated from the two source areas converge and create a fan-like deposit with variable thickness between 0.2 and 1.6 m (intensity 1). The flow does not involve any building but two local roads. Considering an exposure of 50 €/m² and a vulnerability of 0.6, the resulting potential damage is 30 €/m².

5. Discussions

In this work, we exploited the demonstrated potential of satellite interferometric data for geohazard mapping (focusing on landslides) in a new way, by developing a procedure aimed to estimate vulnerability and potential loss of structures and infrastructures at regional scale. Here, interferometric results, intended as ADA or in general moving “hot-spots”, are the key input for landslide intensity and vulnerability estimation which, combined with the exposure of the elements at risk, allow to calculate the potential loss of a structure. The concept of “PS hot-spot” is not new in literature (see for example Bianchini et al., 2012), but the use of moving areas for quantitative or qualitative estimation of landslide impact on built-up areas is uncommon. Some examples of vulnerability estimation from interferometric data are

present in literature. Solari et al., 2018, used a qualitative classification of elements at risk depending on MTInSAR ground velocity maps and on the strategic use of buildings in different civil protection phases. Peduto et al. (2017), took advantage of PS data for fragility and vulnerability curves generation. Usually, interferometric products are a support for landslide activity evaluation (i.e. Rosi et al., 2018), for landslide intensity measures (i.e. Cigna et al., 2013) or landslide mapping (i.e. Strozzi et al., 2005; Barra et al., 2016; Cignetti et al., 2016; Dini et al., 2019). Recently, Intrieri et al. (2018) and Raspini et al. (2018) showed innovative usages for PS data as near-real-time tools for landslide forecasting. It must be recalled that interferometric data are rarely used for quantitative risk estimation (Lu et al., 2014). Thus, our methodology represents one of the few attempts of this kind. This work aims to bridge the gap that exists between retrieving the interferometric information on landslide phenomena, which is a nowadays a well-established field, and feeding these data into hazard and risk assessments procedure.

The methodology relies on MTInSAR data in three different ways: 1) as proxy for ground movement hot-spots (i.e. the ADA), 2) as landslide intensity tool (“ADA-related” approach) and 3) as an effort to detect potential source areas of debris flow (“Model-related” approach). The latter represents an original approach for interferometric data exploitation and has been specifically designed to be implemented in mountainous regions at basin scale or smaller. In the Model-related approach the interferometric data are both a proxy for moving debris deposits and an input for the GPP model, acting as the main factor for the source areas definition. In this way, it is possible to improve the information extracted from each ADA by assuming that a debris

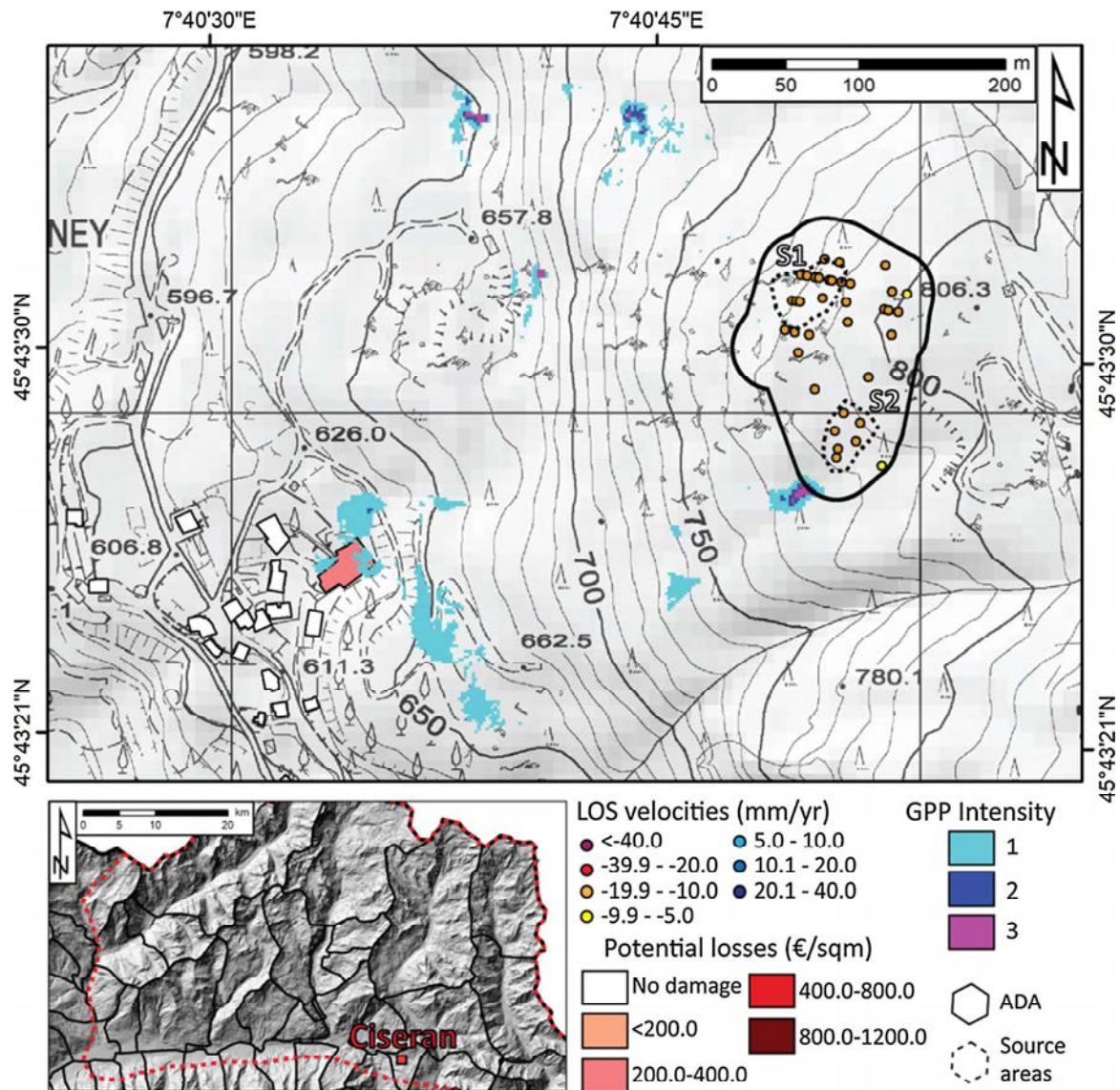


Fig. 8. Landslide potential loss derived using the Model-related intensity approach for the village of Ciseran in the Montjovet municipality. S1 and S2 are referred to the two source areas chosen to run the GPP model. The background image is a 1:10,000 cadastral map of the VdA region.

deposit, already in motion (as testified by the PS data), could evolve into a debris flow if external triggering factors are present (i.e. an intense rainfall period). The distinction between superficial motions and DSGSD long-term movement is one of the potential mismatches of the methodology. We solved this by considering a velocity threshold higher than the maximum average annual velocity value of DSGSD along the Alpine Arc (1 cm/yr - Crosta et al., 2013). Secondly, DSGSD classically show a peculiar flank-scale pattern in which outlier velocities can be easily detected by the ADA. We consider these areas as representative for superficial motions and we select, depending on the presence of geo-indicators, the targets for the GPP model. The focus of our work is in a direct way those landslides showing the highest deformation rates in VdA (complex or rotational) or indirectly the source areas of potential debris flows. We point out that the approach is not aimed to obtain landslide contours, but it can be integrated into existing landslide catalogues (such as IFFI) for estimating the state of activity of these phenomena.

Our methodology is designed for regional scale studies with few ancillary data available. It relies on small scale interferometric

products, based on strict thresholding rules for better limiting atmospheric artifacts and noise in general, and on a basin/flank-scale run-out model. The latter requiring only, in its simplest configuration, a DEM of the slope and a potential source area. Thus, it has not been designed for single landslide characterization. We believe that, although more detailed geomorphological investigations would be required (including an in situ campaign), our approach can offer useful results for future detailed scale analysis. In medical terms, we can define the methodology as a preliminary screening defining where is the pain without fully addressing the symptoms.

The output of the methodology are simple color-scale maps showing the intensity of the potential landslide (as ADA velocity or as height of material deposited by a debris flow) and a value of potential loss (in €/m²), expression of vulnerability (depending on landslide intensity) and exposure (defined as real estate market values) of the elements at risk. The potential loss is not directly related to the real repair cost which is impossible to quantitatively estimate at regional scale, without having access to more detailed building characteristics and renovation costs. The potential end-users, such as Civil Protection entities,

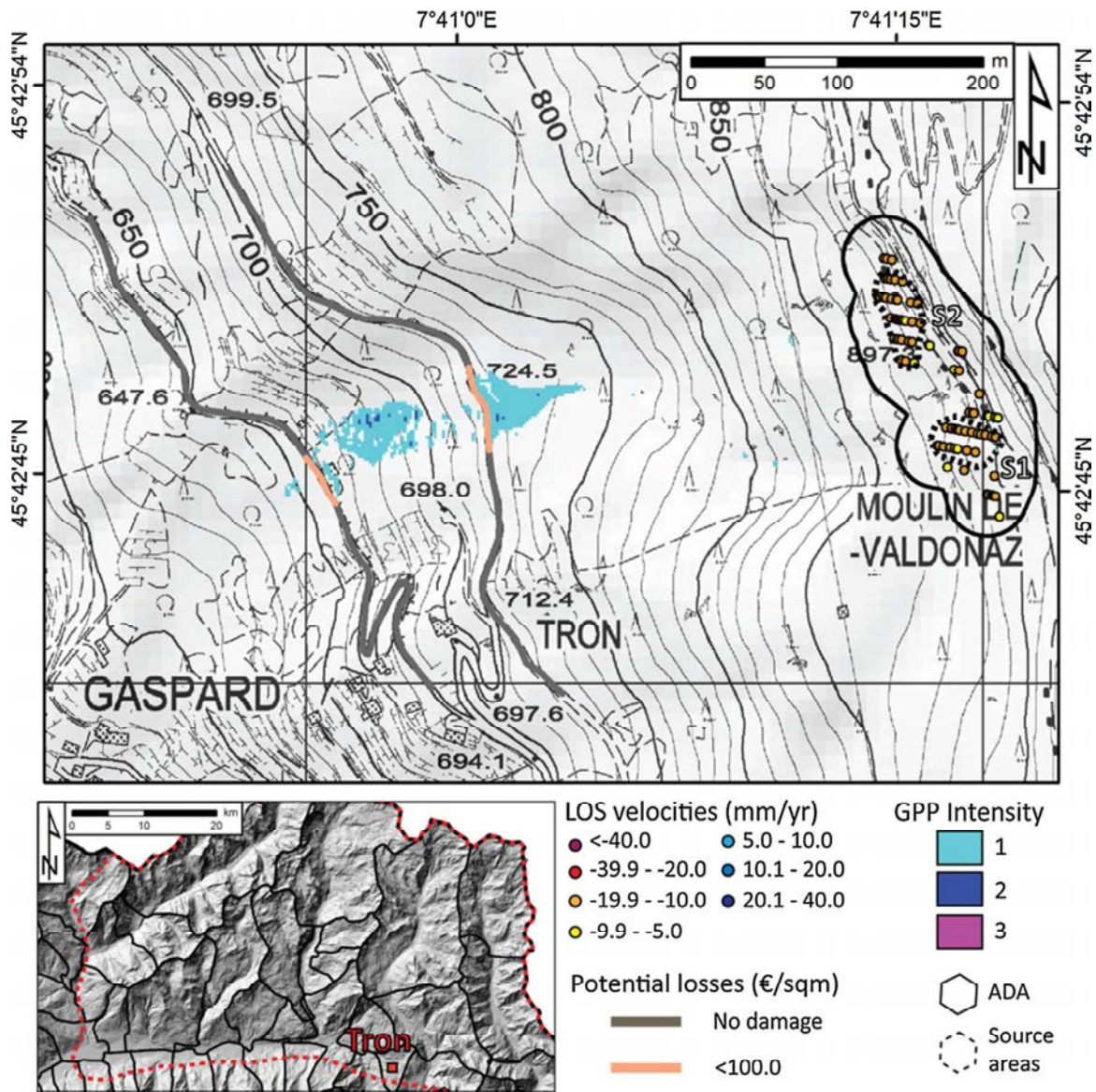


Fig. 9. Landslide potential loss derived using the Model-related intensity approach for the hamlet of Tron in the Montjovet municipality. S1 and S2 are referred to the two source areas chosen to run the GPP model. The background image is a 1:10,000 cadastral map of the VdA region.

emergency responders, as well as risk management actors and insurers, can easily know which are the areas that are moving faster, and which is their potential impact on built-up areas.

The working scale is at the same time an advantage and a limitation. On one side, it is possible to promptly detect those areas showing the highest displacement rates and verify if they affect or could affect one or more elements at risk. On the other side, some assumptions must be made, especially when configuring the GPP model and when selecting the source areas. The economic value of each element at risk cannot be assessed precisely because detailed information about the state of conservation of buildings and roads cannot be gathered in short time over entire basins. The population has not been considered in this work due to the difficulties in estimating day/night occupancy of each edifice. Nevertheless, as further future perspective of this work, the quantification of the human value at risk in the area could be estimated. A possible solution should define a rough people's vulnerability by looking at public buildings (hotels, schools etc.) and private houses, which are inhabited all-year round or rented for holiday. This analysis

could be done only for selected test sites and focused on a worst-case scenario (e.g. day time for schools, i.e. period with maximum occupancy) to provide the maximum potential degree of loss.

A relevant approximation concerns the velocity threshold used to derive the ADA; although it depends on the quality of the interferometric dataset (standard deviation) it assures to take into account and select motions with high deformation rates only, not considering extremely slow deformation that could create damage to buildings and roads over very long periods.

Considering its limitations, the methodology is able to provide useful outputs for risk management at regional scale in a short time. In fact, the selection of moving areas and the calculation of exposure, vulnerability and potential loss requires 2 or 3 weeks of work of an expert in the field of satellite interferometric data interpretation. The same amount of time is required to analyze the SAR images and derive the deformation map. Some phases of the methodology are quite fast, as the generation of moving areas by applying the ADA-finder package (less than a minute). This time requirements allow for the setting up of

a monitoring plan based on 4 or 5 updates of the deformation map every year, re-evaluating each time landslide intensity and the potential damage that could be experienced by buildings and roads, analyzing at the same time the temporal evolution of the phenomena.

The use of the ADA database is practical and useful for quickly and automatically highlighting the fastest moving areas at wide scale and it depends on complying with some input conditions in order to select the suitable approach for the landslide intensity evaluation. Nevertheless, as another limitation of the methodology, it is worth to note that the exploitation of ADA must be carefully performed, since the ADA interpretation does not specifically refer to the type of landslide. Conversely, the moving areas automatically detected by ADA could represent a well-defined failure mechanism within a landslide or it could be just a part of a wider ground motion on a slope; as a result, beyond the limiting conditions of ADA, a robust manual interpretation and validation of such areas of movements should be always carried out to better define and understand them within the dynamics and morphological setting of the selected area of interest.

Our approach is made for a wider exploitation of interferometric products, not only as mapping tools but also as instruments for preliminary risk quantification. The use of both ascending and descending acquisition modes is highly recommended, especially in mountainous areas where shadowing and foreshortening effects prevent the mountainsides to be efficiently seen by the satellite. Unluckily, data acquired by only one orbit were here available, and the elaboration of both acquisition geometries is expected for future work. The acquisition of MTInSAR product over wide areas can be demanding from the point of view of the computational power and rather expensive if in-house processing tools or if open-source codes are not available. In this context, the future launch of the European Ground Motion Service will grant a wider free access to interferometric data (EU-GMS Task Force, 2017). The availability of Sentinel-1 data at regional and national scale will require new efforts for a correct interpretation and dissemination of the results, including a proper definition of downstream services. We believe that our methodology represents an attempt to meet the requirements of this new way of distributing and exploiting satellite interferometric results.

6. Conclusions

This paper presents a methodology for landslide intensity estimation based on satellite interferometric products. The deformation map derived from a MTInSAR analysis of Sentinel-1 radar images is the starting point of the procedure. The first product is the hot-spots of deformation “ADA” and the final goal is estimating potential loss experienced by one or more elements at risk (building and roads) under a given level of landslide intensity (derived in a twofold manner). The final product is a preliminary risk map which includes the definition of all the critical facilities ranked by potential damage or risk. The methodology has been tested in Eastern Valle d’Aosta (north-western Italy) along four lateral valleys of the Dora Baltea Valley, in a territory characterized by steep slopes and widespread landslides and debris deposits.

Fifty-four ADA have been derived from the deformation map of these, 15 have been used for the ADA-related intensity analysis and 30 for the Model-related analysis. The two approaches differ in the way in which the ADA are used for landslide intensity evaluation: as direct estimation of landslide magnitude (and thus intensity) and as an indicator for the presence of unstable debris deposits that could be the source areas of future debris flows, whose runout is foreseen by means of the GPP model. Five case studies have been proposed to illustrate how the two approaches converge to obtain potential loss maps.

In summary, the methodology is able to highlight the fastest motions (detectable from space) at regional scale and then, by estimating the value of the elements at risk and landslide intensity, derive color-scale maps of potential loss expressed in quantitative terms. Considering the current availability of 6-days C-band Sentinel-1 image

with an “open-source” delivery strategy and the future plan of a European deformation map, this sort of methodology represents an example of supporting tool for interferometric data interpretation and dissemination.

Declaration of Competing Interest

The authors declare that they have no known competing financial interests or personal relationships that could have appeared to influence the work reported in this paper.

Acknowledgements

This work has been funded by the European Commission, Directorate-General Humanitarian Aid and Civil Protection (ECHO), through the project U-GEOHAZ – Geohazard Impact Assessment for Urban Areas. Grant Agreement No. 783169.

Appendix A. Supplementary data

Supplementary material related to this article can be found, in the online version, at doi:<https://doi.org/10.1016/j.jag.2019.102028>.

References

- Barra, A., Monserrat, O., Mazzanti, P., Esposito, C., Crosetto, M., Scarascia Mugnozza, G., 2016. First insights on the potential of Sentinel-1 for landslides detection. *Geomat. Nat. Hazards Risk* 7 (6), 1874–1883. <https://doi.org/10.1080/19475705.2016.1171258>.
- Barra, A., Solari, L., Béjar-Pizarro, M., Monserrat, O., Bianchini, S., Herrera, G., Crosetto, M., Sarro, R., González-Alonso, E., Mateos, R.M., Ligüerzana, S., López, C., Moretti, S., 2017. A methodology to detect and update Active Deformation Areas based on Sentinel-1 SAR images. *Remote Sens.* 9 (10), 1002. <https://doi.org/10.3390/rs9101002>.
- Bell, R., Glade, T., 2004. Quantitative risk analysis for landslides—Examples from Bildudalur, NW-Iceland. *Nat. Hazards Earth Syst. Sci.* 4 (1), 117–131. <https://doi.org/10.5194/nhess-4-117-2004>.
- Bianchini, S., Cigna, F., Righini, G., Proietti, C., Casagli, N., 2012. Landslide hotspot mapping by means of persistent scatterer interferometry. *Environ. Earth Sci.* 67 (4), 1155–1172. <https://doi.org/10.1007/s12665-012-1559-5>.
- Bianchini, S., Herrera, G., Mateos, R.M., Notti, D., Garcia, L., Mora, O., Moretti, S., 2013. Landslide activity maps generation by means of persistent scatterer interferometry. *Remote Sens.* 5 (12), 6198–6222. <https://doi.org/10.3390/rs5126198>.
- Bianchini, S., Raspini, F., Ciampalini, A., Lagomarsino, D., Bianchi, M., Bellotti, F., Casagli, N., 2017a. Mapping landslide phenomena in landlocked developing countries by means of satellite remote sensing data: the case of dilijan (Armenia) area. *Geomatics Natural Hazard and Risk* 8 (2), 225–241. <https://doi.org/10.1080/19475705.2016.1189459>.
- Bianchini, S., Solari, L., Casagli, N., 2017b. A GIS-based procedure for landslide intensity evaluation and specific risk analysis supported by persistent scatterers interferometry (PSI). *Remote Sens.* 9 (11), 1093. <https://doi.org/10.3390/rs9111093>.
- Biescas, E., Crosetto, M., Agudo, M., Monserrat, O., Crippa, B., 2007. Two radar interferometric approaches to monitor slow and fast land deformation. *J. Surv. Eng.* 133 (2), 66–71. [https://doi.org/10.1061/\(asce\)0733-9453\(2007\)133:2\(66\)](https://doi.org/10.1061/(asce)0733-9453(2007)133:2(66)).
- Bistacchi, A., Dal Piaz, G.V., Massironi, M., Zattin, M., Balestrieri, M.L., 2001. The Aosta–Ranzola extensional fault system and Oligocene Present evolution of the Austroalpine–Penninic wedge in the north-western Alps. *International Journal of Earth Sciences (Geologisches Rundschau)* 90 (3), 654–667. <https://doi.org/10.1007/s005310000178>.
- Broccolato, Paganone, 2012. Grandi frane permanenti complesse - schede monografiche di frane in Valle d’Aosta analizzate con tecnica PS. Attività B2/C2 Rischi idrogeologici e da fenomeni gravitativi - Progetto Strategico Interreg IVa Risknat. Available online. http://www.risknet-alcotra.org/rna/allegati/risknat-b2-c2-schede-frane-vda_1023.pdf.
- Carraro, F., Giardino, M., 2004. Quaternary glaciations in the Western Italian Alps – a review. In: Ehlers, J., Gibbard, P.L. (Eds.), *Quaternary Glaciations – Extent and Chronology. Part 1. Developments in Quaternary Science*. [https://doi.org/10.1016/s1571-0866\(04\)80071-x](https://doi.org/10.1016/s1571-0866(04)80071-x), 2, 201–208.
- Catani, F., Casagli, N., Ermini, L., Righini, G., Menduni, G., 2005. Landslide hazard and risk mapping at catchment scale in the Arno River basin. *Landslides* 2 (4), 329–342. <https://doi.org/10.1007/s10346-005-0021-0>.
- Catani, F., Segoni, S., Falorni, G., 2010. An empirical geomorphology-based approach to the spatial prediction of soil thickness at catchment scale. *Water Resour. Res.* 46 (5). <https://doi.org/10.1029/2008wr007450>.
- Catani, F., Tofani, V., Lagomarsino, D., 2016. Spatial patterns of landslide dimension: a tool for magnitude mapping. *Geomorphology* 273, 361–373. <https://doi.org/10.1016/j.geomorph.2016.08.032>.
- Cigna, F., Bianchini, S., Casagli, N., 2013. How to assess landslide activity and intensity

- with Persistent Scatterer Interferometry (PSI): the PSI-based matrix approach. *Landslides* 10 (3), 267–283. <https://doi.org/10.1007/s10346-012-0335-7>.
- Cignetti, M., Manconi, A., Manunta, M., Giordan, D., De Luca, C., Allasia, P., Ardizzone, F., 2016. Taking advantage of the esa G-pod service to study ground deformation processes in high mountain areas: A valle d'aosta case study, northern Italy. *Remote Sens.* 8 (10), 852. <https://doi.org/10.3390/rs8100852>.
- Conrad, O., Bechtel, B., Bock, M., Dietrich, H., Fischer, E., Gerlitz, L., Wehberg, J., Wichmann, V., Böhner, J., 2015. System for automated geoscientific analyses (SAGA) v. 2.1. 4. *Geoscientific Model Development* 8 (7), 1991–2007. <https://doi.org/10.5194/gmd-8-1991-2015>.
- Corominas, J., van Westen, C., Frattini, P., Cascini, L., Malet, J.P., Fotopoulou, S., Catani, F., Van Den Eeckhaut, M., Mavrouli, O., Agliardi, F., Pitilakis, K., Winter, M.G., Pastor, M., Ferlisi, S., Tofani, V., Hervás, J., Smith, J.T., 2014. Recommendations for the quantitative analysis of landslide risk. *Bull. Eng. Geol. Environ.* 73 (2), 209–263. <https://doi.org/10.1007/s10064-013-0538-8>.
- Costantini, M., Farina, A., Zirilli, F., 1999. A fast phase unwrapping algorithm for SAR interferometry. *IEEE Trans. Geosci. Remote Sens.* 37 (1), 452–460. <https://doi.org/10.1109/36.739085>.
- Crosetto, M., Monserrat, O., Cuevas, M., Crippa, B., 2011. Spaceborne differential SAR interferometry: data analysis tools for deformation measurement. *Remote Sens.* 3 (2), 305–318. <https://doi.org/10.3390/rs3020305>.
- Crosetto, M., Monserrat, O., Cuevas-González, M., Devanthery, N., Crippa, B., 2016. Persistent scatterer interferometry: a review. *ISPRS J. Photogramm. Remote Sens.* 115, 78–89. <https://doi.org/10.1016/j.isprsjprs.2015.10.011>.
- Crosta, G.B., Frattini, P., Agliardi, F., 2013. Deep seated gravitational slope deformations in the European Alps. *Tectonophysics* 605, 13–33.
- Cruden, D.M., Varnes, D.J., 1996. *Landslides: investigation and mitigation*. Chapter 3. *Landslide Types and Processes*. Transportation research board special report 247.
- Dai, F.C., Lee, C.F., Ngai, Y.Y., 2002. Landslide risk assessment and management: an overview. *Eng. Geol.* 64 (1), 65–87.
- Del Ventisette, C., Righini, G., Moretti, S., Casagli, N., 2014. Multitemporal landslides inventory map updating using spaceborne SAR analysis. *Int. J. Appl. Earth Obs. Geoinf.* 30, 238–246. <https://doi.org/10.1016/j.jag.2014.02.008>.
- Devanthery, N., Crosetto, M., Monserrat, O., Cuevas-González, M., Crippa, B., 2014. An approach to persistent scatterer interferometry. *Remote Sens.* 6 (7), 6662–6679. <https://doi.org/10.3390/rs6076662>.
- Dini, B., Manconi, A., Loew, S., 2019. Investigation of slope instabilities in NW Bhutan as derived from systematic DInSAR analyses. *Eng. Geol.* 259, 105–111.
- EU-GMS Task Force, 2017. *European Ground Motion Service (EU-GMS). A proposed Copernicus service element*.
- Fell, R., Corominas, J., Bonnard, C., Cascini, L., Leroi, E., Savage, W.Z., 2008. Guidelines for landslide susceptibility, hazard and risk zoning for land-use planning. *Eng. Geol.* 102 (3–4), 99–111. <https://doi.org/10.1016/j.enggeo.2008.03.009>.
- Gamma, P., 2000. *dwalk-Ein Murgang-Simulationsprogramm zur Gefahrenzonierung*. Geographisches Institut der Universität Bern.
- Giordan, D., Cignetti, M., Bertolo, D., 2017. The Use of Morpho-Structural Domains for the Characterization of Deep-Seated Gravitational Slope Deformations in Valle d'Aosta. In *Workshop on World Landslide Forum*. May. Springer, Cham, pp. 59–68. https://doi.org/10.1007/978-3-319-53483-1_9.
- Glade, T., Anderson, M.G., Crozier, M.J., 2006. *Landslide Hazard and Risk*. John Wiley & Sons.
- Guzzetti, F., Galli, M., Reichenbach, P., Ardizzone, F., Cardinali, M.J.N.H., 2006. Landslide hazard assessment in the Collazzone area, Umbria, Central Italy. *Nat. Hazards Earth Syst. Sci.* 6 (1), 115–131. <https://doi.org/10.5194/nhess-6-115-2006>.
- Hansen, R., 2001. *Radar Interferometry*. Kluwer Academic Publishers, Dordrecht.
- Herrera, G., Gutiérrez, F., García-Davallillo, J.C., Guerrero, J., Notti, D., Galve, J.P., Fernández-Merodo, J.A., Cooksley, G., 2013. Multi-sensor advanced DInSAR monitoring of very slow landslides: the Tena Valley case study (Central Spanish Pyrenees). *Remote Sens. Environ.* 128, 31–43. <https://doi.org/10.1016/j.rse.2012.09.020>.
- Höbling, D., Füreder, P., Antolini, F., Cigna, F., Casagli, N., Lang, S., 2012. A semi-automated object-based approach for landslide detection validated by persistent scatterer interferometry measures and landslide inventories. *Remote Sens.* 4 (5), 1310–1336. <https://doi.org/10.3390/rs4051310>.
- Horowitz, E., Sahni, S., 1976. *Fundamentals of Data Structures*. Pitman books Ltd, London.
- Hung, O., 1997. Some methods of landslide hazard intensity mapping. In: Cruden, D., Fell, R. (Eds.), *Landslide Risk Assessment*. A.A. Balkema, Rotterdam, pp. 215–226.
- Imaizumi, F., Nishiguchi, T., Matsuoka, N., Trappmann, D., Stoffel, M., 2018. Interpretation of recent alpine landscape system evolution using geomorphic mapping and L-band InSAR analyses. *Geomorphology* 310, 125–137. <https://doi.org/10.1016/j.geomorph.2018.03.013>.
- Intrieri, E., Raspini, F., Fumagalli, A., Lu, P., Del Conte, S., Farina, P., Allevi, J., Ferretti, A., Casagli, N., 2018. The Maoxian landslide as seen from space: detecting precursors of failure with Sentinel-1 data. *Landslides* 15 (1), 123–133. <https://doi.org/10.1007/s10346-017-0915-7>.
- Kaynia, A.M., Papathoma-Köhle, M., Neuhaus, B., Ratzinger, K., Wenzel, H., Medina-Cetina, Z., 2008. Probabilistic assessment of vulnerability to landslide: application to the village of Lichtenstein, Baden-Württemberg, Germany. *Eng. Geol.* 101 (1–2), 33–48. <https://doi.org/10.1016/j.enggeo.2008.03.008>.
- Ko, C.K., Flentje, P., Chowdhury, R., 2004. Landslides qualitative hazard and risk assessment method and its reliability. *Bull. Eng. Geol. Environ.* 63 (2), 149–165. <https://doi.org/10.1007/s10064-004-0231-z>.
- Kumar, V., Venkataraman, G., 2011. SAR interferometric coherence analysis for snow cover mapping in the western Himalayan region. *Int. J. Digit. Earth* 4 (1), 78–90. <https://doi.org/10.1080/17538940903521591>.
- Lari, S., Frattini, P., Crosta, G.B., 2012. Local scale multiple quantitative risk assessment and uncertainty evaluation in a densely urbanised area (Brescia, Italy). *Nat. Hazards Earth Syst. Sci. Discuss.* 12, 3387–3406.
- Latelini, O., Haemmig, C., Raetz, H., Bonnard, C., 2005. Landslide risk management in Switzerland. *Landslides* 2 (4), 313–320. <https://doi.org/10.1007/s10346-005-0018-8>.
- Liu, P., Li, Z., Hoey, T., Kincal, C., Zhang, J., Zeng, Q., Muller, J.P., 2013. Using advanced InSAR time series techniques to monitor landslide movements in Badong of the Three Gorges region, China. *Int. J. Appl. Earth Obs. Geoinf.* 21, 253–264. <https://doi.org/10.1016/j.jag.2011.10.010>.
- Lu, P., Bai, S., Tofani, V., Casagli, N., 2019. Landslides detection through optimized hot spot analysis on persistent scatterers and distributed scatterers. *ISPRS J. Photogramm. Remote Sens.* 156, 147–159.
- Lu, P., Catani, F., Tofani, V., Casagli, N., 2014. Quantitative hazard and risk assessment for slow-moving landslides from Persistent Scatterer Interferometry. *Landslides* 11 (4), 685–696. <https://doi.org/10.1007/s10346-013-0432-2>.
- Martinotti, G., Giordan, D., Giardino, M., Ratto, S., 2011. Controlling factors for deep-seated gravitational slope deformation (DSGD) in the Aosta Valley (NW Alps, Italy). *Geol. Soc. London Spec. Publ.* 351 (1), 113–131. <https://doi.org/10.1144/sp351.6>.
- Mavrouli, O., Corominas, J., 2010. Vulnerability of simple reinforced concrete buildings to damage by rockfalls. *Landslides* 7 (2), 169–180. <https://doi.org/10.1007/s10346-010-0200-5>.
- Navarro, J.A., Cuevas, M., Barra, A., Crosetto, M., 2018. Detection of active deformation areas based on sentinel-1 imagery: an efficient, fast and flexible implementation. In: *Proceedings of 18th International Scientific and Technical Conference*. Crete, Greece, September 24–27.
- Palomba, M., Giardino, M., Ratto, S., Pogliotti, P., 2015. Analysis of factors controlling landslide susceptibility in the aosta Valley (NW Italy): relationship to climatic and environmental changes. *EngineEring Geology for Society and Territory Volume 1*. Springer, Cham, pp. 435–438. https://doi.org/10.1007/978-3-319-09300-0_83.
- Papathoma-Köhle, M., Totschnig, R., Keiler, M., Glade, T., 2012. A new vulnerability function for debris flow—the importance of physical vulnerability assessment in alpine areas. In: *Koboltschnig, G., Hübl, J., Braun, J. (Eds.), Internationales Symposium Interpraevent, Grenoble, April 23–26, 2012. Internationale Forschungsgesellschaft Interpraevent (2012), Klagenfurt*, pp. 1033–1043.
- OMI database, 2018. Agency of Revenues. (accessed 20 May 2019). <https://wwwwt.agenziaentrate.gov.it/geopoiomi/index.php>.
- Pastonchi, L., Barra, A., Monserrat, O., Luzzi, G., Solari, L., Tofani, V., 2018. Satellite data to improve the knowledge of geohazards in world heritage sites. *Remote Sens.* 10 (7), 992. <https://doi.org/10.3390/rs10070992>.
- Peduto, D., Ferlisi, S., Nicodemo, G., Reale, D., Pisciotto, G., Gullà, G., 2017. Empirical fragility and vulnerability curves for buildings exposed to slow-moving landslides at medium and large scales. *Landslides* 14 (6), 1993–2007. <https://doi.org/10.1007/s10346-017-0826-7>.
- Peduto, D., Nicodemo, G., Caraffa, M., Gullà, G., 2018. Quantitative analysis of consequences to masonry buildings interacting with slow-moving landslide mechanisms: a case study. *Landslides* 15 (10), 2017–2030. <https://doi.org/10.1007/s10346-018-1014-0>.
- Pellicani, R., Van Westen, C.J., Spilotro, G., 2014. Assessing landslide exposure in areas with limited landslide information. *Landslides* 11, 463–480. <https://doi.org/10.1007/s10346-013-0386-4>.
- Petley, D.N., Dunning, S.A., Rosser, K., Rosser, N.J., 2005. The analysis of global landslide risk through the creation of a database of worldwide landslide fatalities. In: *Hunger, O., Fell, R., Couture, R., Ebberhardt, E. (Eds.), Landslide Risk Management*. Balkema, Amsterdam, June 30, 2005. Taylor & Francis Group, London, UK, pp. 367–373 2005.
- Polino, R., Dal Piaz, G.V., Gosso, G., 1990. Tectonic erosion at the Adria margin and accretionary processes for the Cretaceous orogeny in the Alps. *Memorie della Societa' Geologica France* 156, 345–367.
- Puissant, A., Van Den Eeckhaut, M., Malet, J.P., Maquaire, O., 2014. Landslide consequence analysis: a region-scale indicator-based methodology. *Landslides* 11 (5), 843–858. <https://doi.org/10.1007/s10346-013-0429-x>.
- Raspini, F., Ciampalini, A., Bianchini, S., Bardi, F., Di Traglia, F., Basile, G., Moretti, S., 2016. Updated landslide inventory of the area between the Furiano and Rosmarino creeks (Sicily, Italy). *J. Maps* 12 (5), 1010–1019. <https://doi.org/10.1080/17445647.2015.1114975>.
- Raspini, F., Bianchini, S., Ciampalini, A., Del Soldato, M., Solari, L., Novali, F., Del Conte, S., Rucci, A., Ferretti, A., Casagli, N., 2018. Continuous, semi-automatic monitoring of ground deformation using Sentinel-1 satellites. *Sci. Rep.* 8 (1), 7253. <https://doi.org/10.1038/s41598-018-25369-w>.
- Ratto, S., Bonetto, F., Comoglio, C., 2003. The October 2000 flooding in Valle d'Aosta (Italy): event description and land planning measures for the risk mitigation. *Int. J. River Basin Manag.* 1 (2), 105–116. <https://doi.org/10.1080/15715124.2003.9635197>.
- Rosi, A., Tofani, V., Tanteri, L., Stefanelli, C.T., Agostini, A., Catani, F., Casagli, N., 2018. The new landslide inventory of Tuscany (Italy) updated with PS-InSAR: geomorphological features and landslide distribution. *Landslides* 15 (1), 5–19. <https://doi.org/10.1007/s10346-017-0861-4>.
- Salvatici, T., Tofani, V., Rossi, G., D'Ambrosio, M., Stefanelli, C.T., Masi, E.B., Rosi, A., Pazzi, V., Vannocci, P., Petrolo, M., Catani, F., Ratto, S., Stevenin, H., Casagli, N., 2018. Application of a physically based model to forecast shallow landslides at a regional scale. *Nat. Hazards Earth Syst. Sci.* 18 (7), 1919–1935. <https://doi.org/10.5194/nhess-18-1919-2018>.
- Sartori, M., 1987. *Structure de la Zone du Combin entre le Diablons et Zermatt*. *Eclogae Geol. Helv.* 80, 789–814.
- Schwendtner, B., Papathoma-Köhle, M., Glade, T., 2013. Risk evolution: how can changes in the built environment influence the potential loss of natural hazards? *Nat. Hazards*

- Earth Syst. Sci. 13 (9), 2195–2207. <https://doi.org/10.5194/nhess-13-2195-2013>.
- Solari, L., Barra, A., Herrera, G., Bianchini, S., Monserrat, O., Béjar-Pizarro, M., Crosetto, M., Sarro, R., Moretti, S., 2018. Fast detection of ground motions on vulnerable elements using Sentinel-1 InSAR data. *Geomat. Nat. Hazards Risk* 9 (1), 152–174. <https://doi.org/10.1080/19475705.2017.1413013>.
- Solari, L., Del Soldato, M., Montalti, R., Bianchini, S., Raspini, F., Thuegaz, P., Bertolo, D., Tofani, V., Casagli, N., 2019. A Sentinel-1 based hot-spot analysis: landslide mapping in north-western Italy. *Int. J. Remote Sens.* 1–24. <https://doi.org/10.1080/01431161.2019.1607612>.
- Sterlacchini, S., Akbas, S.O., Blahut, J., Mavrouli, O.C., Garcia, C., Luna, B.Q., Corominas, J., 2014. *Methods for the characterization of the vulnerability of elements at risk. Mountain Risks: From Prediction to Management and Governance*. Springer, Dordrecht, pp. 233–273.
- Strozzi, T., Farina, P., Corsini, A., Ambrosi, C., Thüring, M., Zilger, J., Wiesmann, A., Wegmüller, U., Werner, C., 2005. Survey and monitoring of landslide displacements by means of L-band satellite SAR interferometry. *Landslides* 2 (3), 193–201. <https://doi.org/10.1007/s10346-005-0003-2>.
- Strozzi, T., Ambrosi, C., Raetzo, H., 2013. Interpretation of aerial photographs and satellite SAR interferometry for the inventory of landslides. *Remote Sens. (Basel)* 5 (5), 2554–2570. <https://doi.org/10.3390/rs5052554>.
- Takahashi, T., Nakagawa, H., Harada, T., Yamashiki, Y., 1992. Routing debris flows with particle segregation. *J. Hydraul. Eng.* 118 (11), 1490–1507. [https://doi.org/10.1061/\(asce\)0733-9429\(1992\)118:11\(1490\)](https://doi.org/10.1061/(asce)0733-9429(1992)118:11(1490)).
- Tomás, R., Pagán, J.L., Navarro, J.A., Cano, M., Pastor Navarro, J.L., Riquelme, A., Cuevas-González, M., Crosetto, M., Barra, A., Monserrat, O., Lopez-Sanchez, J.M., et al., 2019. Semi-automatic identification and pre-screening of geological–Geotechnical deformational processes using persistent scatterer interferometry datasets. *Remote Sens. (Basel)* 11 (14), 1675. <https://doi.org/10.3390/rs11141675>.
- Trigila, A., Iadanza, C., Spizzichino, D., 2010. Quality assessment of the Italian landslide inventory using GIS processing. *Landslides* 7 (4), 455–470. <https://doi.org/10.1007/s10346-010-0213-0>.
- Uzielli, M., Nadim, F., Lacasse, S., Kaynia, A.M., 2008. A conceptual framework for quantitative estimation of physical vulnerability to landslides. *Eng. Geol.* 102 (3–4), 251–256. <https://doi.org/10.1016/j.enggeo.2008.03.011>.
- Van Westen, C.J., Van Asch, T.W., Soeters, R., 2006. Landslide hazard and risk zonation—why is it still so difficult? *Bull. Eng. Geol. Environ.* 65 (2), 167–184. <https://doi.org/10.1007/s10064-005-0023-0>.
- Vranken, L., Van Turnhout, P., Van Den Eeckhaut, M., Vandekerckhove, L., Poesen, J., 2013. Economic valuation of landslide damage in hilly regions: a case study from Flanders, Belgium. *Sci Total Environ* 447, 323–333.
- Wichmann, V., Heckmann, T., Haas, F., Becht, M., 2009. A new modelling approach to delineate the spatial extent of alpine sediment cascades. *Geomorphology* 111 (1–2), 70–78. <https://doi.org/10.1016/j.geomorph.2008.04.028>.
- Wichmann, V., 2017. The Gravitational process Path (GPP) model (v1. 0)—a GIS-based simulation framework for gravitational processes. *Geosci. Model. Dev.* 10 (9). <https://doi.org/10.5194/gmd-2017-5>.
- Winter, M.G., Smith, J.T., Fotopoulou, S., Pitilakis, K., Mavrouli, O., Corominas, J., Argyroudis, S., 2014. An expert judgement approach to determining the physical vulnerability of roads to debris flow. *Bull. Eng. Geol. Environ.* 73 (2), 291–305. <https://doi.org/10.1007/s10064-014-0570-3>.
- Zimmermann, M., Mani, P., Gamma, P., Gsteiger, P., Heiniger, O., Hunziker, G., 1997. *Murganggefahr und Klimaänderung—ein GIS-basierter Ansatz [debris flow risk and climatic change—a GIS-based approach]*. Zürich, vdf Hochschulverlag AG an der ETH Zürich, Switzerland.

7 Conclusions

This thesis has proposed a global approach to exploit regional-scale MTInSAR displacement maps for territorial and geohazard management, especially based on the free and reliable data of the Sentinel-1 satellite constellation. The first evaluation of S1 potentialities for landslides detection has been done at the beginning of this research, when the draft of the methodology proposed here was delineated (see Annex 1). Then, the final workflow (Figure 18) has been achieved by the development of specific methodologies and tools for an improved operational application. The core of the whole workflow is the semiautomatic extraction of Active Deformation Areas (ADAs) in polygonal shapefiles, which allows a fast focusing on the most interesting areas, avoiding long times of analysis (see Section 4, and ADAFinder in Section 5). The ADA polygons resume the main qualities of the MPs within each area, like the statistics of the velocities and the accumulated displacement, and the extension area of each polygon. Those attributes allow a fast characterization and a preliminary intensity association to each moving area. Moreover, a Quality Index is calculated to assess the noise level of the MPs within each ADA, especially important for a reliability consciousness by non-expert InSAR users. Starting from the ADA map, we propose a series of methodologies and applications aimed at deriving improved products for territorial management and geological or anthropogenic hazards risk analysis. All the products have been developed with the specific aims of being operational, mainly for InSAR non-expert users, applicable at regional scale, and being easy to read and interpret. The ADA polygonal map represents a flexible tool that can be easily adapted to several applications and used as input to derive regional and local scale advanced products. The ADAs have been intersected with auxiliary data to make a preliminary assessment of the potential phenomenon causing the movement (see the Geohazard Activity Map, in Annex 2, and the ADAClassifier tool, in Section 5), or to make a fast evaluation on the presence of exposed elements (see the VEAM map, Annex 2). Then, the ADAs allowed changing from regional to local scale risk analysis. Firstly, as a geohazard locator at regional scale, secondly as landslide intensity derivation to locally evaluate the potential loss, vulnerability (Section 6), and damages (Section 3.6), of exposed buildings and infrastructures. In Section 6 the ADAs are used for both a direct intensity evaluation, in case of slow landslides directly affecting structures and infrastructures, and an indirect input for a model-based rapid-landslide intensity estimation, in case of ADAs highlighting source zones of a potential debris flow. The outputs of the methodology are simple colour-scale maps showing the intensity of the potential landslide (as ADA velocity or as height of material deposited by a debris flow) and a value of potential loss (in €/m²), expression of vulnerability (depending on landslide intensity) and exposure (defined as real estate market values) of the elements at risk. The last work, shortly explained in Section 3.6, makes a step forward for slow landslide intensity evaluation based on local gradients of movement. The Potential Damage Map (PDM), the exposed buildings classified based on the local intensity gradients, could be the input value for advanced vulnerability analysis and potential loss estimations. The methodology based on the displacement gradients, from ADAs to PDM, is now being applied in the frame of the project MOMPA (Barra et al., 2021a, 2021b; Fabregat et al., 2022; Gasc-Barbier et al., 2021), to propose actuation protocols based on MTInSAR data for the slow landslide of Canillo (Andorra). The methodology explained in Section 3.6 is totally based on free remote-sensing data (i.e., S1, RSTM, OpenOpenStreetMap), which makes it globally applicable with low costs. After demonstrating the effectiveness of a methodology, an important step is its automatization through user-friendly and fast software implementation. This has been shown to be a key element for widespread distribution and application. A clear example has been the ADAFinder, which has implemented the methodology proposed in Section 4. Apart from several private requests, the software has been distributed to several public institutes, like the Geological and Mining Institute of Spain (Instituto Geológico y Minero de España –

IGME), the Cartographic and Geological Institute of Catalonia (Institut Cartogràfic i Geològic de Catalunya – ICGC), the German Federal Institute for Geosciences and Natural Resources of (Wissenschaftler bei Bundesanstalt für Geowissenschaften und Rohstoffe – BBD-BGR), the Geological Survey of Austria (Geologische Bundesanstalt), the French Geological Survey (BRGM), the Italian National Institute for Environmental Protection and Research (Istituto Superiore per la Protezione e la Ricerca Ambientale-ISPRA), the Research Center on Alpine Environment (CREALP, Switzerland), the University of Alicante (Civil Engineering Department, Spain), the University of Granada (Spain), and the University of Florence (Italy). Moreover, ADAFinder allowed the application of the methodology in several test sites and projects.

The Specific Objectives of this thesis have been achieved through the implementation of several methodologies to derive products that are easy to be interpreted by non-expert InSAR users and easy to be applied over regional scale MTInSAR maps. It is important to underline that all the proposed methodologies can be implemented and applied at the continental scale, provided the perspective given by the EGMS, allowing improved exploitation of S1 based displacement maps for supporting risk analysis and territorial management. Nowadays, the ADAFinder is being improved for its application over the first continental EGMS map, and a WebGIS is being implemented to upload the results and other advanced products. Moreover, the methodology proposed in Section 3.6 is being implemented in software tools, with the aim of an extensive application over the EGMS displacement map.

It is worth underlying that all the semi-automatic results are a first assessment to support the risk management and analysis activities. Nevertheless, the results always need to be validated with a robust manual interpretation and validation.

7.1 Ongoing research and future developments

The proposed methodologies are first attempts towards a wide-scale application for a correct interpretation and dissemination, and towards an improvement in the operational exploitation of satellite interferometric results. Starting from this work, future enhancements are expected in several aspects. First of all, new projects are starting based on the exploitation and development of such tools and considering the lessons learnt in the projects mentioned in this thesis. One example is RASTOOL (UCPM2027-101048474), founded by the European Union Civil Protection Mechanism (UCPM), which aims to provide Civil Protection Authorities practitioners with the appropriate set of tools for simplifying the EGMS data, to automatically analyse them, and to generate maps to support hazard, exposure and risk-assessment against geohazards (both natural and anthropogenic). Another example is PROMETEO (PLEC2021-007842), founded by the NextGenerationEU European recovery plan. One of the objectives of PROMETEO is to perform a wide-area, intelligent early-detection of deformation phenomena, and will be based on the ADAFinder approach. This fully exploits the potentiality of InSAR to monitor several infrastructures at the same time, useful to plan further monitoring activities, which are tailored to the specific needs of each infrastructure.

Moreover, improvements of the proposed methodologies are expected due to a future increasing availability of auxiliary data, like landslide inventories, susceptibility maps, geological maps or structures and infrastructures databases with construction characteristic information.

Other investigations are opened for a wider landslide phenomenon detection and higher exploitation of S1 high frequency data. First, a semiautomatic methodology for the single-interferogram movement detection, as explained in Annex 1, Sections 2.4 and 3.1, and included in the workflow of this PhD, still need to be developed. Secondly, to detect rapid landslide movements, the amplitude has been widely

used (Mondini et al., 2021, 2019), but an improved detection coverage would be given by the parallel use of amplitude and coherence. A first assessment of the coherence suitability for landslide detection has been done through a visual analysis of several rapid events. This allowed to understand the complementarity of both amplitude and coherence images. In fact, some events are visible in amplitude and not in coherence images, and vice versa. The two methodologies are based on different concepts, the amplitude is based on a pixel offset tracking, while the coherence is based on the single pixel backscattering characteristics changes in the images acquired before and after the event. Figure 34 shows an example occurred the 23 of August 2017, at the Swiss-Italian border, where a rock avalanche of approximately 3 million m³ felt and evolved in a debris flow that reached the village of Bondo (Figure 34A and B). Figure 34C shows the coherence image of the interferometric phases before the event (13/08/2017-19/08/2017), and Figure 34D shows the coherence image of the interferometric phases before and after the event (19/08/2017-25/08/2017). A loss of coherence due to the event occurrence is evident in the example of Figure 34. Nevertheless, the automatic detection is not straightforward mainly due to the high number of factors that cause a change in coherence.

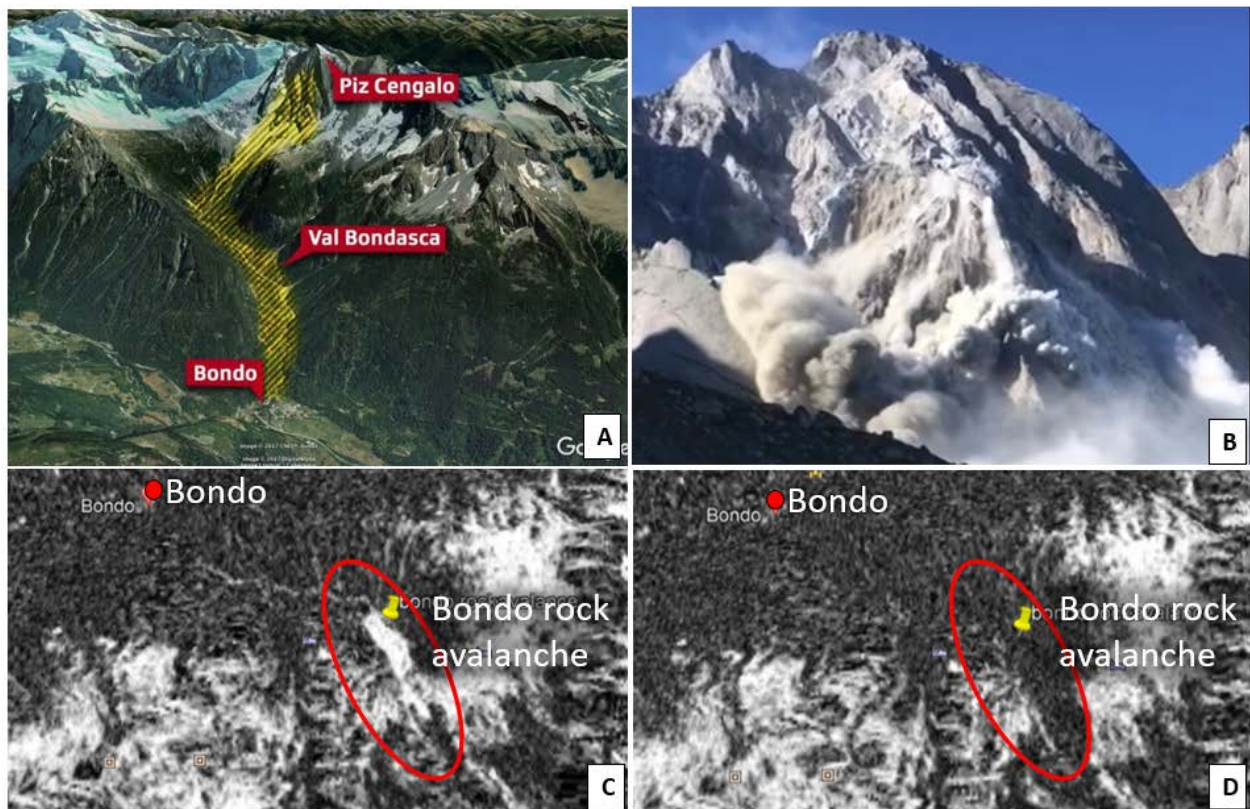


Figure 34 Example of rapid rock avalanche detected with coherence images. The Rock avalanche occurred the 23 of August 2017, at the Swiss-Italian border. A) shows the rock path, from the detachment area up to the Bondo village. B) shows a capture of the rock mass movement; C) shows the coherence image of an interferogram generated with two images acquired before the event (13/08/2017-19/08/2017); D) shows the coherence image of an interferogram generated with two images acquired before and after the event (19/08/2017-25/08/2017).

Acknowledgments

I start expressing many thanks to my supervisor, Oriol Monserrat, who has been my reference point since the beginning for both technical and human aspects. The second aspect has been for me of the same importance as the first one. His way of interacting with others is always respectful without any top-down behaviour, something that is very appreciable and that I will never forget for any of my next professional collaborations. Since the beginning he introduced me throughout his professional network, involving me in many activities related with the projects. Moreover, during those long years he could bear my down moments, always animating and believing in me. He gave me a strong support during the most difficult periods.

I strongly acknowledge my second supervisor, Gerardo Herrera, for the constant enthusiasm about my work, the precious guides, ideas, and suggestions, always present even if physically far from Barcelona.

Then, I must add my third “adopted supervisor”, Michele Crosetto, who, mostly in the last year, have supported and animated me in my PhD activities, with an almost daily communication, and constructive debates and suggestions.

I acknowledge Josep Gili, for his patient acceptance of my always-in-late necessities, and for guiding me through the bureaucratic maze.

Thanks to my parents and my sister, always present, supporting me and believing in my personal and professional journey, even if far from home.

Thanks to all the people, which have collaborated with me, from IGME, the University of Granada, University of Florence, and University of Alicante. And to all the CTTC group of Geomatics Research Unit, for the beautiful environment they make at work, the collaborations, and their support.

Thanks to my friends, bearing to hear so many times the words “NO, I can’t, I have to work on my PhD”.

Finally, thanks to all the Spanish people that I have been meeting in this journey, to make me understand the importance of Beer in a serious and creative process, as it is the research.

References

- Barra, A., Colell, X., Echeverria, A., Trapero, L., Marturia, J., Fabregat, I., Gao, Q., Cuevas, M., Gasc, M., Buxó, P., Dufour, N., Luzi, G., Crosetto, M., 2021a. El proyecto Mompá: protocolos de actuación basados en el monitoreo mediante interferometría satelital radar (INSAR). Proceedings 3rd Congress in Geomatics Engineering -CiGeo 118–126. <https://doi.org/10.4995/CIGEO2021.2021.12709>.
- Barra, A., Marturià, J., Copons, R., Gasc, M., Fabregat, I., Buxó, P., Dufour, N., Pigeot, L., Colell, X., Trapero, L., Crosetto, M., 2021b. MOMPA Project: interregional DInSAR monitoring and action protocol in the Eastern Pyrenees. EGU General Assembly 2021. <https://doi.org/10.5194/egusphere-egu21-12161>.
- Barra, A., Monserrat, O., Crosetto, M., Cuevas-Gonzalez, M., Devanthéry, N., Luzi, G., Crippa, B., 2017a. Sentinel-1 Data Analysis for Landslide Detection and Mapping: First Experiences in Italy and Spain, in: Advancing Culture of Living with Landslides, Workshop on World Landslide Forum. Springer International Publishing, Cham, pp. 201–208. https://doi.org/10.1007/978-3-319-53487-9_23.
- Barra, A., Monserrat, O., Giordan, D., Solari, L., Cignetti, M., Crosetto, M., Bianchini, S., Catani, F., Bertolo, D., 2019. Satellite DInSAR monitoring of Landslides in mountainous areas. Geophysical Research Abstracts - EGU General Assembly 21.
- Barra, A., Monserrat, O., Mazzanti, P., Esposito, C., Crosetto, M., Scarascia Mugnozza, G., 2016. First insights on the potential of Sentinel-1 for landslides detection. Geomatics, Natural Hazards and Risk 7, 1874–1883. <https://doi.org/10.1080/19475705.2016.1171258>.
- Barra, A., Monserrat, O., Solari, L., Herrera, G., Lopez, C., Onori, R., Reichenbach, P., González-Alonso, E., Mateos, R.M., Bianchini, S., Crosetto, M., 2018. The safety project: Sentinel-1 for the management of geological risk, in: WIT Transactions on Engineering Sciences. <https://doi.org/10.2495/RISK180221>.
- Barra, A., Reyes-Carmona, C., Monserrat, O., Glave, J.P., Herrera, G., Mateos, R.M., Sarro, R., Bejar, M., Azañón, J.M., Crosetto, M., 2020. Sentinel-1 for Granada coast landslides monitoring and potential damage assessment, in: EGU General Assembly. <https://doi.org/10.5194/egusphere-egu2020-19236>.
- Barra, A., Reyes-Carmona, C., Pedro Galve, J., Tomás, R., Herrera, G., Bejar, M., Miguel Azañón, J., Navarro, J., Sarro, R., Monserrat, O., 2021c. Sentinel-1 landslides detection: the Granada coast, in: The Fifth World Landslide Forum Abstracts, WLF5. Kyoto.
- Barra, A., Solari, L., Béjar-Pizarro, M., Monserrat, O., Bianchini, S., Herrera, G., Crosetto, M., Sarro, R., González-Alonso, E., Mateos, R.M., Ligüerzana, S., López, C., Moretti, S., 2017b. A methodology to detect and update active deformation areas based on Sentinel-1 SAR images. Remote Sensing 9, 1002. <https://doi.org/10.3390/rs9101002>.
- Barra, A., Solari, L., Béjar-Pizarro, M., Monserrat, O., Herrera, G., Bianchini, S., Crosetto, M., Mateos, R.M., Sarro, R., Moretti, S., 2017c. Sentinel-1 data exploitation for geohazard activity map generation. Geophysical Research Abstracts - EGU General Assembly 19, 14203.

- Béjar-Pizarro, M., Gómez, J.A.Á., Staller, A., Luna, M.P., Pérez-López, R., Monserrat, O., Chunga, K., Lima, A., Galve, J.P., Díaz, J.J.M., Mateos, R.M., Herrera, G., 2018. InSAR-based mapping to support decision-making after an earthquake. *Remote Sensing* 10. <https://doi.org/10.3390/rs10060899>
- Berardino, P., Fornaro, G., Lanari, R., Sansosti, E., 2002. A new algorithm for surface deformation monitoring based on small baseline differential SAR interferograms. *IEEE Transactions on geoscience and remote sensing* 40, 2375–2383. <https://doi.org/10.1109/TGRS.2002.803792>.
- Bianchini, S., Solari, L., Barra, A., Monserrat, O., Crosetto, M., Catani, F., 2021. Sentinel-1 PSI Data for the Evaluation of Landslide Geohazard and Impact, in: *Understanding and Reducing Landslide Disaster Risk*. pp. 447–455. https://doi.org/10.1007/978-3-030-60227-7_52.
- Biescas, E., Crosetto, M., Agudo, M., Monserrat, O., Crippa, B., 2007. Two Radar Interferometric Approaches to Monitor Slow and Fast Land Deformation. *Journal of Surveying Engineering* 133, 66–71. [https://doi.org/10.1061/\(asce\)0733-9453\(2007\)133:2\(66\)](https://doi.org/10.1061/(asce)0733-9453(2007)133:2(66)).
- Boni, R., Pilla, G., Meisina, C., 2016. Methodology for detection and interpretation of ground motion areas with the A-DinSAR time series analysis. *Remote Sensing* 8. <https://doi.org/10.3390/rs8080686>.
- Botey i Bassols, J., Vázquez-Suñé, E., Crosetto, M., Barra, A., Gerard, P., 2021. D-InSAR monitoring of ground deformation related to the dewatering of construction sites. A case study of Glòries Square, Barcelona. *Engineering Geology* 286. <https://doi.org/10.1016/j.enggeo.2021.106041>.
- Bovenga, F., Pasquariello, G., Refice, A., 2021. Statistically-based trend analysis of MTInSAR displacement time series. *Remote Sensing* 13. <https://doi.org/10.3390/RS13122302>.
- Calò, F., Ardizzone, F., Castaldo, R., Lollino, P., Tizzani, P., Guzzetti, F., Lanari, R., Angeli, M.G., Pontoni, F., Manunta, M., 2014. Enhanced landslide investigations through advanced DInSAR techniques: The Ivancich case study, Assisi, Italy. *Remote Sensing of Environment* 142, 69–82. <https://doi.org/10.1016/J.RSE.2013.11.003>.
- Capes, R., European Space Agency GMES, TerraFirma partners, 2009. *The TerraFirma Atlas, Terrain-Motion Across Europe*.
- Cascini, L., Peduto, D., Pisciotta, G., Arena, L., Ferlisi, S., Fornaro, G., 2013. The combination of DInSAR and facility damage data for the updating of slow-moving landslide inventory maps at medium scale. *Natural Hazards and Earth System Sciences* 13, 1527–1549. <https://doi.org/10.5194/nhess-13-1527-2013>.
- Chen, C.W., Zebker, H.A., 2001. Two-dimensional phase unwrapping with use of statistical models for cost functions in nonlinear optimization. *JOSA A* 18, 338–351. <https://doi.org/10.1364/JOSAA.18.000338>
- Cooper, A.H., 2008. The classification, recording, databasing and use of information about building damage due to subsidence and landslides. *Quarterly Journal of Engineering Geology and Hydrogeology* 41. <https://doi.org/10.1144/1470-9236/07-223>.
- Copernicus - The European Union's Earth Observation Program, URL <https://www.copernicus.eu/en> (accessed 3.17.22).

- Costantini, M., 1998. A novel phase unwrapping method based on network programming. *IEEE Transactions on Geoscience and Remote Sensing* 36, 813–821. <https://doi.org/10.1109/36.673674>.
- Costantini, M., Falco, S., Malvarosa, F., Minati, F., 2008. A new method for identification and analysis of persistent scatterers in series of SAR images. *IGARSS 2008-2008 IEEE International Geoscience and Remote Sensing Symposium* 2, 449–452. <https://doi.org/10.1109/IGARSS.2008.4779025>.
- Costantini, M., Minati, F., Trillo, F., Ferretti, A., Novali, F., Passera, E., Dehls, J., Larsen, Y., Marinkovic, P., Eineder, M., Brcic, R., Siegmund, R., Kotzerke, P., Probeck, M., Kenyeres, A., Proietti, S., Solari, L., Andersen, H.S., 2021. European Ground Motion Service (EGMS), in: IEEE (Ed.), 2021 IEEE International Geoscience and Remote Sensing Symposium IGARSS. Institute of Electrical and Electronics Engineers (IEEE), Brussels, Belgium, pp. 3293–3296. <https://doi.org/10.1109/IGARSS47720.2021.9553562>.
- Crosetto, M., Monserrat, O., Cuevas-González, M., Devanthéry, N., Crippa, B., 2016. Persistent Scatterer Interferometry: A review. *ISPRS Journal of Photogrammetry and Remote Sensing* 115, 78–89. <https://doi.org/10.1016/j.isprsjprs.2015.10.011>.
- Crosetto, M., Monserrat, O., Cuevas-González, M., Devanthéry, N., Luzi, G., Crippa, B., 2015. Measuring thermal expansion using X-band persistent scatterer interferometry. *ISPRS Journal of Photogrammetry and Remote Sensing* 100, 84–91. <https://doi.org/10.1016/j.isprsjprs.2014.05.006>.
- Crosetto, M., Monserrat, O., Iglesias, R., Crippa, B., 2010. Persistent Scatterer Interferometry: Potential, limits and initial C- and X-band comparison. *Photogrammetric Engineering and Remote Sensing* 76, 1061–1069. <https://doi.org/10.14358/PERS.76.9.1061>.
- Crosetto, M., Solari, L., Balasis-Levinsen, J., Bateson, L., Casagli, N., Frei, M., Oyen, A., Moldestad, D.A., Mróz, M., 2021. Deformation monitoring at european scale: The Copernicus Ground Motion Service. *International Archives of the Photogrammetry, Remote Sensing and Spatial Information Sciences - ISPRS Archives* 43, 141–146. <https://doi.org/10.5194/ISPRS-ARCHIVES-XLIII-B3-2021-141-2021>.
- Crosetto, M., Solari, L., Balasis-Levinsen, J., Casagli, N., Frei, M., Oyen, A., Moldestad, D.A., 2020a. Ground deformation monitoring at continental scale: The European Ground Motion Service. *International Archives of the Photogrammetry, Remote Sensing and Spatial Information Sciences - ISPRS Archives* 43, 293–298. <https://doi.org/10.5194/ISPRS-ARCHIVES-XLIII-B3-2020-293-2020>.
- Crosetto, M., Solari, L., Mróz, M., Balasis-Levinsen, J., Casagli, N., Frei, M., Oyen, A., Moldestad, D.A., Bateson, L., Guerrieri, L., Comerci, V., Andersen, H.S., 2020b. The evolution of wide-area DInSAR: From regional and national services to the European ground motion service. *Remote Sensing* 12, 2043. <https://doi.org/10.3390/RS12122043>.
- Crozier, M.J., 2005. Multiple-occurrence regional landslide events in New Zealand: Hazard management issues. *Landslides* 2, 247–256. <https://doi.org/10.1007/S10346-005-0019-7>.
- Cruden, D.M., Varnes, D.J., 1996. Landslides: investigation and mitigation. Chapter 3 - Landslide types and processes., in: *Transportation Research Board Special Report*.
- de Zan, F., Guarnieri, A.M., 2006. TOPSAR: Terrain observation by progressive scans. *IEEE Transactions on Geoscience and Remote Sensing* 44, 2352–2360. <https://doi.org/10.1109/TGRS.2006.873853>.

- Dehls, J.F., Larsen, Y., Marinkovic, P., Lauknes, T.R., Stodle, D., Moldestad, D.A., 2019. INSAR.No: A National Insar Deformation Mapping/Monitoring Service in Norway - From Concept to Operations. International Geoscience and Remote Sensing Symposium (IGARSS) 5461–5464. <https://doi.org/10.1109/IGARSS.2019.8898614>.
- Devanathéry, N., Crosetto, M., Monserrat, O., Crippa, B., Mróz, M., 2019. Data analysis tools for persistent scatterer interferometry based on Sentinel-1 data. European Journal of Remote Sensing 52, 15–25. <https://doi.org/10.1080/22797254.2018.1554981>.
- Devanathéry, N., Crosetto, M., Monserrat, O., Cuevas-González, M., Crippa, B., 2014. An Approach to Persistent Scatterer Interferometry. Remote Sensing 2014, Vol. 6, Pages 6662–6679 6, 6662–6679. <https://doi.org/10.3390/RS6076662>.
- EEA Report, Crosetto, M., Solari, L., Frei, M., Balasis-Levinsen, J., Anders Moldestad, D., Romsenter, N., Oyen, A., Casagli, N., Bateson, L., Guerrieri, L., Comerci, V., Mróz, M., 2020. Interaction and cooperation between the European Ground Motion Service and national/regional Ground Motion Services.
- EGMS White Paper, 2017. European Ground Motion Service (EU-GMS) A proposed Copernicus service element. URL <https://land.copernicus.eu/user-corner/technical-library/egms-white-paper> (accessed 3.22.22).
- ESA - Sentinel Online. Sentinel-1 Observation Scenario - Planned Acquisitions. URL <https://sentinel.esa.int/web/sentinel/missions/sentinel-1/observation-scenario> (accessed 3.23.22).
- ESA - User Guides. Sentinel-1 SAR - Interferometric Wide Swath. URL <https://sentinels.copernicus.eu/web/sentinel/user-guides/sentinel-1-sar/acquisition-modes/interferometric-wide-swath> (accessed 3.21.22).
- EuroGeoSurveys. TerraFirma – EGDI. URL <https://www.europe-geology.eu/terrafirma/> (accessed 3.17.22).
- Fabregat, I., Casanovas, J., Marturià, J., Buxó, P., Barra, A., 2022. Semi-automated assessment of geological phenomena of Active Deformation Areas (ADA) detected by radar interferometry in Alt Urgell and Cerdanya, Catalonia (Spain), in: EGU General Assembly 2021. <https://doi.org/10.5194/egusphere-egu21-12368>.
- Ferretti, A., Fumagalli, A., Novali, F., Prati, C., Rocca, F., Rucci, A., 2011. A new algorithm for processing interferometric data-stacks: SqueeSAR. IEEE Transactions on Geoscience and Remote Sensing 49, 3460–3470. <https://doi.org/10.1109/TGRS.2011.2124465>.
- Ferretti, A., Prati, C., Rocca, F., 2001. Permanent scatterers in SAR interferometry. IEEE Transactions on Geoscience and Remote Sensing 39, 8–20. <https://doi.org/10.1109/36.898661>.
- Ferretti, A., Prati, C., Rocca, F., 2000. Nonlinear subsidence rate estimation using permanent scatterers in differential SAR interferometry. IEEE Transactions on Geoscience and Remote Sensing 38, 2202–2212. <https://doi.org/10.1109/36.868878>.
- Gabriel, A.K., Goldstein, R.M., Zebker, H.A., 1989. Mapping small elevation changes over large areas: differential radar interferometry. Journal of Geophysical Research 94. <https://doi.org/10.1029/JB094iB07p09183>.

- Galve, J.P., Reyes-Carmona, C., Barra, A., Monserrat, O., Pérez-Peña, V., Ruano, P., Azañón, M., María, R., 2019. Monitoring unstable urbanized slopes in Granada coast through InSAR analysis of Sentinel-1 images. *Geophysical Research Abstracts - EGU General Assembly 21*, 17631.
- Gasc-Barbier, M., Barra, A., Buxó, P., Trapero, L., Crosetto, M., Colell, X., Fabregat, I., Echeverria, A., Marturia, J., 2021. Monitoring deformations related to geological risks with InSAR data – the MOMPA project. *OP Conference Series: Earth and Environmental Science*, IOP Publishing, 2 833, 12142. <https://doi.org/10.1088/1755>.
- Ghiglia, D.C., Pritt, M.D., 1998. Two-dimensional phase unwrapping: theory, algorithms, and software. A Wiley Interscience Publication.
- Hanssen, R.F., 2001. *Radar interferometry: data interpretation and error analysis*, Springer Science & Business Media.
- Hooper, A., 2008. A multi-temporal InSAR method incorporating both persistent scatterer and small baseline approaches. *Geophysical Research Letters* 35. <https://doi.org/10.1029/2008GL034654>.
- Hooper, A., Zebker, H., Segall, P., Kampes, B., 2004. A new method for measuring deformation on volcanoes and other natural terrains using InSAR persistent scatterers. *Geophys Res Lett* 31, 1–5. <https://doi.org/10.1029/2004GL021737>.
- Hyogo Framework 2005- 2015, 2007. Hyogo Framework for Action 2005-2015: Building the resilience of nations and communities to disasters | UNDRR. URL <https://www.undrr.org/publication/hyogo-framework-action-2005-2015-building-resilience-nations-and-communities-disasters> (accessed 3.22.22).
- Kalia, A.C., 2017. User driven products in the context of the ground motion service Germany. *International Geoscience and Remote Sensing Symposium (IGARSS)*, 2017, 1688–1691. <https://doi.org/10.1109/IGARSS.2017.8127299>.
- Kalia, A.C., Frei, M., Lege, T., 2017. A Copernicus downstream-service for the nationwide monitoring of surface displacements in Germany. *Remote Sensing of Environment* 202, 234–249. <https://doi.org/10.1016/J.RSE.2017.05.015>.
- Krishnakumar, V., Qiu, Z., Monserrat, O., Barra, A., López-Vinielles, J., Reyes-Carmona, C., Gao, Q., Cuevas-González, M., Palamà, R., Crippa, B., Gili, J.A., 2021. Sentinel-1 a-dinsar approaches to map and monitor ground displacements. *Remote Sensing* 13. <https://doi.org/10.3390/rs13061120>.
- Lanari, R., Casu, F., Manzo, M., Zeni, G., Berardino, P., Manunta, M., Pepe, A., 2007. An overview of the Small Baseline Subset algorithm: A DInSAR technique for surface deformation analysis. *Pure and Applied Geophysics* 164, 637–661. <https://doi.org/10.1007/S00024-007-0192-9>.
- López-Vinielles, J., Ezquerro, P., Fernández-Merodo, J.A., Béjar-Pizarro, M., Monserrat, O., Barra, A., Blanco, P., García-Robles, J., Filatov, A., García-Davalillo, J.C., Sarro, R., Mulas, J., Mateos, R.M., Azañón, J.M., Galve, J.P., Herrera, G., 2020. Remote analysis of an open-pit slope failure: Las Cruces case study, Spain. *Landslides* 17, 2173–2188. <https://doi.org/10.1007/s10346-020-01413-7>.
- Massonnet, D., Briole, P., Arnaud, A., 1995. Deflation of Mount Etna monitored by spaceborne radar interferometry. *Nature* 1995 375:6532 375, 567–570. <https://doi.org/10.1038/375567a0>.

- Massonnet, D., Feigl, K.L., 1998. Radar interferometry and its application to changes in the earth's surface. *Reviews of Geophysics* 36, 441–500. <https://doi.org/10.1029/97RG03139>.
- Massonnet, D., Rossi, M., Carmona, C., Adragna, F., Peltzer, G., Feigl, K., Rabaute, T., 1993. The displacement field of the Landers earthquake mapped by radar interferometry. *Nature* 1993 364:6433 364, 138–142. <https://doi.org/10.1038/364138A0>.
- Mateos, R.M., López-Vinielles, J., Poyiadji, E., Tsagkas, D., Sheehy, M., Hadjicharalambous, K., Liscák, P., Podolski, L., Laskowicz, I., Iadanza, C., Gauert, C., Todorović, S., Auflič, M.J., Maftelj, R., Hermanns, R.L., Kociu, A., Sandić, C., Mauter, R., Sarro, R., Béjar, M., Herrera, G., 2020. Integration of landslide hazard into urban planning across Europe. *Landscape and Urban Planning* 196. <https://doi.org/10.1016/j.landurbplan.2019.103740>.
- Mirmazloumi, S.M., Wassie, Y., Navarro, A., Palamà, R., Krishnakumar, V., Barra, A., Cuevas-González, M., Crosetto, M., Monserrat, O., 2022. Classification of ground deformation using sentinel-1 persistent scatterer interferometry time series. *GIScience & Remote Sensing* 59, 374–392. <https://doi.org/10.1080/15481603.2022.2030535>.
- Mondini, A.C., Guzzetti, F., Chang, K.T., Monserrat, O., Martha, T.R., Manconi, A., 2021. Landslide failures detection and mapping using Synthetic Aperture Radar: Past, present and future. *Earth-Science Reviews* 216, 103574. <https://doi.org/10.1016/J.EARSCIREV.2021.103574>.
- Mondini, A.C., Santangelo, M., Rocchetti, M., Rossetto, E., Manconi, A., Monserrat, O., 2019. Sentinel-1 SAR Amplitude Imagery for Rapid Landslide Detection. *Remote Sensing* 2019, Vol. 11, Page 760 11, 760. <https://doi.org/10.3390/RS11070760>.
- Monserrat, O., 2012. Deformation measurement and monitoring with Ground-Based SAR. *Castelldefels*.
- Monserrat, O., Barra, A., Herrera, G., Bianchini, S., Lopez, C., Onori, R., Reichenbach, P., Sarro, R., Mateos, R.M., Solari, L., Ligüérezana, S., Carralero, I.P., 2018. SAFETY project: Sentinel-1 based tools for geohazards monitoring and management, in: *International Archives of the Photogrammetry, Remote Sensing and Spatial Information Sciences - ISPRS Archives*. <https://doi.org/10.5194/isprs-archives-XLII-3-W4-351-2018>.
- Monserrat, O., Barra, A., Herrera, G., Solari, L., González-Alonso, E., Béjar-Pizarro, M., Bianchini, S., Sarro, R., Fernández García, A., Reichenbach, P., Catani, F., Crosetto, M., 2019. The U-Geohaz project: Sentinel-1 to support geohazards early warning systems and impact assessment. *Geophysical Research Abstracts - EGU General Assembly* 21, 13569.
- Monserrat, O., Béjar-Pizarro, M., Moretti, S., Lopez, C., Garcia-Cañada, L., Á Benito-Saz, M., 2017. The Safety project: Sentinel-1 for Civil Protection geohazards management. *Geophysical Research Abstracts - EGU General Assembly* 19, 2017–15406.
- Mora, O., Mallorqui, J.J., Broquetas, A., 2003. Linear and nonlinear terrain deformation maps from a reduced set of interferometric SAR images. *IEEE Transactions on Geoscience and Remote Sensing* 41, 2243–2253. <https://doi.org/10.1109/TGRS.2003.814657>.

- Navarro, J.A., Cuevas, M., Tomás, R., Barra, A., Crosetto, M., 2019a. Automating the Detection and Classification of Active Deformation Areas—A Sentinel-Based Toolset. Proceedings of The II Geomatics Engineering Conference 19, 15. <https://doi.org/10.3390/PROCEEDINGS2019019015>.
- Navarro, J.A., Cuevas, M., Tomás, R., Barra, A., Crosetto, M., 2019b. A Toolset to Detect and Classify Active Deformation Areas using Interferometric SAR Data. Proceedings of the 5th International Conference on Geographical Information Systems Theory, Applications and Management (GISTAM 2019) 167–174. <https://doi.org/10.5220/0007617701670174>.
- Navarro, J.A., Cuevas-González, M., Barra, A., Crosetto, M., 2018. Detection of Active Deformation Areas based on Sentinel-1 imagery: an efficient, fast and flexible implementation. Proceedings of the 18th International Scientific and Technical Conference, Crete, Greece 24–27. <https://doi.org/10.5281/ZENODO.2531722>.
- Navarro, J.A., Tomás, R., Barra, A., Pagán, J.I., Reyes-Carmona, C., Solari, L., Vinielles, J.L., Falco, S., Crosetto, M., 2020. ADAtools: Automatic detection and classification of active deformation areas from PSI displacement maps. ISPRS International Journal of Geo-Information 9. <https://doi.org/10.3390/IJGI9100584>.
- Notti, D., Herrera, G., Bianchini, S., Meisina, C., García-Davalillo, J.C., Zucca, F., 2014. A methodology for improving landslide PSI data analysis. International Journal of Remote Sensing 35, 2186–2214. <https://doi.org/10.1080/01431161.2014.889864>.
- Novellino, A., Cigna, F., Brahmi, M., Sowter, A., Bateson, L., Marsh, S., 2017. Assessing the Feasibility of a National InSAR Ground Deformation Map of Great Britain with Sentinel-1. Geosciences (Switzerland) 7. <https://doi.org/10.3390/geosciences7020019>.
- Papoutsis, I., Kontoes, C., Alatza, S., Apostolakis, A., Loupasakis, C., 2020. InSAR Greece with Parallelized Persistent Scatterer Interferometry: A National Ground Motion Service for Big Copernicus Sentinel-1 Data. Remote Sensing 12, 1–27. <https://doi.org/10.3390/RS12193207>.
- Perissin, D., Wang, T., 2012. Repeat-pass SAR interferometry with partially coherent targets. IEEE Transactions on Geoscience and Remote Sensing 50, 271–280. <https://doi.org/10.1109/TGRS.2011.2160644>.
- Prats-Iraola, P., Rodriguez-Cassola, M., de Zan, F., Scheiber, R., López-Dekker, P., Barat, I., Geudtner, D., 2015. Role of the Orbital Tube in Interferometric Spaceborne SAR Missions. IEEE Geoscience and Remote Sensing Letters 12, 1486–1490. <https://doi.org/10.1109/LGRS.2015.2409885>.
- Przyłucka, M., Herrera, G., Graniczny, M., Colombo, D., Béjar-Pizarro, M., 2015. Combination of conventional and advanced DInSAR to monitor very fast mining subsidence with TerraSAR-X data: Bytom City (Poland). Remote Sensing 7, 5300–5328. <https://doi.org/10.3390/rs70505300>.
- Raspini, F., Bianchini, S., Ciampalini, A., del Soldato, M., Solari, L., Novali, F., del Conte, S., Rucci, A., Ferretti, A., Casagli, N., 2018. Continuous, semi-automatic monitoring of ground deformation using Sentinel-1 satellites. Scientific Reports 8, 1–11. <https://doi.org/10.1038/s41598-018-25369-w>.
- Reyes-Carmona, C., Barra, A., Galve, J.P., Monserrat, O., Pérez-Peña, J.V., Mateos, R.M., Notti, D., Ruano, P., Millares, A., López-Vinielles, J., Azañón, J.M., 2020. Sentinel-1 DInSAR for monitoring active

- landslides in critical infrastructures: The case of the Rules reservoir (Southern Spain). *Remote Sensing* 12. <https://doi.org/10.3390/RS12050809>.
- Reyes-Carmona, C., Barra, A., Monserrat, O., Galve-Arnedo, J.P., Vicente Pérez-Peña, J., Ruano, P., Azañón, M., María, R., 2019. A Sentinel-1 InSAR study for monitoring landslide movement in the Rules Reservoir. *Geophysical Research Abstracts - EGU General Assembly 21*, 15073.
- Reyes-Carmona, C., Galve, J.P., Moreno-Sánchez, M., Riquelme, A., Ruano, P., Millares, A., Teixidó, T., Sarro, R., Pérez-Peña, J.V., Barra, A., Ezquerro, P., López-Vinielles, J., Béjar-Pizarro, M., Azañón, J.M., Monserrat, O., Mateos, R.M., 2021. Rapid characterisation of the extremely large landslide threatening the Rules Reservoir (Southern Spain). *Landslides* 2021 1–18. <https://doi.org/10.1007/S10346-021-01728-Z>.
- Roberti, G., Ward, B.C., van Wyk De Vries, B., Falorni, G., 2018. Landslides and glacier retreat at Mt. Meager volcano: hazard and risk challenges Characterization of glacier-dammed lakes through space and time View project.
- Salvi, S., Stramondo, S., Funning, G.J., Ferretti, A., Sarti, F., Mouratidis, A., 2012. The Sentinel-1 mission for the improvement of the scientific understanding and the operational monitoring of the seismic cycle. *Remote Sensing of Environment* 120, 164–174. <https://doi.org/10.1016/j.rse.2011.09.029>.
- Sánchez-Gámez, P., Navarro, F.J., 2017. Glacier Surface Velocity Retrieval Using D-InSAR and Offset Tracking Techniques Applied to Ascending and Descending Passes of Sentinel-1 Data for Southern Ellesmere Ice Caps, Canadian Arctic. *Remote Sensing* 9, 442. <https://doi.org/10.3390/RS9050442>.
- Sendai Framework 2015-2030. What is the Sendai Framework? | UNDRR. URL <https://www.undrr.org/implementing-sendai-framework/what-sendai-framework> (accessed 3.22.22).
- Sentinel-1 Intensity Analysis in ENVI SARscape Tutorial. URL <https://www.l3harrisgeospatial.com/docs/sentinel1intensityanalysistutorial.html> (accessed 3.18.22).
- Sharma, S., Senzaki, K., Senda, Y., Aoki, H., 2018. CNN-based ship classification method incorporating SAR geometry information. <https://doi.org/10.1117/12.2325282> 10789, 108–116. <https://doi.org/10.1117/12.2325282>.
- Skempton, A.W., Macdonald, D.H., 1956. THE ALLOWABLE SETTLEMENTS OF BUILDINGS. *Proceedings of the Institution of Civil Engineers* 5, 727–768. <https://doi.org/https://doi.org/10.1680/ipeds.1956.12202>.
- Snoeij, P., Attema, E., Davidson, M., Floury, N., Levrini, G., Rosich, B., Rommen, B., 2008. Sentinel-1, the GMES radar mission. 2008 IEEE Radar Conference 1–5. <https://doi.org/10.1109/RADAR.2008.4720735>.
- Solari, L., Barra, A., Herrera, G., Bianchini, S., Monserrat, O., Béjar-Pizarro, M., Crosetto, M., Sarro, R., Moretti, S., 2018. Fast detection of ground motions on vulnerable elements using sentinel-1 InSAR data. *Geomatics, Natural Hazards and Risk* 9, 152–174. <https://doi.org/10.1080/19475705.2017.1413013>.

- Solari, L., Bianchini, S., Franceschini, R., Barra, A., Monserrat, O., Thuegaz, P., Bertolo, D., Crosetto, M., Catani, F., 2020a. Satellite interferometric data for landslide intensity evaluation in mountainous regions. *International Journal of Applied Earth Observation and Geoinformation* 87. <https://doi.org/10.1016/J.JAG.2019.102028>.
- Solari, L., Montalti, R., Barra, A., Monserrat, O., Bianchini, S., Crosetto, M., 2020b. Multi-temporal satellite interferometry for fast-motion detection: An application to salt solution mining. *Remote Sensing* 12, 1–21. <https://doi.org/10.3390/RS12233919>.
- Tomás, R., Pagán, J.I., Navarro, J.A., Cano, M., Pastor, J.L., Riquelme, A., Cuevas-González, M., Crosetto, M., Barra, A., Monserrat, O., Lopez-Sanchez, J.M., Ramón, A., Ivorra, S., del Soldato, M., Solari, L., Bianchini, S., Raspini, F., Novali, F., Ferretti, A., Costantini, M., Trillo, F., Herrera, G., Casagli, N., 2019. Semi-automatic identification and pre-screening of geological-geotechnical deformational processes using persistent scatterer interferometry datasets. *Remote Sensing* 11. <https://doi.org/10.3390/rs11141675>.
- Torres, R., Levrini, G., Rost, F., Piet, A., Snoeij, P., L'abbat, M., Geudtner, D., Bibby, D., Davidson, M., Attema, E., Potin, P., Rommen, B., Floury, N., Brown, M., Navas Traver, I., Deghaye, P., Duesmann, B., Rosich, B., Miranda, N., Bruno, C., L'abbate, M., Croci, R., Pietropaolo, A., Huchler, M., Rostan, F., 2012. GMES Sentinel-1 mission. *Remote Sensing of Environment* 120, 9–24. <https://doi.org/10.1016/j.rse.2011.05.028>.
- Vassilakis, E., Kaviris, G., Kapetanidis, V., Papageorgiou, E., Foumelis, M., Konsolaki, A., Petrakis, S., Evangelidis, C.P., Alexopoulos, J., Karastathis, V., Voulgaris, N., Tselentis, G.-A., 2022. The 27 September 2021 Earthquake in Central Crete (Greece) - Detailed Analysis of the Earthquake Sequence and Indications for Contemporary Arc-Parallel Extension to the Hellenic Arc. *Applied Sciences* 12, 2815. <https://doi.org/10.3390/APP12062815>.

Annex 1

First insights on the potential of Sentinel-1 for landslides detection

First insights on the potential of Sentinel-1 for landslides detection

Anna Barra^a, Oriol Monserrat^a, Paolo Mazzanti^{b,c}, Carlo Esposito^b, Michele Crosetto^a and Gabriele Scarascia Mugnozza^{b,c}

^aCentre Tecnològic de Telecomunicacions de Catalunya (CTTC), Division of Geomatics, Castelldefels, Barcelona, Spain; ^bDipartimento di Scienze della Terra, Università degli Studi di Roma 'La Sapienza', Rome, Italy; ^cNHAZCA S.r.l., spin off Università degli Studi di Roma 'La Sapienza', Rome, Italy

ABSTRACT

This paper illustrates the potential of Sentinel-1 for landslide detection, mapping and characterization with the aim of updating inventory maps and monitoring landslide activity. The study area is located in Molise, one of the smallest regions of Italy, where landslide processes are frequent. The results achieved by integrating Differential Synthetic Aperture Radar Interferometry (DInSAR) deformation maps and time series, and Geographical Information System (GIS) multilayer analysis (optical, geological, geomorphological, etc.) are shown. The adopted methodology is described followed by an analysis of future perspectives. Sixty-two landslides have been detected, thus allowing the updating of pre-existing landslide inventory maps. The results of our ongoing research show that Sentinel-1 might represent a significant improvement in terms of exploitation of SAR data for landslide mapping and monitoring due to both the shorter revisit time (up to 6 days in the close future) and the wavelength used, which determine a higher coherence compared to other SAR sensors.

ARTICLE HISTORY

Received 28 October 2015
Accepted 23 March 2016

KEYWORDS:

InSAR; Sentinel-1; landslide inventory map; landslide activity; monitoring

1. Introduction

A precise inventory map containing information on landslide activity is an essential input to landslide susceptibility and hazard analyses. The contribution of satellite Synthetic Aperture Radar (SAR) interferometry to landslide risk mitigation is well known within the scientific community and many encouraging results have been obtained (Catani et al. 2005; Herrera et al. 2009; Righini et al. 2012; Cigna et al. 2013; Crosetto et al. 2013; Raspini et al. 2013; Frangioni et al. 2014; Ciampalini et al. 2015; Rocca et al. 2015). Areas characterized by high coherence of images (e.g. due to rock lithology or urban setting) are required to obtain results and, in this regard, the expected increased capabilities of Sentinel-1, compared to other SAR sensors such as ERS, ENVISAT or ALOS, for landslide mapping and monitoring are related to both the wavelength (55.5 mm) and the short temporal baseline (12 days) (Ferretti et al. 2007). The latter is expected to be a key feature for enhanced coherence and, therefore, to define monitoring and updating plans. A set of 14 Sentinel-1 images acquired over the Molise region, Southern Italy (Figure 1), a critical area geologically susceptible to landslides, were processed with the aim of assessing these potentialities. Even though the Molise region is mostly covered by agricultural fields and forests (63% and 35%, respectively; Di Somma 2011),

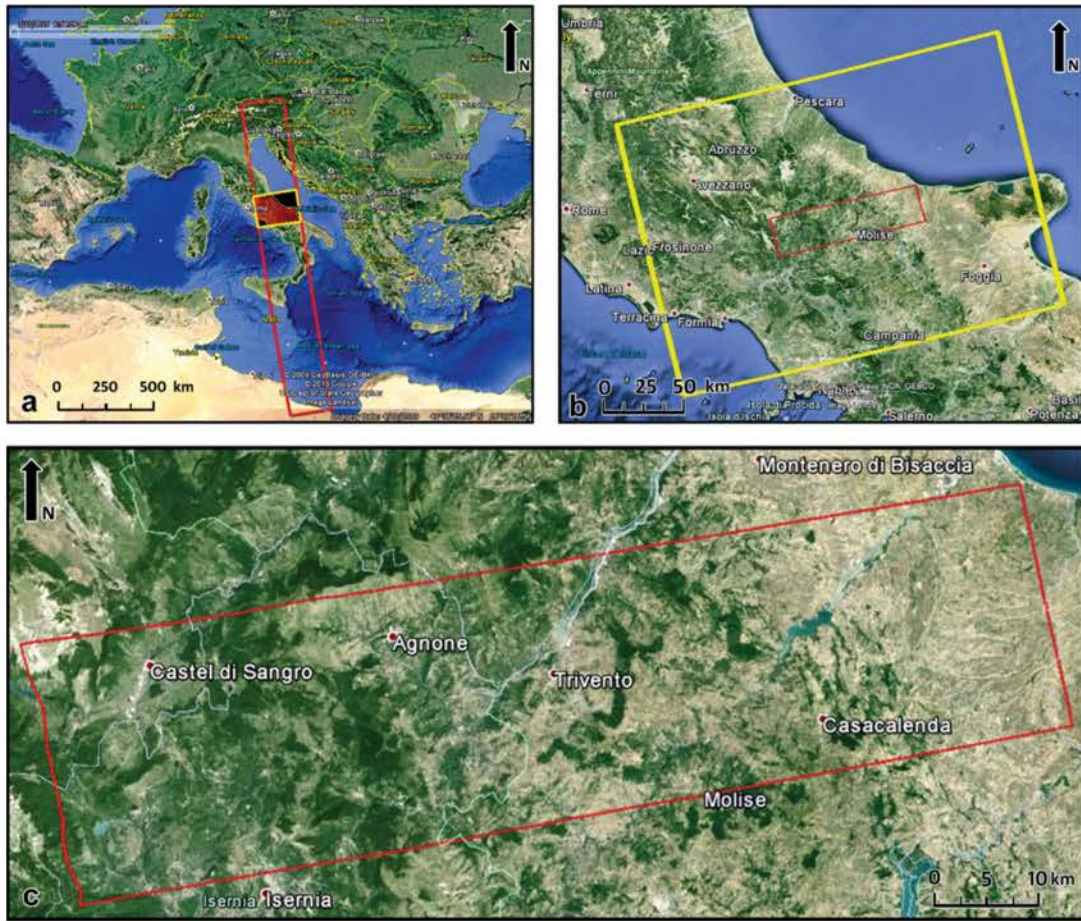


Figure 1. (a) The Sentinel-1 strip and the selected frame (ESA); (b) zoom of the selected frame and location of the analyzed area, corresponding to a single burst; (c) zoom of the analyzed area.

indicating non-optimal conditions for SAR coherence, promising results have been obtained by spatially and temporally examining 12-days interferograms followed by a multilayer analysis in a Geographical Information System (GIS) environment.

2. Study area: the Molise region

The Molise region is located in Southern Italy and is one of the Italian regions most affected by landslide phenomena (Roskopf & Aucelli 2007). From the geo-lithological point of view (Molise Region 2001; Sgrosso & Naso 2012), Molise is composed by sedimentary formations: marine environment formations (from Triassic to Pleistocene) and recent continental deposits (Pliocene-Holocene). The study area (Figure 2) is mostly characterized by the turbidite sedimentation of Molisian Basin (Paleogene–Miocene), which includes the basal complex of ‘Varicolor Clays’ and flysches with different composition (marly-calcareous, marly-arenitic or mostly arenitic). A few zones, situated in the western part of the area, are characterized by calcareous-dolomitic lithologies of the carbonate platform (Piattaforma Abruzzese-Campana, Triassic–Cretaceous) and by calcareous-marl detrital sedimentation of the transitional ramp (Cretaceous–Miocene). The north-eastern area is characterized by the sandy-clayey deposits of the Adriatic Foredeep Basin (Pliocene–Pleistocene).

The geo-lithological and geomorphological settings make the Molise region prone to landslide movements. In fact, according to a recent study based on the Italian Inventory of Landslide Phenomena (IFFI) synthesized by Trigila et al. (2013), almost 18% of the Molise region is affected by landslides. The IFFI also classify as active about 67% of the identified landslides in Molise. The main

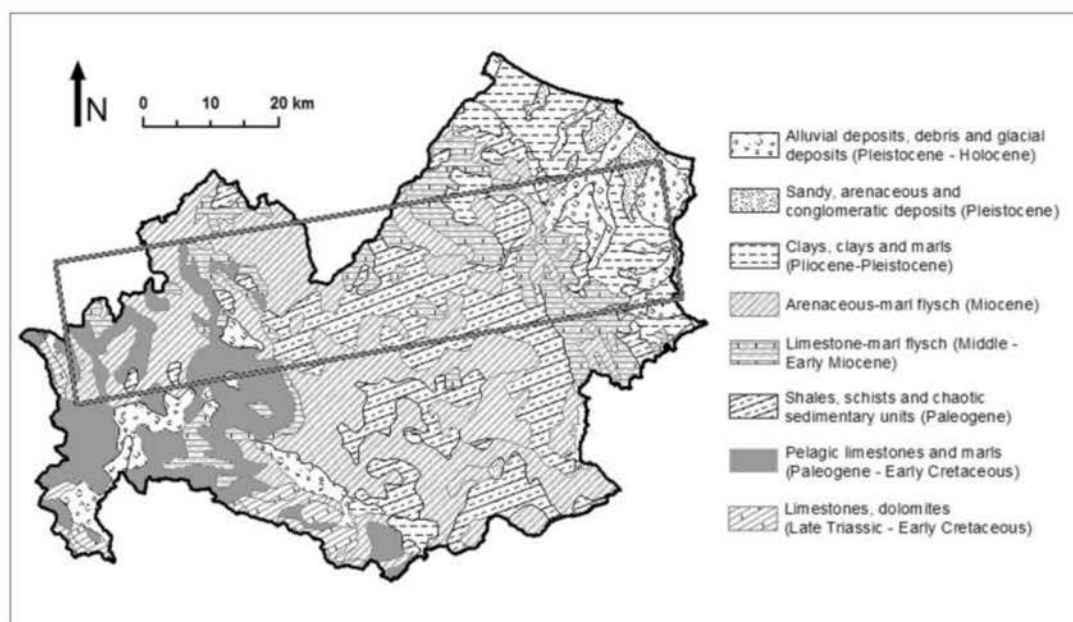


Figure 2. Lithologic map of the Molise region (scale 1:500,000). Data provided by the Institute for Environmental Protection and Research, ISPRA (Istituto Superiore per la Protezione e la Ricerca Ambientale).

landslide typologies are earth flows and complex movements (Figure 3) and are usually associated with the fluvial evolution (Aucelli et al. 2001) and triggered by intense rainfall events.

The study area was affected by several landslides (Figure 3(c,e)) during the analyzed period (October 2014–April 2015), mainly triggered by intense rainfalls occurred from December 2014 to March 2015 (Figures 5 and 6(c)).

3. Sentinel-1 data analysis

The Differential SAR Interferometry (DInSAR) procedure (Crosetto et al. 2011) used in this study (Figure 4) is explained in this section. Our investigation has focused on a single burst (Figure 1) of a set of 14 Sentinel-1 Interferometric Wide Swath images (single polarization VV) acquired in ascending orbit spanning the period November 2014–March 2015 (the acquisition dates of the images are shown in Figure 5(c)).

The procedure is divided into two main steps: the DInSAR analysis and the Multilayer GIS analysis. The first step is performed in SAR geometry and consists in the analysis of the interferometric data, both at spatial and temporal levels, with the aim of detecting areas affected by deformation and, therefore, characterizing landslide activity. The main output is a set of areas potentially affected by deformation. The second step (multilayer GIS analysis) consists in the integration of DInSAR derived data with geological and geomorphological data to interpret and validate the detected areas of deformation and, consequently, to update the pre-existing landslide inventory maps.

The steps of the procedure followed in this study (Figure 4) are:

- *Interferogram generation*: generation of the network of interferograms to be used in the analysis. Only interferometric pairs with the minimum temporal baseline (12 days, except one of 36 days) were estimated.
- *Spatial analysis*: visual inspection of the interferograms to identify spatial patterns with the potential to be deformation areas (Figures 5(b) and 6(a)) (Rocca et al. 2014). Note that this analysis only provides information on movements that are fast enough to be observed in 12 day periods. Once the patterns are detected, the pairwise logic (Massonnet & Feigl 1998) is

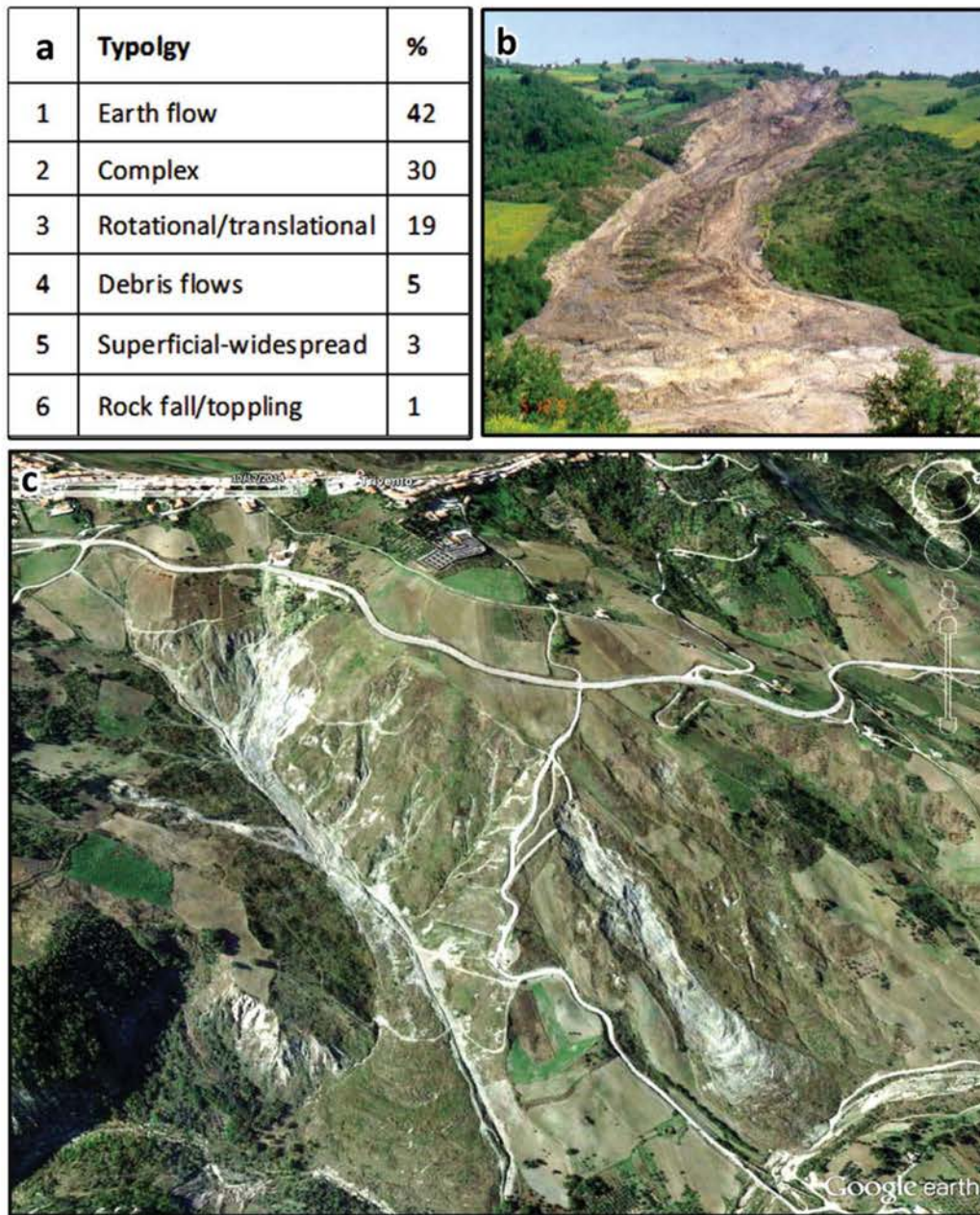


Figure 3. (a) Percentage of landslide typologies in the Molise region (Roskopf & Aucelli, 2007, Cruden & Varnes, 1996); (b) landslide of Ribalimosani (Campobasso), April 1996 (Roskopf & Aucelli, 2007); (c) Google Earth satellite image showing landslides near Trivento city (acquisition date: 10 December 2014).

used to discard patterns attributable to other sources, such as topographic errors or atmosphere (Hanssen 2001). The result of this step is a set of areas potentially affected by deformation.

- *Temporal analysis (time series estimation)*: time series generation over a selected subset of pixels. The procedure involves unwrapping the interferograms (Costantini 1998) using only pixels with a coherence value higher than a given threshold (0.2 in this work). The temporal series are then obtained by integrating the unwrapped phases as follows:

$$\begin{cases} \varphi_j = \varphi_{j-1} + \Delta\varphi_{j(j-1)} \\ \varphi_0 = 0 \end{cases} \quad (1)$$

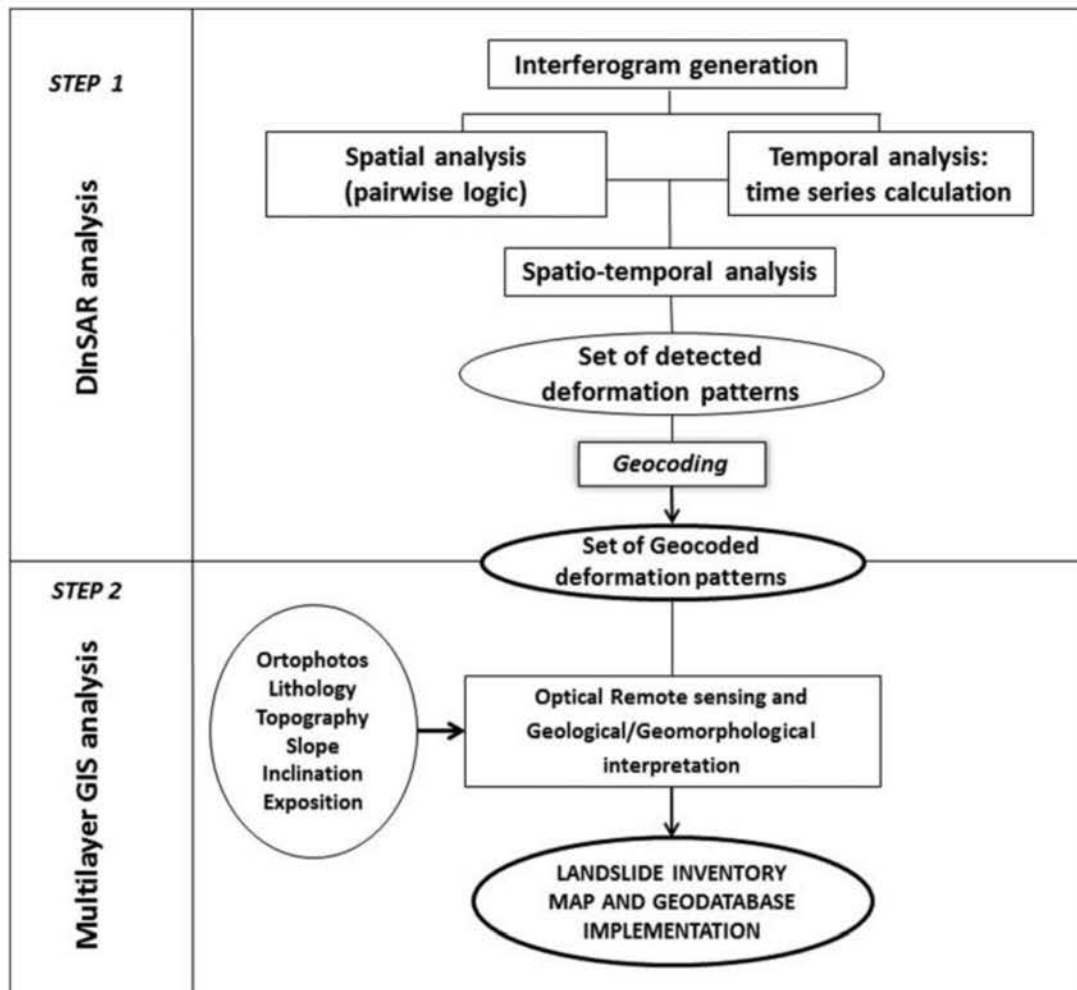


Figure 4. Flow-chart of the procedure used in this study.

where φ_j and φ_0 are the accumulated and the reference phases, and $\Delta\varphi_{j(j-1)}$ is the interferometric phase calculated from images $j - 1$ and j . Thus, the temporal evolution of the phase is obtained for each point. Finally, the map of accumulated deformation is analyzed to search for new spatial patterns characterized by slow deformation rates (Figure 6(b)). It is worth underlining that the analysis of the time series is done with respect to a local stable reference to avoid critical atmospheric effects.

- *Spatio-temporal analysis*: the potential areas of deformation detected in the previous steps are analyzed together with the time series. This combined analysis is useful to: (i) detect phase unwrapping errors (aliasing); (ii) assess the temporal behaviour of each detected deformation phenomenon; (iii) confirm or modify the shape of the deformation area detected. The result of this step is the final set of detected deformation phenomena.

The first block ends with the georeferencing of the deformation phenomena to a known coordinate system.

- *Multilayer GIS analysis*: geological/geomorphological interpretation of the detected areas by the exploitation of different information layers in a GIS environment: Digital Elevation Model and derived data (e.g. aspect and slope), ortophoto interpretation, geo-lithological maps, existing landslide inventory maps, etc. The previously identified potential deformation areas are confirmed, denied or modified in this phase and the results can be used to update landslide inventory maps.

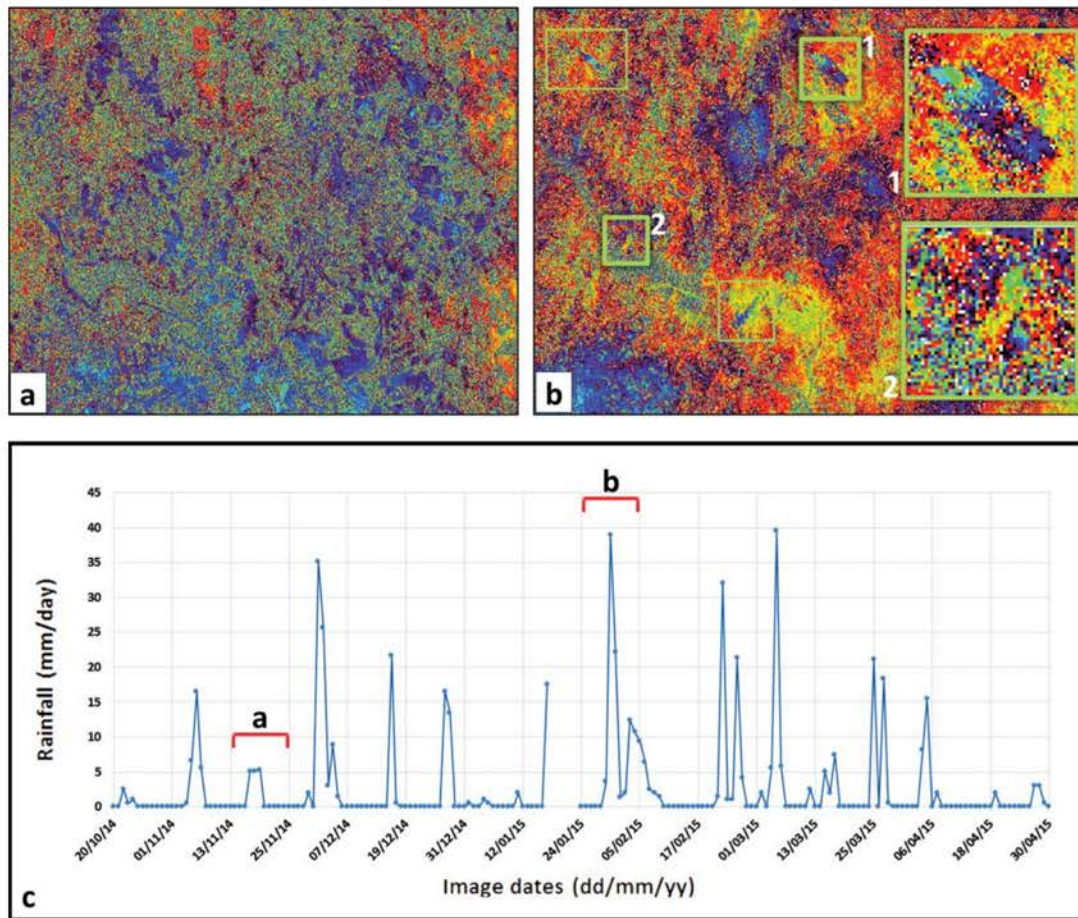


Figure 5. Interferograms derived from images collected on 13 November 2014 and 25 November 2014 (a) and on 24 January 2015 and 5 February 2015 (b). The rectangles in (b) highlight several potential deformation phenomena and two of them are zoomed (squares 1 and 2); (c) daily rainfall during the analyzed period, where the a and b letters mark the periods of the interferograms from (a) and (b). (b) shows more deformation patterns than (a), which is coherent with the higher precipitation amount of the related period.

4. Achieved results

The potential deformation phenomena detected during the interferometric analysis (Figure 5) are mostly concentrated in the interferograms including high precipitation periods. This is a promising result since intense rainfall is the main triggering/accelerating factor of the studied landslides.

Figure 6 displays an example of landslide detected in an interferogram that clearly shows the shape of the deformation area. Figure 6(b) shows the same area in the accumulated deformation map, where the colours represent the deformation in line of sight (LOS) because SAR sensors can only measure the projection of the real movement along the LOS. Two deformation areas with opposite sign (the red and the blue one) are displayed. This is the effect of the combination between landslide movement and radar LOS direction (see Figure 6(d)): in the blue area the main slope inclination is toward the satellite (SW direction), while in the red one it is outward (E–SE direction). Furthermore, the central area appears to suffer smaller displacements because the main direction of the deformation is almost parallel to LOS, which is not detectable with this technique. The shape of the landslide area is better bounded by jointly analyzing the interferogram and the accumulated deformation map. Aliasing errors can be checked at the time series (Figure 6(c)) by analyzing the consistency with the displacement information of the interferogram. Furthermore, Figure 6(c) shows how the time series analysis allowed characterizing the temporal activity of the landslide, even when the deformation is not fast enough to be well observed in a 12-day interferogram. The

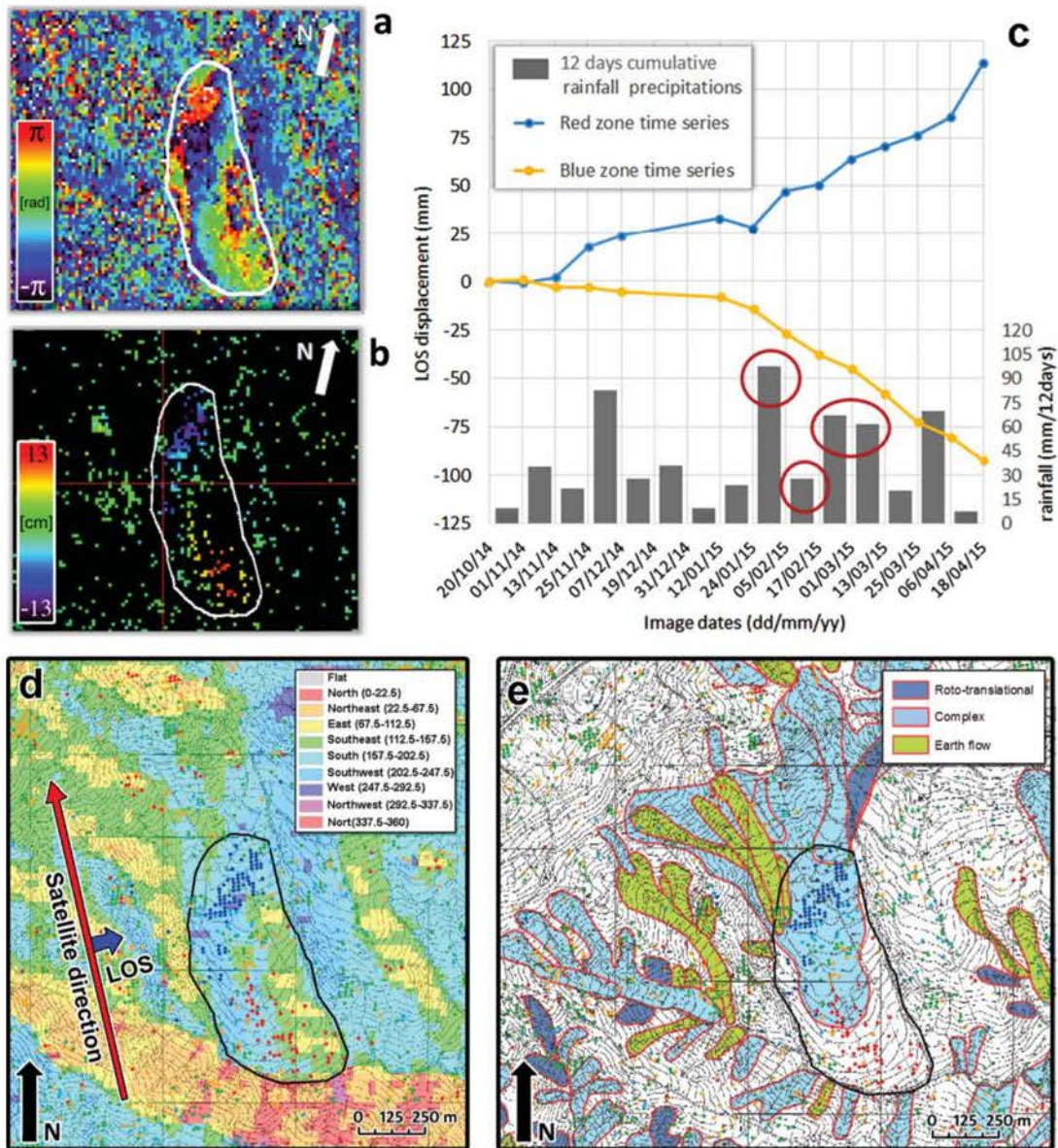


Figure 6. (a) Potential deformation phenomenon in the 12-day interferogram covering the period from 24 January 2015 to 5 February 2015; (b) the same deformation pattern in the total accumulated deformation map (over the selected subset of pixels). Two main areas can be distinguished: the red one and the blue one; (c) time series in line of sight (LOS) of the two areas (blue and red) and 12-day cumulative rainfall corresponding to each interferogram. Red circles indicate the periods when the interferograms clearly show the deformation pattern; (d) and (e) the accumulated deformation map (coloured points) superimposed to a topographic base-map. The black polygon represents the detected deformation area. In (d) is also showed the slope exposition map and the satellite and LOS directions; in (e) the coloured polygons are the landslides of the Italian Landslide Phenomena Inventory (IFFI). Note that the colour scale of the points in (d) and (e) is the same of figure (b).

retrieved deformation pattern allowed a better definition of the boundary and the activity of an existing landslide (Figure 6(e)).

A set of 29 potential deformation phenomena were detected during the DInSAR analysis (Figure 4), which were then georeferenced and integrated with other information layers in the GIS analysis that confirmed the areas to be affected by landslides. Moreover, in some cases, the analysis of a single detected deformation area allowed to distinguish different landslide bodies (Figure 7). Table 1 summarizes the results obtained compared with the existing inventory: a total of 62 active landslides were detected of which 13 are new, 31 have been updated in terms of spatial delimitation and 18 have been confirmed to be active.

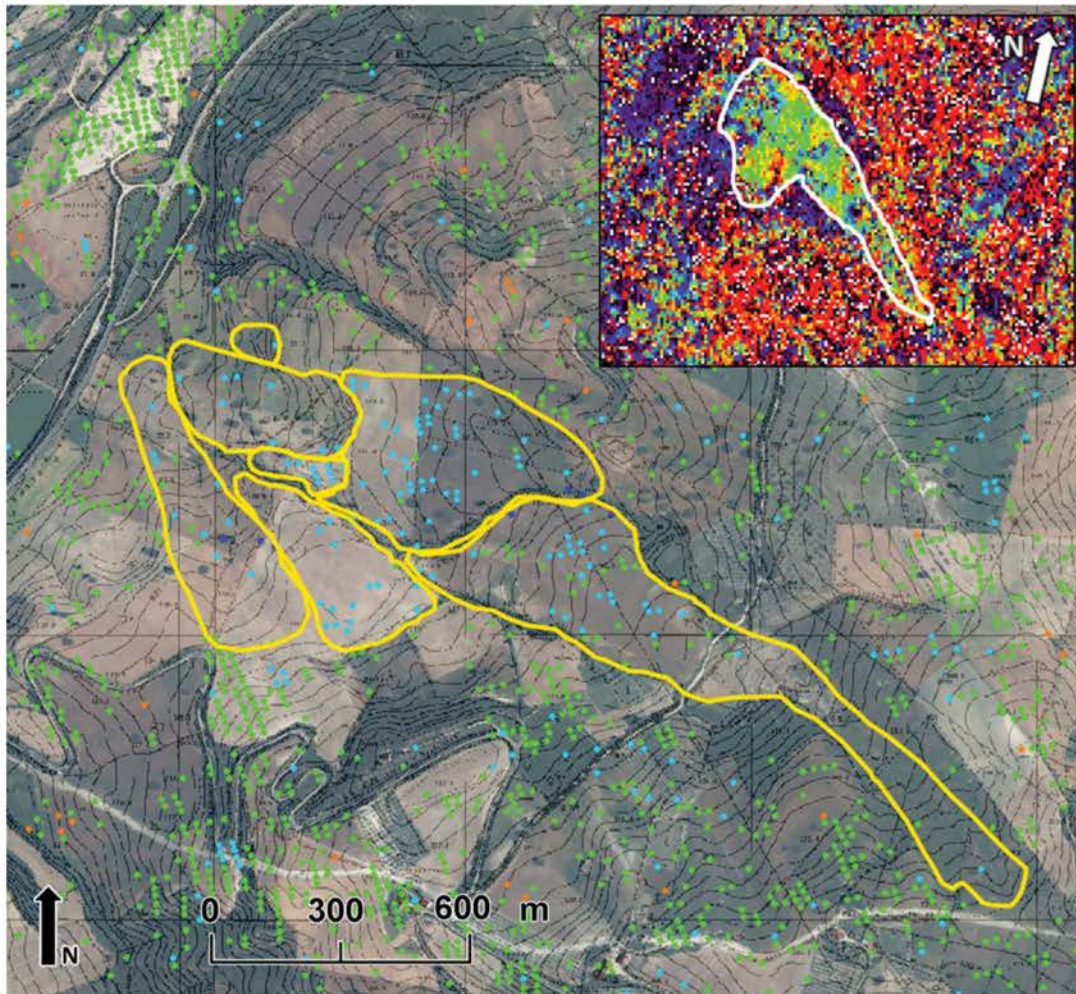


Figure 7. Example of landslide bodies distinguished during the multilayer GIS analysis step are shown in this figure, that also displays the accumulated deformation map (coloured points) superimposed on a topographic base. The image at the upper-right shows the deformation pattern (bounded by a white line) detected in an interferogram.

Table 1. Detected potential deformation phenomena and confirmed landslides.

	Detected deformation patterns	Landslide polygons	Comparison with the existing inventory		
			NEW	UPDATED	CONFIRMED
Abs. Number	29	62	13	31	18

5. Conclusions and outlook

The research carried out in this work is aimed at evaluating the performance of Sentinel-1 data for landslide mapping and monitoring. Fourteen Sentinel-1 SLC images, acquired during a temporal span of seven months in the Molise region (Italy), have been processed. A single burst of a Sentinel-1 frame (approximately 1875 km²) has been analyzed by integrating DInSAR techniques with geological/geomorphological data in a multilayer GIS environment.

Despite the short period of time and, therefore, the small number of images available, 62 active landslides have been detected, thus allowing updating the pre-existing inventory maps both in terms of landslide boundaries and activity. These results demonstrate the potential of Sentinel-1 for landslide analysis and monitoring. Besides, a better understanding of landslide behaviour and its relationship with the triggering factors is expected when longer Sentinel-1 time series are available for analysis. This will be a key issue to perform hazard analyses.

The main disadvantage of the procedure used in this study is the manual data analysis and interpretation which makes the analysis cumbersome and operator-dependent. In this regard, further research will be focused on developing algorithms to automatically detect and extract patterns in the interferograms and rules to ease the GIS analysis. This will be done by integrating Sentinel-1 data and other types of data, in particular Sentinel-2 imagery.

Acknowledgments

This research has been partially funded by the European Commission, Directorate-General Humanitarian Aid and Civil Protection (ECHO), through the SAFETY project (Ref. ECHO/SUB/2015/718679/Prev02) and by the Spanish Ministry of Economy and Competitiveness through the project MIDES (Ref:CGL2013-43000-P).

Disclosure statement

No potential conflict of interest was reported by the authors.

References

- Aucelli PP, Cinque A, Roskopf C. 2001. Geomorphological map of the Trigno basin (Italy): explanatory notes. *Geogr Fis Din Quat.* 24:3–12.
- Catani F, Casagli N, Ermini L, Righini G, Menduni G. 2005. Landslide hazard and risk mapping at catchment scale in the Arno River basin. *Landslides.* 2:329–342.
- Ciampalini A, Raspini F, Bianchini S, Frodella W, Bardi F, Lagomarsino D, Di Traglia F, Moretti S, Proietti C, Pagliara P, et al. 2015. Remote sensing as tool for development of landslide databases: the case of the Messina Province (Italy) geodatabase. *Geomorphology.* 249:103–118.
- Cigna F, Bianchini S, Casagli N. 2013. How to assess landslide activity and intensity with Persistent Scatterer Interferometry (PSI): the PSI-based matrix approach. *Landslides.* 10:267–283.
- Crosetto M, Gili JA, Monserrat O, Cuevas-González M, Corominas J, Serral D. 2013. Interferometric SAR monitoring of the Vallcebre landslide (Spain) using corner reflectors. *Nat Hazard Earth Syst Sci.* 13:923–933.
- Crosetto M, Monserrat O, Cuevas M, Crippa B. 2011. Spaceborne differential SAR interferometry: data analysis tools for deformation measurement. *Remote Sens.* 3:305–318.
- Costantini M. 1998. A novel phase unwrapping method based on network programming. *IEEE Trans Geosci Remote Sens.* 36:813–821.
- Cruden DM, Varnes DJ. 1996. Landslide types and processes. In: *Special Report 247 – Landslides: Investigation and mitigation.* Washington DC: Transportation Research Board.
- Di Somma A. 2011. *L'uso del suolo agrario d'Italia.* Roma: VALMAR. Italian.
- Ferretti A, Monti-Guarnieri A, Prati C, Rocca F, Massonet D. 2007. *InSAR Principles-Guidelines for SAR Interferometry Processing and Interpretation,* 19. The Netherlands: Esa Publications.
- Frangioni S, Bianchini S, Moretti S. 2014. Landslide inventory updating by means of persistent scatterer interferometry (PSI): The Setta basin (Italy) case study. *Geomat Nat Hazard Risk.* 6:419–438.
- Hanssen RF. 2001. *Radar interferometry: data interpretation and error analysis.* The Netherlands: Kluwer Academic Publishers.
- Herrera G, Davalillo JC, Mulas J, Cooksley G, Monserrat O, Pancioli V. 2009. Mapping and monitoring geomorphological processes in mountainous areas using PSI data: Central Pyrenees case study. *Nat Hazard Earth Syst Sci.* 9:1587–1598.
- Massonet D, Feigl KL. 1998. Radar interferometry and its application to changes in the Earth's surface. *Rev Geophys.* 36:441–500.
- Meteoweb. 2015. Available from: <http://www.meteoweb.eu/2015/02/maltempo-situazione-critica-in-molise- evacuazioni-strade-interrotte-trivento-bojano/402570/>. Italian.
- Molise Region. 2001. *Mitigazione del rischio sismico dei centri storici e degli edifici di culto dell'area del Matese nella Regione Molise.* [Seismic risk mitigation in the historic centers and religious buildings in the Matese area of Molise region]. Gruppo Nazionale per la Difesa dai Terremoti, Istituto Nazionale di Geofisica e Vulcanologia, Italy. Italian.
- Raspini F, Moretti S, Casagli N. 2013. Landslide mapping using SqueeSAR data: Giampileri (Italy) case study. In *Landslide science and practice.* Berlin Heidelberg: Springer-Verlag; p. 147–154.
- Righini G, Pancioli V, Casagli N. 2012. Updating landslide inventory maps using Persistent Scatterer Interferometry (PSI). *Int J Remote Sens.* 33:2068–2096.

- Rocca A, Mazzanti P, Perissin D, Bozzano F. 2014. Detection of past slope activity in a desert area using multi-temporal DInSAR with ALOS PALSAR data. *Ital J Eng Geol Environ*; p. 35–49. Italy.
- Rocca A, Mazzanti P, Bozzano F, Perissin D. 2015. Advanced characterization of a landslide-prone area by satellite a-DInSAR. In: *Engineering geology for society and territory*, Volume 5. Switzerland: Springer International Publishing; p. 177–181
- Roskopf CM, Aucelli PPC. 2007. Analisi del dissesto da frana in Molise. In: *Rapporto sulle frane in Italia - Il Progetto IFFI - Metodologia, Risultati e rapporti regionali*, APAT [Analysis of landslide instabilities in Molise]. In: *Report on landslides in Italy – The IFFI Project – Methodology, results and regional reports*, APAT; p. 493–508, Cap. 19. Italian.
- Sgrosso I, Naso G. 2012 Note illustrative della Carta Geologica d'Italia in scala 1:50.000, Foglio n. 393, Trivento. [Notes of the Geological Map of Italy at scale 1 : 50,000, sheet no. 393, Trivento]. Roma: Servizio Geologico d'Italia (ISPRA). Italian.
- Trigila A, Frattini P, Casagli N, Catani F, Crosta G, Esposito C, Iadanza C, Lagomarsino D, Lari S, Scarascia-Mugnozza G, et al. 2013. Landslide susceptibility mapping at national scale: the Italian case study. In *Landslide science and practice. Inventory and hazard assessment*. Berlin Heidelberg: Springer-Verlag; Vol. 1, p. 287–296.

Annex 2

Fast detection of ground motions on vulnerable elements using Sentinel-1 InSAR data

Fast detection of ground motions on vulnerable elements using Sentinel-1 InSAR data

Lorenzo Solari ^a, Anna Barra ^b, Gerardo Herrera ^c, Silvia Bianchini ^a,
Oriol Monserrat ^b, Marta Béjar-Pizarro ^c, Michele Crosetto ^b, Roberto Sarro^c and
Sandro Moretti^a

^aEarth Sciences Department, University of Firenze, Firenze, Italy; ^bCentre Tecnològic de Telecomunicacions de Catalunya (CTTC/CERCA), Geomatics Division, Castelldefels, Spain; ^cGeohazards InSAR Laboratory and Modelling Group (InSARlab), Geoscience Research Department, Geological Survey of Spain (IGME), Madrid, Spain

ABSTRACT

The detection of active movements that could threaten the infrastructures and the population is one of the main priorities of the risk management chain. Interferometric Synthetic Aperture Radar (InSAR) techniques represent one of the most useful answers to this task; however, it is difficult to manage the huge amount of information derived from the interferometric analysis. In this work, we present a procedure for deriving impact assessment maps, over a regional test site, using as starting point Sentinel-1 SAR (Synthetic Aperture Radar) images and a catalogue of elements at risk that acts as a second input of the methodology. We applied the proposed approach, named as Vulnerable Elements Activity Maps (VEAM), to the islands of Gran Canaria, La Gomera and Tenerife (Spain), where we analysed SAR images covering the time interval November 2014–September 2016. The methodology, meant to be a powerful tool for reducing the time needed for a complete analysis of a full stack of InSAR data, is ideally suited for Civil Protection Authorities. The application of the methodology allowed to detect 108 areas affected by active deformation that are threatening one or more elements at risk in 25 municipalities of the three islands.

ARTICLE HISTORY

Received 29 August 2017
Accepted 29 November 2017

KEYWORDS

InSAR; Sentinel-1 satellite;
impact assessment analysis;
geohazards

Introduction

An integrated risk management chain needs the exchange of information and experience between public authorities (i.e. Civil Protection entities) and research structures (universities and research centres) to guarantee the interconnection between the natural system and the anthropic elements at risk (Salvati et al. 2016). One of the key features for every geohazard risk analysis and for providing useful information to the Civil Protection authorities is the definition of where and with which magnitude a certain geohazard is affecting a territory at different spatial scales, ranging from a single city to an entire region.

In this framework, the radar remote sensing technique is particularly suited for the multiscale analysis of ground deformations (Fell et al. 2008). Differential InSAR represents the first widely used technique to exploit the phase difference (interferogram) between two radar images to derive ground displacements with millimetre accuracy (Massonnet and Feigl 1998). The technological evolution of this approach led to the development of specific algorithms of analysis for large stacks of SAR images, known as Advanced Differential InSAR, that allow to derive the time series of

deformation of each measurement point (Crosetto et al. 2016). One of the most commonly used Advanced Differential InSAR techniques is the Persistent Scatterer Interferometry (PSI), successfully applied by many authors in the monitoring of different geohazards, such as volcanic activity (i.e. Peltier et al. 2010; Bonforte et al. 2011; Lagios et al. 2013), tectonic motions (i.e. Massironi et al. 2009; Vilardo et al. 2010; Lagios et al. 2012; Lee et al. 2017), subsidence (i.e. Abidin et al. 2013; Tomás et al. 2014; Solari et al. 2016; Béjar-Pizarro et al. 2017) or landslides (i.e. Notti et al. 2010; Herrera et al. 2013; Kim et al. 2015; Oliveira et al. 2015). Moreover, the temporal and spatial resolution of the PSI products has been also exploited to define the state of activity of geohazards and update pre-existent geohazard inventories in order to provide useful information for the risk management and urban planning of a region or a municipality (e.g. Roessner et al. 2005; Hölbling et al. 2012; Righini et al. 2012; Barra et al. 2016; Bianchini et al. 2016; Calvello et al. 2016; Ciampalini et al. 2016; Raspini et al. 2016).

This work exploits the above-mentioned characteristics of the PSI analysis for the fast estimation of active geohazards using a methodology for deriving the impact of the detected deformations on buildings and infrastructures. This procedure has been applied to a regional test site represented by three islands of the Canaries archipelago: Gran Canaria, La Gomera and Tenerife (Spain). The PSI approach has been applied to the SAR images acquired by the C-band constellation Sentinel-1 composed by two twin satellites travelling on the same orbit: 1A, launched on April 2014 and 1B, launched on April 2015. This geometry guarantees a significant reduction in the revisit time on an area with respect to the previous C-band sensors (ERS 1/2 and Envisat), allowing to obtain an image every 12–6 days. Moreover, the 250-km ground coverage of the images associated with a spatial resolution of 4×14 m permits to acquire at high resolution on very wide areas with high frequency (Torres et al. 2012).

The monitored sites were selected in the framework of the European ECHO (European Civil Protection and Humanitarian Aid Operations) project SAFETY (Sentinel for Geohazards Regional Monitoring and Forecasting) for their predisposition to different types of geohazards (i.e. landslides, subsidence and volcanic activity) that threaten the urban fabric and the population, for the availability of significant thematic and environmental data and for the specific interest of the Civil Protection Authorities involved in the risk management of the Islands. In particular, the Canary Islands Civil Protection is under the responsibility of the Ministry of Territorial Policy, Sustainability and Security of the regional government of the Canary Islands. This entity acts at regional and local level, governed by two structures: the Centre for Emergency and Security Coordination and the Emergency and Rescue Group. The first one is a public service that regulates every emergency call received in the Canary Islands and supervises the resources allocation during an emergency. The second one is the action group in charge of search and rescue missions for regional government and it is aimed at giving a quick response to every unexpected situation that could take place in the autonomous community.

The proposed methodology aims at defining a fast, reliable and simply applicable way to use the huge amount of data obtained from the InSAR processing of Sentinel-1 radar satellite images, detecting active deformation areas (ADA) that could be due to an active geohazard, evaluating the potential impact of these deformations on the vulnerable structures (buildings, roads, etc...). The final output of the methodology is called VEAM and represents a product ideally suited for Civil Protection Authorities, defining those areas, at municipality and local scale, which represent a potential risk for the population.

Methodology description

Procedure

The procedure aims at generating VEAM throughout the definition of a simple work flow, whose final output is ideally suited for Civil Protection entities. The methodology consists of three parallel

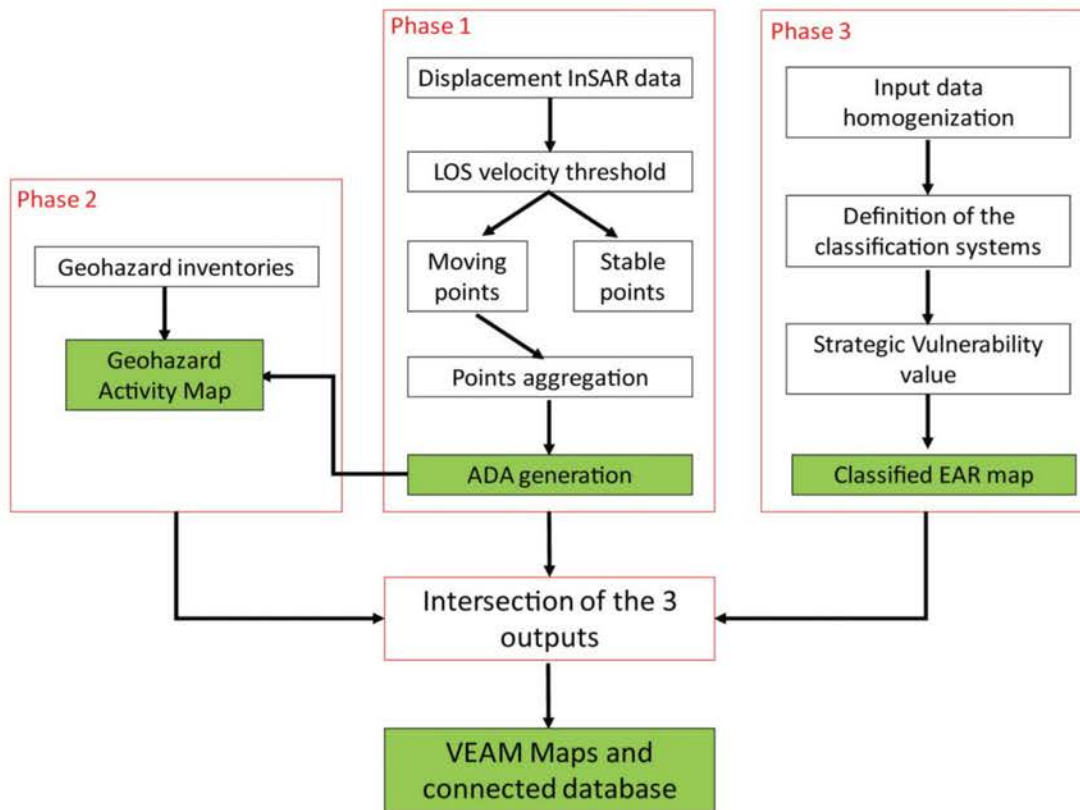


Figure 1. Workflow for the proposed procedure. The light blue and green rectangles represent the intermediate and final outputs, respectively. ADA, active deformation areas; EAR, elements at risk; VEAM, Vulnerable Elements Activity Map.

phases: (1) generation of ADA derived from the interferometric products, which can be periodically updated at every new processing of the radar data, (2) generation of Geohazard Activity Maps, through the intersection between geohazard inventories and the PSI-derived ADA and (3) the classification of the elements at risk catalogues. This classification is performed by using a system of 3 tables defined on the basis of the Strategic Vulnerability values of the different structures within each Civil Protection phase (Prevention and Preparedness, Emergency and Recovery). Finally, a fourth phase is required to intersect the three previously generated outputs in order to derive the VEAM final output (Figure 1). All the phases are described below, however a more detailed description of the PSI processing, the ADA extraction and the Geohazard Activity Maps updating can be found in Barra et al. (2017b).

All the data are managed in a Geographic Information System (GIS) and all the analysis and elaborations needed for the generation of the final output are implemented throughout the basic tools of a standard GIS platform.

Input data

The methodology here proposed is based on two input datasets:

- (1) PSI-derived ground deformation map;
- (2) Elements at risk catalogues of buildings, road network and infrastructures.

Deformation activity map

In this work, SAR images, acquired by the Sentinel-1A satellite, have been exploited to derive ground deformation maps for the three islands. The ground resolution of the sensor, in TOPS (Terrain Observation by Progressive Scans) mode, is about 4 m in range direction and 14 m in azimuth

direction. Using only one of the two Sentinel-1 satellites, the revisit time on the area of interest is equal to 12 days. This high temporal sampling allows to reduce the temporal decorrelation of the interferometric pairs and to increase the number of coherent points (Hanssen 2001).

Fifty-one SAR images, spanning the period between 05/11/2014 and 19/09/2016, were analysed by means of the PSI technique. The used SAR images were acquired by the sensor in descending orbit with a VV polarization and an incidence angle of the radar signal ranging from 30° to 45° . The analysis of the images has been carried out with a PSI approach subdivided in two phases: the first consists in the calculation of the stack of interferograms and coherences; the second involves the generation of the deformation maps. The latter are derived applying the approach described by Devan  ry et al. (2014) which exploits a 2+1D phase unwrapping using a set of redundant interferograms. The SRTM Digital Elevation Model (Farr et al. 2007) is used to process the Sentinel-1 images.

The obtained outputs reflect the radiometric characteristics of the Canary Islands where the large areas of sparse vegetation and rocky surfaces, especially at high altitude and around the main volcanic structures, bring to a high density of measurement points. On the other hand, in the areas where the vegetation cover increases, especially in the humid northern flanks, the density of Persistent Scatterers decreases (Figure 2).

The obtained deformation map is composed of 1256701 PS points; the 58% of the total number of PSs is found in the Tenerife Island, the 36% in the Gran Canaria Island whereas only the 6% is found in La Gomera Island. At each Persistent Scatterer is associated the value of the annual linear velocity (mm/yr), estimated over the analysed period and the displacement accumulated at each sensor acquisition date (mm). The measures are referred to the movement of the ground point in the satellite Line of Sight (LOS) direction; movements towards the sensor are positive (represented in blue in the deformation maps) and movements away from the sensor are negative (represented in

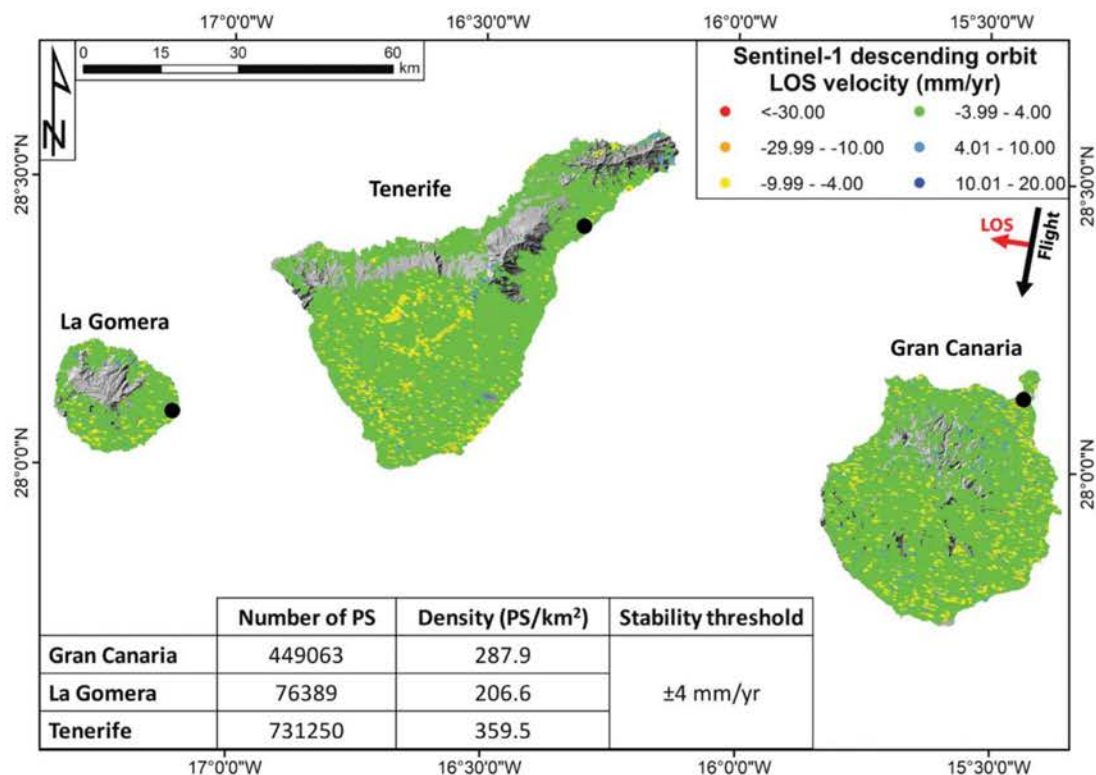


Figure 2. Deformation maps over the test site islands. The black dots represent the reference points, one for each island, chosen for the interferometric data processing. These points have been selected knowing *a priori* the areas characterized by no deformation. The image is overlaid on a 5×5 DEM-derived hillshade relief.

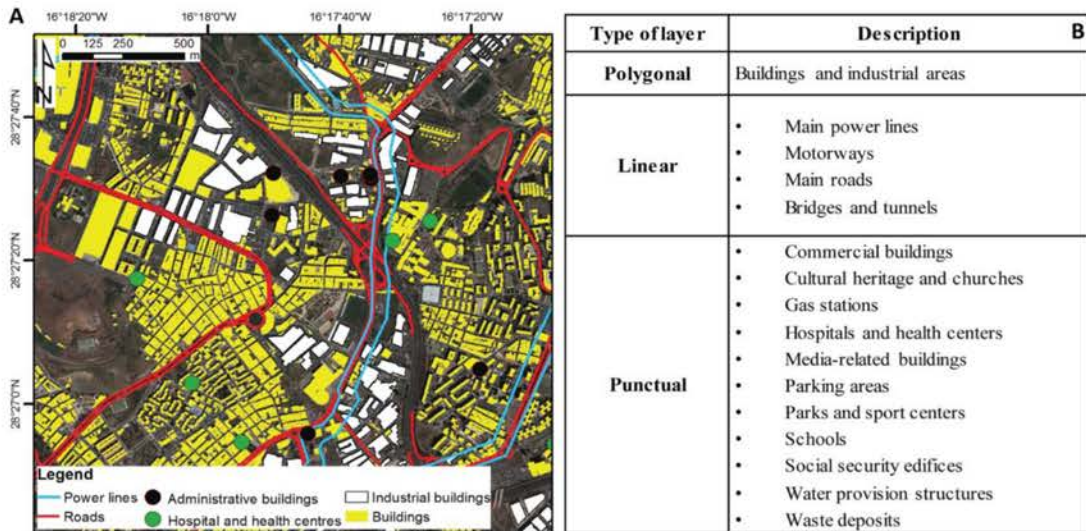


Figure 3. (A) example of elements at risk catalogue in the Tenerife Island (Santa Cruz de Tenerife municipality). (B) Available layers constituting the elements at risk catalogue for the test site.

red). The stable points, defined by a stability threshold (equal to 4 mm/yr) that represent the sensitivity of the map (Barra et al. 2017a), are represented in green (Figure 2).

Elements at risk catalogue

The elements at risk catalogues are a fundamental input of the proposed procedure, because of the necessity of a simple and fast way for qualitatively quantifying the possible impacts on the territory of the active movements detected with the PSI technique. According to the commonly used definition of an element at risk catalogue (Dai et al. 2002; Fell et al. 2005, 2008), the databases contains information about private buildings, economic and industrial activities, public services utilities and infrastructures. Furthermore, the catalogues are not referred to a specific geohazard but can be related to urban planning uses and are sometimes derived from cadastral inventories (Montoya and Masser 2005). The data used in this work were provided by the Cartographic Service of the Canary Islands and derived from the digitalization of recently updated cadastral inventories.

As shown in Figure 3, the elements at risk catalogue contain layers in three different formats: polygonal, linear and punctual. The polygonal layers, containing information about private buildings and industrial areas, were derived from topographic bases at 1:5000 nominal scale. These layers are referred to different years, depending on the island: 2012 for Gran Canaria 2014 for Tenerife and 2015 for La Gomera. The information about the distribution of the main power line tracks is only available in the Tenerife Island. The road network information contains the motorway tracks along the coastal areas and the main roads that connect the coast to the inland.

Intermediate outputs of the methodology

The methodology to derive the VEAM is based on three intermediate outputs derived from the PSI product and from the elements at risk catalogues:

- (1) ADA map that represent critical areas characterized by active movements, extracted from the deformation activity map (see the 'Deformation activity map' section) using statistical tools;
- (2) Geohazard Activity Maps that represent the integration of the PSI-derived ADA with the pre-existent geohazard inventories;
- (3) Classified Elements at Risk Maps that is the final product of the classification of the elements at risk with a triple system of tables based on Civil Protection phases.

Active deformation areas

The ADA generation procedure is an adapted version of the methodology proposed by Bianchini et al. (2013), Herrera et al. (2013) and Notti et al. (2014). The input PSI dataset, composed of hundreds of thousand/millions of points, are analysed by means of statistical tools to define those areas affected by an active deformation of a certain magnitude, above a specific threshold, that constitute a potential geohazard.

The definition of the ADA starts from the selection of those Persistent Scatterers considered 'active', on the basis of a standard deviation threshold applied to the value of velocity along the LOS of the sensor of every measurement point. The next step consists in aggregating the active deformation points in clusters that contain five or more Persistent Scatterers. This number is considered the minimum number of points for the detection of a small landslide (Herrera et al. 2013; Oliveira et al. 2015). For every Persistent Scatterer, an area of influence is defined on the basis of the size of the ground resolution cell of the multi-looked SAR images analysed (28×40 m). This parameter is used to facilitate the clustering process. Barra et al. (2017b) contains a description in detail of the methodology.

Applying this methodology to the three islands (Figure 4), we obtain a total number of 388 ADA, 218 in the Tenerife Island (56% of the total), 150 in the Gran Canaria Island (38% of the total) and 20 in La Gomera Island (6% of the total).

Geohazard activity maps

The Geohazard Activity Map constitutes an improvement of the level of information obtainable from a single ADA (localization and magnitude of an active movement) adding a qualitative estimation of the possible geohazard that is threatening a certain area.

The methodology to derive the Geohazard Activity Maps can be summarized as an intersection between the ADA maps and the available and pre-existent geohazard catalogues. In the case of the Canary Islands, specific databases of slow-moving landslides, that are the target of an InSAR analysis, are not available; whereas, for the volcanic hazard in the Tenerife Island, which is hosting a quiescent volcanic system, a susceptibility map of the possible openings of new volcanic vents is available. Moreover, different types of input and field data are available for the three islands, confirming the difficulties in finding similar and reliable ancillary data above large areas and when different entities are involved. For this last reason, we chose to distinguish between Tenerife and the other two islands (Gran Canaria and La Gomera). In fact, the first has a database of geomorphological landforms derived by the authors in the framework of the SAFETY project that could not be now reproduced for the other two islands. In addition, Tenerife is the only island that records the presence of a quiescent volcanic system that requires a specific Geohazard Activity Map.

Considering these limitations, for the island of Tenerife two Geohazard Activity Maps are derived:

- (1) Volcanic Susceptibility Areas with Deformation (Figure 5). This map represents the overlapping between the ADA and the volcanic susceptibility contours that define the highest spatial probability of hosting a volcanic vent, as defined by Martí and Felpeto (2010). This Geohazard Activity Map allows selecting those ADA that could be possibly related to a volcanic motion and to observe the vector of deformation, intended as positive or negative sign of the ADA mean velocity. This map represents a preliminary information for Civil Protection Authorities for knowing a-priori the presence of active movements in areas in which a potential volcanic activity can develop (i.e. defined by the susceptibility contours). The presence of an existing correlation between the ground motions detected by this Geohazard Activity Map and the volcanic activity is not within the aims of this paper, requiring specific site information now not available.
- (2) Tenerife Geohazard Activity Map (Figure 6). This map represents a first attempt of generating a catalogue of the potential slope instabilities and terrain settlement in the island, based on geological and geomorphological interpretation. The map is derived according to field

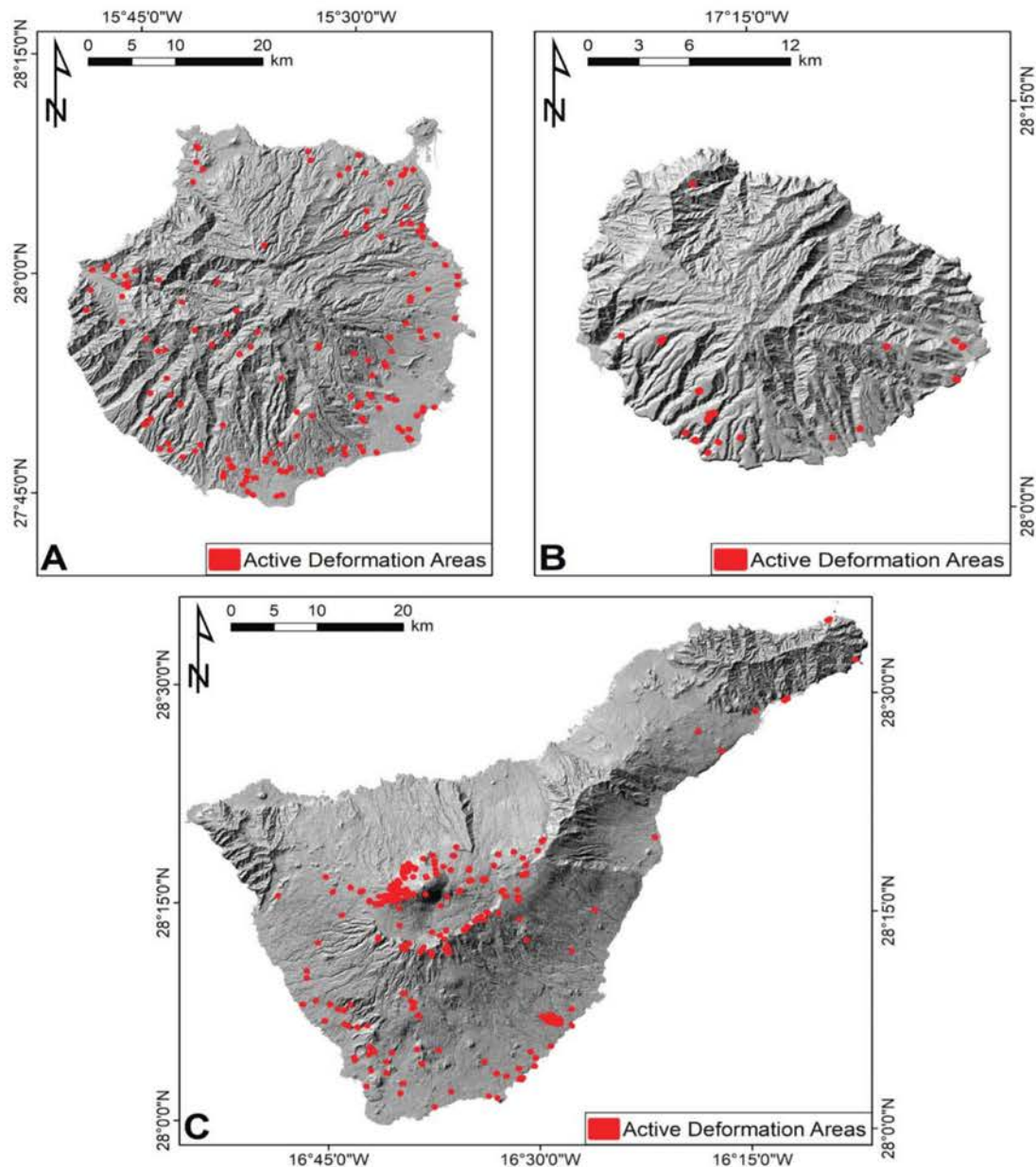


Figure 4. Active deformation areas derived from the analysis of the Sentinel-1 dataset. (A) Gran Canaria island, (B) La Gomera island and (C) Tenerife island.

observations, analysis of digital orthophotos (referred to years 2012 and 2015) and the available geological map (Carracedo et al. 2001) at a 1:25.000 scale. The final output is a geomorphological database in which pyroclastic deposit, debris flow and anthropic activity areas are mapped. In this sense, the Tenerife Geohazard Activity Map is derived by a geological interpretation that has been made combining the inputs data and field work. Hence, the ADA composing this map have been classified in four groups: (i) pyroclastic deposits in slopes greater than 20° where slope instabilities are responsible for the ADA; (ii) ADA related to already mapped debris flows; (iii) ADA related to anthropogenic causes (artificial fill and urban waste dumps compaction, quarries and mining activity); iv) ADA of unknown interpretation because of the lack of terrain or ancillary information.

Comparing the two Geohazard Activity Maps derived for Tenerife, it is noticeable that some ADAs (mainly around the northern flank of the Teide volcano) are potentially related to multiple

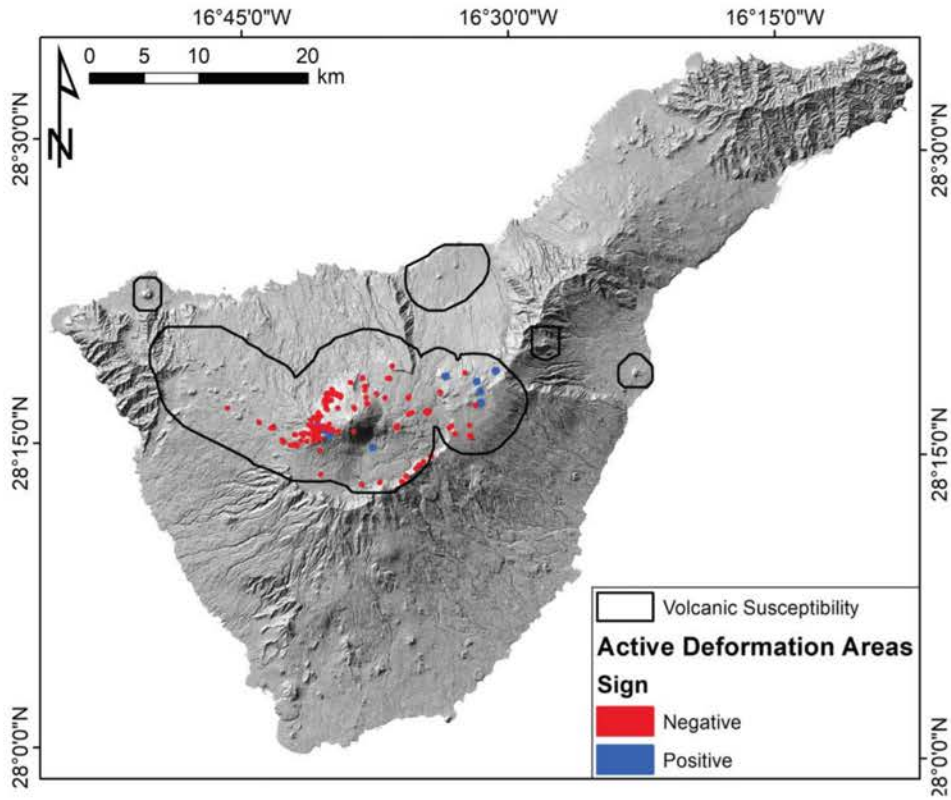


Figure 5. Volcanic susceptibility areas with deformation map for the Tenerife island.

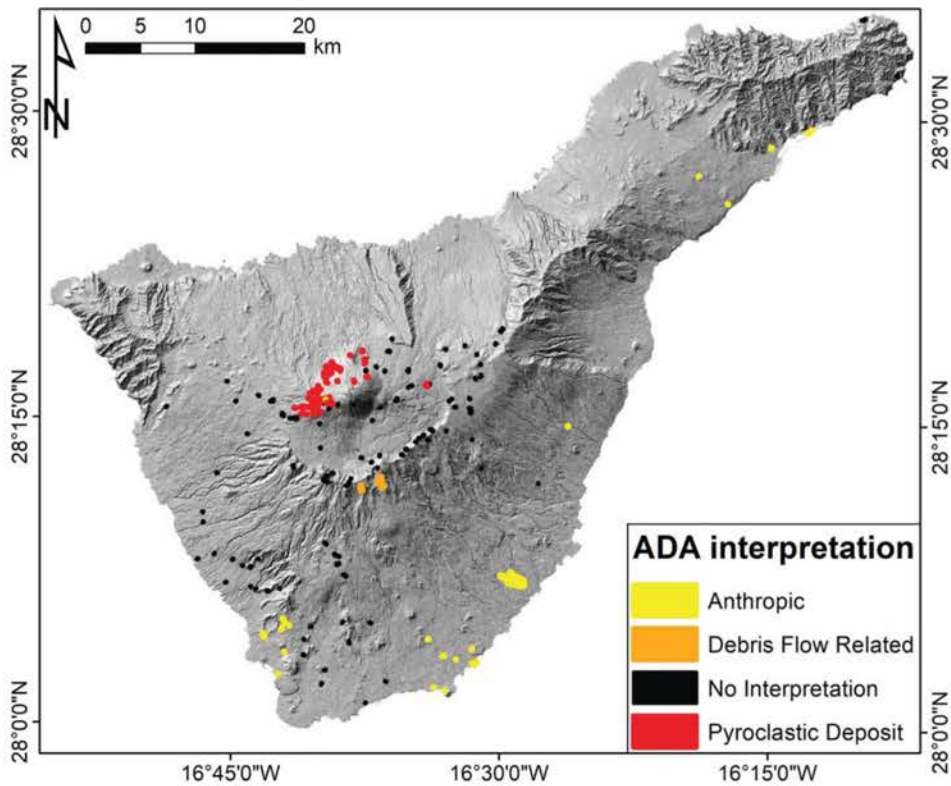


Figure 6. Geohazard Activity Map for the Tenerife Island derived from geological-geomorphological interpretation of field and ancillary data.

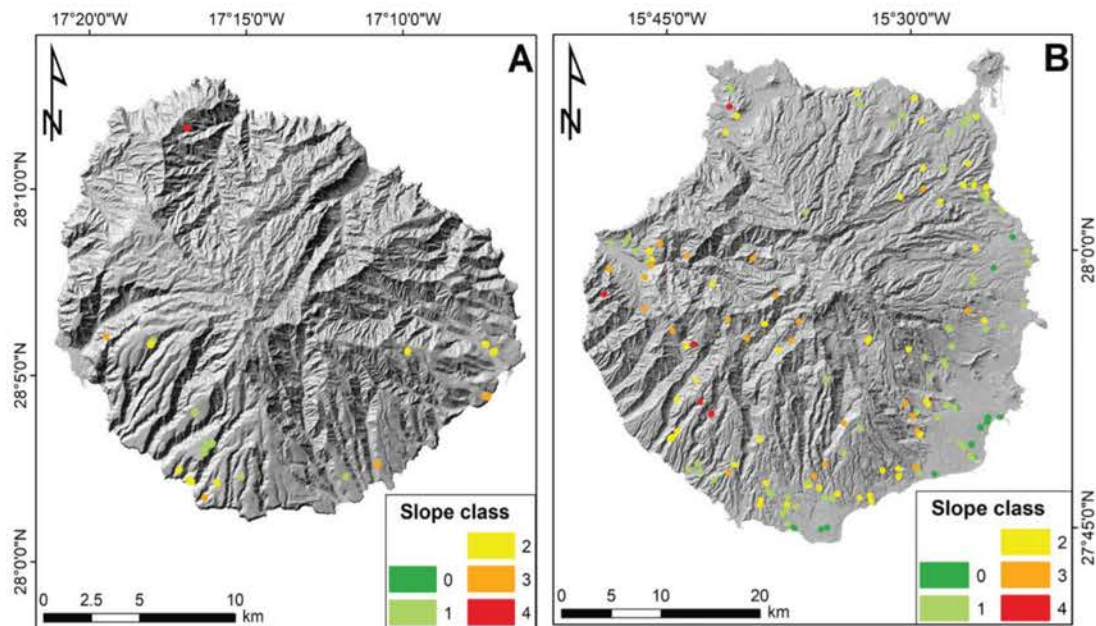


Figure 7. Landslide Prone Active Areas map for the Islands of La Gomera (A) and Gran Canaria (B).

geohazards (volcanic motion and slope instability). At this stage, both the classifications are kept, but a field validation and a comparison with other data is necessary for a correct interpretation that will be performed in the future.

For the islands of Gran Canaria and La Gomera it is possible to derive only a simplified version of the Geohazard Activity Map, based on a 5-m DEM-derived slope map. This map is named Landslide Prone Active Areas and represents a qualitative classification of the terrain to define the possibility or not of a landslide movement (Figure 7). Every ADA is assigned to a class value, ranging from 0 to 4, indicating how much a registered movement can be related to a landslide. The value 0 is assigned to those ADA with mean slope value lower than 5° , the value 1 (low degree landslide-prone area) is assigned to those ADA with slope angle ranging from 5° to 15° , value 2 (medium degree landslide-prone area) if the slope angle ranges from 15° to 25° , slope angles equal to 25° to 35° are assigned to the value of 3 (high degree landslide-prone area) while the value 4 is referred to the slope angles higher than 35° (very high degree landslide-prone area).

Classified elements at risk maps

The vulnerability of a structure is defined as the ‘expected degree of loss experienced by the elements at risk for a given magnitude of hazard’ (Glade et al. 2005). Following this definition, we consider the ‘degree of loss’ of buildings and roads as a loss in serviceability, potentially arriving to the service limit state of an infrastructure. Moreover, the ‘given magnitude of hazard’ is represented by the mean LOS velocity of the PSs within the perimeter of each ADA. Many qualitative and quantitative classification systems for deriving the vulnerability of an element at risk have been proposed by different authors. Fell et al. (2005) stated that, for a correct risk analysis, the elements at risk, structures or persons, should be quantified in terms of ‘vulnerability either as conditional probability of damage to property, or conditional probability of loss of life or injury’. Kong (2002) subdivided the elements at risk into a system of four classes: general buildings, transportation infrastructures, population patterns and essential facilities. A similar generic classification has been used also by Calcaterra et al. (2003), classifying the elements on the basis of the main land use (urban, industrial, infrastructures and agricultural). Papatoma-Köhle et al. (2007) proposed an ‘elements at risk database’ that considered the characteristics of buildings and inhabitants, the use of the buildings and their importance in the local economy. This type of detailed structural analysis of buildings has

Table 1. Strategic vulnerability values for the three different Civil Protection phases and for each type of element at risk considered.

Type of element at risk	Number of elements	SV value for prevention phase	SV value for emergency phase	SV value for recovery phase
<i>Cultural heritage</i>	715	High	Medium	Medium
<i>Agricultural activities</i>	2319	Medium	Low	Low
<i>Gas stations and fuel deposits</i>	330	Low	Medium	Low
<i>Hospitals and health centres</i>	309	High	Very High	High
<i>Hotels and accommodation facilities</i>	1965	High	High	Low
<i>Industries</i>	2782	Medium	Medium	High
<i>Markets and shopping malls</i>	337	Medium	Low	Low
<i>Media-related structures</i>	20	Medium	Medium	Low
<i>Road and railway network</i>	10920 (4381 km)	High	Very High	High
<i>Parking areas and parking lots</i>	764	Low	Low	Low
<i>Power lines (only for Tenerife)</i>	37 (548 km)	High	Very High	High
<i>Private houses</i>	236716	High	High	Medium
<i>Public administration buildings</i>	628	High	Very High	High
<i>Recreational areas</i>	2481	Low	Low	Low
<i>Schools</i>	1474	High	High	Medium
<i>Sport centres</i>	54	Low	High	Low
<i>Urban security and Civil Protection structures</i>	186	High	Very High	High
<i>Waste deposits</i>	18	Medium	Medium	Low
<i>Water supply network and facilities</i>	434	High	Very High	High

been also proposed by Spence et al. (2004) in the case of the Vesuvius pyroclastic flows. Conversely, Uzielli et al. (2008) classified the elements at risk with a system of ‘susceptibility factors’ for buildings and people.

These bibliographic examples show that a unique way to manage the elements at risk catalogue does not exist. Moreover, the result is dependent on the quality and scale of detail of the input inventories. In this paper the available catalogues, provided by regional and local entities, contain only simple information about the location and the type of the structures: neither the structural state of the infrastructures nor the information about the occupancy of buildings were available.

In this framework, we propose a qualitative classification system based on the *Strategic Vulnerability* that considers the potential damages of a certain structure that is already used and that plays a crucial role in the risk management chain of an area or of a municipality. This value is defined for three scenarios, referred to the three Civil Protection phases (Table 1):

- (1) First scenario – Prevention Phase. As defined by the European Union (Decision No 1313/2013/EU of the European Parliament), prevention means ‘any action aimed at reducing risks or mitigating adverse consequences of a disaster for people, the environment and property, including cultural heritage’. In particular, the proposed PSI-based methodology provides to this phase tools to reduce the potential risks by forecasting and mapping potential geohazards.

For this scenario, we define three classes of Strategic Vulnerability:

- High. Elements with not occasional occupancy or with high flow of tourism, emergency and health infrastructures, main road and supply networks;
 - Medium. Elements with occasional occupation with an economic or environmental or social value;
 - Low. Elements with occasional occupation with a less relevant economic value;
- (2) Second scenario – Emergency Phase. The response to a certain geo-hydrogeological event is defined by the United Nations Office for Disaster Risk Reduction as ‘the provision of emergency services and public assistance during or immediately after a disaster in order to save lives, reduce health impacts, ensure public safety and meet the basic subsistence needs of the people affected’. In this phase, PSI-derived data are used to monitor the post-event residual deformations threatening the population and affecting the most strategic infrastructures used

within the emergency chain as well as to map secondary geohazards induced by the main hydrogeological event.

For this scenario, we define four classes of Strategic Vulnerability:

- Very High. Most strategic elements, active part of the emergency chain in case of an event;
 - High. Elements with people living inside or/and that can be used as recovery structures in case of an event;
 - Medium. Elements that can be useful for single phases of the emergency management or with a relevant economic value that represent a valuable resource for the restoration of an area after an event;
 - Low. Elements that not constitute a main priority during the event management;
- (3) Third scenario – Recovery Phase. The recovery after a hydrogeological or volcanic event is defined by the United Nations Office for Disaster Risk Reduction as ‘the restoration of facilities, livelihoods and living conditions of disaster-affected communities including efforts to reduce disaster risk factors’. InSAR data are used in the Recovery Phase to evaluate the possible reactivation of already set off phenomena or the presence of precursors of new movements affecting the areas involved in the reconstruction.

For this scenario, we define three classes of Strategic Vulnerability:

- High. Elements that represent a main priority in case of damages restoration or reconstruction works because of their economic or strategic value.
- Medium. Elements that represent an artistic or social value that have to be restored after the main priority elements.
- Low. Elements with a subordinate importance in case of the definition of the actions related to the damages restoration activities.

A simple procedure, managed in a GIS system, is applied for generating the final vulnerable elements map for the test sites. Firstly, every group of elements at risk (as shown in Table 1) is associated to a value of Strategic Vulnerability depending on the chosen scenario. Then, each classified group is rasterized on the basis of its Strategic Vulnerability value. Finally, the different obtained raster layers are merged to obtain the final Reclassified Elements at Risk map. Regarding the strategy of analysis of the different formats of the input data we chose two different ways for the point and polygonal features. For what concern the point features, the raster cell size was fixed at 100 m in order to ensure an area of influence around the buildings and the structures and thus to guarantee the association with the neighbourhood ADA. For the polygonal feature, a buffer of 50 m is applied to the original shapefile and then a raster conversion, at 100m cell resolution, is performed. At each pixel of the Classified Elements at Risk Map is associated the Strategic Vulnerability class related to each Civil Protection phase (Figure 8). When a single pixel represents different strategic elements at risk, with different Strategic Vulnerability values, only the highest Strategic Vulnerability class is assigned.

Final output of the methodology

The information derived from the three intermediate products is finally merged to obtain the VEAM: each ADA is associated both to the Geohazard Activity Maps information, related to the potential geohazards (landslide, settlement or volcanic), and the Strategic Vulnerability class of the intersecting element at risk. The VEAM includes only the ADA that potentially affect one or more elements a risk, discarding the remaining ADA that do not coincide with elements found within the reclassified elements at risk catalogue, because they represent movements that are not affecting any infrastructure.

Three maps, produced for every scenario previously defined, constitute the final outputs of the methodology. These outputs contain not only the information related to the ADA but also to the territorial units in which the Islands can be subdivided. For the application of the proposed

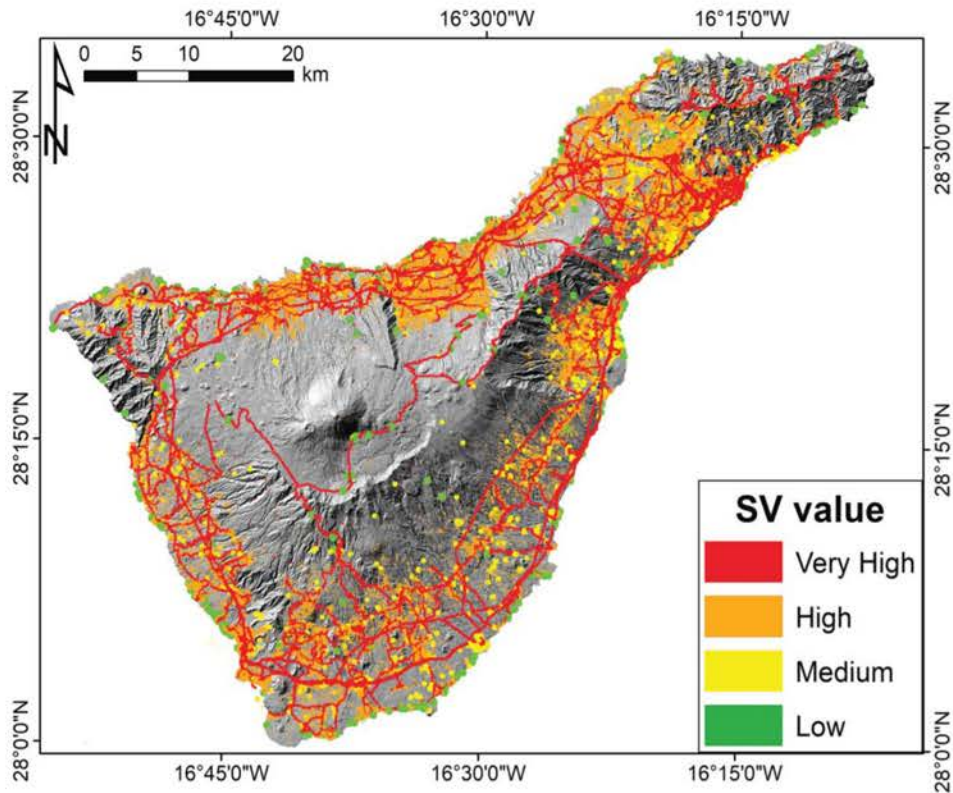


Figure 8. Classified Elements at Risk map for the Island of Tenerife. The Strategic Vulnerability value is referred to the Emergency Phase scenario.

methodology, we chose to use the municipalities of the three islands as territorial units (21 for Gran Canaria, 6 for La Gomera and 31 for Tenerife). The final maps are composed as follows:

- (1) Classified territorial units: polygons representing the chosen territory division. In this work the polygons represent the municipality boundaries (an example will be illustrated in the 'Results' Section). They are classified by the number of the VEAM-selected ADA. A colour scale is used for representing the classification. If no ADA are found the polygon are left blank;
- (2) Pie charts: the pie charts represent the distribution of the VEAM-selected ADA in terms of their Strategic Vulnerability classification. The Strategic Vulnerability classes are symbolized by a colour scale, depending on the Civil Protection phase, as presented in Table 1. Each VEAM includes a pie chart for each territorial unit and a general pie chart representing the total distribution. The last one includes also the percentages of the VEAM-selected ADA for each Strategic Vulnerability class (see the 'Results' Section for an example of VEAM for the Emergency Phase).

A second output of the methodology is composed by a GIS database for each VEAM-selected ADA characterized by the following information:

- Information over the geographical localization of the ADA (coordinates in a reference cartographic system, municipality and nearest road name or local toponym);
- Brief geological information extracted from the available cartographic or bibliographic sources;
- Mean LOS velocity, in terms of absolute value, of the Persistent Scatterers within each ADA;

- Quality index that indicates the reliability of each ADA. It is based on the temporal and spatial noise level of the deformation time series of each Persistent Scatterer composing the ADA. For an in-depth explanation of the methodology used to derive the Quality Index we refer to Barra et al. (2017b);
- The higher Strategic Vulnerability class of the elements at risk included in the ADA, for each Civil Protection scenario;
- Only for the Tenerife Island, a field indicating if the ADA can be associated or not with a volcanic-related deformation and to slope movement or ground settlement (see the Geohazard Activity Maps section);
- For the Gran Canaria and La Gomera Islands, a field indicating if the ADA can be associated to a potential landslide-related motion (see the Geohazard Activity Maps section).

The two outputs of the methodology will be used to define those areas that represent a major threat for the Islands governments and so for the population. This is done throughout a selection process performed on the VEAM database that aims at choosing and at creating a 'priority list' of the most hazardous ADA. Field checks are finally required to verify these satellite-derived information, identifying ground evidences of active movements or possible future failures. At the moment, a campaign of field checks is being planned in accordance with the Civil Protection authority of the Canary Islands. The VEAM outputs will be also cross compared with available or newly acquired geophysical data, such as Global Positioning System or seismic and geoelectrical surveys.

Test site characterization

The Canary Islands Archipelago is located westward from the African coast and developed as a result of the eastward movement of the African plate over a mantle hotspot (Holik et al. 1991). In this geodynamical context, the western islands are the oldest in the archipelago (Acosta et al. 2003). Starting from the biggest one, Tenerife, a brief geological description of each island is now introduced.

Tenerife Island geological and geomorphological characterization

Tenerife is the biggest (2.057 km²) and most populated (889000 inhabitants) island in the Canary Archipelago. Its highest point, Mount Teide, with an elevation of 3.718 m a.s.l., is the third largest volcano in the world from its base at the bottom of the sea.

The current morphological complexity of the island is directly related to its volcanic evolution (Figure 9(A)). The caldera system that is visible today in the centre of the island (Cañadas caldera) was produced by the vertical collapse of this edifice after an intense explosive volcanic activity (Martí et al. 1997; Martí and Gudmundsson 2000). The area is now partially occupied by the Teide-Pico Viejo strato-volcano and filled by the materials emitted in the different eruptions that took place. The island is also characterized by the presence of three rift zones with scatter vents, aligned cones and eruptive fissures. These structures are: Santiago del Teide (NW-SE rift zone), Dorsal (ENE-WSW rift zone) and the Southern Volcanic Zone (Carracedo 1996). The main geohazards are mainly related to the volcanic activity of the island (the Teide-Pico Viejo complex has a permanent and active magmatic chamber), involving also a regional seismicity activity with magnitude lower than 5.0 (Mezcua et al. 1992). The Island is characterized also by the presence of six large paleo-landslides, whose age ranges from Upper Pliocene to Middle Pleistocene (Hürlimann et al. 2004). The largest and most representative phenomena are Güümar, La Orotava and Icod landslides (Figure 9 (A)). These instabilities produced large amphitheatres and their actual presence was confirmed by offshore geophysical data (Watts and Masson 2001). Their origin is related to a series of complex and concurrent causes, such as: the rifting activity along the island that produced gravitational sliding (Carracedo 1994), the presence of a level of volcanic breccia acting as an impermeable layer that

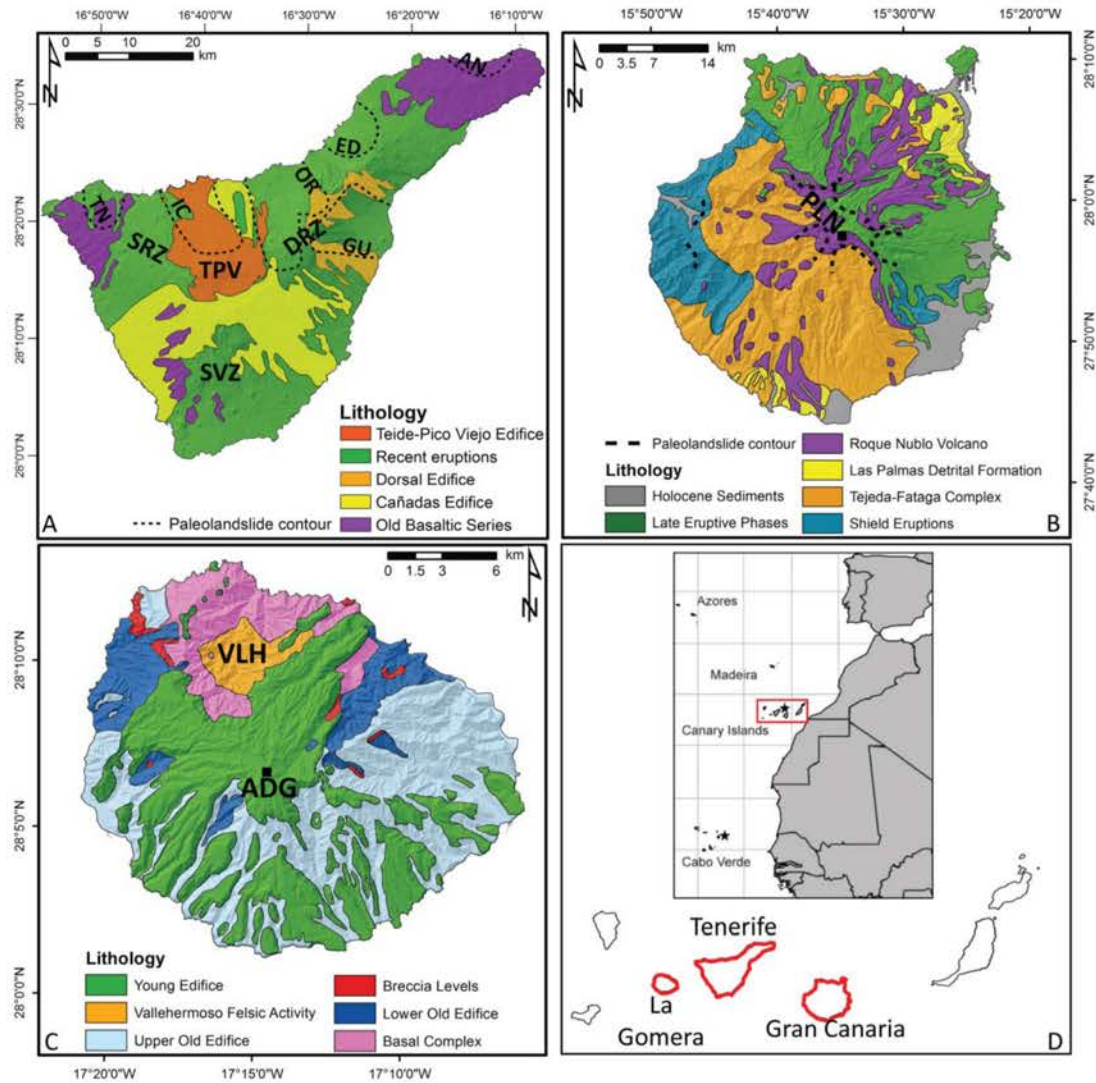


Figure 9. Simplified geological maps (overlaid on a 5×5 DEM-derived hillshade relief) and geographical localization of the three islands. (A) Geological map of Tenerife Island (modified after Sobradelo and Martí 2010); SRZ, Santiago rift zone; DRZ, dorsal rift zone; SVZ, southern volcanic zone; TPV, Teide-Pico Veijo stratovolcano. The black dashed lines represent the contour of the paleo-landslides (modified after Hürlimann et al. 2004). AN, Anaga landslide; ED, East Dorsal landslide; GU, Güimar landslide; IC, Icod landslide; OR, La Orotava landslide; TN, Teno landslide. (B) Geological map of Gran Canaria Island (modified after Rodríguez-González et al. 2009); PLN, Pico de Las Nieves. (C) Geological map of La Gomera Island (modified after Llanes et al. 2009). ADG, Alto de Garajonay; VLH, Vallehermoso area. (D) Geographical location of the three islands, the red contours represent the study areas.

creates a main sliding surface (Ancochea et al. 1999) and a direct mechanical relation with the collapse of the Cañadas caldera (Martí et al. 1997).

Gran Canaria geological and geomorphological characterization

Gran Canaria is the third island of the archipelago for surface (1532 km^2) and its highest point is located at 1950 m a.s.l. in its central part (Pico de Las Nieves, Figure 9(B)). The island shows a clear climatic distinction between the southern flanks, with arid to semi-arid conditions, and the northern flanks that are characterized by humid to sub-humid climatic conditions. Combining the climatic conditions and the age of volcanism, the island can be subdivided into four sectors: ‘young’ eastern sector with arid (SE) and humid (NE) climates and an ‘old’ western sector with the same internal climatic subdivision (Menéndez et al. 2008).

As for Tenerife, its current morphology is determined by the emplacement of different volcanic cycles that started about 15 Ma with the formation of a shield volcano that afterward collapsed,

forming the Tejeda caldera, subsequently filled by ignimbritic materials ('Tejeda-Fataga complex', Figure 9(B)) that mantled the pre-existent slopes of the shield volcano (Carracedo et al. 2002). After this volcanic activity, an intense strong erosional trend took place (Carracedo et al. 2002), cutting deep the slopes of the shield volcano and forming the present-day network of ravines, locally known as 'barrancos'. At present the residual slopes of the shield edifice dominates the southern sector of the island (Menendez et al. 2008). During this erosional phase, in the S-SE and N-NW sectors of the island a high volume of alluvial and fan-delta sediments was deposited, forming the 'Las Palmas Detritic Formation' (Schmincke 1993).

A new intense volcanic phase (Roque Nublo stratovolcano) took place in the central part of the island where lava and pyroclastic flows filled the valleys carved in the northern flank of the shield edifice, generating extensive northward sloping platform-lava surfaces that were subsequently re-incised by the action of new quaternary barrancos (Menendez et al. 2008). After the construction of the Roque Nublo stratovolcano several giant landslides, flank collapses and debris avalanches developed (Lomoschitz et al. 2008).

La Gomera geological and geomorphological characterization

With 380 km², La Gomera is the sixth island for surface of the Archipelago; the Alto the Garajonay is its highest point, located at 1487 m a.s.l. (Figure 9(C)).

The geological context reflects the three main growth stages of this volcanic island (Ancochea et al. 2004 2006): the Basal Complex, the Old Edifice and the Young Edifice (Figure 5(C)). In particular, the Basal Complex, which outcrops in the northern part of the island, is composed by mafic plutonic rocks (Cendrero 1971). After the erosion of this mafic complex, a new volcanic system, centred in the Vallehermoso area, took place. It is represented by the Old Edifice shield volcano, characterized by hundreds of meters of basaltic lava flows with felsic lavas on top of the sequence ('Vallehermoso Felsic Rocks', Ancochea et al. 2006). The most recent volcanic activity of the island is related to the basaltic, trachybasaltic, and trachyandesitic lava flows emitted during the activity of the Young Edifice, that do not cover the entire island, as the previous ones, but are limited to the central and south-eastern portion of the island (Llanes et al. 2009). After these latest events, the island is considered inactive and is only affected by intense fluvial and marine erosive phenomena (Llanes et al. 2009). This erosional stage is similar to the one recognized in the Gran Canaria Island (Paris et al. 2005).

Results

Applying the VEAM methodology to the test site areas we detect 108 ADA (28% of the total) that affect one or more elements at risk, involving 25 municipalities in total.

In the Gran Canaria Island, 65 VEAM-selected ADA are found, representing the 43% of the ADA of the island and covering 0.7 km² (Figure 10(A)). At least one of these potential hazard areas is detected in 13 municipalities, two of them register the presence of a number of ADA higher than 10 (Figure 11(A)): Las Palmas de Gran Canaria and San Bartolomé de Tiránjana (16 and 15 ADA, respectively). The highest density of VEAM-selected ADA is found in the south-eastern part of the island, where the urban density is the highest, and in the Las Palmas de Gran Canaria municipality, that represent the most populated area of the island. The 90% of the VEAM-selected ADA in the Prevention phase scenario registered a High vulnerability value, being private houses, main roads and hotels. In the Emergency phase, the 38% of the ADA intersect elements at risk with 'Very High' vulnerability, mainly represented by roads, while, the 58% of the deformation detected affect private houses and touristic structures classified as 'High' Strategic Vulnerability value (Figure 6(A)). In the Recovery phase, the greatest part (64% of the total) of the VEAM-selected ADA outline element at risk with 'Medium' vulnerability (private houses mainly).

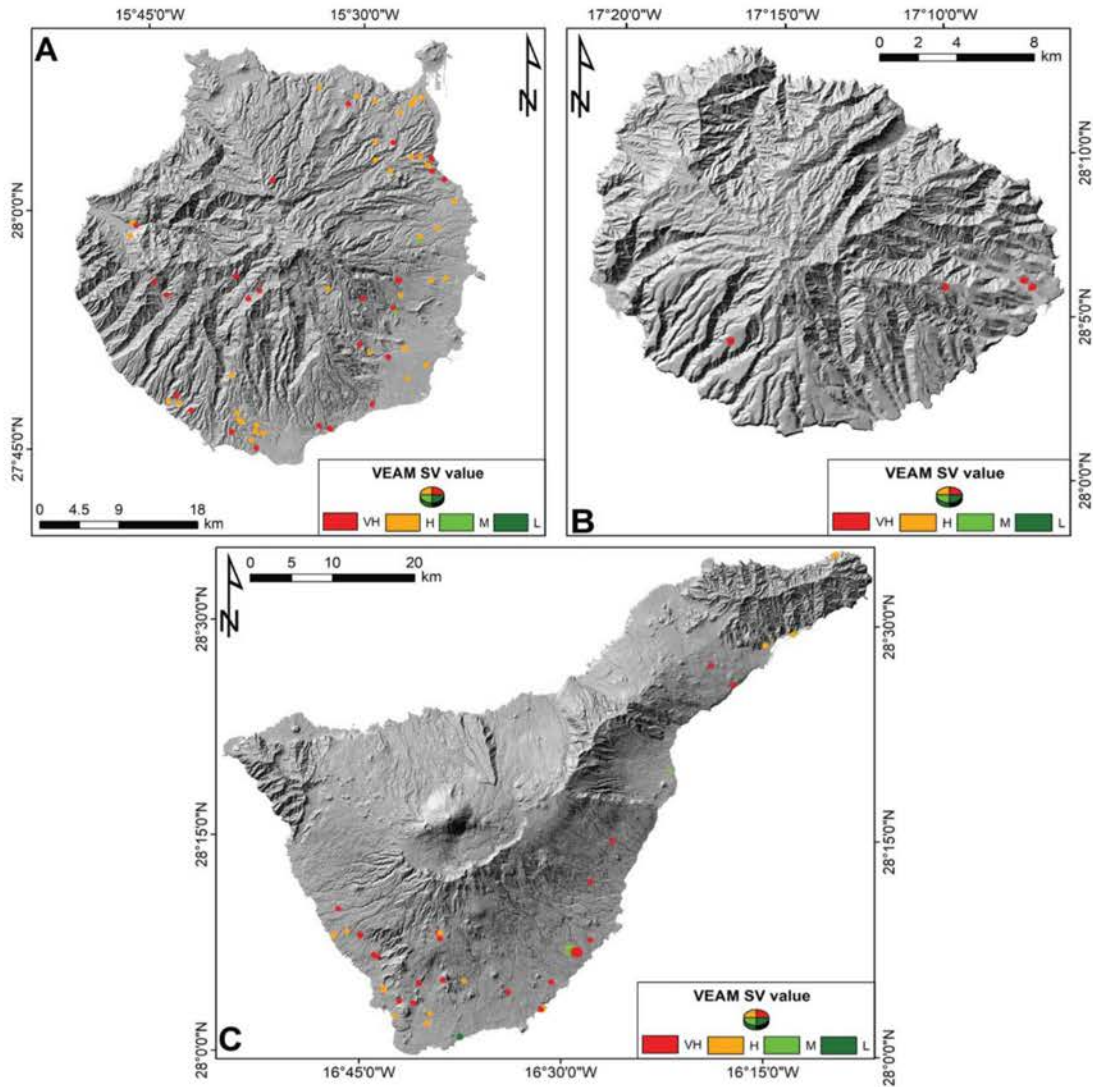


Figure 10. VEAM-selected ADA for the three islands of the Canary Archipelago. The VEAM classification here presented is referred to the Emergency Phase scenario. (A) Gran Canaria island, (B) La Gomera island and (C) Tenerife island.

In La Gomera Island, 4 VEAM-selected ADA are registered (25% of the ADA), covering only 0.05 km² (Figure 10(B)). The municipalities of San Sebastián de La Gomera (3 areas with active deformation) and Alajeró (1 area with active deformation) are the only two administrative entities involved (Figure 11(B)). The obtained results are highly dependent on the low density of measurement points and so of the resulting ADA, related to the vegetation cover of the central portion of the island, in addition to the absence of wide urban areas and of a dense road network. The definition of the vulnerability of the elements at risk affected by an active deformation give the same result for both the Prevention and Emergency phase, classifying all the ADA in the highest class of vulnerability (High and Very High for Prevention and Emergency scenarios, respectively). In the third scenario (Recovery phase) the 50% of the ADA are classified as 'High' vulnerability and 50% as 'Medium' vulnerability, the latter representing single or groups of private houses (Table 2).

Finally, 39 VEAM-selected ADA are recorded in the Tenerife Island, representing the 18% of the Island ADA and covering a territory equal to 0.2 km² (Figure 10(C)). Ten municipalities are affected by active movements involving elements at risk; the maximum number of ADA, equal to 7, is registered in both the Adeje and Arona municipalities in the southern part of the island where the highest density of ADA was found (Figure 11(C)). The Island of Tenerife shows the lowest percentage of VEAM-selected ADA in respect to the original number of ADA; this is due to the high density of

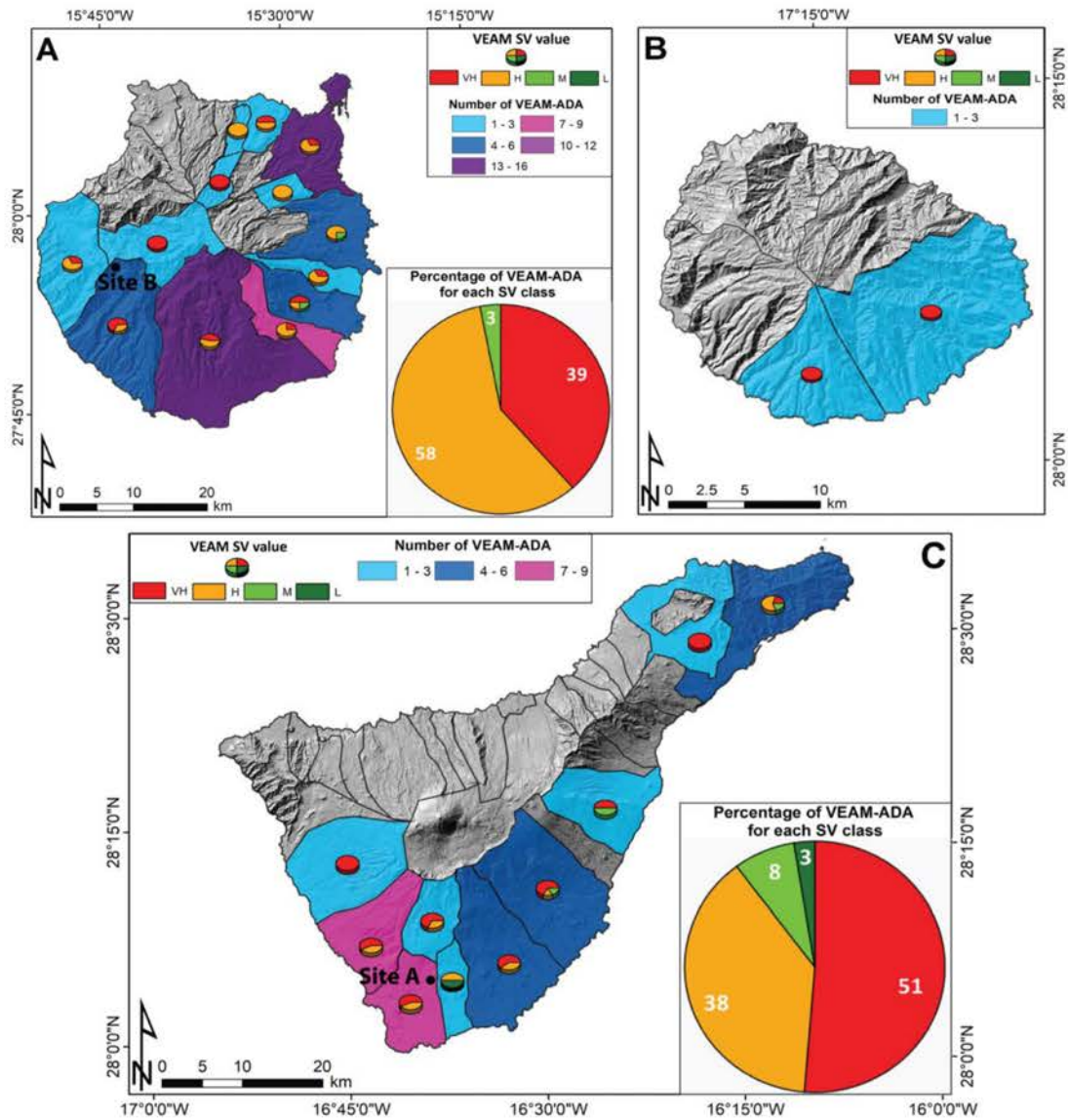


Figure 11. VEAM final output for the three islands test sites of the methodology. The VEAM here presented is referred to the second scenario – emergency phase. The islands are subdivided in municipalities considered as reference territorial units. (A) Gran Canaria island, (B) La Gomera island and (C) Tenerife island. All the maps are overlaid on a 5 × 5 DEM-derived hillshade. The black dots in (A) and (C) indicate two case studies explained in Figure 12.

areas falling into the Cañadas Caldera and around the steep slopes of the Teide and Pico Viejo volcanoes. In this area, that constitutes a national park and an UNESCO heritage, the road network is reduced to the strictly necessary and only few touristic edifices are found; this lead to a lower probability of intersection of the element at risk catalogue with the ADA map, resulting in the absence of these areas in the final VEAM output. For the Prevention phase scenario, the VEAM analysis applied to the Tenerife Island give as a result the 80% of the ADA affecting elements at risk with

Table 2. Summary of the results obtained in the Canary Islands. For each scenario are shown the number of ADA for each of the vulnerability class.

Island	VEAM ADA	Municipalities involved	Prevention			Emergency				Recovery		
			L	M	H	L	M	H	VH	L	M	H
Gran Canaria	65	13	2	4	59	0	2	38	25	2	42	21
La Gomera	4	2	0	0	4	0	0	0	4	0	2	2
Tenerife	39	10	2	6	31	1	3	14	21	4	13	22

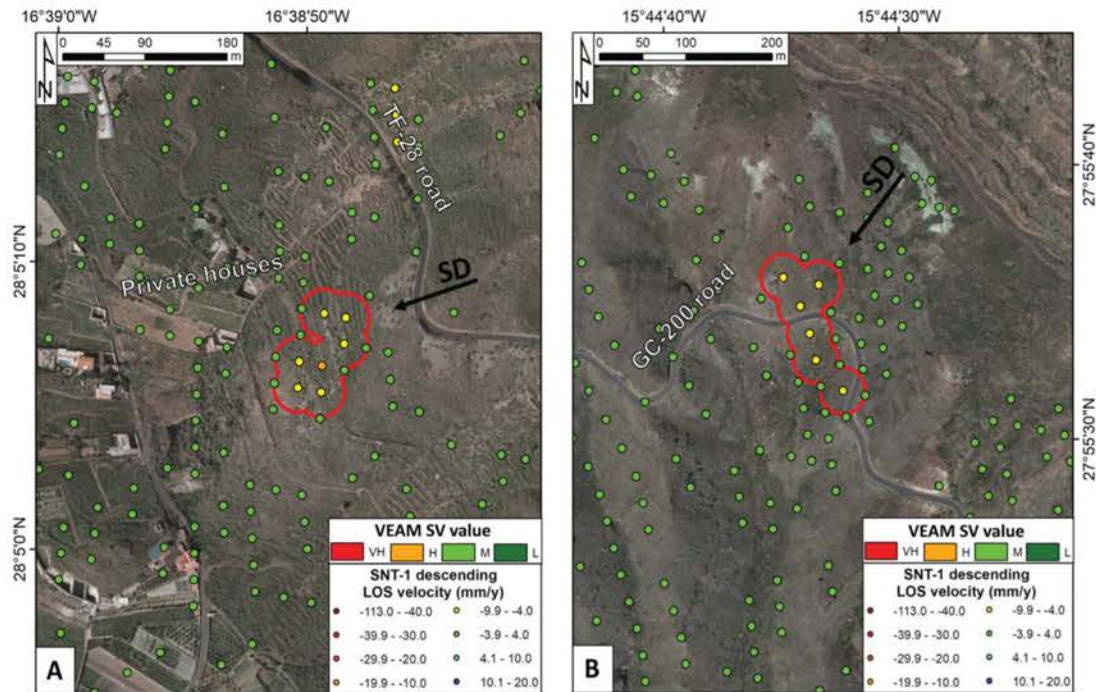


Figure 12. Selected case studies within the VEAM database for the Emergency phase scenario. (A) VEAM-selected ADA near Valle de San Lorenzo, southern part of the Tenerife Island. (B) VEAM-selected ADA along the GC-200 road near the Tasarte town in the south-eastern sector of the Gran Canaria Island. The black arrows indicate the slope direction (SD).

‘High’ vulnerability, being road network and power line sectors and private houses. The 54% of the ADA in the Emergency phase scenario affect elements at risk with ‘Very High’ strategic vulnerability (road network and power line sectors), while 36% affect elements with ‘High’ vulnerability, essentially private houses. For the Recovery phase scenario, these percentages are similarly subdivided between the ‘High’ and ‘Medium’ vulnerability classes.

In Figure 12 two case studies are shown to better explain the type of result obtainable throughout the application of the VEAM methodology. The first example shows an ADA composed by seven measurement points with a mean velocity value equal to -6.5 mm/yr, negative sign coherent with a movement away from the sensor along the slope direction (SD – Figure 12(A)). From the point of view of the potential geohazard causing the registered deformation, since the ADA do not fall within the Volcanic Susceptibility Areas with Deformation contours and the mean slope angle value is 20.5° , it could be classified as a landslide-prone area. The ADA registers a ‘Very High’ strategic vulnerability, value obtained choosing the Emergency phase scenario classification; in particular, the element that shows the maximum vulnerability in this scenario is the TF-28 road, placed at the edge of the slope affected by the deformation. This road constitutes the main road connection between the cities of Valle de San Lorenzo and San Miguel that is located 5 km eastward. InSAR data suggest a possible movement of a sector of the slope, that could not only impact the road, with a retrogressive movement, but also the private houses located at the bottom of the slope.

The second example exhibits a six measurement points ADA with mean velocity of -6.0 mm/yr affecting the GC-200 road in the sector that connects Tasarte with Mogan (Figure 12(B)). This coastal road is considered as one of the most hazardous roads in Spain regarding rockfalls (Sarro et al. 2017) and is a critical connection for the town and villages of the western part of the Gran Canaria Island with the biggest centres of the north (i.e. Las Palmas de Gran Canaria); moreover, this road is heavily used by local, commercial and touristic traffic because it is more direct and larger than the mountainous roads of the centre of the island (Longpré et al. 2008). The ADA accounts for a mean slope angle of 28° classified and it could be also classified as a landslide prone area. Considering the Emergency phase scenario, the GC-200 road is classified as a ‘Very high’ vulnerable

element at risk, representing a main transport route for the island. As shown by InSAR data, this situation requires certain attention because a possible landslide movement affecting this section of the road track could lead to its partial or complete interruption, causing social and economic repercussions for the population of the island. However, due to the low magnitude and reduce extent of both ADA, no direct action seems to be necessary (e.g. field work). Nevertheless, this ADA should be targeted in future monitoring upgrades performed with new Sentinel-1 acquisitions. In the case that the ADA magnitude and extension is increased fieldwork should be necessary to map the threatening landslide as well as the implementation of in situ monitoring techniques.

Discussion

The proposed methodology permitted to detect 108 areas of ‘potential risk’ in the three islands selected as test site for the procedure. The most powerful VEAM feature is its discriminatory ability to derive, in a reasonable time, those areas that recorded active deformation affecting one or more elements at risk starting from a very high number of input measurements (more than 1 million in this case). This is done by using a reproducible workflow that allows to drastically reduce the time needed for analysing a whole interferometric dataset on large areas (around 4000 km² for the test sites proposed).

The VEAM indicates in a simple way where and with which intensity a geohazard is affecting a territorial unit (municipality or district, depending on the working scale) and an element at risk, classified on the basis of its Strategic Vulnerability. This is the main feature of the methodology, designed to be a part of the risk management chain of the Civil Protection Authorities and intended as a way to facilitate the definition of the more hazardous areas of a territory starting from large datasets of measurement, thus providing a list of potential active phenomena that are affecting the infrastructures of a region, a municipality or a city. Thanks to this type of results, a campaign of periodical checks and ground surveys can be implemented in the Civil Protection Authorities procedures.

Another important feature is the scalability and versatility of the methodology; in fact, as shown by the test site applications, it is pertinent to completely different environmental contexts at different working scales, from a single municipality to an entire region. For example, in this paper we used as territorial units the municipalities of the island but it is possible to enlarge the scale of analysis, using cities, single district or other type of territorial subsets (i.e. slope units).

The methodology is also suited for a multi-temporal update of the InSAR dataset because of the relatively short time needed for its application. Using satellites with high revisit time such as Sentinel-1 (6 days using both satellites of the constellation) it is possible to update the results with a high temporal frequency, evaluating the presence of new ADA and the evolution of the already detected ones. The idea is to plan a new update of the Deformation Map, and so of the derived products (ADA map, Geohazard Activity Maps, VEAM) every 6 months or less by adding the new InSAR data (i.e. the interferograms) to the already existing interferograms network.

The applicability of the methodology and the expected results are influenced by intrinsic factors and limitations of the input data. From the interferometric point of view, the methodology can be applied using every type of SAR images (C-, X- and L-band sensors) as input of the InSAR analysis. The major limitation in the use of this type of data is the maximum displacement measurable between two acquisitions that is equal to $\lambda/4$, where λ is the wavelength of the radar signal, i.e. 1.4 cm for C-band sensors; considering not only the wavelength but also the revisiting time, the maximum deformation rate detectable by Sentinel-1 is 42.6 cm/yr (Crosetto et al. 2016). For this reason, phenomena with deformation rates below these thresholds can be successfully detected, such as volcanic deformations, subsidence and ‘slow-moving landslide’ (as defined by Cruden and Varnes 1996). Another limitation is the impossibility of finding reliable results in densely vegetated areas, where the coherence of the images falls down not allowing to obtain a network of measurement points suitable for the approach proposed. In addition, the level of information contained in

the elements at risk catalogue is another crucial issue that can invalidate the obtainable results; in fact, detailed data about the road network and the type of buildings are at least needed for the main urban agglomerations of the area of interest.

The classification proposed for the elements at risk was designed considering Civil Protection Authorities requirements, but it can be modified depending on specific needs of the final users without compromising the performances of the system.

Conclusions

In this work, we present a methodology, named VEAM, for the generation of impact assessment maps starting from InSAR-derived displacement data. The methodology aims at providing a simple product to the Civil Protection Authorities in which the areas of active deformation, defined on the basis of a velocity threshold and a clustering law, are classified on the basis of the vulnerability of the elements at risk present in these areas. The methodology has been tested in the Canary Islands (in particular Gran Canaria, La Gomera and Tenerife) where Sentinel-1 data and a catalogue of elements at risk were used as input of the proposed approach. The methodology allowed to detect more than 100 areas (involving 25 municipalities) that registered deformation rates above 4 mm/yr affecting one or more elements at risk categorized on the basis of a triple scenario classification system.

The obtained results are conceived to reduce the time needed for the analysis of an entire InSAR dataset (composed by millions of measurements), detecting those areas that represent a critical issue for a territorial unit (municipality) and that can be monitored and validated by ground check surveys. Moreover, this working strategy can be applied in other environments, using also different types of input InSAR data. The final goal is to provide a reproducible work flow that could be used not only by the Canary Islands Civil Protection but by other European Entities, adapting the methodology, in particular the vulnerability classification, to the needs of other entities.

Acknowledgements

This work was carried out in the framework of the European Project ‘SAFETY – Sentinel-1 for geohazard prevention and forecasting’, ECHO/SUB/2015/718679/Prev02-SAFETY. The authors thank Dr. Alicia Felpeto of the Instituto Geográfico Nacional (Madrid, Spain) for providing the volcanic susceptibility map.

Disclosure statement

No potential conflict of interest was reported by the authors.

ORCID

Lorenzo Solari  <http://orcid.org/0000-0003-3637-2669>
 Anna Barra  <http://orcid.org/0000-0001-6254-7931>
 Gerardo Herrera  <http://orcid.org/0000-0002-6633-9184>
 Silvia Bianchini  <http://orcid.org/0000-0003-2724-5641>
 Oriol Monserrat  <http://orcid.org/0000-0003-2505-6855>
 Marta Béjar-Pizarro  <http://orcid.org/0000-0001-7449-4048>
 Michele Crosetto  <http://orcid.org/0000-0001-8545-5490>

References

Abidin HZ, Andreas H, Gumilar I, Sidiq TP, Fukuda Y. 2013. Land subsidence in coastal city of Semarang (Indonesia): characteristics, impacts and causes. *Geomat Nat Haz Risk*. 4:226–240.

- Acosta J, Uchupi E, Muñoz A, Herranz P, Palomo C, Ballesteros M. 2003. Geologic evolution of the Canary Islands of Lanzarote, Fuerteventura, Gran Canaria and La Gomera and comparison of landslides at these islands with those at Tenerife, La Palma and El Hierro. *Mar Geophys Res.* 24:1–40.
- Ancochea E, Huertas MJ, Cantagrel JM, Coello J, Fúster JM, Arnaud N, Ibarrola E. 1999. Evolution of the Cañadas edifice and its implications for the origin of the Cañadas Caldera (Tenerife, Canary Islands). *J Volcanol Geotherm Res.* 88:177–199.
- Ancochea E, Brändle JL, Cubas CR, Hernán F, Herrera R, Huertas MJ. 2004. La Gomera. In: Vera JA, editor. *Geología de España [Geology of Spain]*. Madrid: InSGE-IGME; p. 658–660. Spanish.
- Ancochea E, Hernán F, Huertas MJ, Brändle JL, Herrera R. (2006.) A new chronostratigraphical and evolutionary model for La Gomera: implications for the overall evolution of the Canary Archipelago. *J Volcanol Geother Res.* 157:271–293.
- Barra A, Monserrat O, Mazzanti P, Esposito C, Crosetto M, Scarascia Mugnozza G. 2016. First insights on the potential of Sentinel-1 for landslides detection. *Geomat Nat Haz Risk.* 7:1–10.
- Barra A, Solari L, Béjar-Pizarro M, Monserrat O, Herrera G, Bianchini S, Crosetto M, Mateos RM, Sarro R, Moretti S. 2017a. Sentinel-1 data exploitation for geohazard activity map generation. *Proceedings of the 19th EGU General Assembly*; Apr 23–28; Vienna, Austria.
- Barra A, Solari L, Béjar-Pizarro M, Monserrat O, Bianchini S, Herrera G, Crosetto M, Sarro R, González-Alonso E, Mateos RM, et al. 2017b. A Methodology to Detect and Update Active Deformation Areas Based on Sentinel-1 SAR Images. *Remote Sens.* 9:1002.
- Béjar-Pizarro M, Ezquerro P, Herrera G, Tomás R, Guardiola-Albert C, Hernández JMR, Fernandez Merodo JA, Marchamalo M, Martínez R. 2017. Mapping groundwater level and aquifer storage variations from InSAR measurements in the Madrid aquifer, Central Spain. *J Hydrol.* 547:678–689.
- Bianchini S, Herrera G, Mateos RM, Notti D, Garcia I, Mora O, Moretti S. 2013. Landslide activity maps generation by means of Persistent Scatterer Interferometry. *Remote Sens.* 5:6198–6222.
- Bianchini S, Raspini F, Ciampalini A, Lagomarsino D, Bianchi M, Bellotti F, Casagli N. 2016. Mapping landslide phenomena in landlocked developing countries by means of satellite remote sensing data: the case of Dilijan (Armenia) area. *Geomat Nat Haz Risk.* 1–17.
- Bonforte A, Guglielmino F, Coltelli M, Ferretti A, Puglisi G. 2011. Structural assessment of Mount Etna volcano from permanent scatterers analysis. *Geochem Geophys Geosy.* 12:1–19.
- Calcaterra D, de Riso R, Santo A. 2003. Landslide hazard and risk mapping: experiences from Campania, Italy. In: Picarelli L, editor. *Fast slope movements, prediction and prevention for risk mitigation*. Bologna: Patron Editore; p. 63–70.
- Calvello M, Peduto D, Arena L. 2016. Combined use of statistical and DInSAR data analyses to define the state of activity of slow-moving landslides. *Landslides.* 14:473–489.
- Carracedo JC. 1994. The Canary Island: an example of structural control on the growth of large oceanic-island volcanoes. *J Volcanol Geotherm Res.* 60:225–241.
- Carracedo JC. 1996. Morphological and structural evolution of the western Canary Islands: hotspot-induced three-armed rifts or regional tectonic trends? *J Volcanol Geotherm Res.* 72:151–162.
- Carracedo JC, de la Nuez J, Pérez Torrado FJ, Rodríguez Badiola E, Guillou H. 2001. Geological map of the Teide-Pico Viejo volcanoes and the northwest and northeast rifts of Tenerife. Digital. CSIC database. [accessed 2017 Jul 25]. <http://hdl.handle.net/10261/4431>
- Carracedo JC, Pérez-Torrado FJ, Ancochea E, Meco J, Hernán F, Cubas CR, Casillas R, Rodríguez-Badiola E, Ahijado A. 2002. Cenozoic volcanism II, The Canary Islands. In: Gibsson W, Moreno T, editors. *The geology of Spain*. London: The Geological Society; p. 439–472.
- Cendrero, A. 1971. Estudio geológico y petrológico del complejo basal de la isla de La Gomera (Canarias) [Geological study of the basal complex in the La Gomera Island (Canaries)]. *Estud Geol.* 27:3–73. Spanish.
- Ciampalini A, Raspini F, Lagomarsino D, Catani F, Casagli N. 2016. Landslide susceptibility map refinement using PSInSAR data. *Remote Sens Environ.* 184:302–315.
- Crosetto M, Monserrat O, Cuevas-González M, Devanthery N, Crippa B. 2016. Persistent scatterer interferometry: a review. *ISPRS J Photogramm Remote Sens.* 115:78–89.
- Cruden DM, Varnes DJ. 1996. Landslide types and processes. In: Turner AK, Schuster RL. *Landslides: investigation and Mitigation*, Transportation research board special report (247). Washington (DC): National Academy Press; p. 36–75
- Devanthery M, Crosetto O, Monserrat M, Cuevas-González M, Crippa B. 2014. An approach to persistent scatterer interferometry. *Remote Sens.* 6:6662–6679.
- Dai FC, Lee CF, Ngai YY. 2002. Landslide risk assessment and management: an overview. *Eng Geol.* 64:65–87.
- Farr TG, Rosen PA, Caro E, Crippen R, Duren R, Hensley S, et al. 2007. The shuttle radar topography mission. *Rev Geophys.* 45:1–33.
- Fell R, Ho KK, Lacasse S, Leroi E. 2005. A framework for landslide risk assessment and management. In: Hungr O, Fell P, Couture R, Eberhardt E, editors. *Landslide risk management*. London: Taylor & Francis Group; p. 3–25.
- Fell R, Corominas J, Bonnard C, Cascini L, Leroi E, Savage WZ. 2008. Guidelines for landslide susceptibility, hazard and risk zoning for land-use planning. *Eng Geol.* 102:99–111.

- Glade T, Anderson M, Crozier M. 2005. *Landslide hazard and risk*. Chichester: John Wiley & Sons Publisher Ltd.
- Hanssen R. (2001.) *Radar interferometry*. Dordrecht: Kluwer Academic Publishers.
- Herrera G, Gutiérrez F, García-Davalillo JC, Guerrero J, Notti D, Galve JP, Fernandez-Merodo JA, Cooksley G. 2013. Multi-sensor advanced DInSAR monitoring of very slow landslides: the Tena Valley case study (Central Spanish Pyrenees). *Remote Sens Environ.* 128:31–43.
- Höbbling D, Füreder P, Antolini F, Cigna F, Casagli N, Lang S. 2012. A semi-automated object-based approach for landslide detection validated by persistent scatterer interferometry measures and landslide inventories. *Remote Sens.* 4:1310–1336.
- Holik JS, Rabinowitz PD, Austin JA. 1991. Effects of Canary hotspot volcanism on structure of oceanic-crust off Morocco. *J Geophys Res Solid Earth Planets.* 96:12039–12067.
- Hürlimann M, Martí J, Ledesma A. 2004. Morphological and geological aspects related to large slope failures on oceanic islands: the huge La Orotava landslides on Tenerife, Canary Islands. *Geomorphology.* 62:143–158.
- Kim JW, Lu Z, Qu F, Hu X. 2015. Pre-2014 mudslides at Oso revealed by InSAR and multi-source DEM analysis. *Geomat Nat Haz Risk.* 6:184–194.
- Kong WK. 2002. Risk assessment of slopes. *Q J Eng Geol.* 35:213–222.
- Lagios E, Papadimitriou P, Novali F, Sakkas V, Fumagalli A, Vlachou K, Del Conte S. 2012. Combined seismicity pattern analysis, DGPS and PSInSAR studies in the broader area of Cephalonia (Greece). *Tectonophysics.* 524:43–58.
- Lagios E, Sakkas V, Novali F, Bellotti F, Ferretti A, Vlachou K, Dietrich V. 2013. SqueeSARTM and GPS ground deformation monitoring of Santorini Volcano (1992–2012): tectonic implications. *Tectonophysics.* 594:38–59.
- Lee WJ, Lu Z, Jung HS, Ji L. 2017. Measurement of small co-seismic deformation field from multi-temporal SAR interferometry: application to the 19 September 2004 Huntoon Valley earthquake. *Geomat Nat Haz Risk.* 1–17.
- Llanes P, Herrera R, Gómez M, Muñoz A, Acosta J, Uchupi E, Smith D. 2009. Geological evolution of the volcanic island La Gomera, Canary Islands, from analysis of its geomorphology. *Mar Geol.* 264:123–139.
- Lomoschitz A, Hervas J, Yepes J, Meco J. 2008. Characterisation of a Pleistocene debris-avalanche deposit in the Tenetiguada Basin, Gran Canaria Island, Spain. *Landslides.* 5:227–234.
- Longpré MA, del Potro R, Troll VR, Nicoll GR. 2008. Engineering geology and future stability of the El Risco landslide, NW-Gran Canaria, Spain. *Bull Eng Geol Environ.* 67:165.
- Martí J, Hürlimann M, Ablay GJ, Gudmundsson A. 1997. Vertical and lateral collapses in Tenerife and other oceanic volcanic islands. *Geology.* 25:879–882.
- Martí J, Gudmundsson A. 2000. The Las Cañadas caldera (Tenerife, Canary Islands): an overlapping collapse caldera generated by magma-chamber migration. *J Volcanol Geotherm Res.* 103:161–174.
- Martí J, Felpeto A. 2010. Methodology for the computation of the volcanic susceptibility. Example for mafic and felsic eruptions on Tenerife (Canary Islands). *J Volcanol Geotherm Res.* 195:69–77.
- Massironi M, Zampieri D, Bianchi M, Schiavo A, Franceschini A. 2009. Use of PSInSARTM data to infer active tectonics: Clues on the differential uplift across the Giudicarie belt (Central-Eastern Alps, Italy). *Tectonophysics.* 476:297–303.
- Massonnet D, Feigl KL. 1998. Radar interferometry and its application to changes in the Earth's surface. *Rev Geophys.* 36:441–500.
- Menendez I, Silva PG, Martin-Betancor M, Perez-Torrado FJ, Guillou H, Scaillet S. 2008. Fluvial dissection, isostatic uplift, and geomorphological evolution of volcanic islands (Gran Canaria, Canary Islands, Spain). *Geomorphology.* 102:189–203.
- Mezcua J, Buforn E, Udías A, Rueda J. 1992. Seismotectonics of the Canary Islands. *Tectonophysics.* 208:447–452.
- Montoya L, Masser I. 2005. Management of natural hazard risk in Cartago, Costa Rica. *Habitat Int.* 29:493–509.
- Notti D, Davalillo JC, Herrera G, Mora O. 2010. Assessment of the performance of X-band satellite radar data for landslide mapping and monitoring: Upper Tena Valley case study. *Nat Hazards Earth Sys.* 10:1865.
- Notti D, Herrera G, Bianchini S, Meisina C, García-Davalillo JC, Zucca F. 2014. A methodology for improving landslide PSI data analysis. *Int J Remote Sens.* 35:2186–2214.
- Oliveira SC, Zêzere JL, Catalão J, Nico G. 2015. The contribution of PSInSAR interferometry to landslide hazard in weak rock-dominated areas. *Landslides.* 12:703–719.
- Papathoma-Köhle M, Neuhäuser B, Ratzinger K, Wenzel H, Dominey-Howes D. 2007. Elements at risk as a framework for assessing the vulnerability of communities to landslides. *Nat Hazards Earth Sys.* 7:765–779.
- Paris R, Guillou H, Carracedo JC, Pérez-Torrado FJ. 2005. Volcanic and morphological evolution of La Gomera (Canary Islands), based on new K–Ar ages and magnetic stratigraphy: implications for oceanic island evolution. *J Geol Soc. London* 162:501–512.
- Peltier A, Bianchi M, Kaminski E, Komorowski JC, Rucci A, Staudacher T. 2010. PSInSAR as a new tool to monitor pre-eruptive volcano ground deformation: Validation using GPS measurements on Piton de la Fournaise. *Geophys Res Lett.* 37:1–5.
- Rodriguez-Gonzalez A, Fernandez-Turiel JL, Perez-Torrado FJ, Hansen A, Aulinas M, Carracedo JC, Gimeno D, Guillou H, Paris R, Paterne M. 2009. The Holocene volcanic history of Gran Canaria island: implications for volcanic hazards. *J Quaternary Sci.* 24:697–709.

- Raspini F, Bardi F, Bianchini S, Ciampalini A, Del Ventisette C, Farina P, Ferrigno F, Solari L, Casagli, N. 2016. The contribution of satellite SAR-derived displacement measurements in landslide risk management practices. *Nat Hazards*. 84:1–25.
- Righini G, Pancioli V, Casagli N. 2012. Updating landslide inventory maps using Persistent Scatterer Interferometry (PSI). *Int J Remote Sens*. 33:2068–2096.
- Roessner S, Wetzel HU, Kaufmann H, Sarnagoev A. 2005. Potential of satellite remote sensing and GIS for landslide hazard assessment in Southern Kyrgyzstan (Central Asia). *Nat Hazards*. 35:395–416.
- Salvati P, Pernice U, Bianchi C, Marchesini I, Fiorucci F, Guzzetti F. 2016. Communication strategies to address geohydrological risks: the POLARIS web initiative in Italy. *Nat Hazard Earth Sys*. 16:1487–1497.
- Sarro R, Mateos RM, Herrera G, García-Moreno I, Reichenbach P, Carralero IP, Naranjo J, Bejar-Pizarro M, Monserrat O, Solari L, et al. 2017. Methodology for assessing rockfall susceptibility within the ambit of civil protection: the Safety project. Proceedings of the 6th Interdisciplinary Workshop on Rockfall Protection, Barcelona, Spain.
- Schmincke HU. 1993. Geological field guide of Gran Canaria. 6th ed. Kiel: Pluto Press.
- Sobradelo R, Martí J. 1993. Bayesian event tree for long-term volcanic hazard assessment: Application to Teide-Pico Viejo stratovolcanoes, Tenerife, Canary Islands. *J Geophys Res B: Solid Earth*. 115:B5.
- Solari L, Ciampalini A, Raspini F, Bianchini S, Moretti S. 2016. PSInSAR analysis in the Pisa Urban Area (Italy): a case study of subsidence related to stratigraphical factors and urbanization. *Remote Sens*. 8:120.
- Spence RJ, Baxter PJ, Zuccaro G. 2004. Building vulnerability and human casualty estimation for a pyroclastic flow: a model and its application to Vesuvius. *J Volcanol Geotherm Res*. 133:321–343.
- Tomás R, Romero R, Mulas J, Marturìà JJ, Mallorquí JJ, López-Sánchez JM, Herrera G, Gutiérrez F, González PJ, Fernández J, et al. 2014. Radar interferometry techniques for the study of ground subsidence phenomena: a review of practical issues through cases in Spain. *Environ Earth Sci*. 71:163–181.
- Torres R, Snoeij P, Geudtner D, Bibby D, Davidson M, Attema E, Potin P, Rommen B, Floury N, Brown M, et al. 2012. GMES Sentinel-1 mission. *Remote Sens Environ*. 120:9–24.
- Uzielli M, Nadim F, Lacasse S, Kaynia AM. 2008. A conceptual framework for quantitative estimation of physical vulnerability to landslides. *Eng Geol*. 102:251–256.
- Vilardo G, Isaia R, Ventura G, De Martino P, Terranova C. 2010. InSAR Permanent Scatterer analysis reveals fault reactivation during inflation and deflation episodes at Campi Flegrei caldera. *Remote Sens Environ*. 114:2373–2383.
- Watts A, Masson D. 2001. New sonar evidence for recent catastrophic collapses of the north flank of Tenerife, Canary Islands. *Bull Volcanol*. 63:8–19.